

**BRILLOUIN LIGHT SCATTERING STUDIES OF
EPITAXIAL FERROMAGNETIC FILMS**

by

John Robert Dutcher

B.Sc. (Engineering-Physics), Dalhousie University, 1983

M.Sc., University of British Columbia, 1985

A THESIS SUBMITTED IN PARTIAL FULFILLMENT OF
THE REQUIREMENTS FOR THE DEGREE OF
DOCTOR OF PHILOSOPHY

in the Department

of

Physics

© John Robert Dutcher 1988

SIMON FRASER UNIVERSITY

September 1988

All rights reserved. This work may not be
reproduced in whole or in part, by photocopy
or other means, without permission of the author.

APPROVAL

Name: John Robert Dutcher

Degree: Doctor of Philosophy

Title of Thesis: Brillouin Light Scattering Studies of Epitaxial Ferromagnetic Films

Examining Committee:

Chairman: M. Plischke

J.F. Cochran
Senior Supervisor

B. Heinrich

J.C. Irwin

A.S. Arrott

C.E. Patton
External Examiner
Department of Physics
Colorado State University

Date Approved: September 15, 1988

PARTIAL COPYRIGHT LICENSE

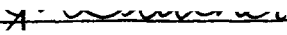
I hereby grant to Simon Fraser University the right to lend my thesis, project or extended essay (the title of which is shown below) to users of the Simon Fraser University Library, and to make partial or single copies only for such users or in response to a request from the library of any other university, or other educational institution, on its own behalf or for one of its users. I further agree that permission for multiple copying of this work for scholarly purposes may be granted by me or the Dean of Graduate Studies. It is understood that copying or publication of this work for financial gain shall not be allowed without my written permission.

Title of Thesis/Project/Extended Essay

Brillouin Light Scattering Studies of

Epitaxial Ferromagnetic Films

Author:


(signature)

John Robert DUTCHER

(name)

SEPTEMBER 19, 1988

(date)

ABSTRACT

A Brillouin light scattering (BLS) system using a high contrast, tandem Fabry-Perot interferometer was designed and constructed. BLS from thermally excited magnetic waves in epitaxial, ferromagnetic films was measured in air at room temperature. Both ultrathin iron films grown by molecular beam epitaxy and thick iron whisker crystals were studied.

BLS measurements were made on ultrathin iron films grown on single crystals of silver and copper, bcc Fe/Ag(001) and fcc Fe/Cu(001) respectively, and superlattices of ultrathin iron and copper films. BLS signals were observed easily for samples as thin as 3 monolayers of iron. Large magnetic surface anisotropies with the easy axis along the sample normal were observed in all of the films. For the fcc Fe/Cu(001) single films and superlattices and one of the bcc Fe/Ag(001) films, the anisotropies were large enough to orient the magnetization perpendicular to the sample surface in zero applied field at room temperature. Ultrathin bilayers of nickel and iron grown on silver single crystals, Ni/Fe/Ag(001), were also studied.

BLS measurements were also made on a Fe(001) whisker covered with epitaxial gold and silver. The surface mode frequencies were measured to within ± 0.03 GHz. Observation of the 180° domain wall enabled very accurate determinations of the surface spin pinning and the sample heating due to the incident laser light.

The frequencies of the normal modes of a magnetic film and the intensities of light scattered from these modes were calculated. Magnetic damping and metallic conductivity were included. Exchange and the spin pinning boundary conditions were included for magnetizations lying in the sample plane. Calculations which allowed the magnetization to tilt out of the sample plane did not include exchange and spin pinning. For the ultrathin films, the magnetic parameters were obtained by comparison of experiment with theory;

they were in very good agreement with ferromagnetic resonance results. For the iron whisker, excellent fits to the data were obtained using magnetic parameters that were within 1% of published values for iron. The spin pinning parameters for the whisker covered with gold and silver were $K_z^F = 0.54$ and 0.79 erg/cm² respectively, with the easy axis perpendicular to the sample surface. These values agreed very well with K_z^F values determined for ultrathin iron films covered with gold and silver.

ACKNOWLEDGEMENTS

It has been a pleasure and an honour to work with John Cochran. His direct involvement with the light scattering project has greatly improved the quality of this work. John is responsible for the calculation presented in section 3.1.

I thank Bretislav Heinrich for his many excellent suggestions concerning experimental techniques and interpretation of the data.

I gratefully acknowledge the contribution of Carl Patton, who performed the initial design and construction of the light scattering system.

I thank John, Bret, Carl, Chuck Irwin and Tony Arrott for their valuable comments on this thesis.

I extend many thanks to Frank Wick and the members of the machine and electronics shops. They constructed much of the hardware of the apparatus quickly and expertly.

I was very fortunate to have an abundance of samples available for study. Ultrathin single films of iron on silver and ultrathin bilayer films of nickel and iron on silver were provided by Bret Heinrich, Ken Urquhart and Stephen Purcell. Ultrathin single films and superlattices of iron on copper were supplied by Bill Egelhoff, Dan Steigerwald and Issac Jacob. The iron whisker crystal was grown by Xuanzeng Li and was prepared in ultrahigh vacuum by Bret Heinrich. I thank one and all.

To my co-workers Jeff Rudd, Stephen Purcell, Ken Urquhart and Ken Myrtle go my thanks for their many valuable contributions to this work. I am grateful to Srinivasan Gopalan for teaching me the tricks of the trade during a visit to Colorado State University. Also, I thank Bill McMullan, Mike Thewalt, Andrew Kurn and Don Hunter for useful discussions.

I thank my wife Heather for her support and encouragement during the course of this work, as well as for all of her help in the preparation of this thesis.

I am grateful to the Natural Sciences and Engineering Research Council of Canada, Simon Fraser University and the O'Brien Foundation for financial support.

TABLE OF CONTENTS

Approval		ii
Abstract		iii
Acknowledgements		v
List of Tables		x
List of Figures		xi
1.	Introduction	1
1.1	Brillouin light scattering	1
1.2	Historical perspective	10
1.3	Scope of thesis	16
2.	Experimental Apparatus	18
2.1	Fabry-Perot interferometry	18
2.1.1	Single interferometer	18
2.1.2	Multipassed single interferometer	28
2.1.3	Multipassed tandem interferometer	30
2.1.4	The Sandercock interferometer	36
2.2	The Brillouin light scattering system	39
2.2.1	Incident beam optics	39
2.2.2	Collected beam optics	44
2.2.3	Fabry-Perot multipassing optics	46
2.2.4	Photomultiplier optics	49
2.2.5	Data collection electronics	51
2.2.6	High resolution frequency measurements	51
2.2.7	Experimental uncertainties	56
2.2.8	System performance	63

3.	Calculation of the Light Scattering from Thermal Magnons in Thin Magnetic Films	71
3.1	The light scattering calculation with the magnetization lying in the sample plane	72
3.1.1	The normal modes of a thin magnetic film	72
3.1.2	The energy stored in a normal mode	91
3.1.3	The polarization distribution corresponding to a normal mode	95
3.1.4	The intensity of the scattered radiation	101
3.1.5	Discussion	107
3.1.5.1	The surface mode	107
3.1.5.2	Effect of metallic conductivity on resonant frequencies	109
3.1.5.3	Comparison with the theory of Camley and Mills	111
3.1.5.4	Application to ultrathin films	113
3.1.5.4.1	The calculation without surface pinning	113
3.1.5.4.2	The calculation with surface pinning	116
3.1.5.4.3	Comparison with ferromagnetic resonance condition	125
3.2	The light scattering calculation allowing the magnetization to tilt out of the sample plane	130
3.2.1	The surface mode frequency	131
3.2.2	The energy stored in a normal mode	150
3.2.3	The polarization distribution and the scattered light intensity	152
3.2.4	Discussion	154
3.3	Application of the calculation to the experiment	159

4.	Ultrathin Iron Single Films and Nickel/Iron Bilayer Films Grown on Silver	162
4.1	Iron on Silver	162
4.1.1	Introduction	162
4.1.2	Sample preparation	165
4.1.3	Brillouin light scattering results and discussion	169
4.2	Nickel/Iron on Silver	186
4.2.1	Introduction	186
4.2.2	Sample preparation	189
4.2.3	Brillouin light scattering results and discussion	192
5.	Ultrathin Iron Single Films and Superlattices Grown on Copper	205
5.1	Introduction	205
5.2	Sample preparation	209
5.3	Brillouin light scattering results and discussion	213
6.	An Iron Whisker Prepared in Ultrahigh Vacuum	232
6.1	Introduction	232
6.2	Sample preparation	236
6.3	The light scattering calculation for thick magnetic films	243
6.4	Brillouin light scattering results and discussion	246
7.	Summary and Conclusions	262
	References	266

LIST OF TABLES

Table	Page
1.1 The real and imaginary parts of the index of refraction and the optical skin depth for different metals. _____	9
2.1 Calculated signal peak frequencies for Figure 2.17 (c) and (d) within the frequency range +8.5 GHz to -8.5 GHz. _____	55
3.1 A comparison of the calculated resonant frequencies of a metallic magnetic film of thickness d . _____	110
4.1 The Fe on Ag(001) samples studied by BLS. _____	168
4.2 The magnetic parameters for the Fe on Ag(001) samples of Table 4.1. _____	180
4.3 The Ni/Fe on Ag(001) bilayer samples studied by BLS. _____	191
4.4 The magnetic parameters for the Ni/Fe on Ag(001) bilayer samples of Table 4.3, as determined by FMR. _____	194
5.1 The fcc Fe on Cu(001) single film and superlattice samples studied by BLS. _____	211
5.2 The magnetic parameters for the fcc Fe on Cu(001) single film and superlattice samples of Table 5.1. _____	225
6.1 The percentage change in δf for a 5% change in each of the magnetic parameters for a thick magnetic film. _____	258

LIST OF FIGURES

Figure	Page
1.1 Scattering geometry for a light wave of wavevector k_i incident on a magnetic wave of wavevector k . _____	3
1.2 Scattering geometry for a light wave of wavevector k_i incident on a magnetic wave of wavevector k in an opaque sample. _____	11
2.1 A plane Fabry-Perot interferometer. _____	19
2.2 Calculated transmitted intensity versus plate separation for monochromatic light of wavelength λ . _____	21
2.3 Calculated transmitted intensity versus plate separation for light with monochromatic components of wavelength λ and λ' . _____	24
2.4 Calculated transmitted intensity versus plate separation and frequency shift. _____	26
2.5 A cube corner used to multipass a FP interferometer. _____	29
2.6 Calculated transmitted intensity versus frequency shift for 1, 2 and 3 passes of light through the FP interferometer. _____	31
2.7 Two FP interferometers in tandem. _____	33
2.8 Calculated transmitted intensity versus relative plate separation for each FP in the tandem interferometer. _____	34
2.9 Calculated transmitted intensity versus relative plate separation for tandem interferometer. _____	35
2.10 The Sandercock tandem interferometer. _____	37
2.11 The BLS system. _____	40
2.12 The incident beam optics. _____	41
2.13 Sample holder geometry. _____	43
2.14 The collected beam optics. _____	45
2.15 The FP multipassing optics. _____	48
2.16 The photomultiplier optics. _____	50
2.17 Calculated transmitted intensity versus frequency shift for a 25Å thick iron film. _____	53
2.18 Scattering geometry. _____	59
2.19 Scattering geometry, including the nonzero collection angle of the Nikon camera lens. _____	61
2.20 BLS spectrum for sample 5.2 ($H = 5.81$ kOe). _____	65
2.21 BLS spectrum for a 50Å thick permalloy film ($H = 1.92$ kOe). _____	66

2.22	BLS spectrum for a 15 ML Au/Fe(001) whisker in zero applied magnetic field. _____	68
2.23	BLS spectrum for sample 4.11 ($H = 3.99$ kOe). _____	69
3.1	The geometry used for the light scattering calculation with an in-plane magnetization. _____	73
3.2	The light scattering spectrum calculated using our formalism for an 850\AA thick "iron" film. _____	112
3.3	The light scattering spectrum calculated by Camley and Grimsditch for an 850\AA thick "iron" film. _____	114
3.4	The light scattering spectrum calculated using our formalism for an 850\AA thick "iron" film showing the natural linewidths. _____	115
3.5	Calculated frequency versus magnetic film thickness d for the lowest normal modes of the film. _____	117
3.6	Calculated scattering intensity versus magnetic film thickness d for the lowest frequency normal modes of the film. _____	118
3.7	Calculated surface mode frequency versus magnetic film thickness for an "iron" film. _____	120
3.8	Calculated scattering intensity versus magnetic film thickness d for an "iron" film. _____	122
3.9	Calculated surface mode frequency versus applied magnetic field for a 10\AA thick "iron" film. _____	124
3.10	Calculated scattering intensity versus applied magnetic field for a 10\AA thick "iron" film. _____	126
3.11	The geometry used for the light scattering calculation with the magnetization tilted out of the sample plane. _____	133
3.12	Calculated surface mode frequency as a function of applied magnetic field for a 10\AA thick iron film for different values of the first and second order uniaxial anisotropies. _____	155
3.13	Calculated tilt angle of the magnetization as a function of applied magnetic field for a 10\AA thick iron film for different values of the first and second order uniaxial anisotropies. _____	158
3.14	Calculated scattered intensity as a function of applied magnetic field for a 10\AA thick iron film for different values of the first and second order uniaxial anisotropies. _____	160

Figure	xiii Page
4.1 The growth of bcc Fe on fcc Ag(001). _____	163
4.2 Fe on Ag(001) sample geometry. _____	166
4.3 BLS spectrum and magnetic field dependence of the surface mode frequency for sample 4.1. _____	170
4.4 BLS spectrum and magnetic field dependence of the surface mode frequency for sample 4.2. _____	171
4.5 BLS spectrum and magnetic field dependence of the surface mode frequency for sample 4.3. _____	172
4.6 BLS spectrum and magnetic field dependence of the surface mode frequency for sample 4.4. _____	173
4.7 BLS spectrum and magnetic field dependence of the surface mode frequency for sample 4.5. _____	174
4.8 BLS spectrum and magnetic field dependence of the surface mode frequency for sample 4.6. _____	175
4.9 BLS spectrum and magnetic field dependence of the surface mode frequency for sample 4.7. _____	176
4.10 BLS spectra for sample 4.8. _____	177
4.11 BLS spectra for sample 4.9. _____	178
4.12 Magnetic field dependence of the surface mode frequency for samples 4.8 and 4.9. _____	179
4.13 Surface mode frequency versus magnetic film thickness d for Au-covered Fe on Ag(001) crystals. _____	182
4.14 Effective magnetization versus magnetic film thickness d for Au-covered Fe on Ag(001) crystals. _____	185
4.15 Magnetic field dependence of the surface mode frequency for sample 4.6, with calculated fits using $g = 2.00$ and $g = 2.09$. _____	187
4.16 Ni/Fe bilayer sample geometry. _____	190
4.17 BLS spectra for sample 4.10 for the easy and hard ₁ axes. _____	195
4.18 BLS spectrum for sample 4.10 for the hard ₂ axis and magnetic field dependence of the surface mode frequency for sample 4.10. _____	196
4.19 Surface mode frequency and linewidth as a function of the in-plane angle between the applied field and the crystal (001) axis for sample 4.10. _____	198

4.20	BLS spectrum and magnetic field dependence of the surface mode frequency for sample 4.11. _____	199
4.21	The frequency difference Δf as a function of the in-plane angle between the applied field and the crystal (001) axis for sample 4.11. _____	201
4.22	BLS spectrum and magnetic field dependence of the surface mode frequency for sample 4.12. _____	202
5.1	The growth of fcc Fe on fcc Cu(001). _____	207
5.2	Fe on Cu(001) sample geometry. _____	210
5.3	BLS spectra for sample 5.1. _____	214
5.4	Magnetic field dependence of the surface mode frequency for samples 5.1 and 5.2. _____	215
5.5	BLS spectra for sample 5.2. _____	216
5.6	BLS spectrum and magnetic field dependence of the surface mode frequency for sample 5.3. _____	217
5.7	BLS spectrum and magnetic field dependence of the surface mode frequency for sample 5.4. _____	218
5.8	BLS spectrum and magnetic field dependence of the surface mode frequency for sample 5.5. _____	219
5.9	BLS spectra for sample 5.6. _____	220
5.10	BLS spectrum and magnetic field dependence of the surface mode frequency for sample 5.6. _____	221
5.11	BLS spectrum and magnetic field dependence of the surface mode frequency for sample 5.7. _____	222
5.12	BLS spectra for sample 5.8. _____	223
5.13	Magnetic field dependence of the surface mode frequency for sample 5.8 and BLS spectrum for sample 5.10. _____	224
5.14	Scattering intensity as a function of applied magnetic field for sample 5.6. _____	231
6.1	The domain structure of a perfect Fe(001) whisker in zero applied field H . _____	234
6.2	The domain structure of a perfect Fe(001) whisker for $H = 0$ and $0 \leq H \leq H_d$. _____	235

6.3	RHEED pattern obtained for clean Fe(001) whisker surface with the electron beam along the [110] direction of the whisker. _____	238
6.4	RHEED pattern obtained for clean Fe(001) whisker surface with the electron beam along the [100] direction of the whisker and RHEED patterns obtained for 15 ML Au on the Fe(001) whisker. _____	240
6.5	RHEED specular spot intensity oscillations during the growth of Au on the Fe(001) whisker. _____	242
6.6	Calculated spectrum for a 5 μ thick iron film for H = 5.033 kOe. _____	245
6.7	BLS spectrum for the 15 ML Au/Fe(001) whisker using the tandem interferometer and H = 5.003 kOe. _____	247
6.8	BLS spectrum for the 15 ML Au/Fe(001) whisker using the single interferometer with a large FSR to observe the 180° domain wall. _____	250
6.9	BLS spectrum for the 15 ML Au/Fe(001) whisker using the single interferometer with a small FSR to observe the 180° domain wall. _____	251
6.10	Calculated spectra for a 5 μ thick iron film for H = 0. _____	252
6.11	Measured dependence of the frequency shift Δf on the incident laser power. _____	254
6.12	Calculated surface mode frequency as a function of sample temperature. _____	256
6.13	Calculated dependence of the frequency shift Δf on the spin pinning coefficient K_z^F . _____	257
6.14	Magnetic field dependence of the surface mode frequency for the 15 ML Au/Fe(001) whisker. _____	261

CHAPTER ONE

INTRODUCTION

The work presented in this thesis concerns the scattering of light from thermally excited magnetic waves in epitaxial, metallic, ferromagnetic films. Such experiments have been possible since the recent advances in the experimental techniques of Brillouin light scattering (BLS) by Sandercock (Sandercock, 1970; and Sandercock, 1980a) and in the growth of ferromagnetic films by molecular beam epitaxy techniques (Prinz, 1985; and Heinrich et al., 1988a). The unique magnetic properties expected from carefully deposited magnetic films with thicknesses of only a few atomic layers served as an impetus to construct the BLS system described in this thesis. In the light scattering experiment, measurement of the frequency and wavevector of the scattered light wave and knowledge of these attributes for the incident light wave determines the frequency and wavevector of the magnetic waves in the sample. By relating the frequency and wavevector of the magnetic waves to the magnetic properties of the sample using a phenomenological theory, BLS can be used as a tool to characterize the magnetic properties of the sample.

In section 1.1, a simple description of BLS is presented, and the application of BLS to the study of magnetic waves in opaque materials is discussed. The historical perspective for the BLS experiments of this thesis is provided in section 1.2, and in section 1.3 the contents of the remainder of this thesis are summarized.

1.1 Brillouin light scattering

In the light scattering experiment, most of the incident light is scattered from static modulations in the sample. The scattered light has the same frequency as the incident light and the process is called elastic light scattering. The rest of the incident light is scattered from waves moving in the sample. The frequency of the light scattered from the moving

waves is shifted with respect to that of the incident light and the process is called inelastic light scattering.

The inelastic light scattering process can be described in simple terms. A light wave of frequency f_i and wavevector \mathbf{k}_i scatters from a second wave of frequency f and wavevector \mathbf{k} . For the purposes of illustration, we take the second wave to be a magnetic wave with its frequency f in the microwave range ($\sim 10^{10}$ Hz). The light wave is in general, obliquely incident on the magnetic wave, as shown in figure 1.1(a). The scattered wave has frequency f_s and wavevector \mathbf{k}_s . We assume that the scattering process takes place in a material which does not attenuate the optical waves; in other words, the material has a real index of refraction n . The frequencies and wavevectors of the waves must obey conservation rules (see, for example, Sandercock, 1982):

$$f_s = f_i \pm f \quad (1.1)$$

$$\mathbf{k}_s = \mathbf{k}_i \pm \mathbf{k} \quad (1.2)$$

With reference to figure 1.1(a), the conservation rule for the wavevectors can be written in component form as

$$k_s \sin\theta_s = -k_i \sin\theta + k \sin\theta_m \quad (1.3)$$

$$-k_s \cos\theta_s = k_i \cos\theta - k \cos\theta_m . \quad (1.4)$$

For the special case of 180° backscattering of the light, \mathbf{k}_s and \mathbf{k}_i are antiparallel ($\theta = \theta_s = \theta_m$). For this case, see figure 1.1(b), equation (1.4) becomes

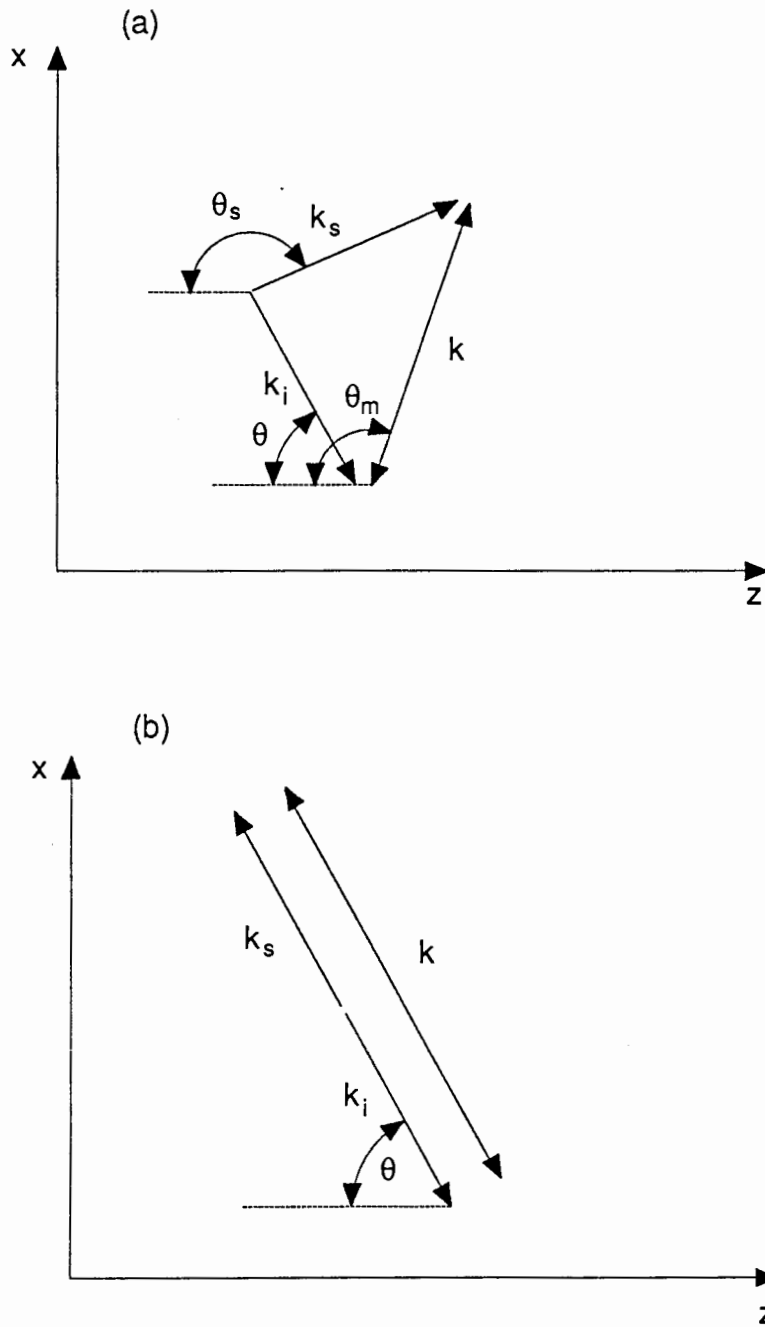


Figure 1.1

Scattering geometry for a light wave of wavevector k_i incident on a magnetic wave of wavevector k . The scattered wave wavevector is k_s . The angles θ , θ_m and θ_s are measured between the z -axis and k_i , k and k_s respectively.

- (a) Incident light wave and magnetic wave noncollinear.
- (b) Incident light wave and magnetic wave collinear.

$$k = k_i + k_s. \quad (1.5)$$

As mentioned above, we take f to be small compared to f_i . From equation (1.1), $f_s \sim f_i$. Therefore $k_s \sim k_i$, since $k_s = 2\pi n f_s / c$ and $k_i = 2\pi n f_i / c$, and equation (1.5) becomes

$$k = 2k_i = 2k_s. \quad (1.6)$$

The frequency shift of the scattered light with respect to the incident light can be understood in terms of the concept of Doppler frequency shifts; there is a clear discussion of this point by Slater (Slater, 1958). We consider a reference frame fixed in the laboratory (lab frame) and a reference frame moving with the magnetic wave at speed v (moving frame). For 180° backscattering, the frequency f_i' of the incident light wave measured in the moving frame is given by

$$f_i' = f_i \left(1 \pm \frac{nv}{c} \right), \quad (1.7)$$

where f_i is the frequency of the incident light wave measured in the lab frame, n is the index of refraction of the surrounding medium and c/n is the speed of light in the surrounding medium. The plus and minus signs refer to the magnetic wave moving toward and away from an observer in the lab frame, respectively. The frequency f_s of the scattered light wave measured in the lab frame is given by

$$f_s = \frac{f_i'}{\left(1 \mp \frac{nv}{c} \right)}. \quad (1.8)$$

Therefore the frequency f_s of the scattered light wave in the lab frame can be expressed in terms of the frequency f_i of the incident light wave in the lab frame as

$$f_s = f_i \left(\frac{1 \pm \frac{nv}{c}}{1 \mp \frac{nv}{c}} \right). \quad (1.9)$$

Since $v \ll c/n$, we can write

$$f_s = f_i \pm f_i \left(\frac{2nv}{c} \right) = f_i \pm \left(\frac{2k_i f}{k} \right). \quad (1.10)$$

Using equation (1.6), we get

$$f_s = f_i \pm f. \quad (1.11)$$

Equation (1.11) is the same equation as equation (1.1). The scattered wave is either upshifted or downshifted in frequency relative to the incident wave. The scattering process can be described in terms of the conservation rules for frequency, equation (1.1), and wavevector, equation (1.2). The incident wavevector is known since the wavelength of the incident light and its direction in space are known. The scattered wavevector is fixed by the scattering geometry. This determines the wavevector of the magnetic wave inside the sample. By measuring the frequency of the scattered light wave relative to that of the incident light wave, the frequency of the magnetic wave inside the sample is also determined.

The terms Brillouin light scattering (BLS) and Raman light scattering (RLS) are both used to describe the inelastic scattering of light. Both scattering processes involve excitation wavevectors that are small ($\sim 10^5 \text{ cm}^{-1}$) compared with the wavevector value at

the edge of the Brillouin zone ($\sim 10^8 \text{ cm}^{-1}$), so that the scattering events involve excitations having wavevectors which correspond to the center of the Brillouin zone. The two processes are distinguished by the size of the frequency shift between the incident and scattered light. In this thesis, the unit of measure for frequency shifts will be GHz, where $30 \text{ GHz} = 1 \text{ cm}^{-1} = 0.12 \text{ meV}$. BLS frequency shifts range from approximately 1 GHz to 500 GHz, whereas RLS frequency shifts range from approximately 500 GHz to 10^5 GHz . Because of the large difference in the size of the frequency shifts for BLS and RLS, different experimental techniques are used. In a BLS experiment, a Fabry-Perot interferometer is used to separate the inelastically scattered light from the elastically scattered light (the Fabry-Perot interferometer is described in detail in section 2.1); in a RLS experiment, a grating spectrometer is used for the same purpose (see, for example, Cottam and Lockwood, 1986). BLS is the experimental technique used in the work described in this thesis.

BLS usually refers to the scattering of light from thermally excited sound waves. Instead, we are interested in the scattering from thermally excited magnetic waves. Thermal fluctuations excite the magnetic normal modes of the film, causing the magnetization to precess about its equilibrium direction. The precessing magnetization modulates the index of refraction of the film. The interaction between the modulated index of refraction and the electric field of the incident optical wave generates a distribution of electric dipoles. These dipoles oscillate at a frequency which is equal to the optical frequency plus and minus the frequency of the magnetic normal mode and the dipole distribution generates the scattered optical wave. This scattering process is described in detail in Chapter Three. The scattering process from sound waves is identical to that described above, except that the electric field of the incident optical wave is coupled to the thermally excited lattice displacement amplitudes of the sound wave through either the elasto-optic or the surface corrugation effects (Sandercock, 1982).

We are interested in BLS from magnetic waves in metallic films which are opaque to optical radiation. The penetration depth of the light into a metallic sample can be obtained from the imaginary part of the index of refraction of the metal. The electric field E of a plane light wave propagating into the metal along the sample normal (+z-axis) has the spatial dependence $E \sim e^{ikz}$, where $k = n(\omega/c)$ is the wavevector of the light wave inside the metal and n is the complex index of refraction of the metal. We write n in terms of its real and imaginary parts, $n = n_r + i n_i$, where n_r and n_i are real quantities. The spatial and temporal dependence of the electric field can be written as

$$E \sim e^{-\frac{\omega}{c}n_i z} e^{i\frac{\omega}{c}n_r z} e^{-i\omega t}. \quad (1.12)$$

The real part of the electric field can be written as

$$E \sim e^{-\frac{\omega}{c}n_i z} \cos\left(\frac{\omega}{c}n_r z - \omega t\right) \quad (1.13)$$

The intensity of the light $I = E^2$ is therefore

$$I = E^2 \sim e^{-2\frac{\omega}{c}n_i z} \cos^2\left(\frac{\omega}{c}n_r z - \omega t\right). \quad (1.14)$$

When averaged over time, the squared cosine term becomes equal to $\frac{1}{2}$ and we have

$$\langle I \rangle = \langle E^2 \rangle \sim e^{-2\frac{\omega}{c}n_i z} \quad (1.15)$$

The factor $e^{-2\frac{\omega}{c}n_i z}$ in equation (1.15) determines the attenuation of the intensity of the light as it travels into the metal. We define the skin depth δ_{opt} of the light as

$$\delta_{\text{opt}} = \frac{c}{2\omega n_i} \quad (1.16)$$

such that the spatial dependence of the time-averaged intensity of the light is given by

$$\langle I \rangle = \langle E^2 \rangle \sim e^{-z/\delta} \quad (1.17)$$

For $z = \delta_{\text{opt}}$, $\langle I \rangle$ is equal to $\frac{1}{e}$ of its value at $z = 0$. For light of wavelength $\lambda = 514.5$ nm, equation (1.16) becomes

$$\delta_{\text{opt}} = \frac{409 \text{ \AA}}{n_i} \quad (1.18)$$

The complex indices of refraction have been carefully measured as a function of frequency by Johnson and Christy for noble metals (Johnson and Christy, 1972) and transition metals (Johnson and Christy, 1974). The values of n_r and n_i ($\lambda = 514.5$ nm) for the different metals studied in this thesis are listed in table 1.1. A typical value of δ_{opt} is 150 Å: the light is attenuated within a very short distance from the surface.

There are two important aspects of BLS from opaque materials. First of all, the BLS technique is surface sensitive, in that the light probes only the region of the sample which is essentially within a distance δ_{opt} of the surface. Therefore BLS is necessarily sensitive to the surface properties of opaque samples. A consequence of the limited penetration of the light is that the amount of elastic scattering is determined primarily by the smoothness of the surface, since light is elastically scattered from the imperfections on the surface of the

sample. It is important that the film surface be smooth on the scale of the wavelength of light ($\lambda \sim 0.5 \mu$). Another important aspect of BLS from opaque materials is that only the wavevector parallel to the sample surface is conserved in the scattering process; this is a simple consequence of the boundary conditions which must be satisfied by the optical electromagnetic fields. The Fourier transform of equation (1.11) for the spatial dependence of E normal to the sample surface yields a distribution of wavevectors perpendicular to the sample surface (Sandercock and Wetling, 1979); the real part of this distribution exhibits a maximum at $k_z = n_r \frac{\omega}{c}$ and has a full width at half-maximum of $\Delta k_z = \frac{1}{\delta_{\text{opt}}}$. Since δ_{opt} is small ($\sim 150 \text{ \AA}$), the uncertainty in the perpendicular wavevector k_z is large ($\sim 10^6 \text{ cm}^{-1}$) and there is no conservation rule for k_z . The wavevector conservation rule applies only to k_x , see equation (1.3), for opaque materials. This is illustrated in figure 1.2 for the backscattering geometry ($\theta_s = \theta$); the wavevector conservation rule for components along the sample surface is given by

$$k_x = 2k_i \sin\theta . \quad (1.19)$$

1.2 Historical perspective

Inelastic scattering of light from acoustic sound waves was predicted by Brillouin (Brillouin, 1922) in 1922 and, independently, by Mandelstam (Mandelstam, 1926) in 1926. This effect was first observed experimentally in transparent liquids by Gross (Gross, 1930) in 1930 and it is now commonly known as Brillouin light scattering (BLS).

The possibility of using the BLS technique for the study of magnetic waves in solids became a reality in 1970 due to a significant innovation of Sandercock (Sandercock, 1970; and Sandercock, 1971). He demonstrated that the sensitivity of the Fabry-Perot interferometer could be dramatically increased by passing the scattered light several times

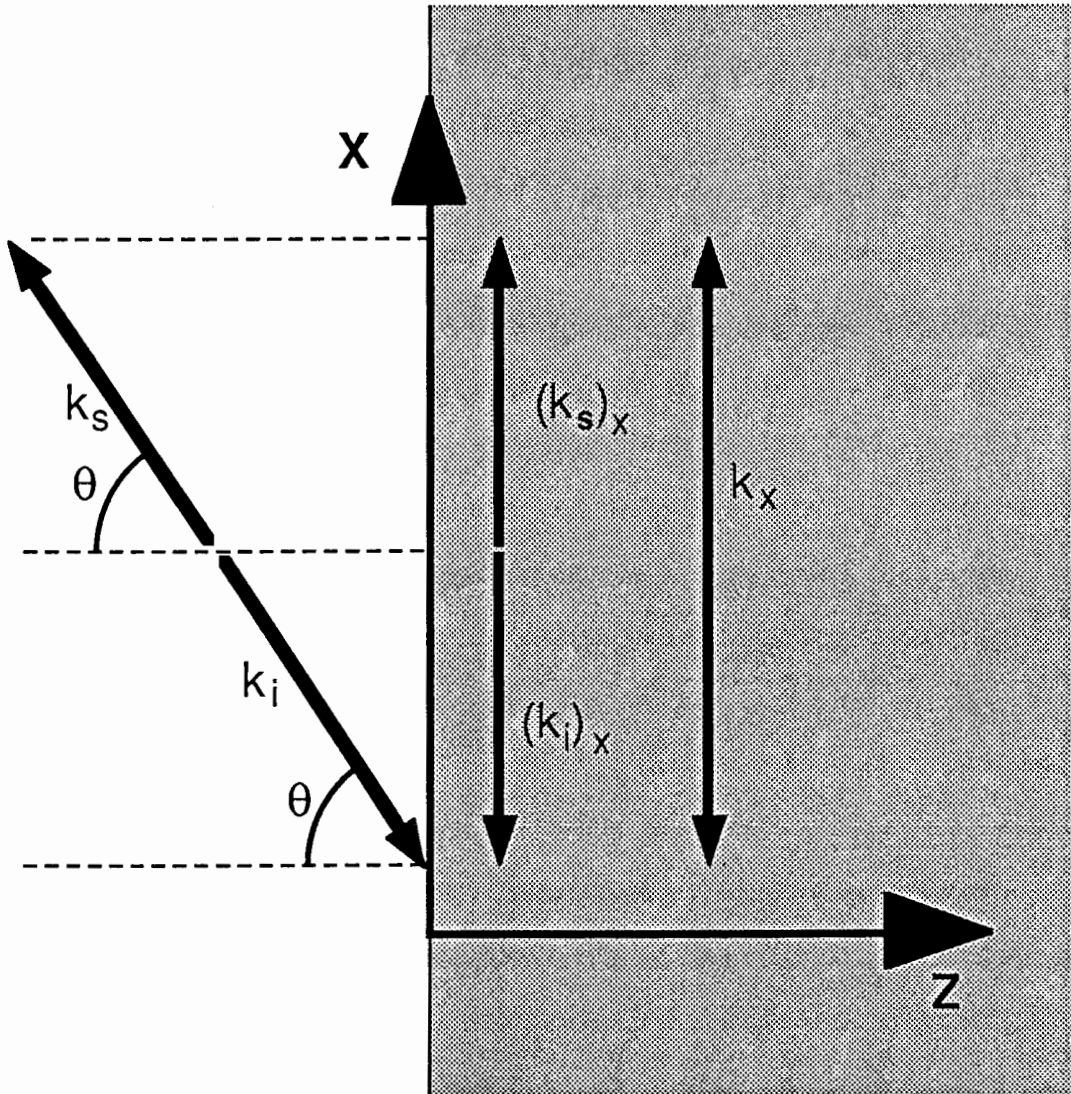


Figure 1.2

Scattering geometry for a light wave of wavevector k_i incident on a magnetic wave of wavevector k in an opaque sample. The angle of incidence is θ . The scattered wave wavevector is k_s . Only the x-components of the wavevectors (parallel to the sample surface) are conserved.

through the same interferometer using cube corner prisms or retroreflectors. This improvement led to the observation of thermally excited phonons in the semiconductors Si and Ge (Sandercock, 1972) in 1972, and thermally excited magnons in the ferrimagnet yttrium iron garnet (YIG) by Sandercock and Wettling (Sandercock and Wettling, 1973) in 1973, and the ferromagnet CrBr_3 by Sandercock (Sandercock, 1974) in 1974.

In 1961, Damon and Eshbach (Damon and Eshbach, 1961) calculated the mode spectrum of a magnetic slab of finite thickness. They predicted the existence of modes localized at the surfaces of the slab, or surface modes. These modes were first observed with microwaves in a YIG plate by Brundle and Freedman (Brundle and Freedman, 1968) in 1968. They applied a 3 GHz radio frequency driving field at one end of the sample and detected the driven surface modes at the opposite end of the sample. Thermally excited surface modes were observed with BLS in the opaque ferromagnetic semiconductor EuO by Grünberg and Metawe (Grünberg and Metawe, 1977) in 1977 using three passes through a single Fabry-Perot interferometer. Sandercock and Wettling successfully observed surface and bulk modes in the opaque ferromagnetic metals iron and nickel in 1978 (Sandercock and Wettling, 1978) and 1979 (Sandercock and Wettling, 1979), using tandem operation of two Fabry-Perot interferometers (three passes-plus-two passes and five passes-plus-two passes, respectively). Sandercock and Wettling were able to demonstrate experimentally several important features of the surface and bulk modes in the spectra obtained for their iron and nickel samples, such as changes in the spectra upon rotation of the polarization of the incident light and rotation of the magnetic field into the scattering plane. However, their results cannot be taken as representative of pure iron and nickel since they used highly strained, polycrystalline samples. Standing spin waves were observed in 1060Å thick amorphous $\text{Fe}_{80}\text{B}_{20}$ films by Grimsditch et al. (Grimsditch et al., 1979) in 1979 using five passes through a single interferometer.

The details of Sandercock's tandem interferometer design were published in 1980 (Sandercock, 1980a; Sandercock, 1980b). Sandercock used a single scanning stage to scan two interferometers in tandem. Dil et al. (Dil et al., 1981) proposed a different, more complicated tandem interferometer design, in which the two interferometers were scanned individually. The successful operation of two interferometers in tandem eliminated the ambiguity associated with the assignment of frequency shifts in the interferometer spectra, as discussed in section 2.1.3.

The discussion at this point will focus on the work that has been done in BLS from metallic samples, since the BLS studies described in this thesis were performed using metallic samples. Other notable BLS experiments that involve high power microwave effects in yttrium iron garnet (YIG) are those by Wettling et al. (Wettling et al., 1983).

Grünberg et al. (Grünberg et al., 1982) noticed that there was a large increase in the intensity of the surface mode for film thicknesses of approximately 50\AA as compared with films of greater thicknesses. They studied the behavior of the surface mode for iron films as thin as 30\AA deposited on sapphire, and observed crossover between the surface mode and standing spin wave modes by using films of different thicknesses. Crossover between the modes was directly observed by Kabos et al. (Kabos et al., 1984a) for individual iron films by varying the angle of incidence of the laser light. Kabos et al. (Kabos et al., 1984b) also studied the dependence of the surface mode frequency on the angle of incidence of the laser light for different angles between the magnetic field and the scattering plane. They found significant departures from the behavior expected from simple theory. Similar anomalies were obtained for permalloy films (Srinivasan and Patton, 1987). Grünberg (Grünberg, 1985; Grünberg et al., 1986) has pioneered experiments on exchange coupled double layers, in which the exchange coupling between two 100\AA thick iron films was varied by varying the thickness of intervening nonmagnetic and antiferromagnetic spacer layers. Other recent BLS experiments of Grimsditch et al.

(Grimsditch et al., 1983; Kueny et al., 1984) and Hillebrands et al. (Hillebrands et al., 1986; Hillebrands et al., 1988) have concerned the study of collective modes in superlattices of magnetic layers separated by nonmagnetic layers. In these experiments, the superlattices were deposited by sputtering techniques.

Very recently, Hillebrands et al. (Hillebrands et al., 1987) have measured in-situ BLS from Fe(110) films as thin as 10\AA grown epitaxially on W(110) under ultrahigh vacuum conditions. They found a strong increase in the surface mode frequency with decreasing thickness which was due to the influence of surface spin pinning which tended to pull the magnetization into the sample plane.

BLS has also been used extensively to study the elastic properties of metallic single films and superlattices (Kueny et al., 1982; Zanoni et al., 1987).

The calculation of Brillouin light scattering frequencies and intensities for magnetic films has proceeded along two quite different paths. One method involved the calculation of the normal modes of the magnetic film assuming plane wave solutions and the other method involved the calculation of the response of the magnetic system using a Green's function approach. As mentioned above, Damon and Eshbach (Damon and Eshbach, 1961) calculated the mode spectrum for a magnetic slab of finite thickness. They used Maxwell's equations in the magnetostatic approximation, together with the Landau-Lifshitz equation of motion for the magnetization and the electromagnetic boundary conditions, to calculate the resonant modes. The magnetostatic approximation is equivalent to ignoring both conduction and displacement current densities. They did not include the effects of exchange. Using this simple theory, Damon and Eshbach predicted the presence of surface modes which were later observed experimentally, as discussed above. Wolfram and DeWames (Wolfram and DeWames, 1971) extended the Damon-Eshbach calculation to include exchange as a perturbation, and also considered the effect of the inclusion of metallic conductivity. Both the Damon-Eshbach and the Wolfram-DeWames calculations

yielded the resonant frequencies of the normal modes, but did not give the intensity of light scattered from the modes. Camley and Mills, inspired by the experimental observation of surface and bulk modes in EuO (Grünberg and Metawe, 1977) and iron and nickel (Sandercock and Wettling, 1978), decided to apply the formalism of Green's functions to the light scattering problem. They calculated the susceptibility response functions from Maxwell's equations, the Landau-Lifshitz equation (including exchange) and the electromagnetic and spin pinning boundary conditions. Then they related the susceptibility response functions to the frequency spectrum of the thermal fluctuations in the spins via the fluctuation-dissipation theorem. The thermal spin fluctuation spectrum was used to construct a spectral density function which exhibited a resonant behavior at the frequency of the magnetic mode of the sample. In their calculations, they used the magnetostatic approximation, as well as simplified forms of magnetic damping and spin pinning at the film surfaces. Camley and Mills calculated the light scattering intensity as a function of frequency for the case of a semi-infinite slab (Camley and Mills, 1978) and the case of a slab of finite thickness (Camley et al., 1981).

The calculation described in Chapter Three of this thesis and in several recent articles (Cochran and Dutcher, 1988a; Cochran and Dutcher, 1988b) is an extension of the Damon-Eshbach/Wolfram-DeWames normal mode approach to the light scattering problem. It includes the effects of metallic conductivity, exchange, the Gilbert form for the magnetic damping and the Rado-Weertman spin pinning boundary conditions (Rado and Weertman, 1959), as well as the calculation of the light scattering intensity from each normal mode of the magnetic film. The calculation has recently been extended to allow the calculation of the light scattering intensities from the lowest frequency modes in a system consisting of two exchange coupled thin films (Cochran and Dutcher, 1988c). A calculation of the normal mode frequencies which is very similar to that presented in Chapter Three, except that

damping and metallic conductivity have been neglected, was presented recently by Rado and Hicken (Rado and Hicken, 1988).

There are several review articles that discuss the experimental and theoretical aspects of BLS. Sandercock (Sandercock, 1982) has described BLS from both magnetic and sound waves for transparent and opaque materials. Patton (Patton, 1984) has presented a very clear discussion of normal modes in magnetic films. Grünberg (Grünberg, 1985) has discussed BLS from magnetic single films, double layers and multilayers. Borovik-Romanov and Kreines (Borovik-Romanov and Kreines, 1982) have presented a comprehensive discussion of many aspects of BLS from magnetic waves, including some interesting work on antiferromagnets. Dil (Dil, 1982) has discussed BLS from sound waves in detail. Malozemoff (Malozemoff, 1981) has described BLS from magnetic and sound waves in amorphous metals. In their book, Cottam and Lockwood (Cottam and Lockwood, 1986) have discussed both BLS and Raman light scattering from ferromagnetic, ferrimagnetic and antiferromagnetic materials.

1.3 Scope of Thesis

In the remainder of this thesis, BLS experiments performed on epitaxial, ferromagnetic films, and light scattering calculations which were used to interpret the experimental results, are described. In Chapter Two, the BLS experimental apparatus is described in detail, including a discussion of the theory of operation of the heart of the BLS experiment, the Fabry-Perot interferometer. A calculation of the magnetic normal mode frequencies, and the intensities of light scattered from the modes, is presented in Chapter Three for films with an in-plane magnetization and for films for which the magnetization is allowed to tilt out of the sample plane toward the sample normal. This calculation serves as a basis for the interpretation of all of the BLS experimental results. Ultrathin magnetic films are discussed in Chapters Four and Five, and thick magnetic films are discussed in Chapter

Six. In Chapter Four, BLS studies of body centered cubic (bcc) iron films grown on silver single crystals and nickel/iron bilayer films grown on silver single crystals are described. BLS studies of face centered cubic (fcc) iron films grown on copper single crystals in both single film and superlattice form are described in Chapter Five. BLS studies of an iron whisker, covered with gold and with silver under ultrahigh vacuum conditions, are presented in Chapter Six. The extension of the light scattering calculation to thick magnetic films is described. Chapter Seven contains a summary of the work presented in this thesis, and conclusions based on this work.

CHAPTER TWO

EXPERIMENTAL APPARATUS

2.1 Fabry-Perot Interferometry

2.1.1 Single interferometer

The heart of the BLS experiment is the Fabry-Perot (FP) interferometer. A plane interferometer consists of two flat, parallel plates separated by a distance d , as shown in figure 2.1. The inside surfaces of the plates have reflective coatings with typical reflectivity values of 90% to 95%. The space between the plates contains a transparent medium of refractive index n .

Consider a collimated beam of monochromatic light of frequency f and wavelength λ which is perpendicularly incident on the FP plates. Because the inside plate surfaces are highly reflecting, the light beam bounces back and forth inside the interferometer many times. Interference of the incident and reflected beams affects strongly the intensity of light transmitted through the FP interferometer. The transmitted intensity I_t has been calculated (Born and Wolf, 1975):

$$I_t = I_0 \left(1 - \frac{A}{1 - R}\right)^2 \left[\frac{1}{1 + \frac{4F^2}{\pi^2} \sin^2 \left(\frac{2\pi nd}{\lambda}\right)} \right], \quad (2.1)$$

where I_0 is the incident intensity, n is the refractive index of the material in between the plates, d is the spacing of the plates, and λ is the wavelength of the light. A and R are the absorptivity and reflectivity of the reflective coatings on the inside surfaces of each FP plate. A , R and the transmittivity T are related by

$$A + R + T = 1. \quad (2.2)$$

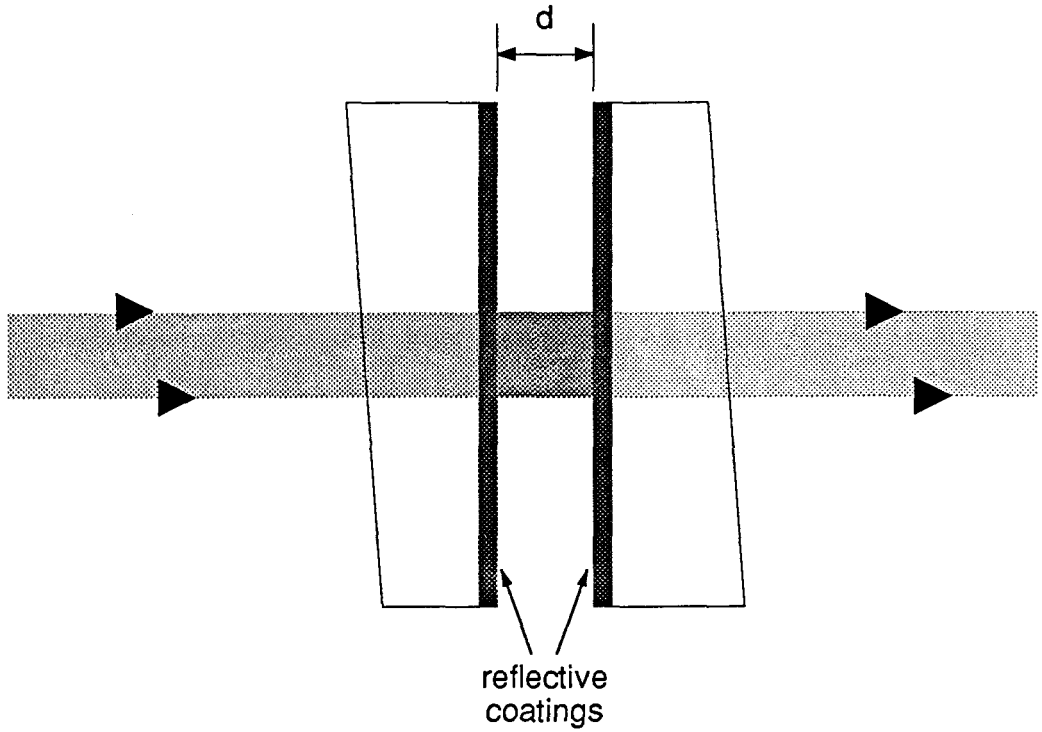


Figure 2.1

A plane Fabry-Perot interferometer consisting of two plates separated by a distance d . A beam of light is perpendicularly incident on the interferometer. The inner surfaces of the plates have highly reflective coatings; the outer surfaces are tilted to avoid standing waves inside each plate. The tilt angle is typically 10 to 15 minutes; it has been purposely exaggerated in this figure.

F is called the finesse of the interferometer. The finesse determines the linewidths of the features in the FP interferometer spectra and the ratio of maximum to minimum transmitted intensity; large values of F are desirable. Equation (2.1) has been derived on the assumption that the finesse is influenced only by the reflectivity R of the FP plates:

$$F = \frac{\pi\sqrt{R}}{1 - R}. \quad (2.3)$$

F is also determined by the flatness of the FP plates, the parallelism between the plates, the divergence of the collimated beam and the angle between the beam and the plate surface, as discussed by Chu (Chu, 1974). The expression in the large square brackets in equation (2.1) is called an Airy function. Maxima in I_t , corresponding to constructive interference of the light beams, occur when the denominator of equation (2.1) is a minimum, i.e. when the product of the refractive index n and the plate spacing d is an integral number of half-wavelengths:

$$nd = m \frac{\lambda}{2}, \quad (2.4)$$

where m is an integer. Changes in I_t can be produced by changes in n , changes in d or changes in both n and d . We will be concerned with the case in which the FP plates are separated by air. In this case n is constant and equal to approximately 1.001, and changes in I_t are produced by changing d . For simplicity in the following discussion, we will take $n = 1$. The minimum value of I_t is controlled by the value of the finesse F .

Figure 2.2 (a) shows the transmitted intensity I_t as a function of the plate separation d for a particular value of the finesse, $F = 20$; figure 2.2 (b) shows I_t for several values of F . The light is monochromatic with frequency f and wavelength λ . We identify the peaks in

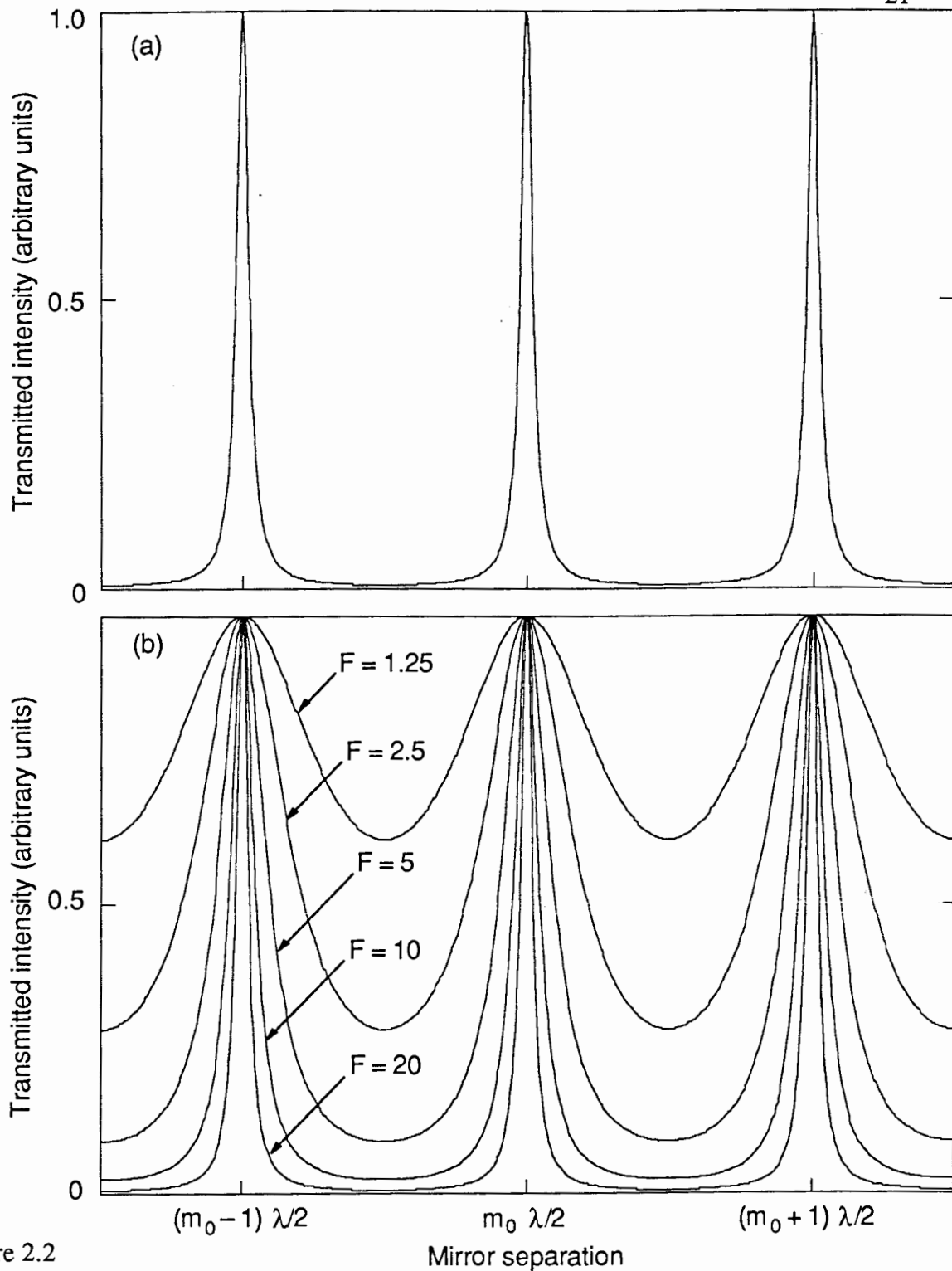


Figure 2.2

- (a) Calculated transmitted intensity versus FP plate separation d for monochromatic light of wavelength λ . m_0 is an integer. The finesse F of the FP is 20.
- (b) Calculated transmitted intensity versus FP plate separation d for monochromatic light of wavelength λ for various values of the finesse F . m_0 is an integer.

the spectrum by the number of half-wavelengths corresponding to the plate spacing. The central peak is of order m_0 corresponding to a plate spacing (for $n = 1$)

$$d_0 = m_0 \frac{\lambda}{2} \quad (2.5)$$

The neighbouring peaks are of order m_{-1} and m_{+1} with plate spacings

$$d_{-1} = m_{-1} \frac{\lambda}{2} = (m_0 - 1) \frac{\lambda}{2} \quad (2.6)$$

and

$$d_{+1} = m_{+1} \frac{\lambda}{2} = (m_0 + 1) \frac{\lambda}{2} \quad (2.7)$$

for the left- and right-hand side peaks respectively.

In addition to the original beam of monochromatic light of frequency f and wavelength λ , we now consider an additional beam of monochromatic light with a slightly larger frequency $f' = f + \Delta f$ where Δf has a positive value. The additional beam has a slightly smaller wavelength $\lambda' = \lambda + \Delta \lambda$, where $\Delta \lambda$ has a negative value. If we think of the original beam as being due to elastically scattered light then the additional beam with its small frequency shift from the original beam could be, for example, due to light scattered from a magnetic wave in the sample. The peak of order m_0 for the additional beam will occur at a smaller value of the plate spacing d_0' than the peak of order m_0 for the original beam since

$$d_0' = m_0 \frac{\lambda'}{2} = d_0 + m_0 \frac{\Delta \lambda}{2} = d_0 + \Delta d \quad (2.8)$$

and $\Delta\lambda$ has a negative value. This situation is shown in figure 2.3 in which the peaks due to the additional beam have been taken to be one-quarter of the intensity of the peaks due to the original beam.

The value of $\Delta\lambda$ required to shift the peak of order m_0 for the additional beam onto the peak of order m_{-1} for the original beam is given by

$$\Delta d = m_0 \frac{\Delta\lambda}{2} = -\frac{\lambda}{2} \quad (2.9)$$

or

$$\Delta\lambda = -\frac{1}{m_0} \lambda. \quad (2.10)$$

This shift in wavelength $\Delta\lambda$ can be converted to an equivalent shift in frequency Δf by using the relation $f = c/\lambda$, where c is the speed of light. This gives

$$\Delta f = -\frac{c}{\lambda^2} \Delta\lambda. \quad (2.11)$$

Therefore the frequency shift required to shift the peak of order m_0 for the additional beam onto the peak of order m_{-1} for the original beam is given by substituting equation (2.10) into equation (2.11), and using equation (2.5):

$$\Delta f = \frac{c}{2} \left(\frac{2}{m_0 \lambda} \right) = \frac{c}{2d_0}. \quad (2.12)$$

This quantity Δf is the frequency shift between neighbouring orders and is known as the free spectral range (FSR) of the interferometer:

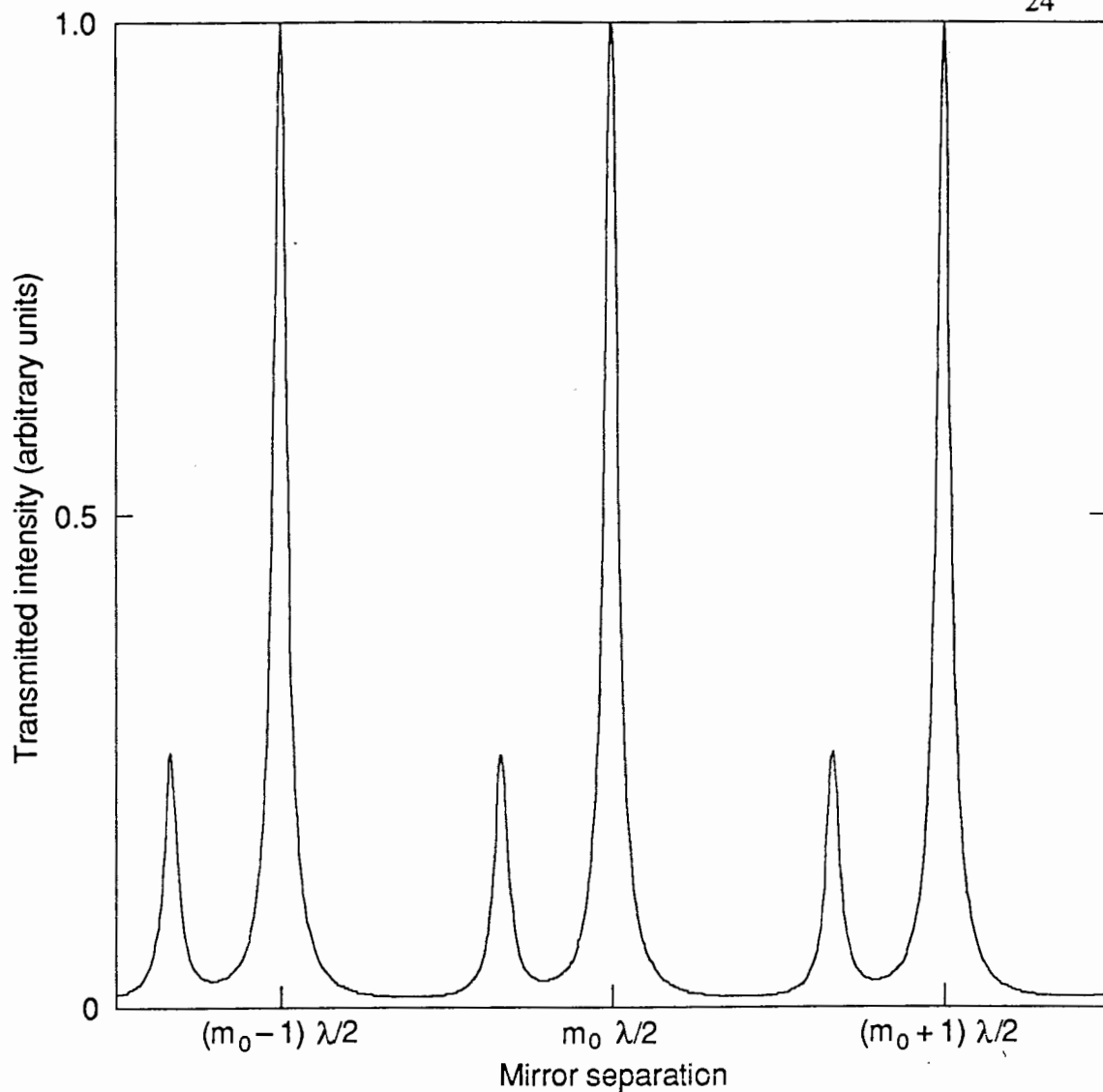


Figure 2.3

Calculated transmitted intensity versus FP plate separation d for light with monochromatic components of wavelength λ and wavelength λ' . The intensity of the light of wavelength λ' has been taken to be $1/4$ of the intensity of the light of wavelength λ . m_0 is an integer. The finesse of the FP is 20.

$$\text{FSR} = \frac{c}{2d_0}. \quad (2.13)$$

The FSR is a fundamental quantity because it is used to calibrate the measured frequency shifts of peaks occurring in the FP spectra. It is convenient from an experimental point of view to regard the Fabry-Perot spectra as intensity versus frequency shift instead of intensity versus plate separation. There is a direct correspondence between a small change in plate separation δd and a small frequency shift δf ; using equations (2.9) and (2.11), δf can be expressed in terms of δd as

$$\delta f = -f \left(\frac{\delta d}{d_0} \right). \quad (2.14)$$

Figure 2.3 has been redrawn as figure 2.4 with both plate separations and frequency shifts labelled. The FSR is altered by changing the equilibrium separation d_0 of the FP plates. In practice, one chooses the FSR such that the signal peaks of interest occur approximately halfway between the elastic peaks. A typical FSR is 50 GHz, corresponding to an equilibrium plate separation of 3 mm.

The transmitted intensity I_t given by equation (2.1) can be rewritten in terms of the frequency f of the light incident on the FP plates and the FSR:

$$I_t(f) = I_0 \left(1 - \frac{A}{1-R} \right)^2 \left[\frac{1}{1 + \frac{4F^2}{\pi^2} \sin^2 \left(\frac{\pi f}{\text{FSR}} \right)} \right]. \quad (2.15)$$

Maxima in $I_t(f)$ occur when f is an integral number of FSR's. Light waves which differ in frequency by an integral number of FSR's will give a signal peak at the same value of the plate spacing for a single FP interferometer. It is also not possible to tell from a single

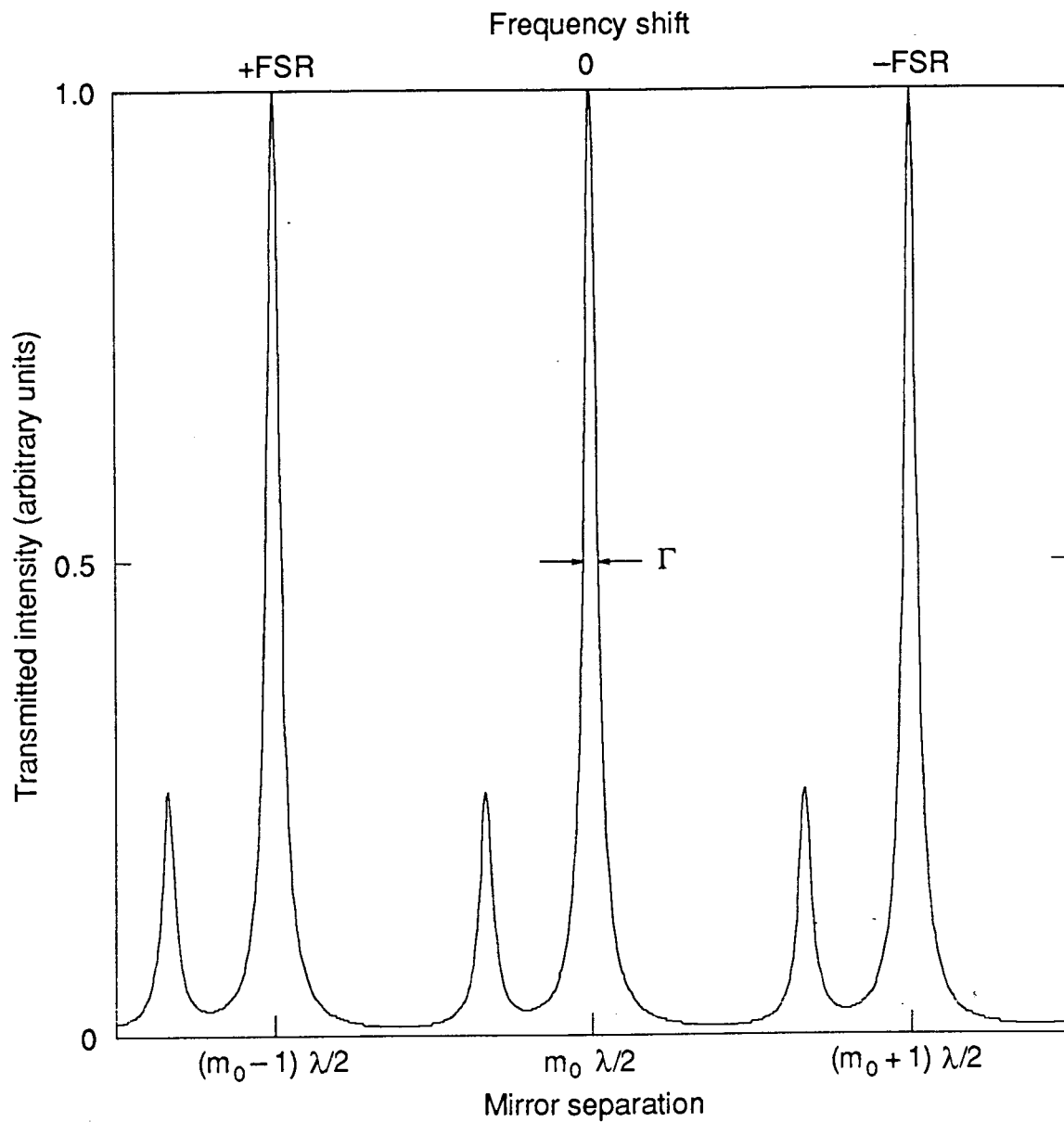


Figure 2.4

Calculated transmitted intensity versus both FP plate separation d and frequency shift for the same spectrum as in Figure 2.3. The full-width at half-maximum Γ in frequency has been indicated.

spectrum if the signal peak is upshifted or downshifted in frequency. For example, the signal peak shown in figure 2.4 could have a frequency shift of $+(p+1/3)FSR$ or $-(p+2/3)FSR$, where $p = 0, 1, 2, 3, \dots$.

The linewidth of the peaks in the Fabry-Perot spectra can be defined in terms of the FSR and the finesse F . For a peak centered about $d = d_0$, the half-width at half-maximum is obtained from equation (2.1), with $n = 1$ and $d = d_0 - \delta d$:

$$\frac{1}{2} = \frac{1}{1 + \frac{4F^2}{\pi^2} \sin^2 \left(\frac{2\pi(d_0 - \delta d)}{\lambda} \right)}, \quad (2.16)$$

or

$$\sin \left(\frac{2\pi(d_0 - \delta d)}{\lambda} \right) = \frac{\pi}{2F}. \quad (2.17)$$

For small, negative δd about a maximum at d_0 , we use equation (2.5) to obtain

$$\delta d = -\frac{\lambda}{4F}. \quad (2.18)$$

This is the half-width at half-maximum expressed in terms of the plate spacing. Using equations (2.13) and (2.14), the full-width at half-maximum Γ expressed in terms of the shift in frequency of the peaks in the Fabry-Perot spectrum can be written as

$$\Gamma = \left(\frac{c}{2d_0} \right) \frac{1}{F} = \frac{FSR}{F}. \quad (2.19)$$

The linewidth Γ is indicated in figure 2.4.

Another important parameter for the FP interferometer is the contrast C , which is the ratio of the maximum to the minimum transmitted intensity. This is a direct measure of signal-to-noise for the interferometer, and it must be large if weak signals are to be detected. From equation (2.1) the contrast is given by

$$C = \frac{(I_t)_{\max}}{(I_t)_{\min}} = 1 + \frac{4F^2}{\pi^2}. \quad (2.20)$$

For large values of the finesse F , we have

$$C = \frac{4F^2}{\pi^2}. \quad (2.21)$$

2.1.2 Multipassed Single Interferometer

It is possible to increase dramatically the contrast of a Fabry-Perot interferometer by passing the light multiple times through the same interferometer. Multipassing is particularly easy with the use of cube corner prisms or retroreflectors, which reflect the light at precisely 180° to the incident light while inverting it about the center of the prism. J.R. Sandercock (Sandercock, 1970; and Sandercock, 1971) has demonstrated their use with a Fabry-Perot interferometer; this is schematically shown in figure 2.5. The transmitted intensity I_{tp} for an interferometer through which the light is passed p times is just the transmitted intensity for a single pass (equation (2.1) with $n = 1$) raised to the p^{th} power:

$$I_{tp} = \{I_t\}^p = \left\{ I_0 \left(1 - \frac{A}{1-R} \right)^2 \left[\frac{1}{1 + \frac{4F^2}{\pi^2} \sin^2 \left(\frac{2\pi d}{\lambda} \right)} \right] \right\}^p. \quad (2.22)$$

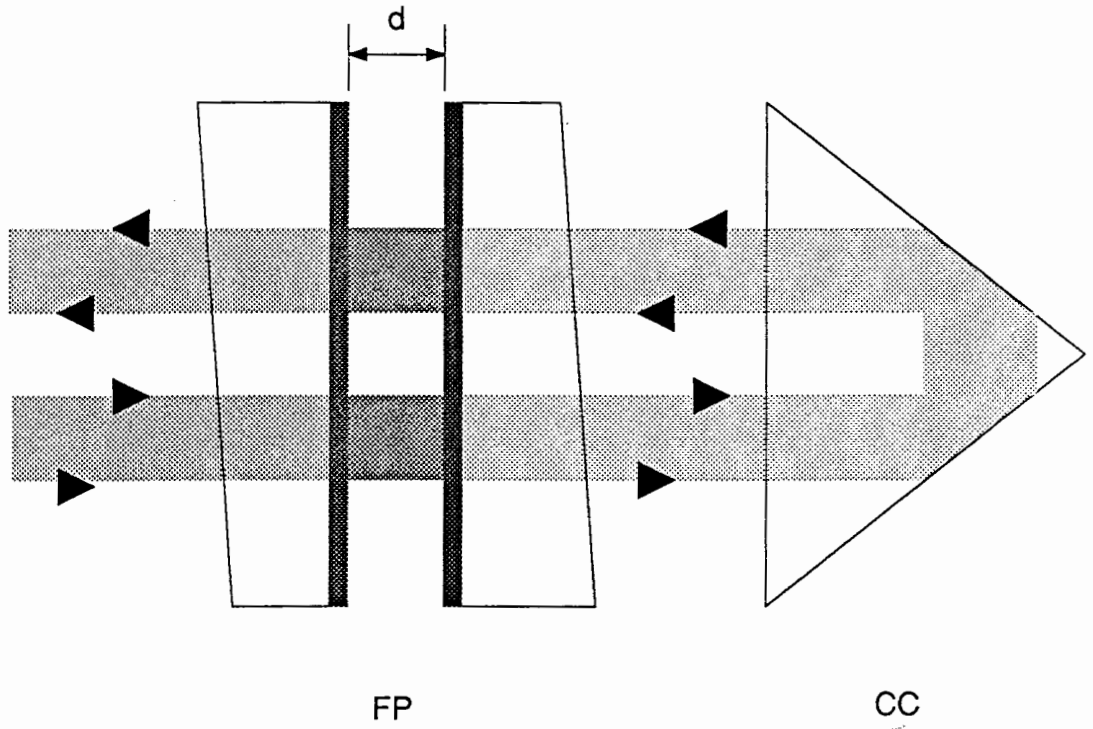


Figure 2.5

A cube corner prism (CC) used to pass a beam of light twice through a FP interferometer.

The contrast (ratio of maximum to minimum transmitted intensity) is dramatically increased by the multipassing technique. The contrast C_p of the multipassed interferometer is

$$C_p = \frac{(I_{tp})_{\max}}{(I_{tp})_{\min}} = C^p = \left(1 + \frac{4F^2}{\pi^2} \right)^p, \quad (2.23)$$

where C is the single-pass contrast given by equation (2.20). Figure 2.6(a) shows the spectrum of figure 2.2(a), and figure 2.6(b) shows the spectrum of figure 2.3, for different numbers of passes p . The transmitted intensity I_{tp} has been indicated on a logarithmic scale in figure 2.6. The increase in the contrast with p is obvious.

The finesse and the linewidth are less affected by the multipassing technique. The finesse F_p is

$$F_p = \frac{F}{\sqrt{2^{1/p} - 1}}, \quad (2.24)$$

where F is the single-pass finesse, and the linewidth Γ_p is

$$\Gamma_p = \Gamma \sqrt{2^{1/p} - 1}, \quad (2.25)$$

where Γ is the single-pass linewidth.

2.1.3 Multipassed Tandem Interferometer

With a single spectrum obtained from a single FP interferometer, it is not possible to determine the absolute frequency shifts of the signal peaks in the spectrum, as discussed in

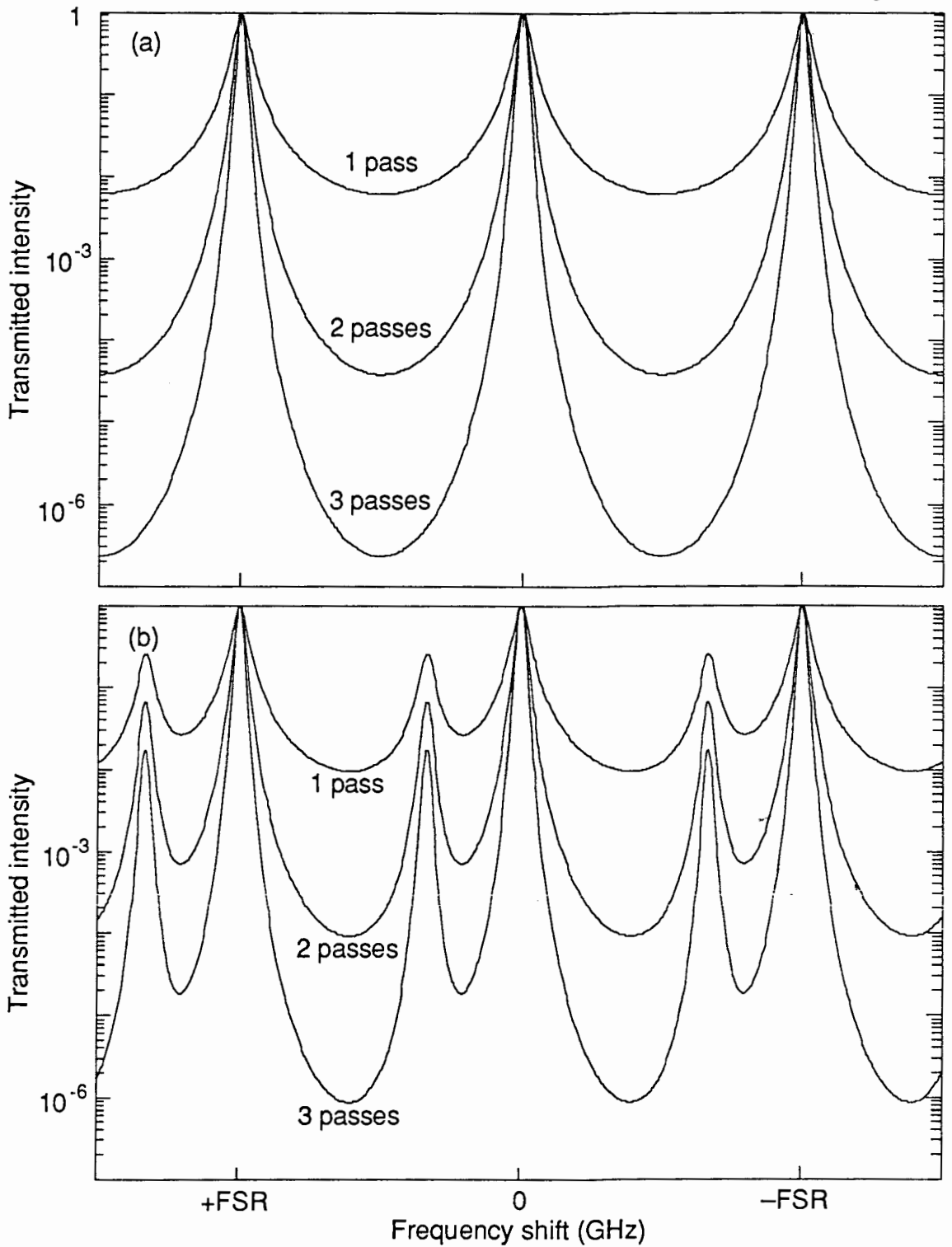


Figure 2.6

Calculated transmitted intensity versus frequency shift for 1, 2 and 3 passes of the light through the FP interferometer for (a) the spectrum in Figure 2.2(a), and (b) the spectrum in Figure 2.3. The transmitted intensity scale is logarithmic.

section 2.1.1. To determine the absolute value of the frequency shifts, it is necessary to collect more data, for example, using a different FSR. By using two interferometers with slightly different plate spacings in tandem, signal peaks from interferometer orders other than the central order are attenuated and the assignment of frequency shifts to the signal peaks belonging to the central order is unambiguous.

Two single-passed interferometers FP_1 and FP_2 in tandem are shown schematically in figure 2.7. The transmitted intensity for each of the interferometers I_{t1} and I_{t2} is given by an expression like equation (2.1) and the transmitted intensity for the tandem combination is given by the product of I_{t1} and I_{t2} . We take the ratio of the plate spacing of the second FP, d_2 , to that of the first FP, d_1 , to be the same as in our apparatus:

$$d_2 = \frac{19}{20} d_1. \quad (2.26)$$

From equation (2.13), the free spectral ranges are related by

$$FSR_2 = \frac{20}{19} FSR_1, \quad (2.27)$$

where FSR_1 and FSR_2 are the free spectral ranges for the first and second interferometers, respectively. Consider light passing through the interferometers consisting of a strong component of frequency f and a weaker component of frequency $f' = f + \Delta f$, where $\Delta f = FSR_1/3$. The spectra for each of the interferometers are shown in figure 2.8, parts (a) and (b). In each spectrum, the intensity has been plotted against the fractional change in the plate separation for each interferometer, $\delta d/d$. The spectra look quite similar because the plate spacings are very nearly equal. Figure 2.9 (a) shows an overlay of the two individual spectra. The relative spacings of the two interferometers have been adjusted such that the two spectra coincide on the central order over the limited number of orders shown; the

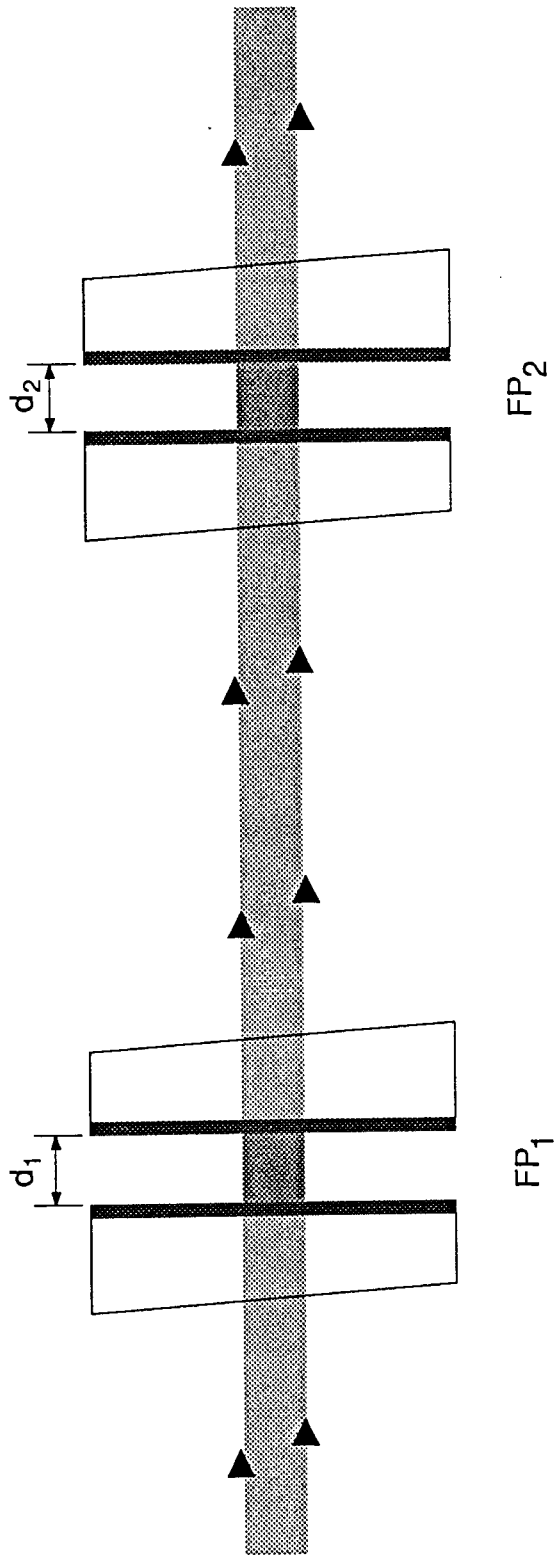


Figure 2.7

Two FP interferometers FP_1 and FP_2 in tandem. The light beam is passed once through each FP. The spacing of FP_1 is d_1 and the spacing of FP_2 is d_2 .

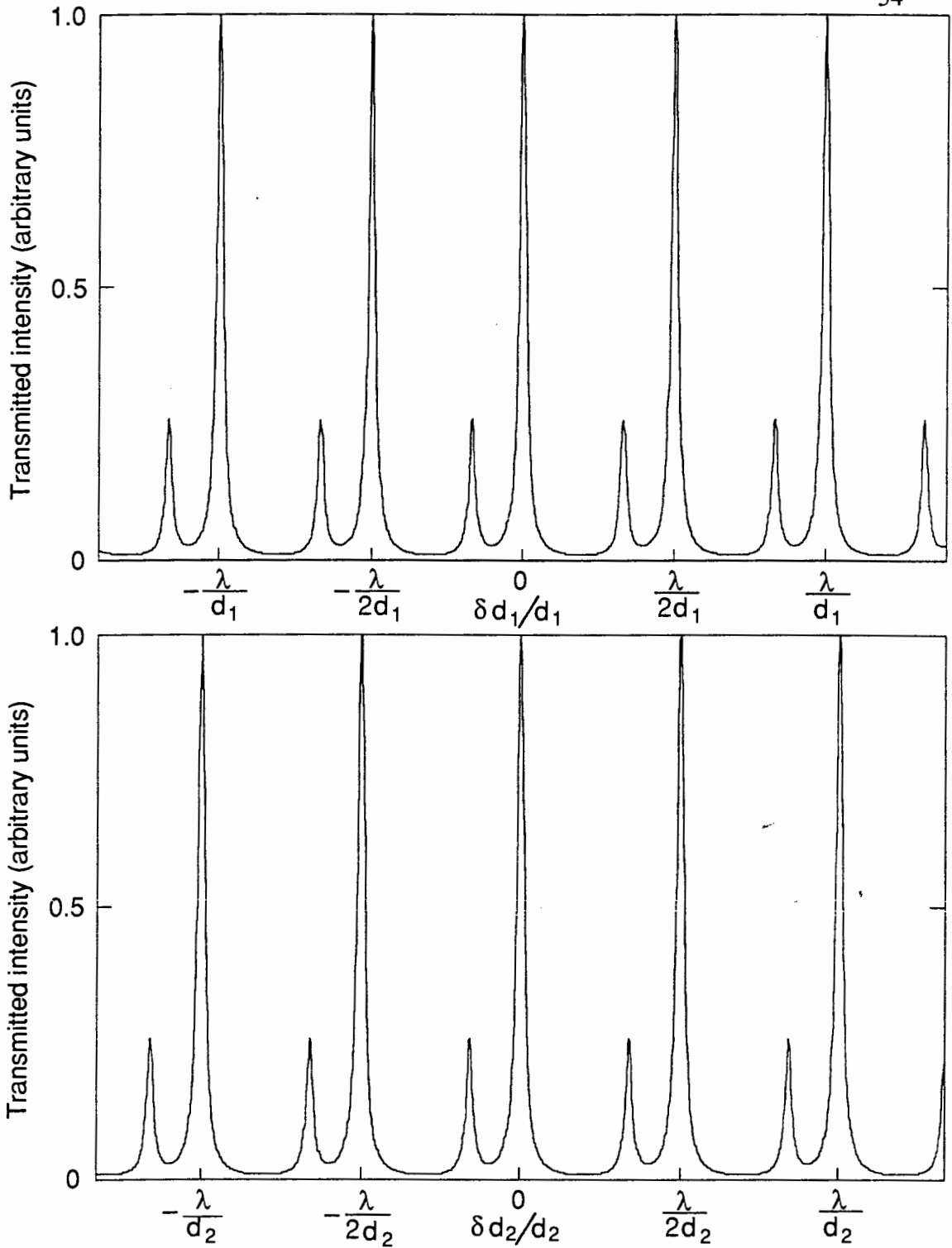


Figure 2.8

Calculated transmitted intensity versus relative plate separation $\delta d/d$ for (a) FP_1 with spacing d_1 ; and (b) FP_2 with spacing d_2 . The light passed through each interferometer has monochromatic components of frequency f and frequency f' .

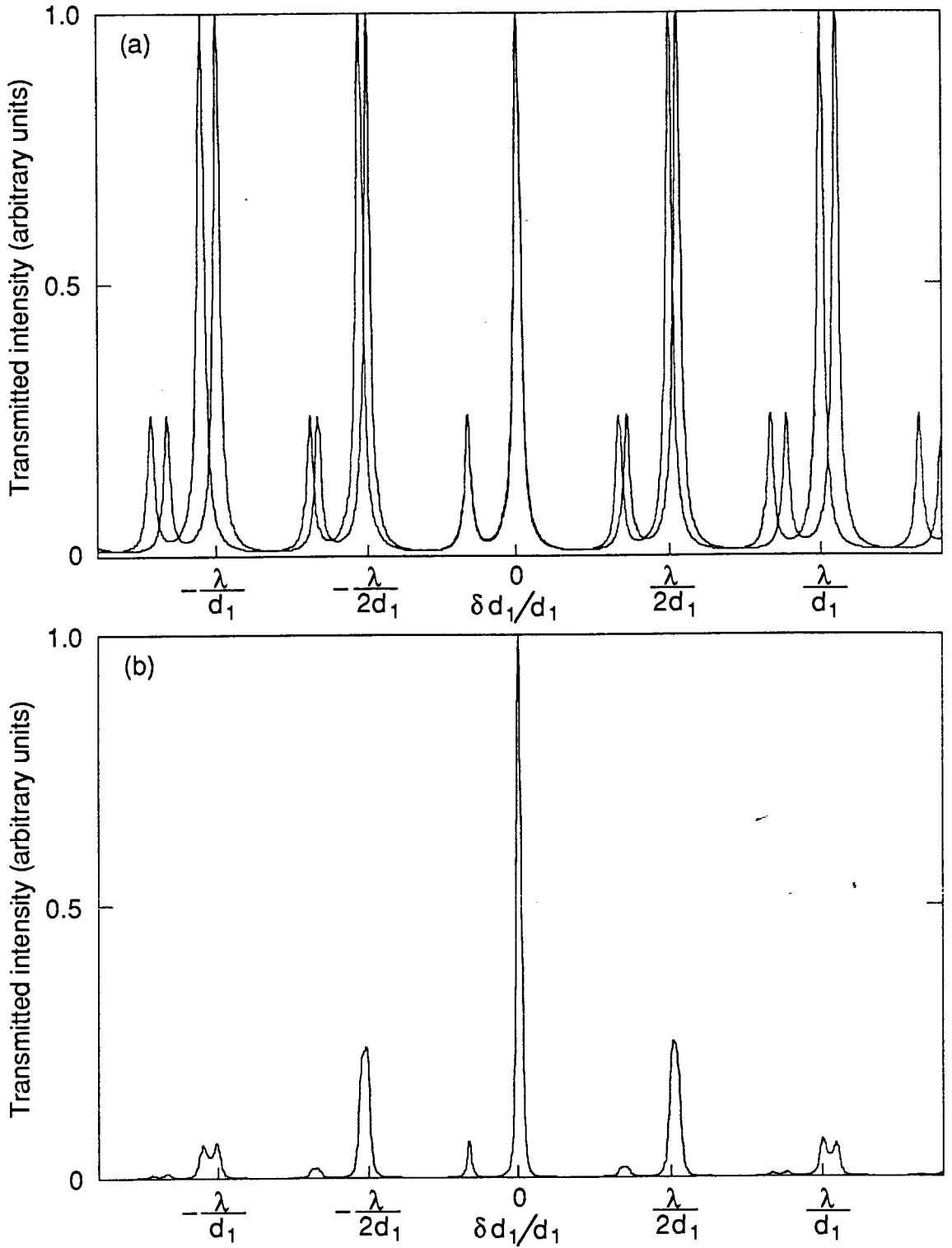


Figure 2.9

Calculated transmitted intensity versus relative FP plate separation $\delta d/d$. Part (a) is an overlay of parts (a) and (b) of Figure 2.8. Part (b) is the product of parts (a) and (b) of Figure 2.8.

spectra actually coincide on every 20th order. An important point to note in figure 2.9 (a) is that both the strong and the weak signals for the central order coincide. The condition for the coincidence of the strong and weak peaks of the central order of the two spectra is that

$$\frac{\delta d_1}{d_1} = \frac{\delta d_2}{d_2} \quad (2.28)$$

This condition is known as the scan synchronization criterion (Sandercock, 1982) and must be satisfied for the proper operation of the tandem interferometer. Part (b) of figure 2.9 shows the tandem spectrum, which is just the product of the two individual spectra in parts (a) and (b) of figure 2.8. The intensity is large for both the strong and the weak signals of the coincident order and is attenuated for the other orders. The intensity of the peaks in the tandem spectrum is a direct measure of the overlap of the orders for the two interferometers.

The above example can be extended to the case in which each of the interferometers is multipassed; the transmitted intensity for each interferometer is then given by an expression like equation (2.22) where p is the number of passes through the interferometer. If FP_1 is multipassed r times and FP_2 is multipassed s times, then the transmitted intensity for the tandem combination is given by $I_{t1}^r I_{t2}^s$.

2.1.4 The Sandercock interferometer

The Sandercock interferometer used in our BLS system (Sandercock, 1980c; and Sandercock, 1982) consists of two FP interferometers with a single scanning stage for scanning both interferometers. One interferometer has its mirror axis parallel to the scan direction with mirror separation d_1 and the other interferometer has its mirror axis inclined at an angle $\alpha = 20^\circ$ to the scan direction with mirror separation d_2 . The geometry is shown schematically in figure 2.10. The plate spacings are chosen so that

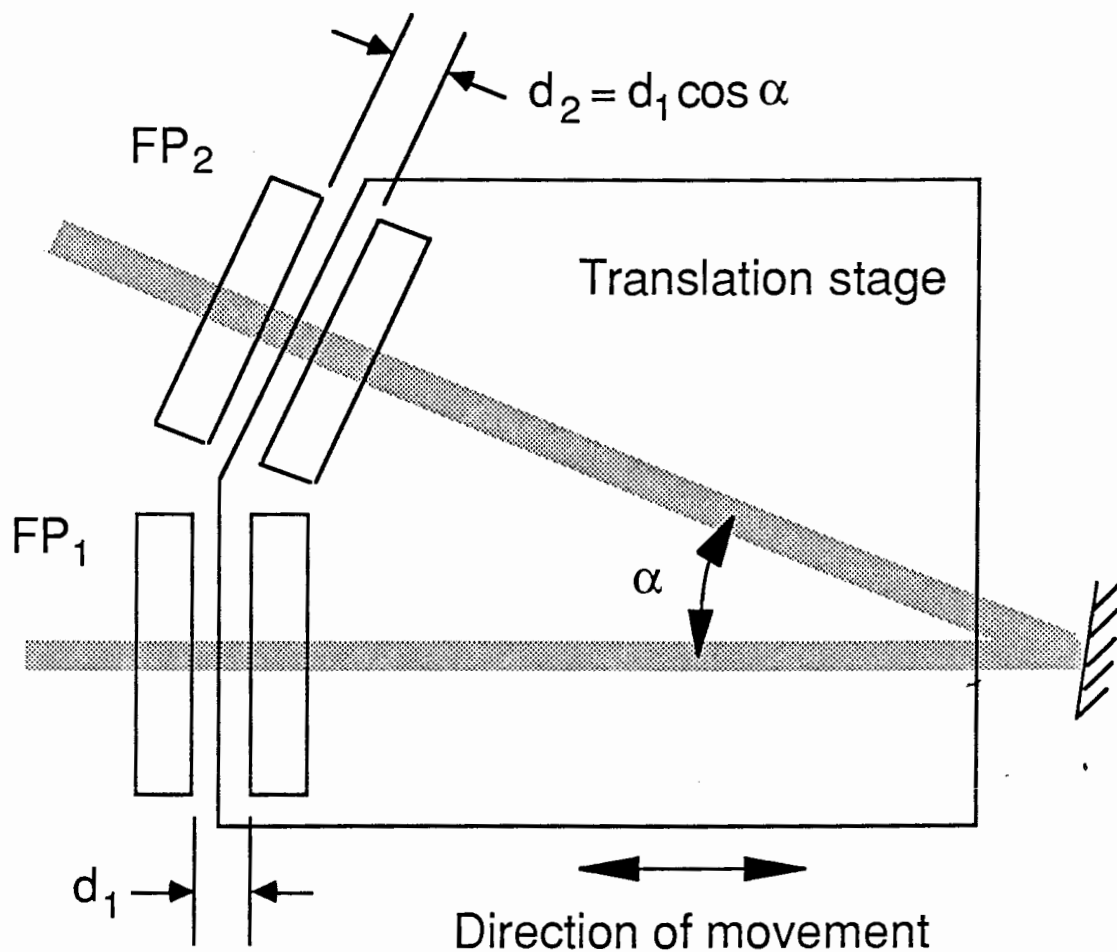


Figure 2.10

The Sandercock tandem interferometer. FP_2 is inclined at an angle α with respect to FP_1 . Both FP's are scanned with a common scanning stage. A single beam of light has been passed once through each FP. The spacing of FP_1 is d_1 and the spacing of FP_2 is d_2 .

$$d_2 = d_1 \cos\alpha, \quad (2.29)$$

and therefore

$$\delta d_2 = \delta d_1 \cos\alpha \quad (2.30)$$

and the necessary scan synchronization criterion given by equation (2.28) is satisfied for this geometry. A deformable parallelogram is used in the scanning stage to maintain mirror alignment to within a few Å's during the scanning of the mirrors. The FP plates are scanned over several microns by the application of a ramp voltage (zero to several hundred volts) to a piezoelectric transducer placed between the base and the top of the deformable parallelogram. The separation of the FP plates can also be varied up to 5 cm on a coarse scale while keeping the plates parallel to within $1/2 \mu$ through the use of a rolling ball translation stage. An air gap parallel plate capacitor is used to maintain the proper FP plate spacing. One plate of the capacitor is mounted on the scanning stage and the other is fixed to the interferometer frame. The change in the spacing of the capacitor plates is just the change in the FP plate separation. The capacitance provides a measure of the plate spacing change.

For each FP, one of the mirrors is fixed to the scanning stage and does not tilt; the other mirror is mounted on a tilt stage on the interferometer frame. The mirrors are aligned by rotation of the tilting mirror about two orthogonal axes in the plane of the mirrors using differential micrometers in series with piezoelectric transducers. The differential micrometers are used for mechanical adjustment of the mirror alignment. High voltages applied to the piezoelectric transducers allow for electronic control of the mirror alignment. Electronic stabilization is used to maintain mirror alignment during the scanning of the FP plates. On successive scans, the mirrors are tilted about the two orthogonal axes, as the

stabilization circuit tries to maximize the strength of the elastic peaks. The relative spacing of the two interferometers is also controlled in the stabilization cycle. The stabilization cycle for the tilts of both FP's and the adjustment of the relative spacing requires 16 successive scans of the interferometer. This cycle is repeated continually during the collection of data. Without the stabilization cycle, the alignment becomes unacceptably poor within minutes, particularly for tandem operation for which careful control of the relative spacing of the interferometers is required.

2.2 The Brillouin light scattering system

The BLS system described below was based directly on the design of the BLS system at Colorado State University and the initial design work for our system was done by Dr. C.E. Patton of Colorado State University when he was a visiting professor in our department.

A schematic diagram of the entire BLS system is shown in figure 2.11. The BLS system can be conveniently divided into the five subsections described below: the incident beam optics, the collected beam optics, the Fabry-Perot multipassing optics, the photomultiplier optics and the data collection electronics.

2.2.1 Incident beam optics

The beam path for the incident beam optics is shown schematically in figure 2.12. Laser light of wavelength $\lambda=514.5\text{nm}$ from a Spectra-Physics 2020-5 continuous wave (CW) Ar⁺ laser was used. A single longitudinal mode of the laser was selected by means of a Spectra-Physics 589 etalon mounted in the laser cavity. The output power level of the laser beam was adjustable between 0 and 5 W on the laser power supply; the power level was also adjusted by passing the beam through a set of neutral-density filters (NDF). Typically, a laser power of several hundred milliwatts (mW) was used. The beam height and direction were adjusted by means of a beamsteerer (BS) consisting of two aluminum

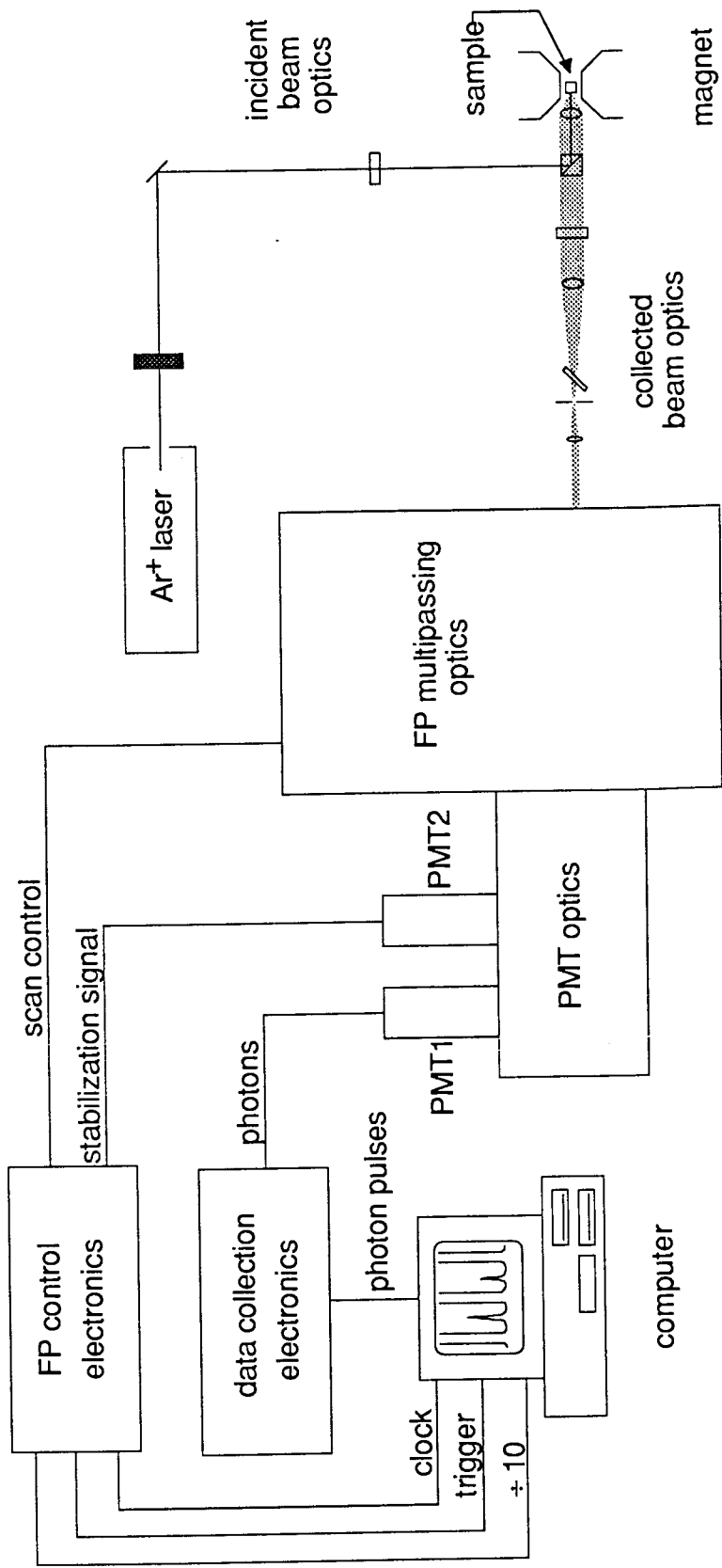


Figure 2.11

The BLS system. It consists of the incident beam optics, the collected beam optics, the FP multipassing optics, the PMT optics and the data collection electronics.

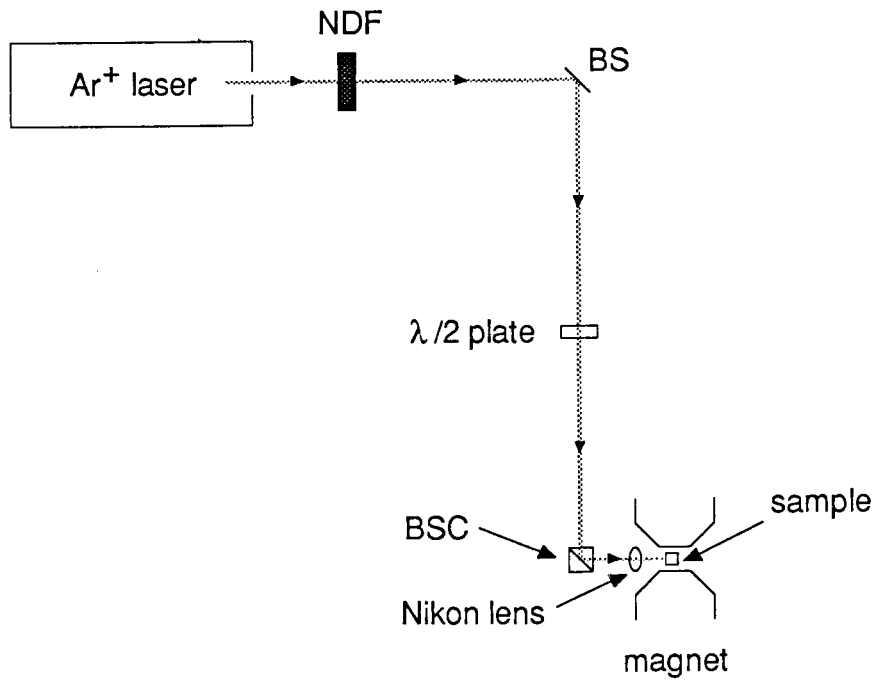


Figure 2.12

The incident beam optics. It consists of an Ar⁺ laser, neutral density filters (NDF), a beamsteerer (BS), a half-wave ($\lambda/2$) plate, a beamsplitter cube (BSC), and a Nikon camera lens. A magnet is used to apply a magnetic field to the sample.

front surface mirrors which were able to withstand the laser powers used in the BLS experiments. The beam from the laser was linearly polarized; the direction of the linear polarization could be rotated about the beam direction by means of a quartz half-wave ($\lambda/2$) plate. A rotation θ of the half-wave plate produced a rotation 2θ of the polarization of the laser beam.

The laser beam was then directed onto either a small quartz prism, 3.2 mm on a side, or onto a large laser line polarizing beamsplitter cube, 25.4 mm on a side. The polarizing beamsplitter cube (BSC) consisted of two right angle prisms cemented together to form a cube (Newport Corporation, part number 10BC16PC.2). Dielectric coatings on the interface provided the polarizing properties: light polarized in the interface plane was reflected through 90° and light with an electric field component perpendicular to the interface was transmitted without deviation. The right-angle quartz prism could be used with an arbitrary rotation of the polarization of the laser beam.

Both the prism and the cube reflected the laser beam through 90° , directing the beam through the center of a Nikon camera lens having a focal length of 50mm and a maximum aperture of 35.7mm (f-number of 1.4). The sample was placed at the focal spot of the Nikon lens. The sample position was adjusted by a translation stage having x, y and z translations (see figure 2.13) which were controlled by micrometers. Two different methods were used for holding the samples. In the first method, the sample was attached to a glass microscope slide, using Scotch tape or nail polish, and the underside of the slide was attached by means of double-sided tape to a post on the translation stage. The post could be rotated about an axis perpendicular to the scattering plane to vary the angle of incidence of the laser beam. The angle θ between the sample normal and the incident light beam could be varied between $\theta = 20^\circ$ and $\theta = 80^\circ$; θ was typically 45° . The second holder accommodated samples in the shape of circular disks less than 15 mm in diameter and allowed for rotation through 360° of the sample in the sample plane. The sample was

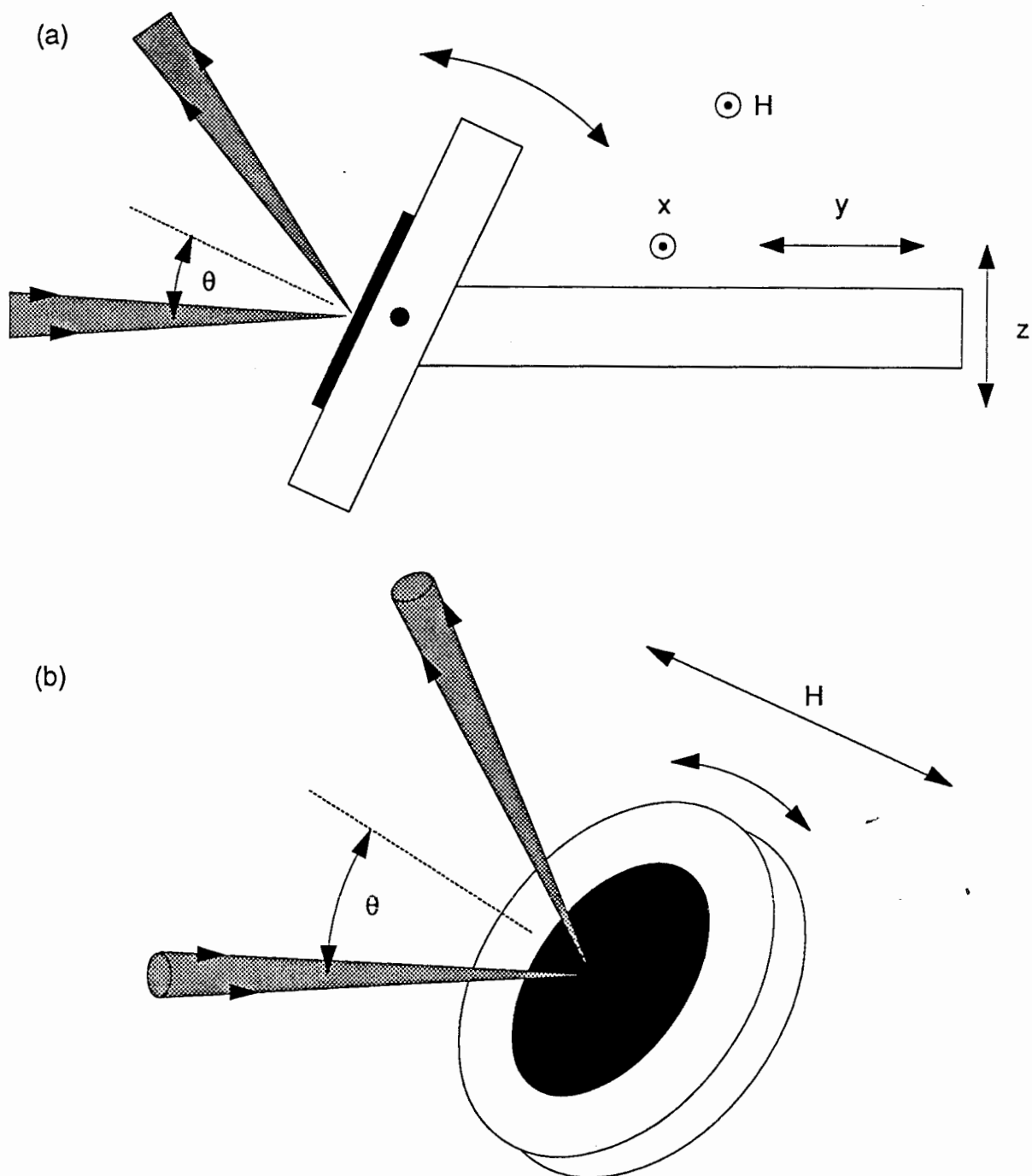


Figure 2.13

Sample holder geometry. In part (a), the sample holder has been shown from the side. The angle of incidence θ can be varied as shown. In part (b), the sample holder has been shown at an oblique angle. The sample can be rotated in the sample plane. The magnetic field H has been shown in both (a) and (b). Also, the samples in both (a) and (b) are shown in black.

clamped by means of a flat plexiglass disk (not shown in figure 2.13) which had a central hole that allowed the incident and scattered light beams to pass between the Nikon lens and the sample surface.

An electromagnet was placed next to the Nikon lens. This produced a d.c. magnetic field variable between 0 and 11 kOe at the sample position. The magnet gap was 1 inch and the magnet poles were tapered from 4 inches in diameter down to 2 inches in diameter over a distance of 2 inches. The magnetic field was measured by means of a Bell 620 gaussmeter and a Bell HTB4-0608 gaussmeter probe mounted on one of the polefaces of the magnet. Careful calibration of this probe against another calibrated Hall probe placed at the sample position allowed measurement of the magnetic field with an accuracy of ± 10 Oe.

2.2.2 Collected beam optics

The Nikon camera lens that was used to focus the incident beam onto the sample surface was also used to collect the scattered light (see figure 2.14). This corresponded to the backscattering geometry, with 180° between the incident and scattered beams. The solid angle of the lens was 0.366 steradians. The specularly reflected beam was not collected by the lens; only diffusely scattered light was collected. Because the scattered light originated at the focal spot of the lens, the beam of light collected by the lens was very well collimated, with a diameter equal to the aperture of the lens. The beam then passed through either the small right-angle prism or the large polarizing beamsplitter cube (BSC). When the prism was used, the small amount of scattered light intercepted by the prism was blocked. When the beamsplitter cube was used, the entire scattered beam passed through the cube, except for a small amount that passed around the cube edges. The polarization of light scattered from magnetic waves is rotated by 90° with respect to the polarization of the incident light, as discussed in Section 3.1.3. This unique property of the scattered light

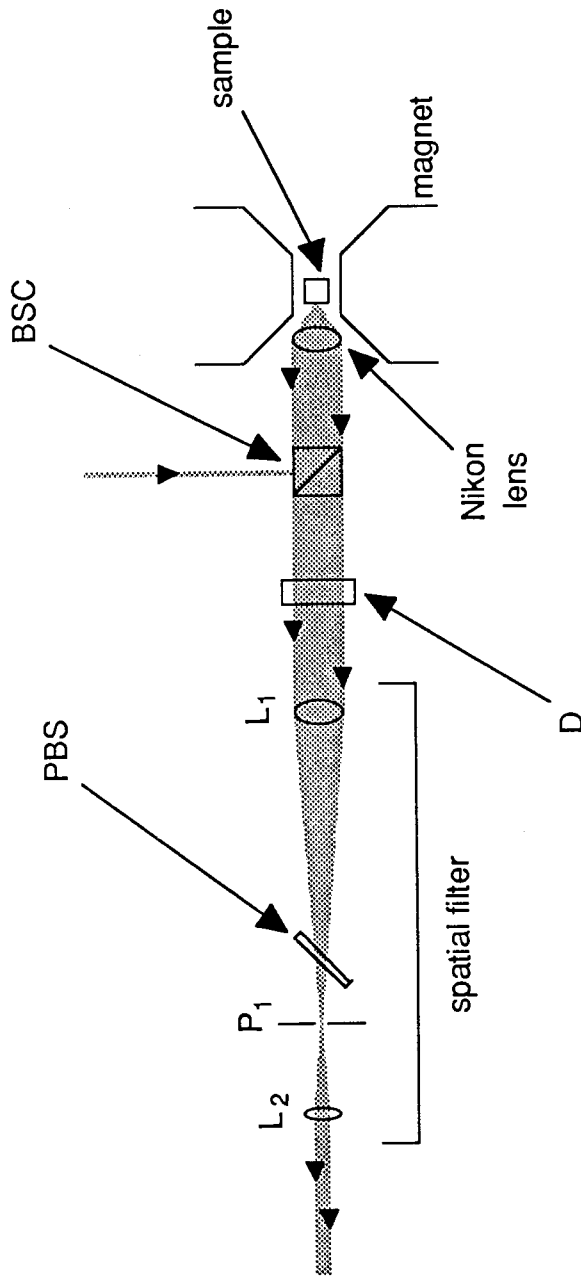


Figure 2.14

The collected beam optics. It consists of a Nikon camera lens, a beamsplitter cube (BSC), an iris diaphragm (D), lenses L₁ ($f = 260$ mm) and L₂ ($f = 56$ mm), a pinhole P₁ (150 μ m diameter) and a pellicle beamsplitter (PBS).

was used to reduce the strength of the elastically scattered light. When using the prism, this required the placement of a 36mm diameter polarizing filter which rejected light with the same polarization as the light incident on the sample. When using the beamsplitter cube, no additional polarizer was necessary: the cube transmitted the light scattered from magnetic waves to the rest of the collected beam optics and light of the other polarization was reflected through 90° . The beamsplitter cube was used for almost all of our measurements. The beam diameter was adjusted by placing a variable aperture iris diaphragm (D) in the path of the beam.

The beam was then passed through a spatial filter, consisting of a lens-pinhole-lens arrangement as depicted in figure 2.14. The pinhole (P_1) was placed at the focal spot of both lenses. This filter removed light in the collected beam which was not collimated and hence not focussed onto the pinhole by the first lens. Both lenses in the spatial filter were anti-reflection coated acromats, with the most steeply curved surface of each lens facing the collimated beam. The light was passed through the centers of both lenses of the spatial filter. A pellicle beamsplitter (PBS) was placed between the first lens (L_1) and the pinhole (P_1) to aid in the alignment of the beam with the Fabry-Perot mirrors. The second lens of the filter (L_2) produced a collimated exit beam with its diameter d given by the incident beam diameter d_0 multiplied by the ratio of the second focal length f_2 to the first focal length f_1 ($d = d_0 f_2 / f_1$). This resulted in an exit beam having a diameter of 8mm which was sent into the multipassing optics of the Fabry-Perot interferometers.

2.2.3 Fabry-Perot multipassing optics

The Fabry-Perot interferometer was designed and constructed by J.R. Sandercock and consisted of two interferometers in tandem, as discussed in section 2.1.4. The Fabry-Perot mirrors were obtained from IC Optical Systems Limited and were quoted as being flat to within $\lambda/200$ over the 46 mm working aperture of the mirrors after the reflective coatings

were applied. The reflectivity of the mirrors was 93% at $\lambda = 514.5$ nm. The Fabry-Perot mirrors were scanned using control electronics supplied by J.R. Sandercock.

The 8mm diameter collimated entrance beam produced by the collected beam optics could be passed 0, 2 or 4 times through the first Fabry-Perot interferometer and 0 or 2 times through the second interferometer. A schematic diagram of the beam paths is shown in figure 2.15. The beam pattern through each interferometer is shown in the inset of the figure. There were two beam heights in the Fabry-Perot multipassing optics, with the exit beam at the same height as the entrance beam. The multipassing optics consisted of mirrors (M5 to M8) and cube corner prisms (CC1 to CC5). The cube corner prisms have the unique property that they reflect light at 180° to the incident light while inverting the light about the center of the prism. The mirrors were dielectrically coated to reflect green light at 45° and the cube corner prisms were anti-reflection coated for green light. The tilts of mirrors M5 and M7 were adjusted such that the beams incident on each set of FP mirrors were as close to perpendicular incidence as possible. The number of passes through the system was changed by moving cube corners CC3 and CC5, and/or mirror M6. The flexibility afforded by the variable number of passes was quite unnecessary, and the system was used in either the 4 + 2 tandem arrangement or with 4 passes through the first interferometer. It was useful, however, to be able to bypass each interferometer for the initial alignment procedure. Opaque masks with holes for the beam pattern were used on the cube corner prisms to reduce the amount of stray light in the system.

All of the Fabry-Perot multipassing optics were placed in a large light-tight box with removable covers, made from black anodized aluminum sheets on a black anodized aluminum frame. Black felt was placed between the sheets and the frame, and the frame and the optical table, to prevent the entry of room light into the box. A light-tight extension from the box out to the pinhole of the collected beam optics spatial filter was found to be unnecessary.

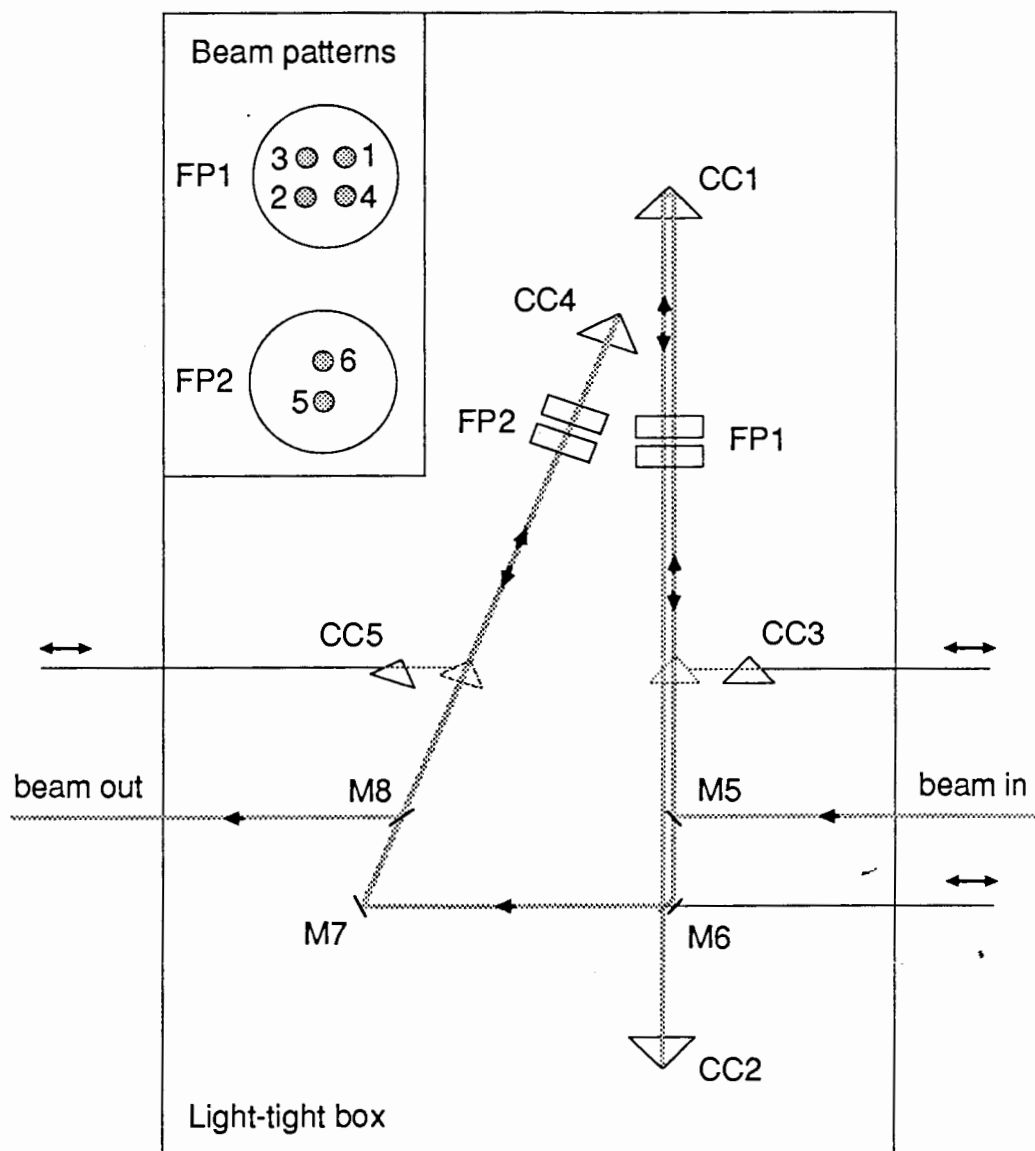


Figure 2.15

The FP multipassing optics. It consists of mirrors M5, M6, M7, M8; cube corners CC1, CC2, CC3, CC4 and CC5; and Fabry-Perot interferometers FP1 and FP2. The beam patterns through each FP have been indicated in the top left hand corner of the Figure.

2.2.4 Photomultiplier optics

The photomultiplier optics are shown schematically in figure 2.16. All of the photomultiplier optics were placed into a light-tight box similar in construction to the light-tight box for the Fabry-Perot multipassing optics. The two boxes were bolted directly together. The exit light beam from the Fabry-Perot multipassing optics was sent directly into a spatial filter, consisting of a lens-pinhole-lens arrangement which blocked most of the light which was not collimated along the beam direction. Both of the lenses (L_3 and L_4) used in the spatial filter were anti-reflection coated acromats, with the most steeply curved surface of each lens facing the collimated beam. The output beam from this filter was passed through a pellicle beamsplitter (PBS) which transmitted 90% of the light and reflected 10% of the light onto a control photomultiplier tube (Hamamatsu 6199). The control photomultiplier was used for stabilizing the interferometer in the presence of a strong elastic scattering signal. The light transmitted through the pellicle beamsplitter was then directed onto an acromat lens which focussed the light onto the small (2.5mm effective diameter) photocathode of an EMI 9863A/100 photomultiplier tube. This photomultiplier tube was used for counting photons and was selected by EMI for low noise and high gain. The measured dark count rate was 0.3 counts/s with the tube cooled to -30°C . A narrow-band laser line interference filter (50% maximum transmission) was placed directly in front of the photomultiplier to discriminate against unwanted background radiation. The use of the interference filter allowed BLS measurements to be performed with the room lights turned on with no increase in the background levels of the measured spectra. Manual shutters were placed between the light-tight box enclosing the photomultiplier optics and each photomultiplier. O-rings were used to seal the shutters to the box, the shutters to the photomultipliers and the narrow-band filter to the box.

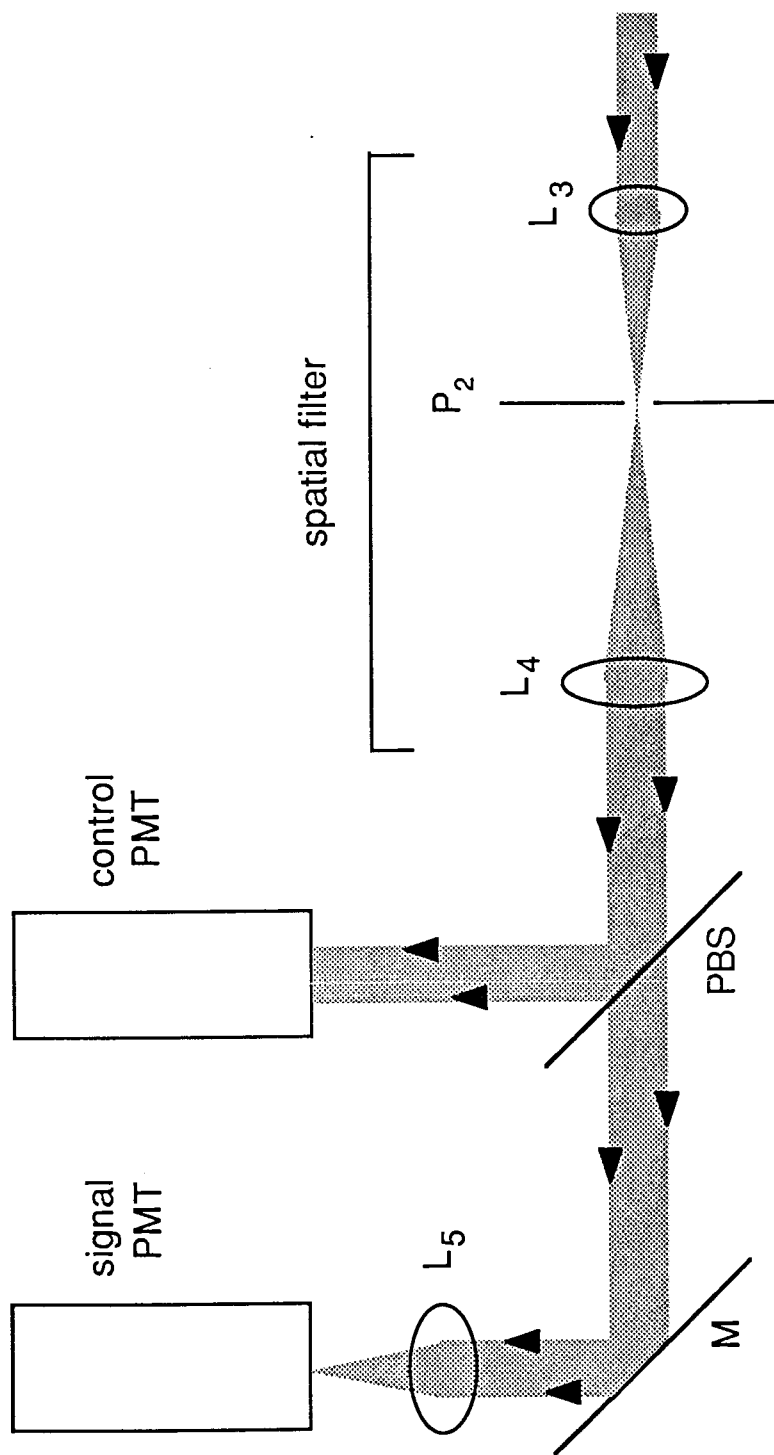


Figure 2.16

Photomultiplier optics, consisting of lenses L_3 ($f = 50$ mm), L_4 ($f = 80$ mm), and L_5 ($f = 140$ mm); pinhole (P_2), pellicle beamsplitter (PBS), mirror M , signal photomultiplier (signal PMT) and control photomultiplier (control PMT). The pinhole diameter was 300μ .

2.2.5 Data collection electronics

Photon pulses from the EMI photomultiplier tube were sent directly into an amplifier/discriminator (EG&G PAR 1121A). The discriminator level was set at 3 mV; for each photon pulse larger than the discriminator level the discriminator produced a TTL pulse (+5V and 30 ns). These TTL pulses were counted using a "homemade" multichannel scaler (MCS) board that was interfaced to an IBM-PC clone computer. The MCS board, based on a design of M.L.W. Thewalt, consisted of three (2 kilobyte \times 8 bit) RAM memory chips which were configured in parallel as part of the computer's memory. Each of the 24 bit memory locations corresponded to a channel of the MCS. The contents of these memory locations were updated on each scan of the Fabry-Perot mirrors. The timing signals for the MCS were supplied by the Fabry-Perot mirror control electronics. There was also a provision for slowing the scan by a factor of 10 during a portion of each scan. The use of a programmable counter chip to control the slow scan timing allowed the entry of the slow scan range on the computer keyboard. The data collection software was written in Turbo Pascal 3.10.

2.2.6 High resolution frequency measurements

In our experiments, the FP plates are scanned over two FSR's, such that the frequency shift ranges from $-FSR$ to $+FSR$, as in the calculated spectrum in figure 2.4. Within this frequency range of $2 \cdot FSR$, data is collected in 2^N channels of the multichannel analyzer (MCA), where $N = 7, 8$ or 9 . The frequencies of peaks in the measured spectra can be determined to within one-half channel width or $FSR/2^N$ GHz. To obtain high frequency resolution, it is necessary to use a small FSR and a large number of MCA channels. Increasing the number of MCA channels increases the data collection time but also the quality of the data. With the tandem interferometer, one cannot use a FSR which is smaller than the signal peak frequency. This is because the signal peaks belonging to the central

order of the interferometer would not appear on the spectrum and the signal peaks belonging to the other orders would be drastically attenuated, as described in section 2.1.3. However, with a single interferometer, the signal peaks belonging to other orders of the interferometer will appear in the spectrum. The measured frequency of a signal peak in the spectrum is the true signal peak frequency modulo an integral number of FSR's, as discussed in section 2.1.1. A spectrum for a single interferometer with a small FSR gives the required high frequency resolution. The FSR must be chosen correctly such that the upshifted and downshifted signal peaks are not obscured by the elastic peaks and do not overlap with each other. The two peaks overlap if they occur at the midpoint between two neighbouring elastic peaks. To ensure visibility of the signal peaks, they should occur at a frequency shift that is approximately one-third of the shift between two neighbouring elastic peaks. Mathematically, we require that

$$f - n \text{ FSR} \sim \pm \frac{1}{3} \text{ FSR}, \quad (2.31)$$

where f is the magnitude of the true signal peak frequency and n is an integer. Therefore, the proper choice of small FSR for high frequency resolution measurements is given by

$$\text{FSR} \sim \frac{f}{n \pm \frac{1}{3}}. \quad (2.32)$$

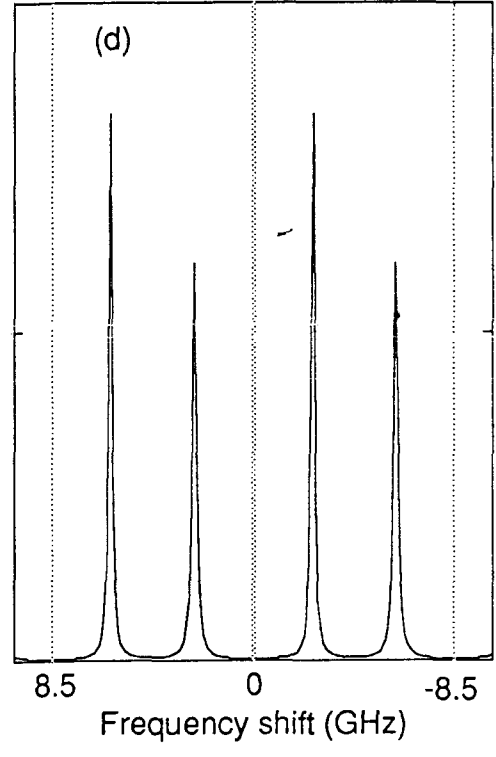
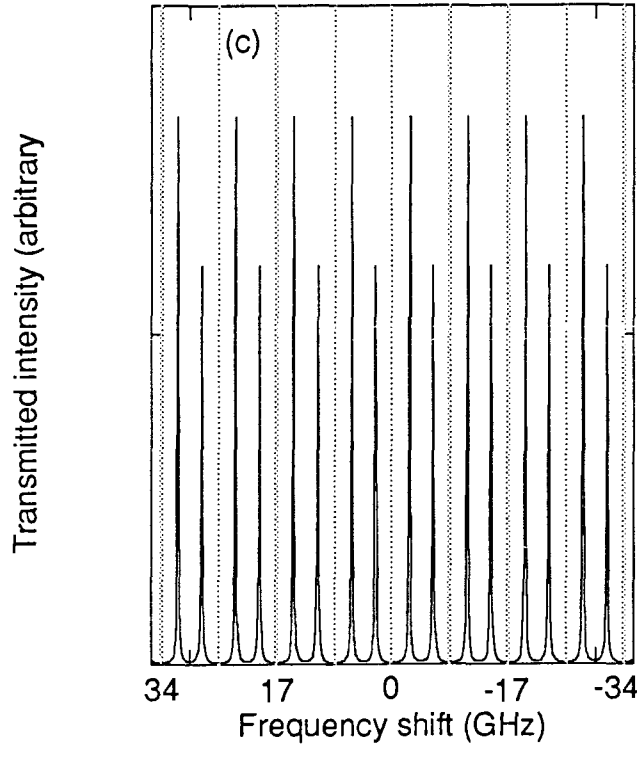
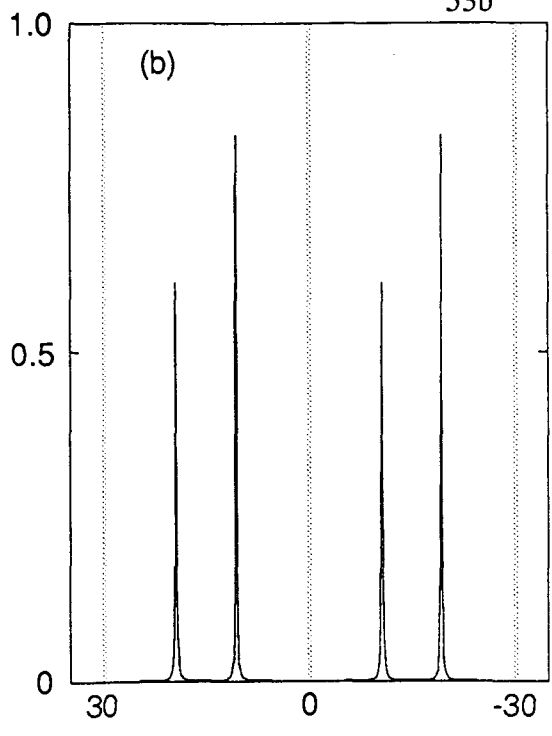
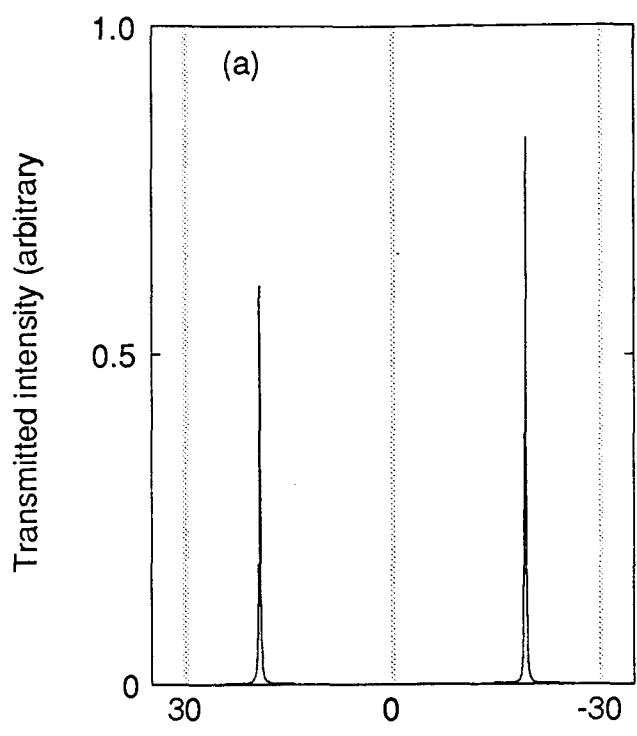
An additional spectrum for a tandem interferometer using a large FSR directly determines the additional number n of small FSR's.

As an example, figure 2.17 shows signal peaks calculated for a 25Å thick iron film having a uniaxial anisotropy field of 6 kOe tending to orient the magnetization along the sample normal, see equation (3.32). The applied magnetic field was 2kOe. Part (a) of this figure shows the calculated spectrum obtained from a tandem interferometer with a FSR of

Figure 2.17

Calculated transmitted intensity versus frequency shift for a 25Å thick iron film with a uniaxial anisotropy field of 6 kOe tending to tilt the magnetization out of the sample plane and an applied magnetic field of 2 kOe. The natural linewidths of the peaks, as determined by the magnetic damping in iron, are shown. The thick dotted lines indicate the positions of the elastically scattered peaks.

- (a) tandem interferometer with a FSR of 30 GHz.
- (b) single interferometer with a FSR of 30 GHz.
- (c) single interferometer with a FSR of 8.5 GHz.
- (d) single interferometer with a FSR of 8.5 GHz.



30GHz. Because of the tandem operation, only the signal peaks that belong to the central elastic peak at 0 GHz frequency shift are observed. The signal peaks have frequencies of ± 20 GHz: one peak is upshifted in frequency and the other peak is downshifted in frequency. The dotted vertical lines correspond to the elastic peaks. The calculated spectrum obtained from a single interferometer with a FSR of 30GHz is shown in part (b). Signal peaks belonging to the central and the two neighbouring elastic peaks appear in the spectrum. For each elastic peak, there is one signal peak that is upshifted in frequency and one peak that is downshifted in frequency. Part (c) shows the calculated spectrum within the frequency range +30GHz to -30GHz obtained from a single interferometer with a FSR of 8.5GHz. Because of the decrease in the FSR compared with the spectra of parts (a) and (b), there is a decrease in the frequency separation between neighbouring elastic peaks. As in part (b), for each elastic peak there is one signal peak that is upshifted in frequency and one peak that is downshifted in frequency. Part (d) shows the same spectrum as in part (c) within the frequency range +8.5GHz to -8.5GHz. In table 2.1 the frequencies of the signal peaks which occur in the spectra of parts (c) and (d) of figure 2.17 between +8.5GHz and -8.5GHz are listed. Also, for each peak, the frequency of the elastic peak to which it belongs is listed.

The spectrum of figure 2.17 (d) shows that large frequency signal peaks can be measured with high resolution using a single interferometer. This spectrum has 2.5 times the frequency resolution as that of figure 2.17 (a), assuming the same number of MCA channels in each case. This increase in resolution is necessary for the measurement of small changes in the signal peak frequencies. In the present case, the two signal peaks have the same frequency, with one peak upshifted and the other downshifted in frequency. In the spectra taken with the single interferometer these two peaks occur symmetrically about the center of each FSR. Because one peak is upshifted and the other downshifted in frequency, changes in the signal peak frequency cause the two peaks to shift in opposite

Table 2.1

Calculated signal peak frequencies for Figure 2.17 (c) and (d) within the frequency range +8.5 GHz to -8.5 GHz. For each peak, the frequency shift of the peak is listed, as well as the frequency shift of the elastic peak to which it belongs.

Peak	Frequency shift (GHz)	Corresponding elastic peak frequency shift (GHz)
1	5.5	25.5
2	3.0	-17.0
3	-3.0	17.0
4	-5.5	-25.5

directions. By measuring the frequency shift between the two peaks, the resolution is increased by a factor of two from that for the shift of a single peak. This technique was used for very careful measurements performed on the iron whisker described in Chapter Six and nickel/iron bilayer films described in Chapter Four.

For very small values of the FSR, the FP plates are separated by a large distance, see equation (2.13). The larger the FP spacing, the more stringent the requirements on the beam incident on the FP because of the increased optical path in between the FP plates. We have made measurements using a FSR of 12.5 GHz, corresponding to an equilibrium plate separation of 12 mm, with no measurable degradation in the finesse of the interferometer.

2.2.7 Experimental uncertainties

The magnetic parameters for a sample were obtained from measurements of the signal peak frequencies as a function of the applied magnetic field. To obtain accurate magnetic parameters, it was necessary to measure the magnetic field and the signal peak frequencies very accurately.

The magnetic field produced by the magnet used in the light scattering experiment was very inhomogeneous within the gap of the magnet. This inhomogeneity prevented the direct use of a NMR probe (Borer and Fremont, 1978) to calibrate the field. Instead, the magnetic field at the sample position was calibrated using an NMR probe in a two step procedure. In the first step, a Hall probe (Bell HTJ8-0608) was attached to an NMR probe and placed in the homogeneous magnetic field produced by a Varian V-3800 electromagnet. For each calibration, the Hall probe was rotated to give a maximum field reading. Three different NMR probes were used to calibrate the Hall probe within the field range from 1 to 10 kOe.

In the second step of the calibration procedure, the Hall probe was accurately placed at the sample position in the gap of the BLS magnet by focussing the laser beam onto the end

of the Hall probe. The second Hall probe, which was permanently fixed to one of the polefaces of the BLS magnet, was calibrated in terms of the Hall probe at the sample position. The two steps of the calibration were combined to obtain the true magnetic field at the sample position from the reading of the Hall probe fixed to the BLS magnet poleface. The accuracy of each step of the calibration procedure, as determined from independent calibration procedures performed on different days, was ± 5 Oe.

The accuracy of the measured frequency shifts was determined by the accuracy to which the spacing of the FP plates was known, as measured by a clock gauge. To obtain accurate values of the FP plate spacing, it was necessary that the zero of the clock gauge correspond to zero FP plate spacing. The gauge was calibrated using the procedure specified by Sandercock (Sandercock, 1980c). A collimated laser beam of diameter 0.8 cm was focussed onto the plate surfaces of the first FP, and the light transmitted through the FP plates was observed on a screen placed 1m from the FP plates. The transmitted light consisted of bright circular fringes separated by dark circular fringes. For large FP plate separations, many fringes were observable. The FP plate spacing was reduced to a value such that only 1 circular fringe, and a central fringe collapsed to a point at the center of the fringe pattern, were observable (2 fringe pattern). The diameter d_A of the outer fringe was measured and the reading of the clock gauge G_A was recorded. Typical values for d_A and G_A were 10cm and 75μ , respectively. The FP plate spacing was then increased such that 2 circular fringes, and a central fringe collapsed to a point, were observable, with the diameter of the outer fringe d_B equal to d_A (3 fringe pattern). The gauge reading G_B was recorded. For FP spacing L_1 , there is a central fringe if $L_1 = n\frac{\lambda}{2}$. The neighbouring fringe in the pattern occurs for the path length $L_2 = (n+1)\frac{\lambda}{2} = L_1 + \frac{\lambda}{2}$. If the plate separation is increased by a factor of two, the path lengths for the two same fringes become $L_3 = 2L_1 = 2n\frac{\lambda}{2}$ and $L_4 = 2L_2 = 2(n+1)\frac{\lambda}{2} = L_3 + 2\frac{\lambda}{2}$. There is a

difference of 2 half wavelengths between these two fringes. Because of this, there must be a fringe halfway between these two fringes, with path length $L_5 = L_3 + \frac{\lambda}{2} = L_4 - \frac{\lambda}{2}$.

Therefore, the FP spacing for the 3 fringe pattern is twice that for the 2 fringe pattern, i.e. $L_B = 2L_A$. Since $L_B - L_A = G_A - G_B$, we have $L_B = 2(G_B - G_A)$. The clock gauge was then adjusted to read $2(G_B - G_A)$. The same procedure was followed for the second FP, with the spacing of the second FP mechanically adjusted such that $G_B = 2G_A$.

The repeatability of the calibration procedure was checked by several independent adjustments of the fringe patterns. The corresponding gauge readings were reproducible to within $\pm 5\mu$. This is the error associated with the FP spacing reading; the error is very small, especially for small FSR measurements. For example, with a FSR of 12.5 GHz, the FP plate spacing is $12\text{mm} \pm 5\mu$.

The angle of incidence θ of the light was accurately measured in the range $\theta = 32^\circ$ to $\theta = 68^\circ$ by observing the specularly reflected light spot on the ceiling of the light scattering room. Outside this angular range the specularly reflected beam did not reach the ceiling. The incident beam was accurately parallel to the optical table top. For an arbitrary angle of incidence, the angle ψ between the specularly reflected beam and the vertical was measured. ψ is positive when measured counterclockwise from the vertical. The geometry is shown in figure 2.18 for ψ positive (a) and ψ negative (b). For both cases

$$\theta = \frac{\pi}{4} - \frac{\psi}{2}. \quad (2.33)$$

The distances X and Y in figure 2.18 were measured to an accuracy of several mm's and the angle ψ was calculated using $\psi = \tan^{-1}\left(\frac{X}{Y}\right)$. Since Y was of the order of 1m, θ was determined to within $\pm 0.2^\circ$.

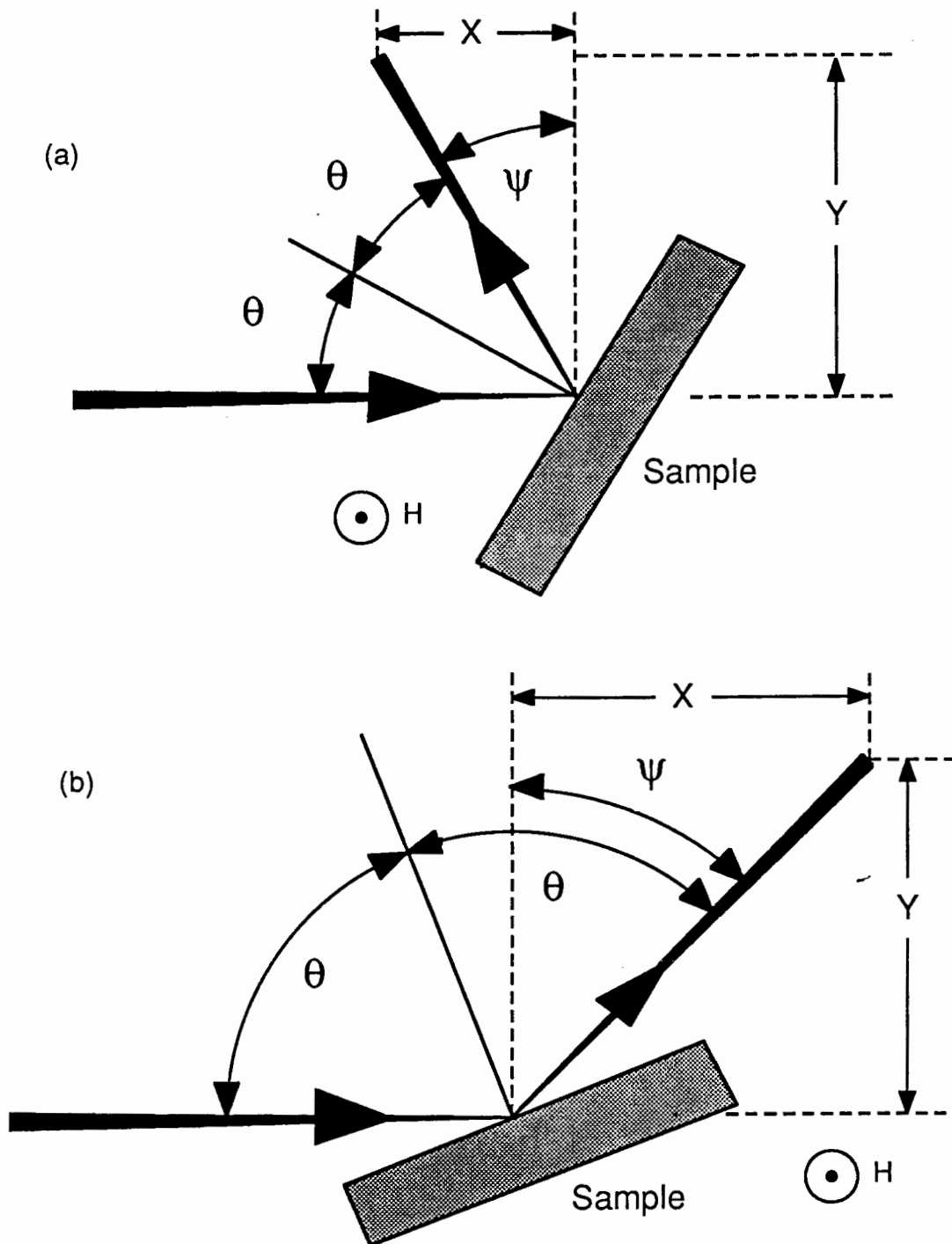


Figure 2.18

Scattering geometry. The laser beam is incident on the sample at an angle θ with the sample normal. The angle ψ between the specularly reflected beam and the vertical was calculated with the measured distances X and Y . ψ is positive (a) when it is measured counterclockwise from the vertical, and negative (b) when measured clockwise from the vertical.

Because of the nonzero aperture of the collection lens, there is an uncertainty in the magnetic wave wavevector involved in the scattering process. We are concerned with light scattering from opaque materials. As discussed in section 1.1, only the wavevector components parallel to the sample surface are conserved in the scattering process, see equation (1.19):

$$(\mathbf{k}_s)_x = (\mathbf{k}_i)_x \pm (\mathbf{k})_x \quad (2.34)$$

where \mathbf{k}_s is the scattered wavevector, \mathbf{k}_i is the incident wavevector, \mathbf{k} is the magnetic wave wavevector and the subscript x denotes the wavevector component parallel to the sample surface. The scattering geometry, including the nonzero collection angle ϕ , is illustrated in figure 2.19. The angle between the incident wavevector and the sample normal is θ . The parallel component of the incident wavevector is given by $(\mathbf{k}_i)_x = k_i \sin \theta$ and the minimum and maximum values of $(\mathbf{k}_s)_x$ are given by

$$[(\mathbf{k}_s)_x]_{\min} = -k_i \sin \left(\theta - \frac{\phi}{2} \right) \quad (2.35)$$

$$[(\mathbf{k}_s)_x]_{\max} = -k_i \sin \left(\theta + \frac{\phi}{2} \right) \quad (2.36)$$

Therefore

$$[(\mathbf{k})_x]_{\min} = k_i \sin \theta + k_i \sin \left(\theta - \frac{\phi}{2} \right) \quad (2.37)$$

$$[(\mathbf{k})_x]_{\max} = k_i \sin \theta + k_i \sin \left(\theta + \frac{\phi}{2} \right) \quad (2.38)$$

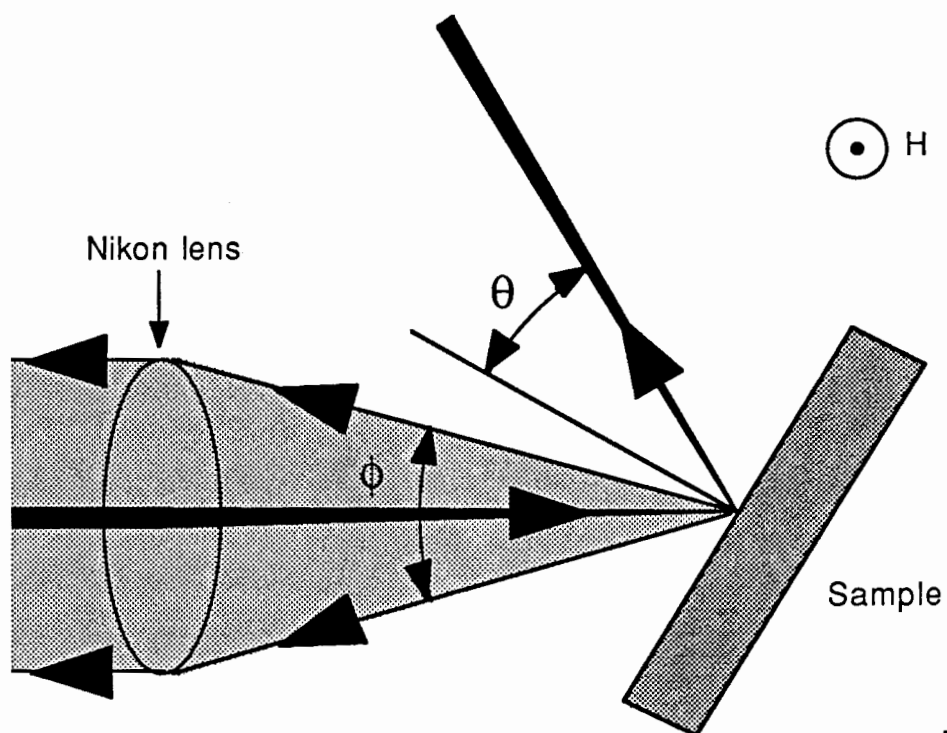


Figure 2.19

Scattering geometry, including the nonzero collection angle ϕ of the Nikon camera lens. The angle between the incident light and the sample normal is θ .

The spread in the component of the magnetic wave wavevector parallel to the surface, $\Delta(\mathbf{k})_x$, is given by

$$\Delta(\mathbf{k})_x = [(\mathbf{k})_x]_{\max} - [(\mathbf{k})_x]_{\min} = 2k_i \cos \theta \sin \frac{\phi}{2} \quad (2.39)$$

For $\phi = 0$, the value of $(\mathbf{k})_x$ is

$$[(\mathbf{k})_x]_{\phi=0} = 2k_i \sin \theta \quad (2.40)$$

Therefore the relative uncertainty in $(\mathbf{k})_x$ is

$$\frac{\Delta(\mathbf{k})_x}{[(\mathbf{k})_x]_{\phi=0}} = \cotan \theta \sin \frac{\phi}{2} . \quad (2.41)$$

Equation (2.41) has its minimum value for $\phi = 0$, of course, and $\theta = 90^\circ$. Our collection lens has an f-number of 1.4, corresponding to

$$\frac{\phi}{2} = \tan^{-1} \left(\frac{1}{2f} \right) = 19.6^\circ . \quad (2.42)$$

For this value of $\phi/2$, the relative uncertainty in $(\mathbf{k})_x$, equation (2.41), varies between 54% for $\theta = 32^\circ$ and 14% for $\theta = 68^\circ$. These are the values of θ between which θ can be measured accurately, as discussed above. For $\theta = 45^\circ$, the relative uncertainty in $(\mathbf{k})_x$ is 34%. This uncertainty in $(\mathbf{k})_x$ leads to a broadening of the measured signal peaks in the FP spectra. This broadening effect can be calculated using the theory described in Chapter Three.

The laser power was measured with the power meter which was built into the laser. A second portable power meter was used to measure the laser power at the sample position relative to that at the exit of the laser. It was found that 70% of the exit power from the laser was transmitted to the sample position.

2.2.8 System performance

The performance of the BLS apparatus will be described in terms of the transmission of the interferometer, the contrast of the interferometer, and the number of counts per second per mW of incident laser power as measured for a standard sample using the photon counting photomultiplier.

The intensity of light transmitted by the FP multipassing optics through six passes of the tandem FP interferometer was measured to be 10% of the intensity of light at the entrance to the FP multipassing optics for a FSR of 12.5 GHz. This value of 10% for the transmission for six passes is very good for a BLS system, according to Wilber (Wilber, 1985) who has constructed a similar system, and corresponds to an equivalent transmission of 70% for a single pass of the interferometer. The transmission for four passes through the first interferometer was measured to be 30%.

The contrast was measured as the ratio of the number of counts for the elastic peak maximum to the number of counts in the background between two neighbouring elastic peaks. For two passes through the FP interferometer (either the first or the second interferometer), contrast values greater than 2×10^4 were directly measured. The maximum contrast that could be measured with this technique was approximately 10^7 , since the maximum count rate was 3×10^6 counts/s, as determined by the photon counting electronics, and the minimum count rate was 0.3 counts/s, as determined by the dark count of the photomultiplier tube. For four and six passes through the interferometer, the

background observed between the elastic peaks was determined by the dark count of the photomultiplier tube.

The best testimony to the performance of the BLS system was that peaks due to magnetic waves in iron films as thin as 3 monolayers thick could be observed easily, as discussed in Chapters Four and Five. A spectrum obtained from a 3 monolayer thick iron film grown on Cu(001) and covered by 60 monolayers of Cu is shown in figure 2.20. The spectrum was collected using a tandem interferometer with a FSR of 30 GHz. The large peaks which occur at 0 and ± 30 GHz are due to elastically scattered light. The peaks which occur at ± 8.6 GHz are due to inelastic scattering from magnetic waves in the 3 monolayer thick iron film; the peaks can be observed clearly above the background noise level in the spectrum.

A standard sample was used to measure the day-to-day performance of the BLS system. Because the beamsplitter cube discussed in section 2.2.1 was usually installed in the incident and collected beam optics, the system was sensitive to scattering from magnetic waves and insensitive to scattering from sound waves. Therefore a standard magnetic sample, consisting of a 50Å thick film of permalloy that had been evaporated onto a silicon substrate, was used. This sample, supplied by Dr. C.E. Patton, gave very large scattering from the magnetic surface mode. With an applied field of 2kOe, the intensity of the surface mode localized at the front surface of the permalloy film was measured. The figure of merit for the BLS system was taken to be the peak number of counts for this mode divided by the product of the counting time for each MCA channel in seconds and the incident laser power in mW. A typical value for the system figure of merit was 3.4 counts/(s-mW). This value compares well with the figure of merit of 2.9 counts/(s-mW) measured with the same sample for the BLS system at Colorado State University. A realignment of the system optics was performed if the figure of merit was less than 2 counts/(s-mW). In figure 2.21 a typical spectrum for the permalloy sample is shown. The spectrum was collected using

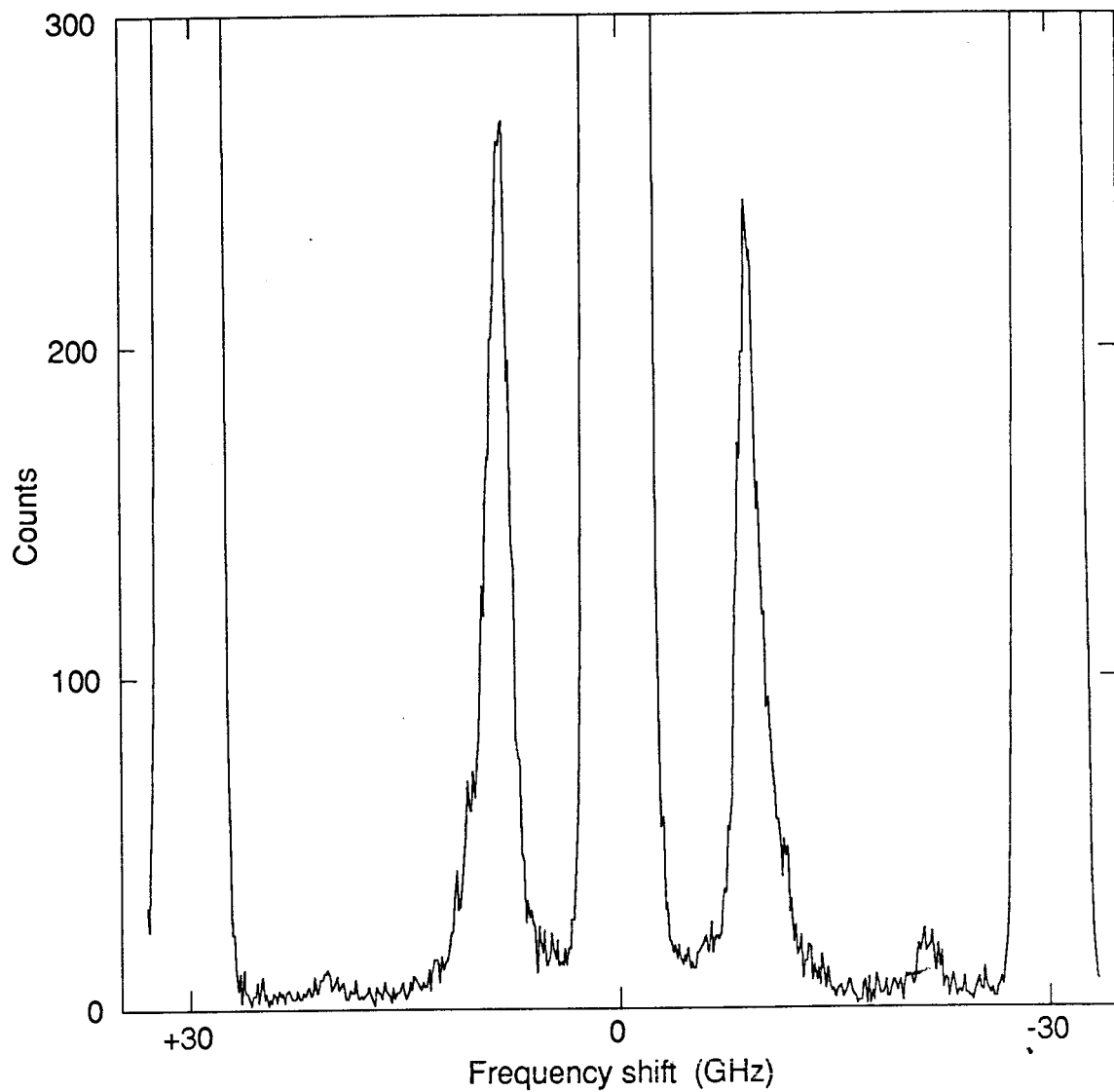


Figure 2.20

BLS spectrum for 3ML Fe on Cu(001) (sample 5.2, see Table 5.1) for an applied field of $H = 5.81$ kOe, an incident laser power of 140 mW and a total counting time for each of the 512 data points of 2.012 s.

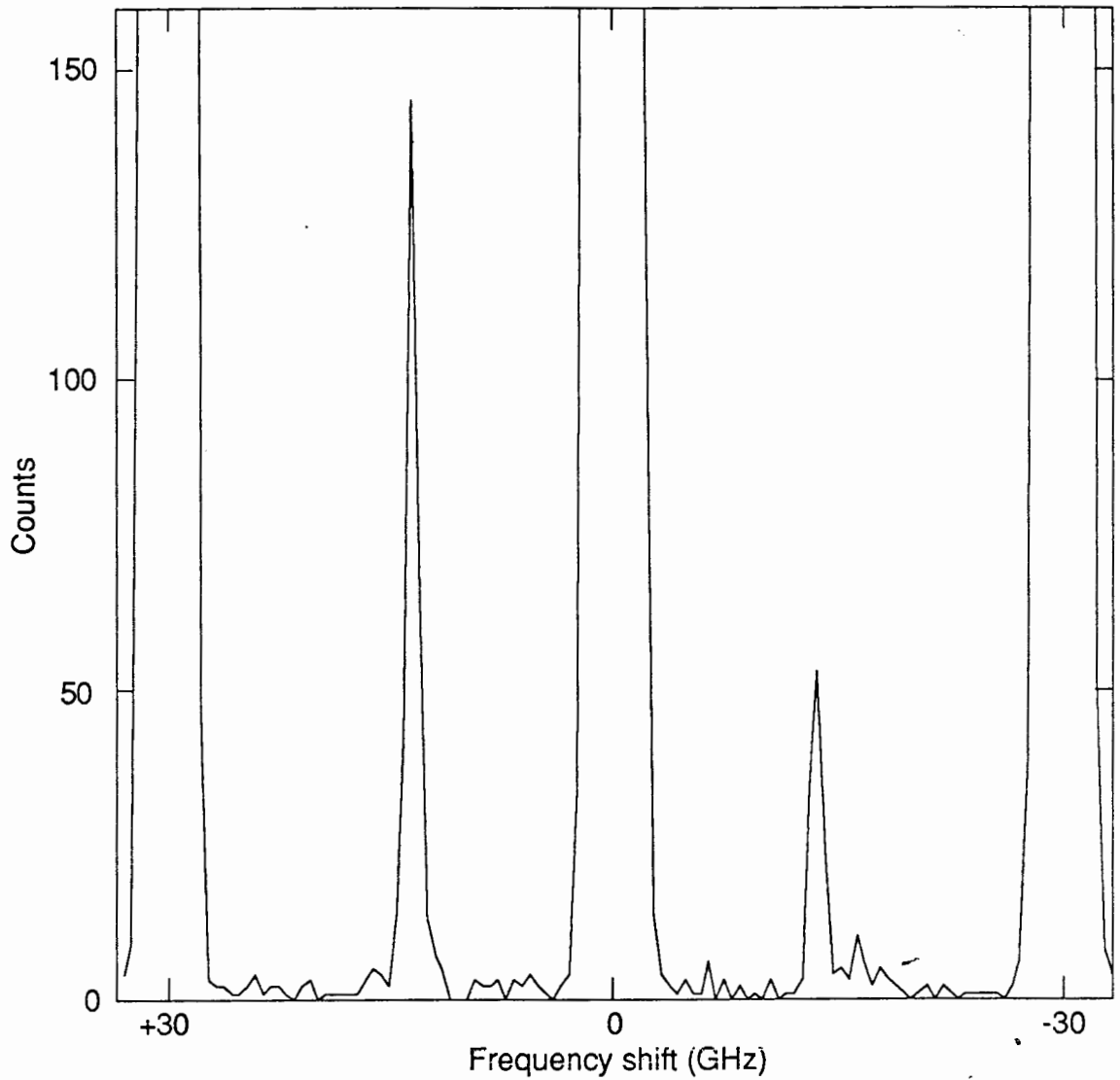


Figure 2.21

BLS spectrum for a 50\AA thick permalloy film (the standard sample) for an applied magnetic field of $H = 1.92\text{ kOe}$, a laser power of 8.8 mW and a total counting time for each of the 128 data points of 4.000 s .

the tandem interferometer with a FSR of 30 GHz. The surface mode peaks are very narrow and well above the background noise level. The permalloy film peaks have an intrinsic linewidth of 0.30 GHz as measured with ferromagnetic resonance.

A typical high resolution frequency measurement is shown in figure 2.22 for domain wall observation in the iron whisker sample described in Chapter 6. The spectrum was collected using a single interferometer with a FSR of 12.5 GHz, corresponding to a FP mirror spacing of 12 mm. Between each set of neighbouring elastic peaks there are two signal peaks; one of these peaks is upshifted in frequency and the other peak is downshifted in frequency. These signal peaks at ± 4.7 and ± 7.4 GHz are well-defined peaks with narrow linewidths; the finesse of the interferometer (the ratio of the FSR to the linewidth) is 20. Therefore, excellent performance of the interferometer is obtained with large FP mirror spacings.

The slow scan option of the interferometer control electronics described in section 2.2.5 was useful for quick determinations of the peak positions in a spectrum because most of the frequency range could be scanned quickly, with a longer data collection time over a small part of the frequency range. Another useful feature of the slow scan option was that quick scanning across the elastic peaks helped to prevent overloading of the photon counting photomultiplier tube. In figure 2.23 is shown a spectrum collected using the slow scan option for one of the ultrathin Ni/Fe bilayer samples discussed in section 4.2. The spectrum was collected using a single interferometer with a FSR of 15 GHz. Of the two signal peaks which appear between 0 and 15 GHz, one is upshifted in frequency and the other is downshifted in frequency. The counting time for each data point in the frequency range +3.6 to +11.4GHz was 4.584 s; outside this frequency range, the counting time for each data point was 0.458 s. This spectrum was collected in 15 minutes of real time. If a counting time of 4.584 s per channel had been used for the entire frequency range, the total data collection time would have been 42 minutes. The reduction in data collection time is

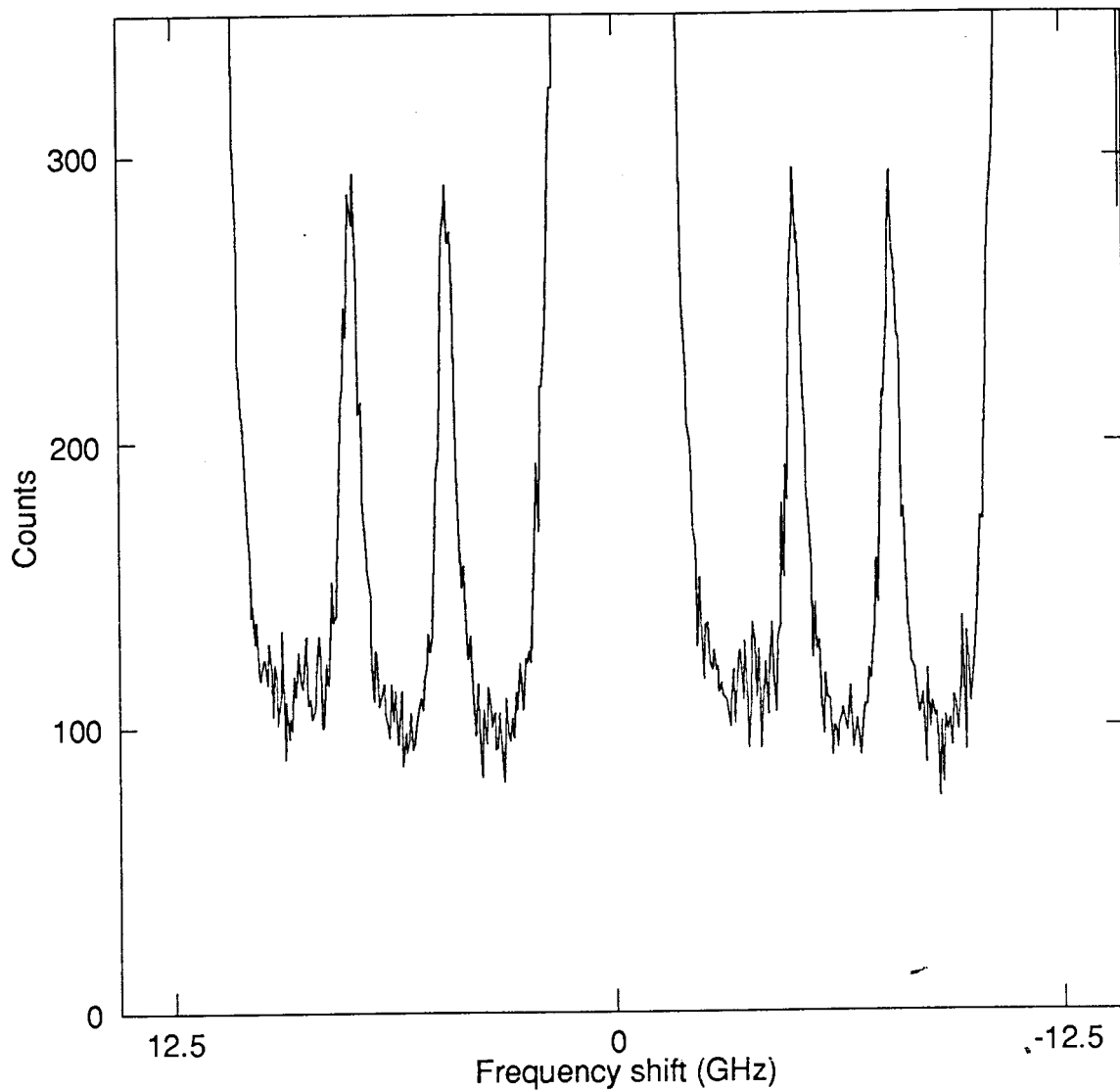


Figure 2.22

BLS spectrum for a 15 ML Au/Fe(001) whisker in zero applied field using a single interferometer and a small free spectral range (12.5 GHz). The surface modes of the whisker are visible. 140 mW of incident laser power was used. The angle of incidence was $\theta = 45^\circ$. The total counting time for each of the 512 data points was 7.388 s.

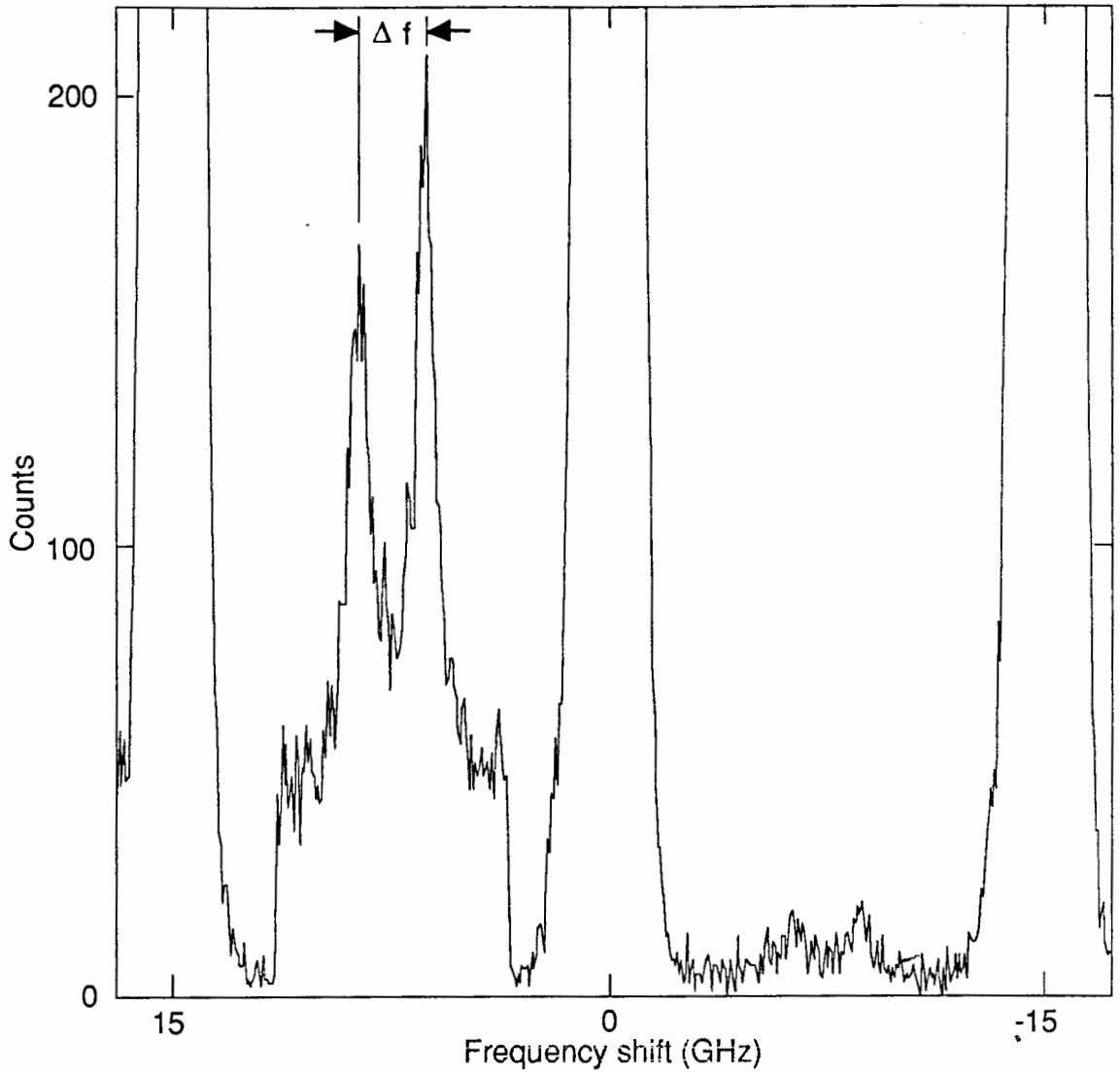


Figure 2.23

BLS spectrum for sample 4.11 (see table 4.3) for an applied field of $H = 3.99$ kOe, an incident laser power of 88 mW and a total counting time for each of the 512 data points of 4.584 s. On the figure, Δf is the frequency difference between the upshifted and downshifted surface mode peaks.

substantial. There is no observable difference in the linewidths of the peaks measured with and without the use of the slow scan option. However, the peaks measured in spectra collected using the slow scan option were shifted in frequency with respect to peaks measured in spectra collected without the use of the slow scan option. Typical shifts in the peak positions were 4 channels of the MCA. These small shifts were probably a consequence of a characteristic response time of the scanning stage as the scanning rate of the FP mirrors was changed by a factor of 10 during the scan of the mirrors. This response time of the scanning stage may be related to the use of a capacitance sensor to control the FP mirror separation.

CHAPTER THREE

CALCULATION OF THE LIGHT SCATTERING FROM THERMAL MAGNONS IN THIN MAGNETIC FILMS

In this chapter, a procedure is described for calculating the intensity of light scattered from thermal magnons in a uniformly magnetized thin film. The calculation takes place in four steps:

- (1) the magnetic normal modes of the thin film are calculated;
- (2) the mean amplitude of the deviation of the magnetization from equilibrium for a normal mode is calculated from its mean thermal energy;
- (3) the magnetization distribution corresponding to a normal mode is used, together with the electric field distribution in the film set up by the incident optical radiation, to calculate the spatial distribution of the electric polarization which oscillates at a frequency given by the incident optical frequency shifted by the magnetic normal mode frequency; and
- (4) the electric dipole distribution from (3) is used to calculate the intensity of the optical radiation scattered from the magnetic normal mode.

In section 3.1, the light scattering calculation for a film that is uniformly magnetized in the sample plane is presented. The description of this calculation closely follows that of Cochran and Dutcher (Cochran and Dutcher, 1988a; Cochran and Dutcher, 1988b). In section 3.2, the light scattering calculation is extended to allow the uniform magnetization to tilt out of the sample plane toward the sample normal. In section 3.3, a very brief discussion of the application of the light scattering calculation to the real BLS experiment is presented.

3.1 The light scattering calculation with the magnetization lying in the sample plane

3.1.1 The normal modes of a thin magnetic film

Consider a thin slab of thickness d , uniformly magnetized in the absence of excitations, and oriented with its normal along the z -axis, see figure 3.1. The film is assumed to be surrounded on both sides by vacuum. The lateral dimensions of the slab are supposed to be very large. We assume that the applied magnetic field lies in the plane of the slab and that the static magnetization is parallel with the applied field. This corresponds to the most commonly used experimental configuration. Let the direction of the magnetic field define the x -axis of a right handed coordinate system (see figure 3.1).

Maxwell's equations, in CGS units and vector form, are

$$\nabla \times \mathbf{e} = -\frac{1}{c} \frac{\partial \mathbf{b}}{\partial t} = -\frac{1}{c} \frac{\partial}{\partial t} (\mathbf{h} + 4\pi \mathbf{m}) \quad (3.1)$$

$$\nabla \times \mathbf{h} = \frac{4\pi\sigma}{c} \mathbf{e} + \frac{1}{c} \frac{\partial \mathbf{d}}{\partial t} = \frac{4\pi\sigma}{c} \mathbf{e} + \frac{\epsilon}{c} \frac{\partial \mathbf{e}}{\partial t} \quad (3.2)$$

$$\nabla \cdot \mathbf{d} = \nabla \cdot \epsilon \mathbf{e} = 4\pi \rho \quad (3.3)$$

$$\nabla \cdot \mathbf{b} = \nabla \cdot (\mathbf{h} + 4\pi \mathbf{m}) = 0. \quad (3.4)$$

In equation (3.2), the current density \mathbf{j} has been written as $\mathbf{j} = \sigma \mathbf{e}$. Because the static field H and the magnetization M_s lie along the x -axis, we set the radio-frequency (rf) magnetic field component $h_x = 0$ and spatial variations in the x -direction are not considered.

Equations (3.1), (3.2) and (3.4) for the magnetically active modes become

$$\frac{\partial e_x}{\partial z} = -\frac{1}{c} \frac{\partial b_y}{\partial t} = -\frac{1}{c} \frac{\partial}{\partial t} (h_y + 4\pi m_y) \quad (3.5)$$

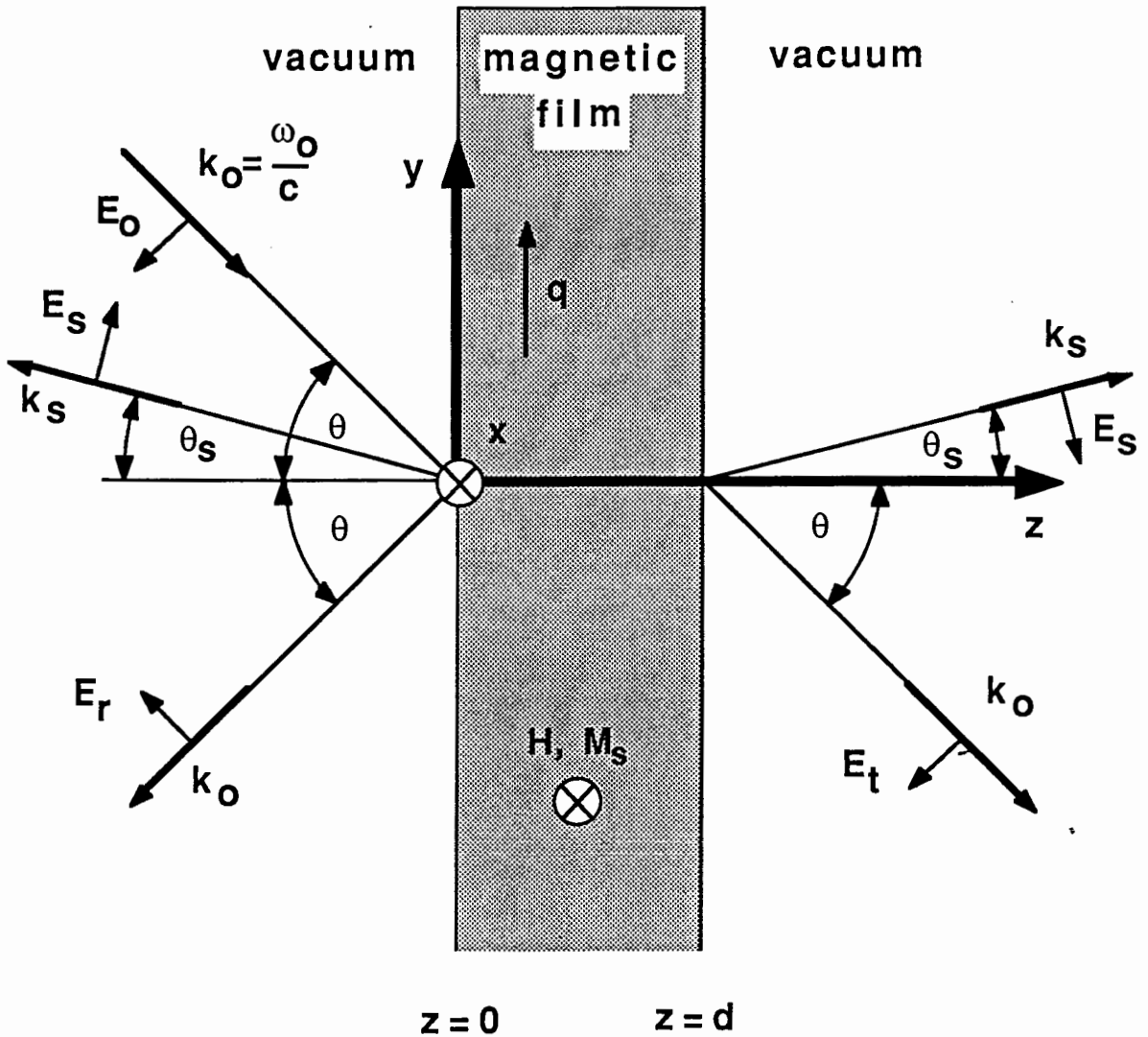


Figure 3.1

The geometry used to calculate the intensity of light scattered from thermal magnons in a thin magnetic film surrounded by vacuum. The static magnetization M_s in the film is assumed to be uniform and parallel with the external dc field H along the x -axis in the sample plane (into the page). The angles of the incident and scattered light, θ and θ_s , are measured with respect to the normal.

$$\frac{\partial e_x}{\partial y} = \frac{1}{c} \frac{\partial b_z}{\partial t} = \frac{1}{c} \frac{\partial}{\partial t} (h_z + 4\pi m_z) \quad (3.6)$$

$$\frac{\partial h_z}{\partial y} - \frac{\partial h_y}{\partial z} = \frac{4\pi\sigma}{c} e_x \quad (3.7)$$

$$\frac{\partial b_y}{\partial y} + \frac{\partial b_z}{\partial z} = 0. \quad (3.8)$$

The displacement current $\frac{\epsilon}{c} \frac{\partial \mathbf{e}}{\partial t}$ has been neglected in equation (3.7) because at microwave frequencies it is very small compared with the conduction current density. Similar equations describe the fields in the vacuum surrounding the magnetic film except that $m_y = m_z = 0$ and the displacement current is included:

$$\frac{\partial e_x}{\partial z} = -\frac{1}{c} \frac{\partial h_y}{\partial t} \quad (3.9)$$

$$\frac{\partial e_x}{\partial y} = \frac{1}{c} \frac{\partial h_z}{\partial t} \quad (3.10)$$

$$\frac{\partial h_z}{\partial y} - \frac{\partial h_y}{\partial z} = \frac{1}{c} \frac{\partial e_x}{\partial t} \quad (3.11)$$

$$\frac{\partial h_y}{\partial y} + \frac{\partial h_z}{\partial z} = 0. \quad (3.12)$$

Solutions of Maxwell's equations are sought which are proportional to the factor $e^{i(qy - \omega t)}$. The disturbances in the surrounding vacuum must all be proportional to the same factor in order that the tangential components of e_x and h_y may be continuous everywhere across the interfaces. The in-plane component of the wavevector q is real, and in a Brillouin light scattering experiment it is determined by the wavelength and the geometry of

the incident and scattered laser light (Sandercock, 1982). We shall take q to lie along the y -axis and perpendicular to the applied field. From the outset the frequency f , where $\omega = 2\pi f$, is taken to be a complex quantity. The real part of the frequency is, of course, the resonant frequency of a normal mode; the imaginary part of f must necessarily be negative since the amplitude of a normal mode which has been stimulated by an impulse must die away with time due to magnetic dissipation and eddy current damping. Solutions of Maxwell's equations in the magnetic film are sought which have a z dependence $\sim e^{ikz}$ where, by definition, the imaginary part of k is taken to be positive.

The fields in the vacuum are assumed to have a z dependence $\sim e^{ik_v z}$. We solve equations (3.9) and (3.10) for h_y and h_z and substitute into equation (3.11) to obtain

$$\left[k_v^2 + q^2 - \left(\frac{\omega}{c} \right)^2 \right] e_x = 0. \quad (3.13)$$

The term in the square bracket of equation (3.13) must vanish. For a typical microwave frequency of 30 GHz, $\frac{\omega}{c} = 6 \text{ cm}^{-1}$. Since $q \sim 10^5 \text{ cm}^{-1}$, $\left(\frac{\omega}{c} \right)^2 \ll q^2$ and we have $k_v^2 = -q^2$. In the vacuum, the fields fall to zero with distance from the film. This requires that $\text{Im}(k_v) < 0$ for $z \leq 0$ and $\text{Im}(k_v) > 0$ for $z \geq d$. Therefore, we have

$$k_v = \begin{cases} -iq & \text{for } z \leq 0 \\ +iq & \text{for } z \geq 0 \end{cases} \quad (3.14)$$

In the magnetic material, Maxwell's equations alone do not determine the allowed values of the wavevector; they provide only one set of relationships between the magnetization components and the magnetic fields. From equations (3.5) to (3.8), one finds

$$4\pi m_y = -(1 + i\delta^2 k^2) h_y + i\delta^2 q k h_z, \quad (3.15)$$

$$4\pi m_z = i\delta^2 q k h_y - (1 + i\delta^2 q^2) h_z. \quad (3.16)$$

where $\delta^2 = c^2/(4\pi\omega\sigma)$. A second set of relationships is provided by the Landau-Lifshitz equation of motion for the magnetization, which can be written as

$$\frac{-1}{\gamma} \frac{\partial \mathbf{M}}{\partial t} = \mathbf{M} \times \mathbf{H}_{\text{eff}}. \quad (3.17)$$

In this equation, $\gamma = g|e|/(2m_e c)$ is the gyromagnetic ratio of the magnetic material, $\mathbf{M} = (M_x, m_y, m_z)$ is the magnetization, and \mathbf{H}_{eff} is the effective magnetic field acting on the magnetization. In words, equation (3.17) states that the time rate of change of the angular momentum, $\mathbf{L} = -\mathbf{M}/\gamma$, is equal to the torque on the magnetization,

$$\boldsymbol{\tau} = \mathbf{M} \times \mathbf{H}_{\text{eff}}. \quad (3.18)$$

The torque causes the magnetization to precess about its equilibrium direction. For a given magnetic material, there are several possible sources of the torque. We will consider the following sources, each of which is discussed in detail below: applied magnetic fields, static shape demagnetizing field, exchange, magnetic anisotropy, and magnetic damping. The torque expressions can be directly obtained from the effective fields using equation (3.18), or from the free energy expressions E by first calculating the effective field,

$$\mathbf{H}_{\text{eff}} = - \frac{\partial E}{\partial \mathbf{M}}, \quad (3.19)$$

and then by using this field to calculate the torque from equation (3.18). In the following discussion, only terms that are linear in the rf magnetization components m_i 's will be considered. The neglect of terms that are second or higher order in the m_i 's is justified if the m_i 's are small compared with the static magnetization M_s . The resulting equations are said to be linearized.

i) Applied static field

The applied static field is directed along the +x-axis, see figure 3.1:

$$H_x^a = H; \quad H_y^a = 0; \quad H_z^a = 0. \quad (3.20)$$

This gives rise to the following torque components:

$$\tau_x^a = 0; \quad \tau_y^a = H m_z; \quad \tau_z^a = -H m_y. \quad (3.21)$$

ii) Static shape demagnetizing field

Because of the magnetic dipole-dipole interaction, magnetic charges appear on the surfaces of a magnetic sample. These charges generate a field within the sample which depends on the geometry of the sample and which tends to oppose the applied magnetic field (Brown, 1978). For uniformly magnetized ellipsoidal samples, the demagnetizing field $\mathbf{H}^{\text{demag}}$ can be written as

$$\mathbf{H}^{\text{demag}} = -4\pi\mathbf{D} \cdot \mathbf{M}_s \quad (3.22)$$

The components of the tensor \mathbf{D} depend on the dimensions of the sample along the three principal axes of the ellipse. Very thin magnetic films of large lateral extent can be treated

as an ellipse with one principal axis much shorter than the other two. For this limiting case, we have

$$H_x^{\text{demag}} = -4\pi D_x M_S \cos \alpha; \quad H_y^{\text{demag}} = 0; \quad H_z^{\text{demag}} = -4\pi D_z M_S \sin \alpha \quad (3.23)$$

where $D_x \sim 0$ and $D_z \sim 1$ for very thin magnetic films, and α is the angle between the equilibrium direction of the magnetization and the sample plane. The magnetization has been assumed to lie in the x - z plane. For α equal to zero, as it is for the calculation described in section 3.1, the shape demagnetizing field can be neglected for very thin magnetic films. The case of α not equal to zero is discussed in section 3.2.

For thicker magnetic films, such as the iron whisker discussed in Chapter Six, the expressions for D are more complicated but results have been tabulated for special geometries (Bozorth, 1951).

Only the static demagnetizing field has been considered in this section. There is also a dynamic demagnetizing field h_z which is taken into account in Maxwell's equations, equations (3.5) to (3.8) (Rudd, 1985).

iii) Exchange

A magnetic material has its lowest energy when all of the spins are parallel. Any nonuniform deviation of the spin directions results in an increase in the energy of the film because of the exchange interaction. The energy of the exchange interaction is given by (Brown, 1978)

$$E_{\text{ex}} = \frac{A}{M_S^2} ((\nabla M_x)^2 + (\nabla M_y)^2 + (\nabla M_z)^2) \quad (3.24)$$

where A is the exchange stiffness parameter in erg/cm. Assuming a spatial variation of $\sim e^{iqy} e^{ikz}$, the effective field due to the exchange interaction can be written as

$$H_x^{\text{ex}} = 0 \quad (3.25)$$

$$H_y^{\text{ex}} = \frac{2A}{M_s^2} \left(\frac{\partial^2 m_y}{\partial y^2} + \frac{\partial^2 m_y}{\partial z^2} \right) = -\frac{2A}{M_s^2} (q^2 + k^2) m_y \quad (3.26)$$

$$H_z^{\text{ex}} = \frac{2A}{M_s^2} \left(\frac{\partial^2 m_z}{\partial y^2} + \frac{\partial^2 m_z}{\partial z^2} \right) = -\frac{2A}{M_s^2} (q^2 + k^2) m_z \quad (3.27)$$

The effective fields due to exchange give rise to the following torque components:

$$\tau_x^{\text{ex}} = 0; \quad \tau_y^{\text{ex}} = \frac{2A}{M_s} (q^2 + k^2) m_z; \quad \tau_z^{\text{ex}} = -\frac{2A}{M_s} (q^2 + k^2) m_y \quad (3.28)$$

The y -dependence of $\sim e^{iqy}$ always gives an exchange contribution for a sample of large lateral extent. For ultrathin films, the z -dependence of $\sim e^{ikz}$ becomes unimportant because the spins are very nearly parallel to one another for low frequency excitations.

iv) Magnetic anisotropy

Because of spin-orbit coupling, the energy of a ferromagnetic sample can depend on the direction of the magnetization relative to a particular axis or axes in the sample. For example, this may be due to the crystal structure or the geometry of the sample. We will consider anisotropies which exhibit four-fold symmetry in the plane of the sample, and two-fold symmetry along the sample normal.

The magnetocrystalline anisotropy energy with four-fold symmetry in the sample plane, assuming that the magnetization lies along a cube axis in the sample plane, has the form

$$E^{MCA} = \frac{K_1}{M_s^4} (M_x^2 M_y^2 + M_y^2 M_z^2 + M_z^2 M_x^2) \quad (3.29)$$

where K_1 is the first order cubic magnetocrystalline anisotropy constant. The effective field components for the magnetocrystalline anisotropy are determined from equation (3.19). To first order in m_y/M_s and m_z/M_s , we have

$$H_x^1 = 0; \quad H_y^1 = -\frac{2K_1}{M_s^2} m_y; \quad H_z^1 = -\frac{2K_1}{M_s^2} m_z; \quad (3.30)$$

and the corresponding torque components are

$$\tau_x^1 = 0; \quad \tau_y^1 = \frac{2K_1}{M_s} m_z; \quad \tau_z^1 = -\frac{2K_1}{M_s} m_y. \quad (3.31)$$

A uniaxial anisotropy energy with the easy axis along the sample normal can be written as

$$E^{UA} = -\frac{K_u^{(1)}}{M_s^2} M_z^2 \quad (3.32)$$

where $K_u^{(1)}$ is the first order uniaxial anisotropy constant. The components of the effective field due to this anisotropy energy, as determined from equation (3.19), are

$$H_x^{u1} = 0; \quad H_y^{u1} = 0; \quad H_z^{u1} = \frac{2K_u^{(1)}}{M_s^2} m_z; \quad (3.33)$$

the corresponding torque components due to the uniaxial anisotropy are

$$\tau_x^{u1} = 0; \quad \tau_y^{u1} = -\frac{2K_u^{(1)}}{M_s} m_z; \quad \tau_z^{u1} = 0. \quad (3.34)$$

v) Magnetic damping

Damping processes which allow the magnetization to relax toward its equilibrium state are accounted for by the inclusion of an effective field, \mathbf{H}^d , which is proportional to the time rate of change of the magnetization:

$$H_x^d = 0; \quad H_y^d = -\frac{G}{\gamma^2 M_s^2} \frac{\partial m_y}{\partial t}; \quad H_z^d = -\frac{G}{\gamma^2 M_s^2} \frac{\partial m_z}{\partial t}, \quad (3.35)$$

where G is the Gilbert damping parameter. For a temporal variation $\sim e^{-i\omega t}$, the torque components due to magnetic damping are

$$\tau_x^d = 0; \quad \tau_y^d = -\frac{i\omega}{\gamma} \frac{G}{\gamma M_s} m_z; \quad \tau_z^d = \frac{i\omega}{\gamma} \frac{G}{\gamma M_s} m_y. \quad (3.36)$$

By substituting equations (3.21), (3.28), (3.31), (3.34) and (3.36) into equation (3.17), the resulting linearized Landau-Lifshitz equations of motion for the magnetization can be written in the form

$$-\left(\frac{i\omega}{\gamma}\right)4\pi m_y + \left(H_y + \frac{2Ak^2}{M_s}\right)4\pi m_z = 4\pi M_s h_z, \quad (3.37)$$

$$\left(H_z + \frac{2Ak^2}{M_s}\right)4\pi m_y + \left(\frac{i\omega}{\gamma}\right)4\pi m_z = 4\pi M_s h_y \quad (3.38)$$

where

$$H_y = H + \frac{2Aq^2}{M_s} + \gamma - i \frac{\omega}{\gamma} \frac{G}{\gamma M_s}, \quad (3.39)$$

$$H_z = H + \frac{2Aq^2}{M_s} + \alpha - i \frac{\omega}{\gamma} \frac{G}{\gamma M_s}, \quad (3.40)$$

and α and γ are anisotropy fields given by

$$\alpha = \frac{2K_1}{M_s} \quad (3.41)$$

$$\gamma = \frac{2K_1}{M_s} - \frac{2K_u^{(1)}}{M_s}. \quad (3.42)$$

Substitution of equations (3.15) and (3.16) for $4\pi m_y$, $4\pi m_z$ into equations (3.37) and (3.38) results in a pair of homogeneous equations for h_y , h_z . The determinant of the coefficients of these two equations must vanish in order to obtain nontrivial solutions, and this requirement leads to an equation which is cubic in k^2 :

$$R_1 k^6 + R_2 k^4 + R_3 k^2 + R_4 = 0. \quad (3.43)$$

where

$$R_1 = \left(\frac{2A}{M_s} \right)^2 \quad (3.44)$$

$$R_2 = \left(\frac{2Aq}{M_s} \right)^2 + \left[\left(\frac{2A}{M_s} \right) \cdot (H_y + H_z + 4\pi M_s) \right] - i \left(\frac{2A}{M_s \delta} \right)^2 \quad (3.45)$$

$$R_3 = \left[\left(\frac{2Aq^2}{M_s} \right) \cdot (H_y + H_z + 4\pi M_s) \right] + \left[(H_y + 4\pi M_s) H_z - \left(\frac{\omega}{\gamma} \right)^2 \right] \\ - i \left(\frac{2A}{M_s \delta^2} \right) \cdot (H_y + H_z + 8\pi M_s) \quad (3.46)$$

$$R_4 = q^2 \left[H_y \cdot (H_z + 4\pi M_s) - \left(\frac{\omega}{\gamma} \right)^2 \right] \\ - \frac{i}{\delta^2} \cdot \left[(H_y + 4\pi M_s) \cdot (H_z + 4\pi M_s) - \left(\frac{\omega}{\gamma} \right)^2 \right]. \quad (3.47)$$

The magnetostatic approximation is often used (Camley and Mills, 1978; Camley, Rahman and Mills, 1981; and Patton, 1984) in which $\nabla \times \mathbf{h}$ is taken to be zero. Equation (3.7) is replaced by

$$kh_y = qh_z. \quad (3.48)$$

When combined with equations (3.5) and (3.6), this approximation leads to the relations

$$h_y = (-q^2 (4\pi m_y) - kq (4\pi m_z)) / (k^2 + q^2) \quad (3.49)$$

$$h_z = (-kq (4\pi m_y) - k^2 (4\pi m_z)) / (k^2 + q^2). \quad (3.50)$$

Upon substituting equations (3.49) and (3.50) into the Landau-Lifshitz equations (3.37) and (3.38) one obtains a secular equation which is quartic in k^2 . It may be shown that (k^2+q^2) is a factor of the secular equation: $k^2 = -q^2$ corresponds to a spurious mode which is of no interest here. Upon factoring (k^2+q^2) out of the secular equation, the interesting values of k^2 are the roots of

$$R_1^0 k^6 + R_2^0 k^4 + R_3^0 k^2 + R_4^0 = 0, \quad (3.51)$$

where

$$R_1^0 = \left(\frac{2A}{M_s} \right)^2 \quad (3.52)$$

$$R_2^0 = \left(\frac{2Aq}{M_s} \right)^2 + \left[\left(\frac{2A}{M_s} \right) \cdot (H_y + H_z + 4\pi M_s) \right] \quad (3.53)$$

$$R_3^0 = \left[\left(\frac{2Aq^2}{M_s} \right) \cdot (H_y + H_z + 4\pi M_s) \right] + \left[(H_y + 4\pi M_s) H_z - \left(\frac{\omega}{\gamma} \right)^2 \right] \quad (3.54)$$

$$R_4^0 = q^2 \left[H_y \cdot (H_z + 4\pi M_s) - \left(\frac{\omega}{\gamma} \right)^2 \right]. \quad (3.55)$$

These coefficients are very similar to those which occur in equations (3.44) to (3.47). The difference between R_2 and R_2^0 is very small because $(2A/M_s\delta^2)$ is typically very small compared with the field $(H_y + H_z + 4\pi M_s)$; for example, $\delta = 6.4 \times 10^{-5}$ cm in iron at 30 GHz, and therefore $(2A/M_s\delta^2) = 0.6$ Oe. The corrections to R_3^0 and R_4^0 are of order $(1/q^2\delta^2)$. For iron at 30 GHz, and for backscattering of 5145 Å laser light incident at 45° ($q = 1.73 \times 10^5$ cm⁻¹), these corrections are of the order of one percent.

The three values for k^2 obtained from equations (3.43) to (3.47) mean that the spatial variation along z of the fields in the film can be described by the superposition of six waves - three forward propagating and three backward propagating waves. We denote the wavevectors of the three forward propagating waves as $k^{(1)}$, $k^{(3)}$ and $k^{(5)}$, and the wavevectors of the backward propagating waves as $k^{(2)} = -k^{(1)}$, $k^{(4)} = -k^{(3)}$, and $k^{(6)} = -k^{(5)}$. For both sets of three waves, one of the waves corresponds to a nonpropagating spin wave; its amplitude is always small. Of the remaining two waves, one corresponds to a propagating spin wave, and the other to a damped surface wave.

Let the component along y of the rf magnetic field amplitude for each of the six waves in the film be $h_y^{(i)}$, for $i = 1, \dots, 6$. The total h_y field is given by

$$h_y = \sum_{i=1}^6 h_y^{(i)} = \sum_{i=1}^6 h_y^{(i)}(0) e^{ik^{(i)}z}, \quad (3.56)$$

where the phases of the $h_y^{(i)}$ fields have been chosen to be zero at $z = 0$. The amplitudes of the rf magnetic field components along z , $h_z^{(i)}$, the rf electric field components, $e_x^{(i)}$, the rf magnetic field components $b_y^{(i)}$ and $b_z^{(i)}$, and the rf magnetization components, $m_y^{(i)}$ and $m_z^{(i)}$, are then proportional to $h_y^{(i)}$ with factors of proportionality determined by the

Landau-Lifshitz equations, equations (3.37) and (3.38), and by Maxwell's equations, equations (3.15) and (3.16). For the forward propagating waves:

$$\frac{h_z^{(i)}}{h_y^{(i)}} = \frac{H_y (iqk\delta^2) + \frac{i\omega}{\gamma} (1 + ik^2\delta^2)}{H_y (1 + iq^2\delta^2) + 4\pi M_s + \frac{i\omega}{\gamma} (iqk\delta^2)} = \zeta^{(i)} \quad (3.57)$$

$$\frac{e_x^{(i)}}{h_y^{(i)}} = \frac{ic}{4\pi\sigma} (q\zeta^{(i)} - k) = \epsilon^{(i)} \quad (3.58)$$

$$\frac{b_y^{(i)}}{h_y^{(i)}} = \frac{c}{\omega} k \epsilon^{(i)} \quad (3.59)$$

$$\frac{b_z^{(i)}}{h_y^{(i)}} = -\frac{c}{\omega} q \epsilon^{(i)} \quad (3.60)$$

$$\frac{4\pi m_y^{(i)}}{h_y^{(i)}} = \frac{c}{\omega} k \epsilon^{(i)} - 1 = \xi_y^{(i)} \quad (3.61)$$

$$\frac{4\pi m_z^{(i)}}{h_y^{(i)}} = -\frac{c}{\omega} q \epsilon^{(i)} - \zeta^{(i)} = \xi_z^{(i)} \quad (3.62)$$

Similar expressions are obtained for the backward propagating waves.

The values of $h_y^{(i)}$, apart from a scaling factor, are determined by the boundary conditions which the rf fields must satisfy at the front ($z=0$) and rear ($z=d$) surfaces of the slab. In the space outside the magnetic film there exist rf electric and magnetic fields which satisfy Maxwell's equations and which are localized near its surfaces. The tangential components of the electric and magnetic fields must be continuous across the interfaces between the magnetic and nonmagnetic regions. For the present problem these boundary conditions result in two equations at each interface. For the front surface ($z=0$):

$$e_x^{vl}(0) = e_x(0) = \sum_{i=1}^6 e_x^{(i)}(0) \quad (3.63)$$

$$h_y^{vl}(0) = h_y(0) = \sum_{i=1}^6 h_y^{(i)}(0) \quad (3.64)$$

where $e_x^{vl}(0)$ and $h_y^{vl}(0)$ are the electric and magnetic field components in the vacuum for $z \leq 0$ evaluated at $z = 0$. For the rear surface ($z = d$):

$$e_x^{vr}(d) = e_x(d) = \sum_{i=1}^6 e_x^{(i)}(d) \quad (3.65)$$

$$h_y^{vr}(d) = h_y(d) = \sum_{i=1}^6 h_y^{(i)}(d) \quad (3.66)$$

where $e_x^{vr}(d)$ and $h_y^{vr}(d)$ are the electric and magnetic field components in the vacuum for $z \geq d$ evaluated at $z = d$.

The electromagnetic boundary conditions are given by the four equations (3.63) to (3.66). These equations can be reduced to two equations by introducing the concept of surface impedance. We define the ratio e_x / h_y at each of the film surfaces to be the surface impedance Z_s . For the vacuum to the left of the film in figure 3.1 ($z \leq 0$), equations (3.9) and (3.14) give

$$Z_s^F = \frac{e_x^{vl}(0)}{h_y^{vl}(0)} = \frac{\omega}{ck_v} = \frac{i\omega}{cq}; \quad (3.67)$$

for the vacuum to the right of the film ($z \geq d$), equations (3.9) and (3.14) give

$$Z_s^R = \frac{e_x^{vR}(d)}{h_y^{vR}(d)} = \frac{\omega}{ck_v} = -\frac{i\omega}{cq}. \quad (3.68)$$

Therefore, we can write the electromagnetic boundary conditions as

$$\frac{e_x(0)}{h_y(0)} = Z_s^F \quad (3.69)$$

for the front surface ($z=0$) and

$$\frac{e_x(d)}{h_y(d)} = Z_s^R \quad (3.70)$$

for the rear surface ($z=d$).

The rf magnetization components in the film must satisfy generalized exchange boundary conditions which may include the possibility of dynamic pinning of the magnetization at each interface (Rado and Weertman, 1959). The spin pinning energy is taken to have the form

$$E_s^F = -\left(\frac{K_y^F}{M_s^2}\right)m_y^2(0) - \left(\frac{K_z^F}{M_s^2}\right)m_z^2(0) \quad (3.71)$$

for the front surface ($z = 0$) and

$$E_s^R = - \left(\frac{K_y^R}{M_s^2} \right) m_y^2(d) - \left(\frac{K_z^R}{M_s^2} \right) m_z^2(d) \quad (3.72)$$

for the rear surface ($z = d$), where K_y^F , K_z^F , K_y^R and K_z^R are the spin pinning coefficients in erg/cm^2 . This sign convention for the spin pinning coefficients is opposite to that used in Cochran and Dutcher (Cochran and Dutcher, 1988a; Cochran and Dutcher, 1988b). In particular, positive values of K_z^F and K_z^R correspond to spin pinning which tends to orient the magnetization along the sample normal. The exchange boundary conditions give an additional four equations. For the front surface ($z = 0$):

$$A \left. \frac{\partial m_y}{\partial z} \right|_0 = -K_y^F m_y(0) \quad (3.73)$$

$$A \left. \frac{\partial m_z}{\partial z} \right|_0 = -K_z^F m_z(0). \quad (3.74)$$

For the rear surface ($z = d$):

$$A \left. \frac{\partial m_y}{\partial z} \right|_d = K_y^R m_y(d) \quad (3.75)$$

$$A \left. \frac{\partial m_z}{\partial z} \right|_d = K_z^R m_z(d) \quad (3.76)$$

The six equations resulting from the boundary conditions, equations (3.69), (3.70) and (3.73) to (3.76), can be manipulated to give a set of six homogeneous equations for the six

magnetic field amplitudes $h_y^{(i)}(0)$. The electric field and magnetization amplitudes can be written in terms of $h_y^{(i)}$ using equations (3.57) to (3.62). Writing these equations explicitly in terms of the $h_y^{(i)}(0)$ components, we have

$$\sum_{i=1}^6 \left[\frac{e_x^{(i)}(0)}{h_y^{(i)}(0)} - Z_s^F \right] h_y^{(i)}(0) = 0 \quad (3.77)$$

$$\sum_{i=1}^6 \left[(iAk^{(i)} + K_y^F) \xi_y^{(i)} \right] h_y^{(i)}(0) = 0 \quad (3.78)$$

$$\sum_{i=1}^6 \left[(iAk^{(i)} + K_z^F) \xi_z^{(i)} \right] h_y^{(i)}(0) = 0 \quad (3.79)$$

$$\sum_{i=1}^6 \left[\left(\frac{e_x^{(i)}(d)}{h_y^{(i)}(d)} - Z_s^R \right) e^{ik^{(i)}d} \right] h_y^{(i)}(0) = 0 \quad (3.80)$$

$$\sum_{i=1}^6 \left[(iAk^{(i)} + K_y^R) \xi_y^{(i)} e^{ik^{(i)}d} \right] h_y^{(i)}(0) = 0 \quad (3.81)$$

$$\sum_{i=1}^6 \left[(iAk^{(i)} + K_z^R) \xi_z^{(i)} e^{ik^{(i)}d} \right] h_y^{(i)}(0) = 0. \quad (3.82)$$

Equations (3.77) to (3.82) have a nontrivial solution only for frequencies, ω , such that the 6×6 determinant of the coefficients of $h_y^{(i)}(0)$ vanishes. This condition determines the complex resonant frequencies, ω , of the magnetic slab. The resonant frequencies can be

easily found since for most problems of interest the imaginary parts of the frequencies are small (~ -0.1 GHz) and the real parts of the frequencies are nearly those calculated from simple theories of surface and spin waves (Patton, 1984). The determinant of the coefficients vanishes if any two wavevectors are equal, or if a wavevector vanishes: it is necessary to guard against these spurious solutions if a computational routine is used to automatically find those frequencies for which the determinant is zero. It should be reiterated that, by the introduction of the concept of surface impedance (equations (3.67) and (3.68)), the boundary value problem was reduced from one of finding the zeroes of an 8×8 determinant to one of finding the zeroes of a 6×6 determinant.

Having found a resonant frequency, ω , the corresponding amplitudes $h_y^{(i)}(0)$ are determined apart from a multiplicative constant. This constant must be chosen so that the average energy stored in the normal mode of the system has the value required for a harmonic oscillator in equilibrium with a bath at temperature T . The frequencies of low lying modes satisfy the condition $k_B T \gg \hbar\omega$ for experiments conducted at room temperature, where k_B is Boltzmann's constant. In that case the average energy of a mode has the equipartition value, $k_B T$.

3.1.2 The energy stored in a normal mode

The increase in energy associated with the excitation of a magnetic normal mode can be written as the sum of five terms.

(i) The energy density

$$E_M = \frac{h^2}{8\pi}, \quad (3.83)$$

where h represents the space and time dependent magnetic field generated by poles due to the spatial variation of the magnetization in the film as well as the magnetic fields generated

by currents in the magnetic film, a metallic overlayer, or in a metallic substrate. The magnetic pole contribution to this energy density has been discussed by William Fuller Brown, Jr. (Brown, 1978).

(ii) The energy of interaction between the magnetization and the applied magnetic field,

$$E^H = -\mathbf{H}^a \cdot \mathbf{M}_s. \quad (3.84)$$

It is assumed that the lowest energy state of the system occurs when the magnetization is uniform and parallel with the applied field, \mathbf{H}^a , and is directed along the x-axis. Any deviation of the magnetization from the direction of \mathbf{H}^a is accompanied by an increase in energy. The x-component of the magnetization can be written as

$$m_x = M_s \left[1 - \frac{1}{M_s^2} (m_y^2 + m_z^2) \right]^{\frac{1}{2}} \sim M_s - \frac{1}{2M_s} (m_y^2 + m_z^2) \quad (3.85)$$

Therefore the increase in the energy density to lowest order is given by

$$E^H = \frac{H}{2M_s} (m_y^2 + m_z^2). \quad (3.86)$$

(iii) The magnetic anisotropy energy, E^A . This contribution depends on the crystal system and upon the relative orientation of the crystal axes and the morphological axes. For illustrative purposes it has been assumed that the magnetization is parallel with the external field in equilibrium. This implies that the increase in anisotropy energy density for a nonuniform magnetization can be written, in lowest order, as

$$E^A = \left(\frac{\alpha}{2M_S} \right) m_y^2 + \left(\frac{\gamma}{2M_S} \right) m_z^2, \quad (3.87)$$

where α and γ are effective magnetic fields given by equations (3.41) and (3.42) which occur together with the applied field in the Landau-Lifshitz torque equations, equations (3.37) and (3.38). Equations (3.41) and (3.42) include the effects of cubic magnetocrystalline anisotropy and uniaxial anisotropy with the easy axis perpendicular to the sample plane, with the cube axes in the sample plane and along the sample normal.

(iv) The exchange energy density. This contribution is given, to lowest order, by substituting $M_x = M_S$ into equation (3.24) and considering only the rf terms:

$$E^{\text{ex}} = \frac{A}{M_S^2} \left[\left(\frac{\partial m_y}{\partial y} \right)^2 + \left(\frac{\partial m_y}{\partial z} \right)^2 + \left(\frac{\partial m_z}{\partial y} \right)^2 + \left(\frac{\partial m_z}{\partial z} \right)^2 \right], \quad (3.88)$$

The y-dependence of the magnetization components is proportional to e^{iqy} where q is a real number. Consequently for computational purposes these terms can be treated separately from the z-dependence and written as

$$E_y^{\text{ex}} = \left(\frac{2Aq^2/M_S}{2M_S} \right) \left(m_y^2 + m_z^2 \right). \quad (3.89)$$

The y-contribution to the exchange energy has the same form as the interaction between the magnetization and the applied field; it simply adds a term to the external field.

(v) The surface anisotropy energy. Pinning of the magnetization at the surfaces of the specimen can be represented by the surface energy densities given by equations (3.71) and (3.72).

The above contributions must be integrated over the z -coordinate and averaged over time. The integral over the energy density term discussed in (i) above must be carried out over the interval $-\infty < z < +\infty$ because the rf magnetic field is not confined to the magnetic film. The time average can be carried out conveniently as one half the product of a complex amplitude with its complex conjugate. The sum over all the energy terms is the time average of the magnetic energy per unit area of film which is associated with the normal mode. The amplitude of the normal mode must be adjusted so that this energy per unit area is just equal to the average thermal energy of a harmonic oscillator having the same frequency, ω . For $\hbar\omega \ll k_B T$ this average energy is just equal to $k_B T$.

It may appear arbitrary to equate the average energy per unit surface area of a normal mode to the average oscillator energy since the total energy contained in the mode must be proportional to the specimen volume. However, for a fixed film thickness, the number of modes which have nearly the same transverse wavenumber, q , and frequency, ω , and which scatter light into a particular direction within a given solid angle is proportional to the specimen area (Wettling et al., 1975). The increase of the scattered light intensity with area due to the increase in density of states corresponding to a given q, ω just compensates the decrease with area of the mean square amplitude of the magnetization which is required to maintain a constant value of the thermal energy in a single mode.

3.1.3 The polarization distribution corresponding to a normal mode

The electric polarization induced in a magnetic medium by a light wave contains small terms which depend upon the magnetization magnitude and direction. The magnetization dependent part of the polarization, \mathbf{P} , induced by the optical electric field, \mathbf{E} , in a cubic crystal can be written (Wettling et al., 1975) $4\pi\mathbf{P} = \Delta\boldsymbol{\varepsilon}\cdot\mathbf{E}$ where $\Delta\boldsymbol{\varepsilon}$ is a dielectric tensor whose elements are given by

$$\Delta\boldsymbol{\varepsilon} = \begin{vmatrix} (G_{11}M_1^2 + G_{12}M_2^2 + G_{12}M_3^2) & (KM_3 + 2G_{44}M_1M_2) & (-KM_2 + 2G_{44}M_1M_3) \\ (-KM_3 + 2G_{44}M_1M_2) & (G_{11}M_2^2 + G_{12}M_1^2 + G_{12}M_3^2) & (KM_1 + 2G_{44}M_2M_3) \\ (KM_2 + 2G_{44}M_1M_3) & (-KM_1 + 2G_{44}M_2M_3) & (G_{11}M_3^2 + G_{12}M_1^2 + G_{12}M_2^2) \end{vmatrix} \quad (3.90)$$

The constants K and G_{ij} are complex first and second order magneto-optic constants related to Faraday rotation and to the Cotton-Mouton effects as described by Wettling et al. (Wettling et al., 1975). The M_i are components of the magnetization referred to cubic axes. It will be assumed that the specimen axes of figure 3.1 are parallel with the cubic crystalline axes since otherwise the elements of the tensor $\Delta\boldsymbol{\varepsilon}$ become complicated. For this case, $M_1 = M_x$, $M_2 = M_y$ and $M_3 = M_z$. Also, it will be assumed that the magnetization M_s lies along the x-axis, as shown in figure 3.1. In that case only the component $M_1 = M_x \equiv M_s$ is large. Furthermore, we have no interest in static effects which simply add small and unimportant corrections to the complex optical index of refraction; we are interested in the terms which are proportional to the components m_y , m_z and which, therefore, oscillate at the magnon frequency. The dielectric tensor becomes, for our purposes,

$$\Delta\varepsilon = \begin{vmatrix} 0 & (Km_z+2G_{44}M_Sm_y) & (-Km_y+2G_{44}M_Sm_z) \\ (-Km_z+2G_{44}M_Sm_y) & 0 & 0 \\ (Km_y+2G_{44}M_Sm_z) & 0 & 0 \end{vmatrix} \quad (3.91)$$

For an incident optical wave polarized with its electric vector in the plane of incidence (a p-wave possessing only components E_y, E_z) one obtains

$$4\pi P_x = (2G_{44}M_S E_y - KE_z)m_y + (KE_y + 2G_{44}M_S E_z)m_z. \quad (3.92)$$

For an incident optical wave polarized with its electric vector perpendicular to the plane of incidence (an s-wave having only the component E_x) one obtains

$$4\pi P_y = 2G_{44}M_S E_x m_y - KE_x m_z, \quad (3.93)$$

$$4\pi P_z = KE_x m_y + 2G_{44}M_S E_x m_z. \quad (3.94)$$

These relations imply that an incident p-wave interacts with a magnetic excitation to produce a scattered s-wave and vice versa. This well-known property of magnetic scattering is often used to reduce the background optical signal due to scattering processes which are of no immediate interest, see section 2.2.2. The products of an optical electric field and a time dependent magnetization in the above equations produce terms which are proportional to the factors $e^{i[(q-Q)y - (\omega_0 + \omega)t]}$ and $e^{-i[(q+Q)y + (\omega_0 - \omega)t]}$ (Landau and Lifshitz, 1960), where $-Q$ is the y-component of the incident optical wavevector, ω_0 is the frequency of the incident light, and q, ω are the y-component of the wavenumber and the frequency corresponding to a magnetization mode. The y-component of the scattered optical radiation wavevector, Q_s , is determined by the angle of observation, θ_s (see figure

3.1); if the small difference between the frequencies of the incident and scattered radiation is neglected, $Q_s = (\omega_0/c)\sin\theta_s$, where θ_s is positive if the scattered wavevector, \mathbf{k}_s , has a positive component along the y-axis. For the commonly used backscattering geometry, $\theta_s = \theta$, the wavevectors of the incident and scattered radiation are antiparallel so that $Q_s = Q$. In that case the magnetic mode characterized by the value $q = (Q+Q_s) = 2Q$ gives scattered light which is upshifted from the incident optical frequency by the magnon frequency; the magnon corresponding to $q = (-Q-Q_s) = -2Q$ gives scattered light which is downshifted from the incident optical frequency. As a consequence of the products which appear in equations (3.92) to (3.94) the amplitudes of the electric polarization which oscillate at frequencies $(\omega_0+\omega)$ and $(\omega_0-\omega)$ are reduced by a factor of two. The components of the polarization which oscillate at $(\omega_0+\omega)$ corresponding to the magnon wavevector component $q = (Q+Q_s)$ are to be calculated from

$$4\pi P_{x+} = (2G_{44}M_s E_y - KE_z) \frac{m_y}{2} + (KE_y + 2G_{44}M_s E_z) \frac{m_z}{2} \quad (3.95)$$

$$4\pi P_{y+} = G_{44}M_s E_x m_y - KE_x \frac{m_z}{2} \quad (3.96)$$

$$4\pi P_{z+} = KE_x \frac{m_y}{2} + G_{44}M_s E_x m_z, \quad (3.97)$$

whereas the components which oscillate at $(\omega_0-\omega)$ corresponding to a magnon wavevector component $q = -(Q+Q_s)$ are to be calculated from

$$4\pi P_{x-} = (2G_{44}M_s E_y - KE_z) \frac{m_y^*}{2} + (KE_y + 2G_{44}M_s E_z) \frac{m_z^*}{2} \quad (3.98)$$

$$4\pi P_{y-} = G_{44}M_s E_x m_y^* - KE_x \frac{m_z^*}{2} \quad (3.99)$$

$$4\pi P_{z-} = KE_x \frac{m_y^*}{2} + G_{44} M_s E_x m_z^* \quad (3.100)$$

where E_i are the complex optical electric field amplitudes and m_i are the complex magnetization amplitudes for the normal mode under investigation.

The induced polarization components vary with z across the film. This dependence is the product of the z -dependence of the optical electric field and the z -dependence of the magnetic normal mode whose in-plane component of the wavevector is q . The spatial dependence of the optical electric field in the film is the solution of a standard boundary value problem in optics. For the geometry shown in figure 3.1 there is one incident and one reflected wave in the vacuum to the left of the film ($z \leq 0$), one forward and one backward travelling wave in the magnetic film ($0 \leq z \leq d$) and one transmitted wave in the vacuum to the right of the film ($z \geq 0$).

For s-polarized incident light, one assumes that the optical electric field E_x inside the film has the form

$$\frac{E_x}{E_0} = [ae^{ik_f z} + be^{-ik_f z}]e^{-i[Qy + \omega_0 t]} \quad (3.101)$$

For p-polarized incident light, one assumes that the optical magnetic field H_x inside the film has the form

$$\frac{H_x}{H_0} = [ae^{ik_f z} + be^{-ik_f z}]e^{-i[Qy + \omega_0 t]} \quad (3.102)$$

E_0 and H_0 are the optical electric and magnetic field amplitudes in the vacuum for $z \leq 0$, $k_f = [\epsilon(\omega_0/c)^2 - Q^2]^{1/2}$ is the z -component of the light wavevector inside the film with $\text{Im}(k_f) >$

0, ϵ is the complex optical dielectric constant of the film, and $Q = (\omega_0/c)\sin\theta$. For the p-polarized incident light, the optical electric field components E_y and E_z can be written as

$$\frac{E_y}{E_0} = \left(\frac{ck_f}{\epsilon\omega_0} \right) [ae^{ik_f z} - be^{-ik_f z}] e^{-i[Qy + \omega_0 t]} \quad (3.103)$$

$$\frac{E_z}{E_0} = \left(\frac{cQ}{\epsilon\omega_0} \right) [ae^{ik_f z} + be^{-ik_f z}] e^{-i[Qy + \omega_0 t]} \quad (3.104)$$

where the coefficients a and b are determined by using the electromagnetic boundary conditions: the normal components of \mathbf{B} and \mathbf{D} and the tangential components of \mathbf{E} and \mathbf{H} must be continuous across each interface of the film. We obtain

$$a = \frac{2(r+1)}{[(r+1)^2 - (r-1)^2 e^{2ik_f d}]} \quad (3.105)$$

$$b = \frac{2(r-1)e^{2ik_f d}}{[(r+1)^2 - (r-1)^2 e^{2ik_f d}]} \quad (3.106)$$

where $r = \left(\frac{ck_f}{\epsilon\omega_0 \cos\theta} \right)$ for the p-polarized light and where $r = \left(\frac{ck_f}{\omega_0 \cos\theta} \right)$ for the s-polarized

light.

From the above discussion, the intensity of scattered light which is upshifted in frequency can be compared with that which is downshifted in frequency. To simplify the comparison, we consider p-polarized incident light and polarization terms involving the first order magneto-optical constant K . The same conclusions hold for s-polarized incident light and the polarization terms involving the second order magneto-optical constant G_{44} .

The polarization component which is upshifted in frequency is given by

$$4\pi P_{x+} = \frac{K}{2} (-E_z m_y + E_y m_z) \quad (3.107)$$

and the polarization component which is downshifted in frequency is given by

$$4\pi P_{x-} = \frac{K}{2} (-E_z m_y^* + E_y m_z^*) \quad (3.108)$$

The optical electric field components E_y and E_z are given by equations (3.103) and (3.104). Since the scattered light amplitude is proportional to the polarization component, the scattered light intensity is proportional to the product of the polarization component and its complex conjugate. For the scattered light intensity which is upshifted in frequency, I_+ , we use equation (3.107) to write

$$I_+ \propto E_y^2 m_z^2 + E_z^2 m_y^2 - E_y^* E_z m_y m_z^* - E_y E_z^* m_y^* m_z \quad (3.109)$$

Similarly, for the scattered light intensity which is downshifted in frequency, I_- , we use equation (3.108) to write

$$I_- \propto E_y^2 m_z^2 + E_z^2 m_y^2 - E_y^* E_z m_y^* m_z - E_y E_z^* m_y m_z^* \quad (3.110)$$

Because the magnetization is precessing about its equilibrium direction, the rf magnetization components m_y and m_z are 90° out of phase. We can write

$$m_y = i \kappa m_z \quad (3.111)$$

$$m_y^* = -i \kappa m_z^* \quad (3.112)$$

where κ is a real number which describes the ellipticity of the precession.

Expressing equations (3.109) and (3.110) for the upshifted and downshifted scattered intensities in terms of the m_z components, we have

$$I_+ \propto \left[E_y^2 + \kappa^2 E_z^2 - i \kappa \left(E_y^* E_z - E_y E_z^* \right) \right] m_z^2 \quad (3.113)$$

and

$$I_- \propto \left[E_y^2 + \kappa^2 E_z^2 + i \kappa \left(E_y^* E_z - E_y E_z^* \right) \right] m_z^2 \quad (3.114)$$

The ratio of the upshifted scattered intensity to the downshifted scattered intensity is

$$\frac{I_+}{I_-} = \frac{E_y^2 + \kappa^2 E_z^2 - i \kappa \left(E_y^* E_z - E_y E_z^* \right)}{E_y^2 + \kappa^2 E_z^2 + i \kappa \left(E_y^* E_z - E_y E_z^* \right)} \quad (3.115)$$

This ratio depends on the phase of the optical electric fields inside the magnetic films. It can be seen from equations (3.101), (3.103) and (3.104) for the electric field components that the phases will depend on the thickness of the magnetic film d and the optical constants of the magnetic film and the surrounding media. Therefore the ratio of the upshifted scattered intensity to the downshifted scattered intensity is not characteristic of a particular magnetic material, but depends very strongly on the sample geometry.

3.1.4 The intensity of the scattered radiation

The oscillating polarization distributions $4\pi\mathbf{P}$ of equations (3.95) to (3.100) constitute current densities $\mathbf{j} = \frac{\partial\mathbf{P}}{\partial t}$. Maxwell's equations for a time dependence $e^{-i\omega_s t}$,

where ω_s is an optical frequency, are given by

$$\nabla \times \mathbf{E} = \frac{i\omega_s}{c} \mathbf{H} \quad (3.116)$$

$$\nabla \times \mathbf{H} = -\frac{i\epsilon\omega_s}{c} \mathbf{E} - \frac{i\omega_s}{c} 4\pi\mathbf{P} \quad (3.117)$$

$$\nabla \cdot \mathbf{B} = \nabla \cdot \mathbf{H} = 0 \quad (3.118)$$

since the permeability $\mu \sim 1$ at optical frequencies (Landau and Lifshitz, 1960). Taking the curl of equation (3.117), and using the vector identity

$$\nabla \times \nabla \times \mathbf{H} = \nabla (\nabla \cdot \mathbf{H}) - \nabla^2 \mathbf{H}, \quad (3.119)$$

as well as equations (3.117) and (3.118), we obtain

$$\nabla^2 \mathbf{H} + \epsilon \left(\frac{\omega_s}{c} \right)^2 \mathbf{H} = \frac{i\omega_s}{c} \nabla \times (4\pi\mathbf{P}). \quad (3.120)$$

From equations (3.117) and (3.120) we can compute the effect of a polarization sheet in the form of a δ -function localized at $z = \zeta$. Discontinuities in the optical fields are produced at $z = \zeta$, and these discontinuities determine the amplitude of the radiation emitted by that polarization sheet. Explicitly, one has for the three components of $4\pi\mathbf{P}$:

$$(i) \quad \underline{4\pi P_x = \delta(z-\zeta) \cdot e^{iQ_s y} \cdot e^{-i\omega_s t}}.$$

This polarization component gives rise to s-polarized scattered optical radiation; the electric field of the scattered radiation lies along the x-direction. The x-component of equation (3.117) is

$$\frac{\partial H_z}{\partial y} - \frac{\partial H_y}{\partial z} = -\frac{i\omega_s \epsilon}{c} E_x - \frac{i\omega_s}{c} \delta(z-\zeta) \cdot e^{iQ_s y} \cdot e^{-i\omega_s t} \quad (3.121)$$

Integrating equation (3.121) from $z = \zeta - \eta$ to $z = \zeta + \eta$, and taking the limit $\eta \rightarrow 0$, we obtain a discontinuity in the y -component of \mathbf{H} :

$$\Delta H_y = \frac{i\omega_s}{c} \cdot e^{iQ_s y} \cdot e^{-i\omega_s t}, \quad (3.122)$$

whereas E_x is continuous at $z = \zeta$. The optical fields can be written as

$$E_x = (\alpha_\gamma e^{ik_f z} + \beta_\gamma e^{-ik_f z}) \cdot e^{iQ_s y} \cdot e^{-i\omega_s t} \quad (3.123)$$

$$H_y = -\frac{ic}{\omega_s} \frac{\partial E_x}{\partial z}, \quad (3.124)$$

where γ is an index which is different depending upon whether the fields are evaluated on the left of $z = \zeta$ ($\gamma = L$) or on the right of $z = \zeta$ ($\gamma = R$). The boundary conditions at $z = \zeta$ (E_x continuous and H_y discontinuous), together with the boundary conditions at the film surfaces (E_x and H_y continuous), completely determine the amplitude of the radiation emitted by the dipole sheet at $z = \zeta$. For the geometry of figure 3.1 the amplitude of the s -polarized radiation is given by

$$E_s = \left(\frac{i}{2\cos\theta_s} \right) \left(\frac{\omega_s}{c} \right) \left[a e^{ik_f \zeta} + b e^{-ik_f \zeta} \right] \cdot e^{iQ_s y} \cdot e^{-i\omega_s t} \quad (3.125)$$

where a , b are specified by equations (3.105) and (3.106) with $r = \frac{ck_f}{\omega_s \cos\theta_s}$,

$k_f^2 = \epsilon \left(\frac{\omega_s}{c}\right)^2 - Q_s^2$, and θ_s is the angle of observation of the scattered light. Equation (3.125)

is the amplitude of the scattered radiation generated by the δ -function polarization distribution at $z = \zeta$; it will be called an optical Green's function. The phase of the scattered light is referred to $z = 0$, as is the phase of the incident light. For the backscattering configuration the angle of observation, θ_s , is the same as the angle of incidence and therefore $Q_s = Q$ for this case. Furthermore, the frequencies of the scattered and incident light are very nearly equal so that the optical dielectric constant and the optical wavevectors can be taken to be the same for the incident and scattered optical fields. Thus for the backscattering configuration the same coefficients a , b describe both the optical field in the film at $z = \zeta$ due to the incident radiation and the Green's function for the scattered radiation, equation (3.125).

$$(ii) \quad \underline{4\pi P_y = \delta(z-\zeta) \cdot e^{iQ_s y} \cdot e^{-i\omega_s t}} .$$

This polarization distribution generates a p-polarized optical field. The y-component of equation (3.117) is given by

$$\frac{\partial H_x}{\partial z} = -\frac{i\omega_s}{c} (4\pi P_y) - \frac{i\epsilon\omega}{c} E_y \quad (3.126)$$

Integrating equation (3.126) from $z = \zeta - \eta$ to $z = \zeta + \eta$ and taking the limit $\eta \rightarrow 0$, we get a discontinuity in the x-component of \mathbf{H} :

$$\Delta H_x = -\frac{i\omega_s}{c} \cdot e^{iQ_s y} \cdot e^{-i\omega_s t} , \quad (3.127)$$

whereas at $z = \zeta$ the electric field component E_y is continuous. The amplitude of the emitted optical electric field which is generated by the singularity in H_x for the geometry of figure 3.1 is

$$E_p = \left(\frac{ik_f}{2\epsilon \cos\theta_s} \right) \cdot \left[a e^{ik_f \zeta} - b e^{-ik_f \zeta} \right] \cdot e^{iQ_s y} \cdot e^{-i\omega_s t}, \quad (3.128)$$

where a, b are given by equations (3.105) and (3.106) with $r = \frac{ck_f}{\epsilon \omega_s \cos\theta_s}$, and as before,

$$k_f^2 = \epsilon \left(\frac{\omega_s}{c} \right)^2 - Q_s^2.$$

$$(iii) \quad \underline{4\pi P_z = \delta(z - \zeta) \cdot e^{iQ_s y} \cdot e^{-i\omega_s t}}.$$

This component of the polarization generates a p-polarized optical field. The x-component of equation (3.120) is

$$-Q_s^2 H_x + \frac{\partial^2 H_x}{\partial z^2} + \epsilon \left(\frac{\omega}{c} \right)^2 H_x = -\frac{\omega Q_s}{c} (4\pi P_z) \quad (3.129)$$

Integrating equation (3.129) from $z = \zeta - \eta$ to $z = \zeta + \eta$ and taking the limit $\eta \rightarrow 0$, we get a discontinuity in $\frac{\partial H_x}{\partial z}$:

$$\Delta \left(\frac{\partial H_x}{\partial z} \right) = -\frac{\omega Q_s}{c} \cdot e^{iQ_s y} \cdot e^{-i\omega_s t} \quad (3.130)$$

Using equation (3.117), we can express equation (3.130) in terms of a discontinuity in the y-component of E :

$$\Delta E_y = -\frac{iQ_s}{\epsilon} \cdot e^{iQ_s y} \cdot e^{-i\omega_s t}. \quad (3.131)$$

At $z = \zeta$ the optical magnetic field, H_x , is continuous. The resulting electric field amplitude of the emitted light wave (phase referred to $z=0$) for the geometry of figure 3.1 is given by

$$E_p = \left(\frac{iQ_s}{2\epsilon \cos\theta_s} \right) \left[a e^{ik_f \zeta} + b e^{-ik_f \zeta} \right] \cdot e^{iQ_s y} \cdot e^{-i\omega_s t}, \quad (3.132)$$

where a, b are given by equations (3.105) and (3.106) with $r = \frac{ck_f}{\epsilon \omega_s \cos\theta_s}$, and

$$k_f^2 = \epsilon \left(\frac{\omega_s}{c} \right)^2 - Q_s^2.$$

Optical Green's functions equivalent to equations (3.125), (3.128) and (3.132) can be constructed corresponding to optical boundary conditions other than those appropriate for figure 3.1. For example, the film might be supported on a metallic or an insulating substrate, or the film might be covered with a layer of a nonmagnetic material. In all cases the form of the Green's functions is closely related to the spatial dependence of the optical electric field set up in the film by the incident light wave.

The amplitude of the light scattered from a magnetic normal mode is calculated as an integral over the thickness of the magnetic film of the product of the appropriate optical Green's functions with the appropriate dipole distribution as calculated from equations (3.95) to (3.100). The terms to be integrated are exponential functions so that it is easy to obtain an expression for the amplitude of the emitted optical radiation field in closed form. The ratio of the intensity of the scattered radiation to the intensity of the incident radiation is obtained from the product of the emitted radiation amplitude with its complex conjugate.

The intensity calculated as described above is the integrated intensity of the scattered light. The magnetic normal mode frequency, or magnon frequency, is not sharply defined because of damping processes, and therefore the frequency of the emitted light has a

corresponding spectral width. One can picture the excitation of the magnetization as being caused by random thermal impulses; after such an impulse the amplitude of the magnetization decays at a rate specified by the imaginary part of the complex frequency, $\omega = \omega_R + i\omega_I$. It follows that the amplitude of the corresponding emitted light is proportional to $e^{-\omega_I t}$ and its intensity decays as $e^{-2\omega_I t}$. The resulting frequency spectrum is Lorentzian;

$$I(\omega) = \frac{I_0}{\pi} \cdot \frac{\omega_I}{[(\omega - \omega_s)^2 + \omega_I^2]} \quad (3.133)$$

where I_0 is the integrated intensity, and ω_s is the optical frequency shifted up or down by the magnon frequency ω_R (Landau and Lifshitz, 1960).

3.1.5 Discussion

3.1.5.1 The surface mode

As discussed in section 3.1.1, a general solution of Maxwell's equations and the Landau-Lifshitz equations of motion for the magnetization for a magnetic film can be written as the superposition of six plane waves: three forward propagating waves and three backward propagating waves. For each set of three waves, there is a nonpropagating wave of small amplitude, a propagating spin wave and a damped surface wave. In the limit that the thickness of the magnetic film becomes infinite, i.e. we have a semi-infinite slab geometry, there exists a solution of the boundary problem at the front surface of the film for which one set of three forward propagating waves is generated. For this set of waves, the amplitude of the damped surface wave is large and the imaginary component of its wavevector along z becomes very nearly equal to the transverse wavevector component Q . This resonant mode is the true surface mode of the magnetic film in that the rf magnetization components decay with distance into the magnetic film. For a magnetic film of finite thickness d there is one mode for each surface of the film similar to the true surface

mode in that the rf magnetization profile across the magnetic film decays from one surface to the other surface. In the limit of ultrathin magnetic films, the rf magnetization profile for this mode is constant across the film since the decay length for the magnetization is much larger than the film thickness; this is the uniform precession mode, the frequency of which is given essentially by the ferromagnetic resonance condition, see equation (3.142).

Throughout the rest of this thesis, it is this mode that will be referred to as the surface mode. Because the effects of exchange have been included in the calculation there are exchange or standing spin waves in the magnetic film. There is a strong interaction between the surface mode and the standing spin wave modes when their frequencies are equal, see section 3.1.5.4.1; near these frequencies, the character of these modes becomes mixed.

The spatial variation of the magnetization for the surface mode is very similar to that of the Damon-Eshbach surface mode for a semi-infinite slab derived from a simple no-exchange theory (Damon and Eshbach, 1961). For a magnetic film of thickness d , the Damon-Eshbach resonance condition is obtained by requiring that the tangential components of the electric and magnetic fields must be continuous across both film surfaces; it can be written as

$$\left(\frac{\omega_{DE}}{\gamma}\right)^2 = H(H + 4\pi M_s) + (2\pi M_s^2)(1 - e^{-2qd}) \quad (3.134)$$

where $\omega_{DE}/2\pi$ is the Damon-Eshbach surface mode frequency, γ is the gyromagnetic ratio, H is the applied field, $4\pi M_s$ is the saturation magnetization, q is the wavevector and d is the thickness of the magnetic film. This resonance condition can be derived from the theory presented in section 3.1.1 by neglecting the conduction and displacement current densities, exchange and magnetic damping effects. In the limit of very large d , the Damon-Eshbach surface mode is essentially equivalent to the true surface mode. In the limit of

very small d , the Damon-Eshbach surface mode is equivalent to the uniform precession mode as given by the ferromagnetic resonance condition, see equation (3.142).

3.1.5.2 Effect of metallic conductivity on resonant frequencies

The frequencies of the lowest frequency magnetic modes have been listed in table 3.1 for an isotropic film having the magnetic properties of iron, for an applied in-plane magnetic field of 1 kOe, and for two different angles of incidence of the 5145Å laser light, $\theta = 10^\circ$ and $\theta = 45^\circ$, as measured between the incident beam and the sample normal. Anisotropy was ignored in the calculations for table 3.1 because it has no direct effect on the frequency shifts caused by the electrical properties of an overlayer or substrate or on shifts due to the conductivity of the magnetic layer. The surface mode frequencies have been calculated for films that are 10 Å and 100Å thick. For the 100Å thick film, the frequencies of the first standing spin wave, i.e. that with one-half wavelength across the thickness of the film, have also been included for those calculations which include exchange.

The frequencies calculated using the Damon-Eshbach theory (Damon and Eshbach, 1961) for a magnetic insulator without exchange and having no losses, as discussed in section 3.1.5.1, are listed in the second column of table 3.1. In the third column of table 3.1 are listed the surface mode frequencies obtained by including metallic conductivity and magnetic damping, but not exchange, in the calculation. The no-exchange frequencies lie remarkably close to the Damon-Eshbach frequencies. The discrepancy decreases with increasing q and increasing magnetic field, but increases with increasing thickness, rising from approximately 1:5000 for a 10Å thick film to 1:300 for a 1000Å thick film.

Exchange effects are included in columns 4 to 7 in table 3.1; these calculations were performed using the theory presented in section 3.1.1. The surface mode frequencies calculated with exchange for the 10Å thick film are within a few percent of those calculated

Table 3.1

A comparison of the resonant frequencies f (in GHz) of a system composed of a metallic magnetic film of thickness d covered by a 40\AA layer of gold (resistivity $= 2.44 \times 10^{-6} \Omega \text{ cm}$) and mounted upon a silver substrate (resistivity $= 1.59 \times 10^{-6} \Omega \text{ cm}$) for an applied magnetic field of 1.0 kOe . The wavevector component of the excitation parallel to the film surface and perpendicular to the magnetic field corresponds to that for backscattered 5145\AA wavelength light incident at $\theta = 10^\circ$ ($q = 42\,413 \text{ cm}^{-1}$) and at 45° ($q = 172\,707 \text{ cm}^{-1}$). The properties of the magnetic film are taken to be those of iron having no magnetocrystalline anisotropy: saturation magnetization, $4\pi M_s = 21.55 \text{ kOe}$; exchange parameter, $A = 2.0 \times 10^{-6} \text{ erg/cm}$; $g = 2.09$; Gilbert damping parameter, $G = 7.0 \times 10^7 \text{ Hz}$; resistivity $= 1.0 \times 10^{-5} \Omega \text{ cm}$. Frequencies for the 100\AA thick magnetic film are listed for the lowest normal mode (the uniform mode) and for the first exchange mode whose wavelength is $\lambda = 2d$. It has been assumed that the magnetization is unpinned at the film surfaces. (a) An iron film (except that $A = 0$) sandwiched between a 40\AA gold overlayer and a silver substrate. (b) An iron film mounted on a silver substrate and covered with a 40\AA thick layer of gold. (c) An iron film mounted on a silver substrate but having no overlayer. (d) An iron film mounted on a substrate whose resistivity is $100 \Omega \text{ cm}$ and covered by a 40\AA thick layer of a material whose resistivity is $100 \Omega \text{ cm}$. (e) A magnetic film having the magnetic properties of iron but its resistivity has been increased to $10^{-3} \Omega \text{ cm}$, mounted on a silver substrate and covered by a 40\AA thick overlayer of gold.

Thickness d (Å)	Angle (degrees)	Damon- Eshbach frequency (GHz)	No-exchange metal film ^(a) frequency (GHz)	Normal case ^(b) frequency (GHz)	Exchange, no overlayer ^(c) frequency (GHz)	High resistivity overlayer and substrate ^(d) frequency (GHz)	Increased resistivity of magnetic metal ^(e) frequency (GHz)
10	10	14.1896	14.1926	14.2226	14.2227	14.2194	14.2226
			- i 0.0953	- i 0.0953	- i 0.0943	- i 0.0765	- i 0.0953
10	45	15.0560	15.0558	15.5188	15.5188	15.5188	15.5188
			- i 0.0818	- i 0.0822	- i 0.0812	- i 0.0770	- i 0.0822
100	10	16.5453	16.5773	16.6112	16.6125	16.5790	16.6113
			- i 0.2373	- i 0.2371	- i 0.2270	- i 0.0781	- i 0.2358
				96.7929	96.7929	96.7929	96.7929
				- i 0.2294	- i 0.2294	- i 0.2294	- i 0.2261
100	45	21.9798	21.9799	22.3769	22.3770	22.3765	22.3769
			- i 0.1109	- i 0.1110	- i 0.1019	- i 0.0784	- i 0.1114
				96.9833	96.9833	96.9833	96.9833
				- i 0.2298	- i 0.2297	- i 0.2297	- i 0.2269

using the Damon-Eshbach theory. Of course, as is to be expected, exchange becomes more important as the wavenumber of the excitation and the thickness of the film increases.

For the "Normal Case" calculation in column 4 of table 3.1, it was assumed that the metallic magnetic thin film had been deposited on a silver substrate and then covered by a 40Å thick overlayer of gold. Both the substrate and overlayer are nonmagnetic metals. This specific configuration was chosen to correspond with the geometry of specimens which are prepared in our laboratory using the techniques of molecular beam epitaxy (Heinrich et al., 1988a). The frequencies calculated in column 4 are to be compared with the frequencies calculated for no overlayer but a silver substrate (column 5), and for a 40Å thick overlayer and a substrate both of which have the very large resistivity value of 100Ω-cm (column 6). Changing the resistivity of the overlayer and the substrate produces a change of approximately 1:500 for the 100Å film and for the smallest value of q . The difference decreases for larger magnetic fields and for larger values of the in-plane wavevector. The resonant frequencies are very insensitive to the resistivity of the magnetic film. The frequencies listed in the last column have been calculated for a magnetic film whose resistivity has been increased two orders of magnitude (from 10^{-5} to 10^{-3} Ω-cm). The resulting frequency shifts are less than $1:10^5$. Therefore the insulating approximation discussed in section 3.1.1 is a reasonable approximation for the light scattering calculation.

3.1.5.3 Comparison with the theory of Camley and Mills

The computational scheme described in sections 3.1.1 to 3.1.4 has been carried through for 5145 Å laser light backscattered from a metallic magnetic thin film deposited on a silver substrate and covered by a 40Å thick overlayer of gold. The overlayer and substrate have very little effect on the magnetic mode frequencies, as shown in section 3.1.5.2; they mainly affect the absolute intensity of the scattered light. In figure 3.2, the scattered intensity has been calculated as a function of frequency shift for an iron film 850Å

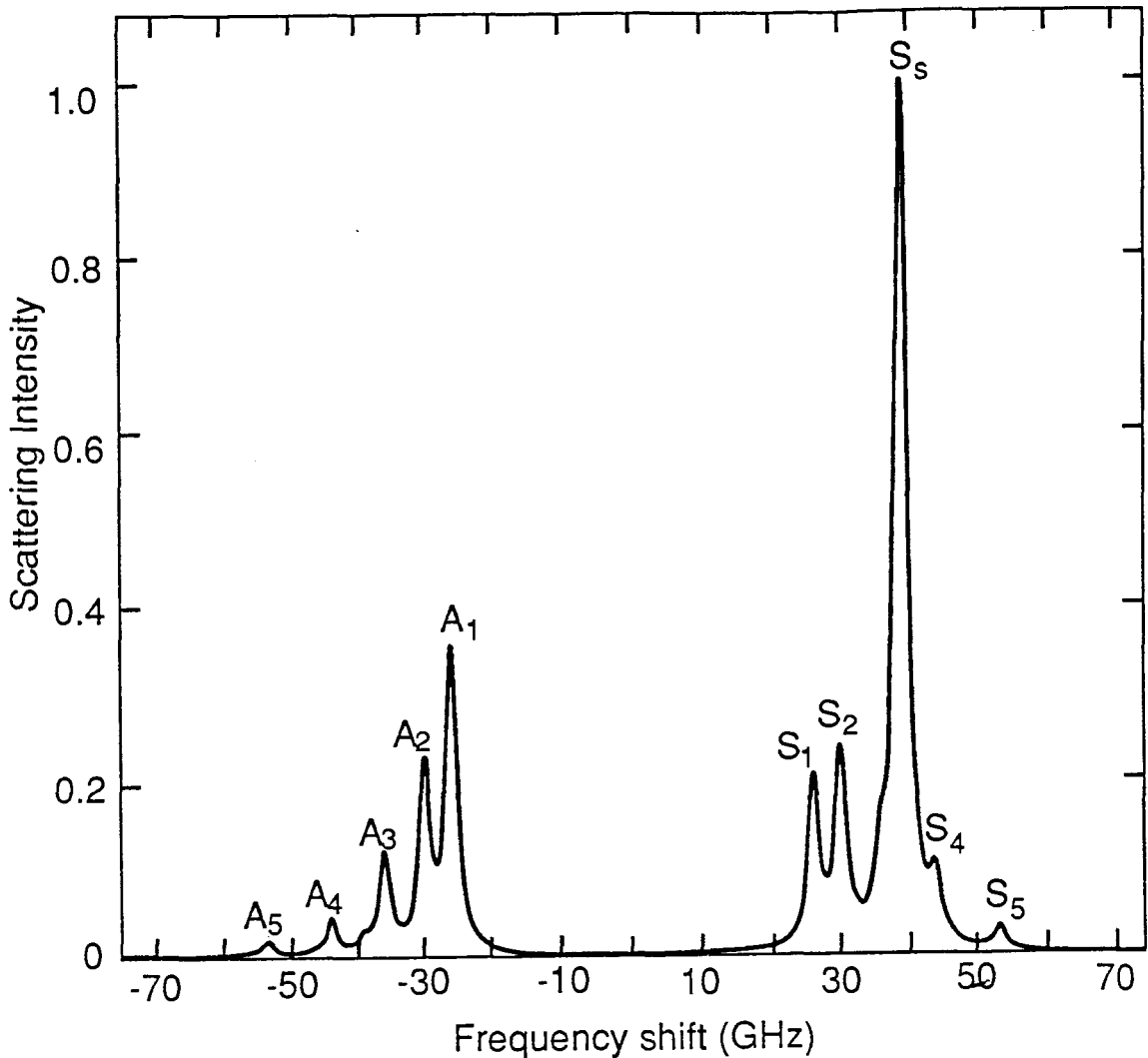


Figure 3.2

The light scattering spectrum calculated using our formalism for an 850Å "iron" film having no magnetocrystalline anisotropy. The numerical subscripts refer to the mode number of the particular standing spin wave and the subscript s refers to the surface mode. The data has been normalized with respect to the intensity of the S_s peak. The spectrum has been calculated for light of wavelength $\lambda = 5145\text{\AA}$ with $H = 3\text{ kOe}$, $\theta = \theta_s = 45^\circ$ and the second order magneto-optic constant $G_{44} = 0$. For the magnetic film, we chose a saturation magnetization $4\pi M_s$ of 21.1 kOe, a g-factor of 2.09 and an exchange constant A of 1.8×10^{-6} erg/cm to agree with Camley and Grimsditch (Camley and Grimsditch, 1980). Additional properties of the magnetic film were taken to be that of bulk iron: Gilbert damping parameter, $G = 7.0 \times 10^7$ Hz and a resistivity of 1.0×10^{-5} Ω -cm. The magnetization was assumed to be unpinned at each interface. Our data has been convolved with a Fabry-Perot instrumental function having an instrumental linewidth of 2 GHz to achieve a linewidth comparable with that in figure 3.3.

thick. This spectrum is to be compared with that shown in figure 3.3 for a similar film calculated using the Camley-Mills formalism (Camley and Grimsditch, 1980). Both spectra have been normalized to unity for the surface peak occurring at +39.4 GHz (S_s) to facilitate a comparison of the relative peak heights in the spectra. Both calculations assumed an applied field of 3 kOe, and the same magnetic parameters were used except for the magnetic damping parameter. The magnetic damping in iron is small; the Landau-Lifshitz damping parameter is estimated to be approximately $G = 7 \times 10^7$ Hz from FMR measurements. This damping parameter leads to a linewidth of approximately 0.4 GHz. The natural linewidths of the peaks, as calculated using our formalism, are shown for the calculated spectrum in figure 3.4. For a Fabry-Perot interferometer with a FSR of 75 GHz, the instrumental linewidth (typically 2 GHz) is much larger than the natural linewidths in figure 3.4. We have therefore convoluted the narrow scattered light spectral distribution with our Fabry-Perot instrumental function to obtain the lineshapes shown in figure 3.2. The intensity profiles calculated by Camley and Grimsditch, figure 3.3, correspond to lines broadened entirely by the large value that they assumed for the magnetic damping. The source of line broadening is not important and the agreement between the calculated intensity distributions in figures 3.2 and 3.3 is excellent.

3.1.5.4 Application to ultrathin films

3.1.5.4.1 The calculation without surface spin pinning

An important aspect of light scattering from thermal magnons is the relatively large intensities which can be observed experimentally for very thin films (Grünberg et al., 1982; Dutcher et al., 1988a). If exchange and pinning of the surface spins are neglected, the calculated light scattering intensity from the surface mode is proportional to thickness for films which are thin compared with the optical skin-depth, reaches a maximum as the thickness becomes comparable with the optical skin-depth, and then decreases to a plateau

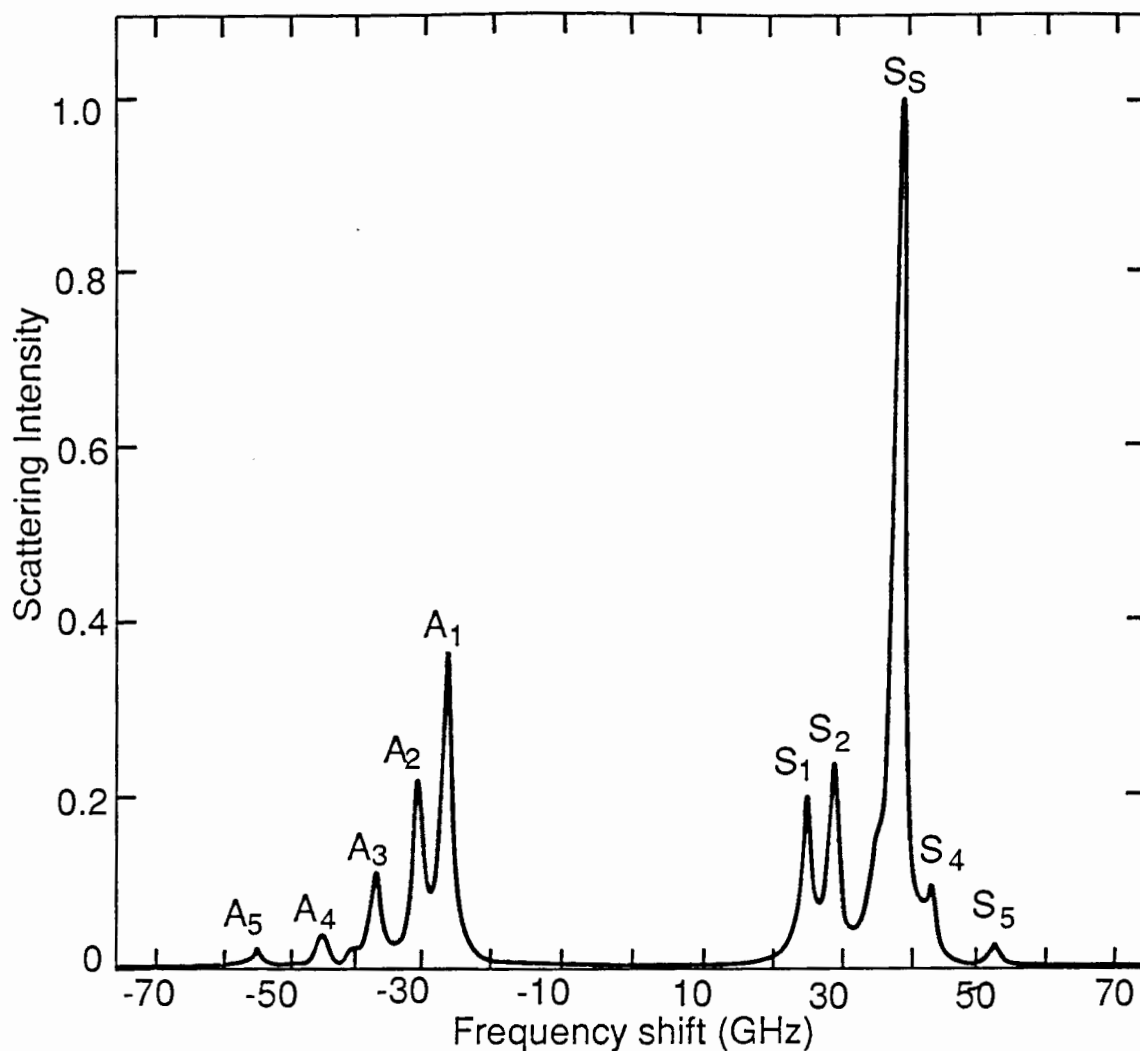


Figure 3.3

The light scattering spectrum calculated by Camley and Grimsditch (Camley and Grimsditch, 1980) for an 850\AA "iron" film having no magnetocrystalline anisotropy. The numerical subscripts refer to the mode number of the particular standing wave and the subscript s refers to the surface mode. The data has been normalized with respect to the intensity of the S_s peak. The spectrum has been calculated for light of wavelength $\lambda = 5145\text{\AA}$ with $H = 3\text{ kOe}$, $\theta = \theta_s = 45^\circ$ and the second order magneto-optic constant $G_{44} = 0$.

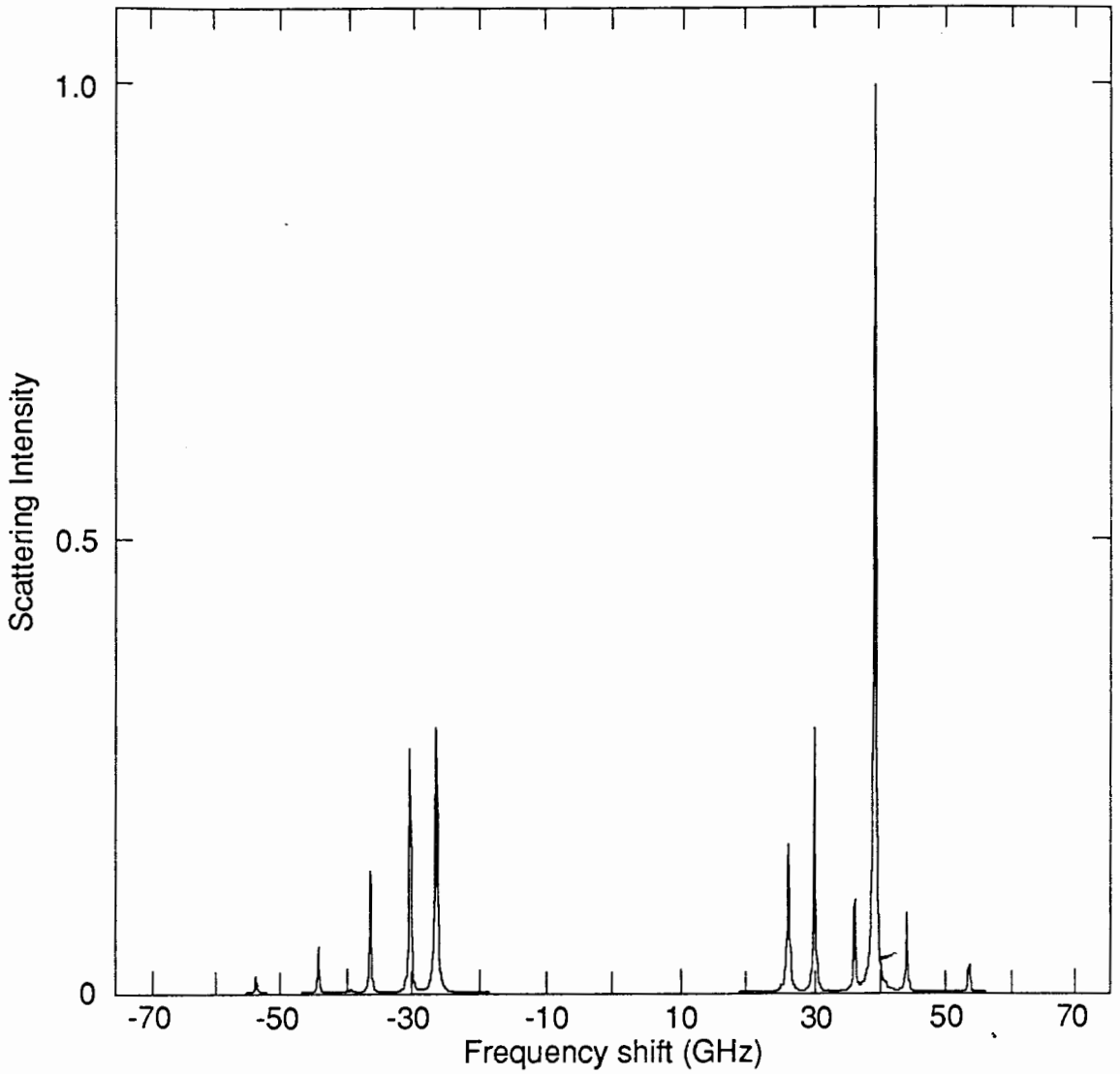


Figure 3.4

The light scattering spectrum calculated using our formalism for an 850Å "iron" film having no magnetocrystalline anisotropy and using the same parameters as for figure 3.2. The peaks have been shown in this figure with their natural linewidths, as calculated using the magnetic damping in iron.

in the thick film limit; this has been shown by Grünberg et al. (Grünberg et al., 1982). If exchange is included, the surface mode interacts strongly with the standing spin wave modes at thickness values for which the surface mode frequency equals the frequency of one of the standing spin wave modes. This strong interaction between modes is clearly seen in figure 3.5 (similar to figure 1 of Grünberg et al. (Grünberg et al., 1982)) near thickness values of $d = 275 \text{ \AA}$ and 502 \AA . In figure 3.6 is shown the effect of the inclusion of exchange on the calculated scattering intensity for the magnetic film of figure 3.5. The overall thickness dependence of the surface mode scattering intensity is similar to that obtained by neglecting exchange. However, sharp dips in the scattering intensity from the surface mode are obtained at those thicknesses which correspond to mode crossings ($d = 275 \text{ \AA}$ and 502 \AA in figure 3.5), along with a sharp increase in the scattering intensity from the corresponding standing spin wave modes. These strong interactions between the modes occur at thickness values larger than the optical skin-depth and the approximate proportionality between scattering intensity and magnetic film thickness, d , for small values of d is preserved. This proportionality is a consequence of two factors: (1) the normal mode amplitude at a given temperature increases with decreasing thickness in order to maintain constant the thermal energy contained in the mode ($\langle m^2 \rangle \propto 1/d$); (2) for a constant optical electric field strength the scattering amplitude increases in proportion with the thickness, and therefore the scattering intensity increases as the square of the thickness. The product of these two factors gives a scattering intensity which is proportional to d (see also the discussion by Grünberg (Grünberg, 1985)).

3.1.5.4.2 The calculation with surface spin pinning

The effects of pinning of the spins at the surfaces of the magnetic film are now included. The spin pinning energies, equations (3.71) and (3.72), are due to the presence of the interfaces between the magnetic film and the surrounding media. For thick magnetic films,

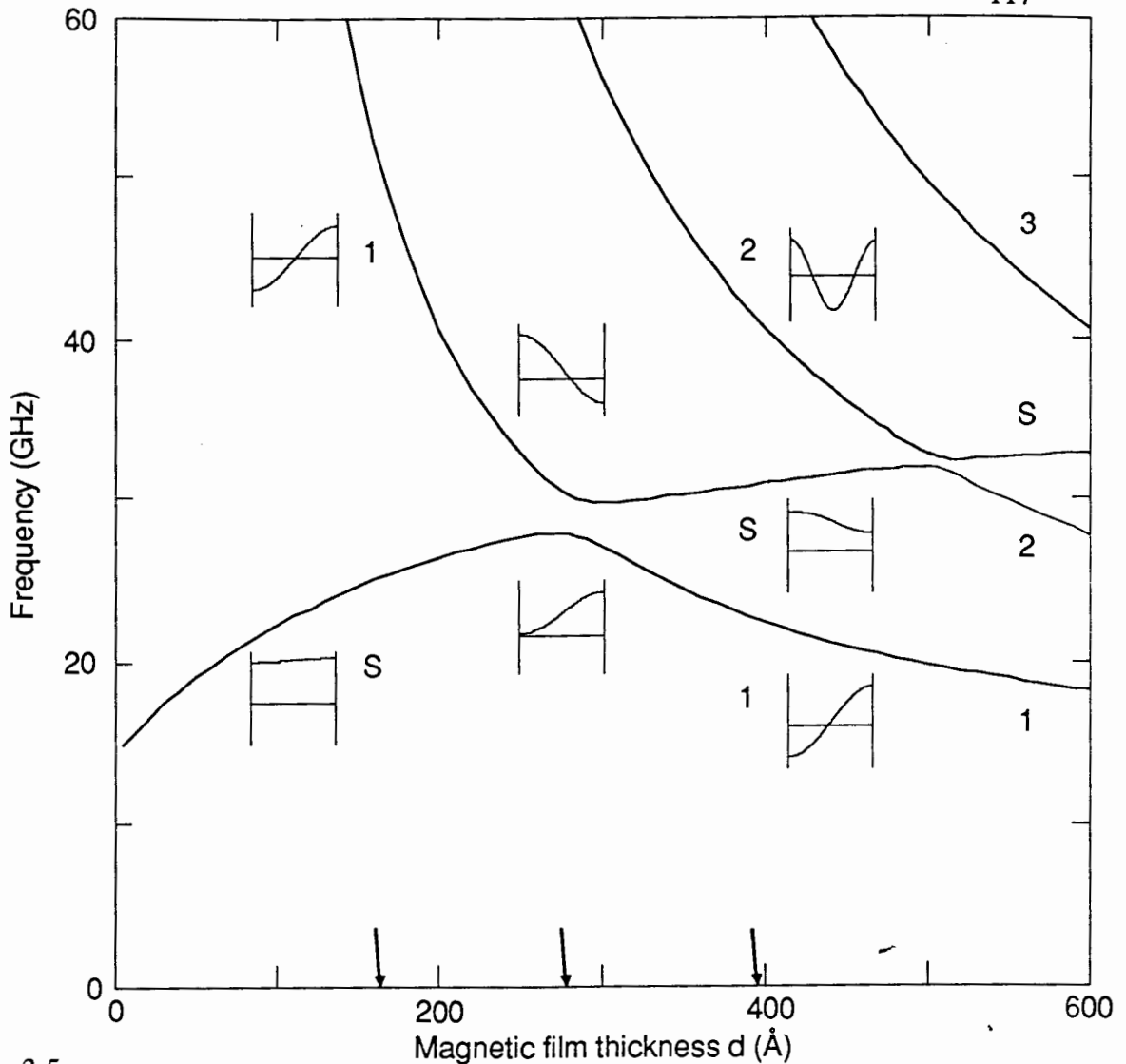


Figure 3.5

Calculated frequency versus magnetic film thickness d for the lowest normal modes of the film. The numbers refer to the mode number of the particular standing spin wave and the S refers to the surface mode. All of the curves have been calculated for light of wavelength $\lambda = 5145 \text{ \AA}$ with $H = 1 \text{ kOe}$ and $\theta = \theta_s = 45^\circ$. The properties of the magnetic film are taken to be those of iron having no magnetocrystalline anisotropy: saturation magnetization $4\pi M_s = 21.55 \text{ kG}$; $g = 2.09$; exchange parameter $A = 2.0 \times 10^{-6} \text{ erg/cm}$; Gilbert damping parameter $G = 7.0 \times 10^7 \text{ Hz}$; and a resistivity of $1.0 \times 10^{-5} \text{ } \Omega\text{-cm}$. The seven small pictures are profiles across the film thickness of the transverse magnetization calculated for the different modes. These profiles are shown for three thickness values, $d = 160 \text{ \AA}$, 275 \AA and 390 \AA , as indicated by the thick vertical arrows. On each profile, the horizontal straight line refers to zero magnetization.

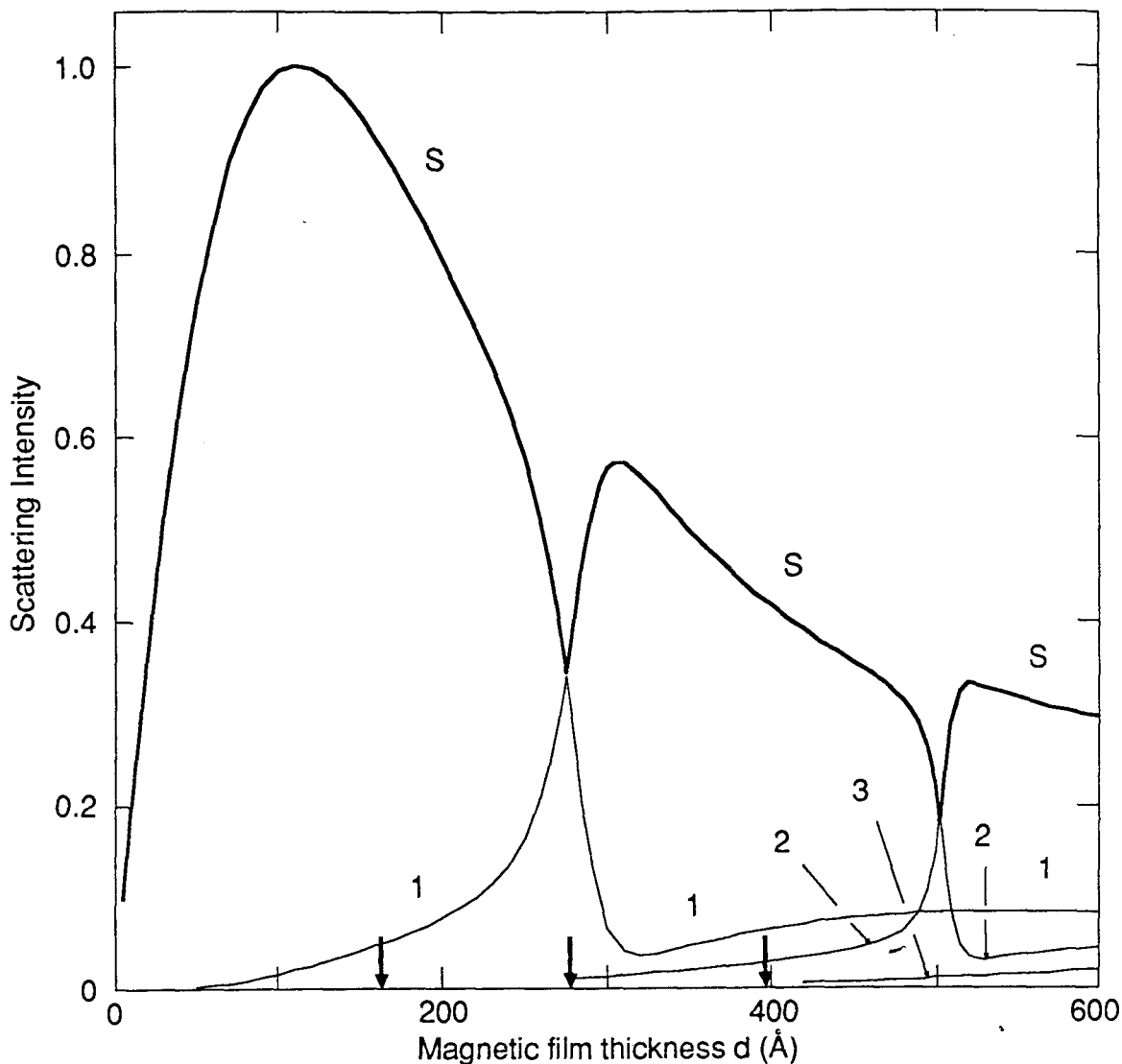


Figure 3.6

Calculated scattering intensity versus magnetic film thickness d for the same parameters as were used in figure 3.5. The numbers refer to the mode number of the particular standing spin wave and the S refers to the surface mode. The intensity values have been normalized with respect to the peak in the S curve. The thick vertical arrows indicate the thickness values, $d = 160\text{Å}$, 275Å and 390Å , for the transverse magnetization profiles shown in figure 3.5. The second order magneto-optic constant G_{44} was taken to be zero. The curve for the surface mode (S), which exhibits two sharp dips, has been drawn with a heavy line.

the surface regions (1 or 2 atomic layers at each surface) form a very small fraction of the total film thickness. However, for magnetic films that are only a few atomic layers thick the surface regions form a substantial portion of the film thickness and spin pinning plays an important role in determining the resonant frequencies and scattered intensities of the magnetic film. As discussed in section 3.1.1, the spin pinning enters the calculation through the generalized exchange boundary conditions, equations (3.73) to (3.76). Rado (Rado, 1982) has shown that for very thin magnetic films the effect of spin pinning is equivalent to adding a surface anisotropy field H_s , where

$$H_s = \frac{2K_s}{M_s d}, \quad (3.135)$$

into the expression for H_y , equation (3.39), in the equation of motion. As the film thickness d becomes very thin, H_s becomes large. The surface spin pinning coefficient K_s includes the effects of perpendicular pinning on both surfaces of the very thin magnetic film: $K_s = K_z^F + K_z^R$. The nature of the pinning will depend upon the material properties of the magnetic film and the covering layer, the crystallographic orientation of the film, and the morphology of the interface.

The effective magnetization of the magnetic film $(4\pi M_s)_{\text{eff}}$ can be written as the difference between the saturation magnetization $4\pi M_s$ and the surface anisotropy field H_s :

$$(4\pi M_s)_{\text{eff}} = 4\pi M_s - \frac{2K_s}{M_s d}. \quad (3.136)$$

This quantity becomes small for large surface pinning.

In figure 3.7 the resonant frequency of the surface mode has been calculated as a function of the magnetic film thickness d for three different values of the spin pinning

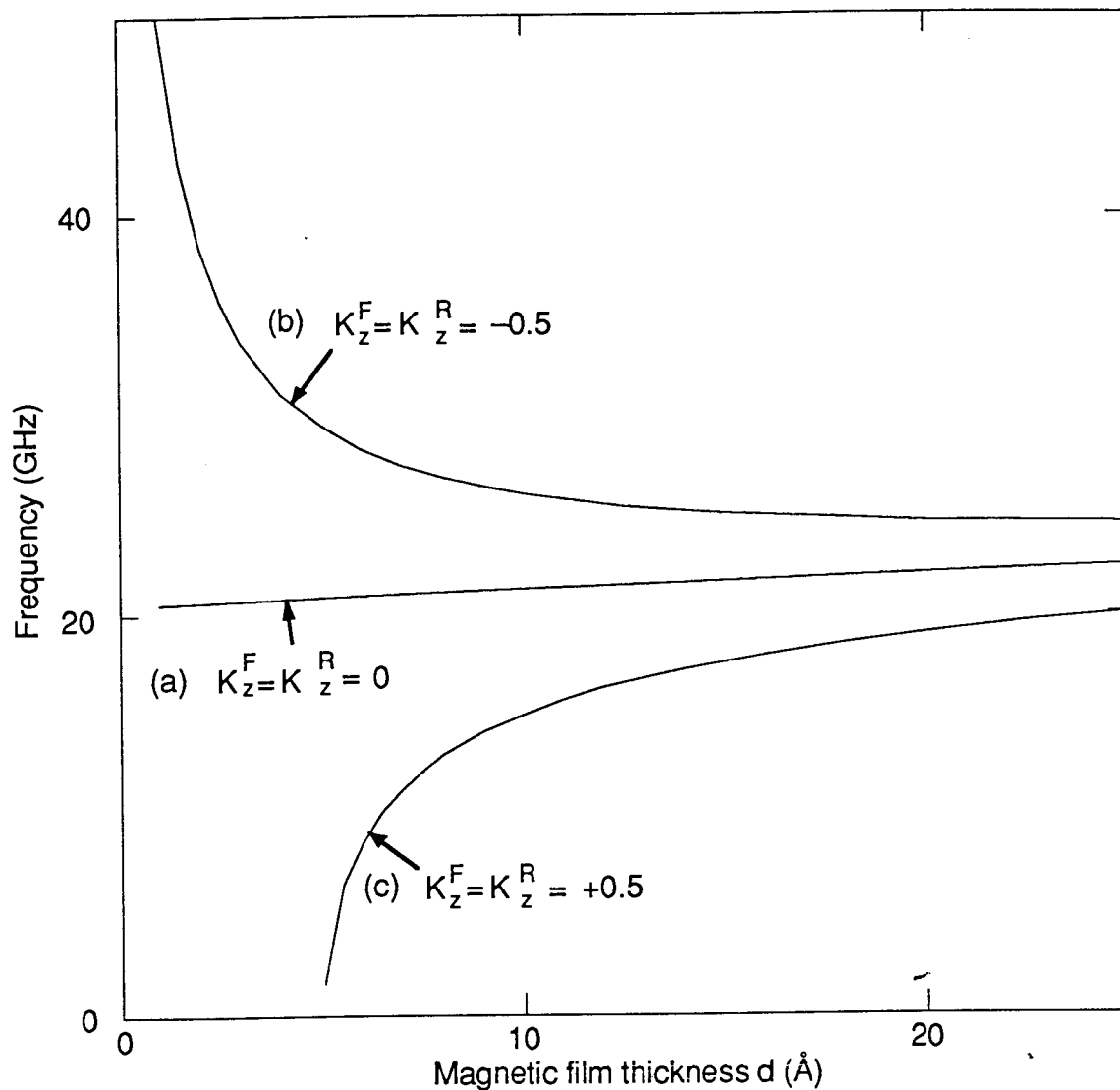


Figure 3.7

Calculated surface mode frequency versus magnetic film thickness d for an "iron" film having no magnetocrystalline anisotropy. The magnetic parameters have been taken to be the same as in figure 3.2, with the exception that three different values of the spin pinning coefficients have been used: (a) $K_y^F = K_y^R = K_z^F = K_z^R = 0$; (b) $K_y^F = K_y^R = K_z^F = K_z^R = -0.5$ erg/cm²; and (c) $K_y^F = K_y^R = K_z^F = K_z^R = +0.5$ erg/cm². An applied magnetic field of 2 kOe was used.

coefficients: (a) $K_y^F = K_y^R = K_z^F = K_z^R = 0$; (b) $K_y^F = K_y^R = 0$, $K_z^F = K_z^R = -0.5 \text{ erg/cm}^2$ and (c) $K_y^F = K_y^R = 0$, $K_z^F = K_z^R = +0.5 \text{ erg/cm}^2$. An applied field value of 2 kOe was

used. Curve (a) corresponds to the absence of surface pinning, see figure 3.5; the surface mode frequency decreases only slightly over the thickness range shown in figure 3.7.

Curve (b) corresponds to pinning which tends to hold the magnetization in the sample plane (in-plane pinning). Curve (c) corresponds to pinning which tends to tilt the magnetization out of the sample plane (out-of-plane pinning). The in-plane pinning increases the surface mode frequency as the film thickness is decreased, whereas the out-of-plane pinning decreases the surface mode frequency as the film thickness is decreased. For the present case the surface mode frequency for out-of-plane pinning becomes zero at $\sim 5\text{\AA}$. For this thickness value the spin pinning field H_s , equation (3.135), equals the sum of the saturation magnetization $4\pi M_s$ and applied field H , i.e. the applied field H plus the effective magnetization $(4\pi M_s)_{\text{eff}}$ is equal to zero. For thicknesses less than 5\AA the magnetization is tilted out of the sample plane; this case is discussed in section 3.2. In-plane pinning has been observed experimentally using BLS by Hillebrands et al. (Hillebrands et al., 1988) for bcc Fe(110) on W(110). The experimental observation of out-of-plane pinning for bcc Fe(001) on Ag(001) (Heinrich et al., 1987a; Heinrich et al., 1988a; and Cochran et al., 1988) and fcc Fe(001) on Cu(001) (Dutcher et al., 1988a; and Heinrich et al., 1988a) is described in Chapters Four and Five of this thesis.

In figure 3.8 is shown the scattered intensities for the surface mode calculated as a function of magnetic film thickness for the same pinning parameters as in figure 3.7. For the calculation with no surface pinning, curve (a), the scattered intensity decreases approximately linearly with decreasing film thickness, as discussed in section 3.1.5.4.1 (see figure 3.6). For in-plane pinning, curve (b), the scattered intensity is less than that for the unpinned case. The most striking result is for out-of-plane pinning, curve (c), for which a dramatic increase in the scattered intensity is obtained below $d = 10\text{\AA}$.

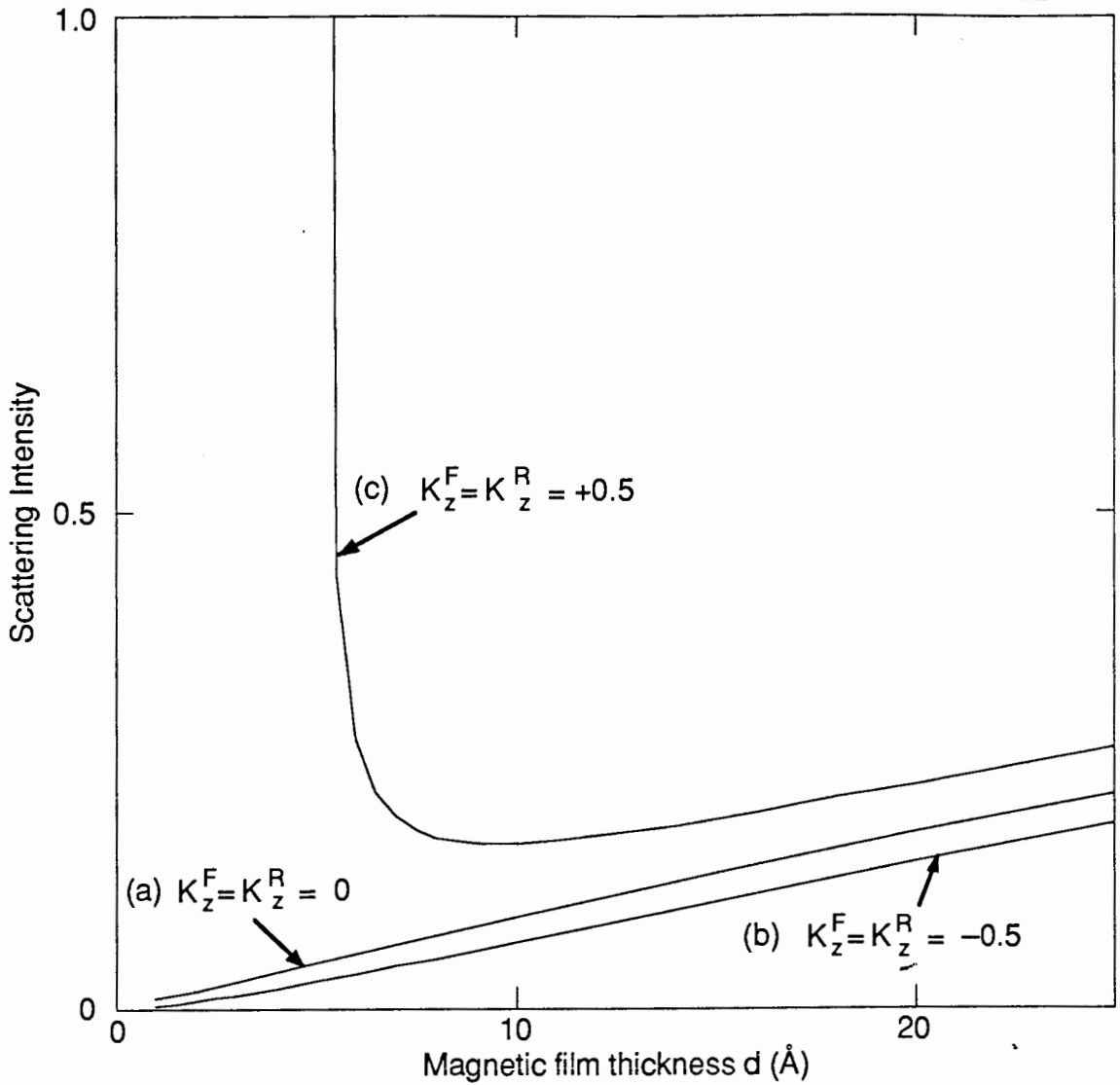


Figure 3.8

Calculated scattering intensity versus magnetic film thickness d for the same magnetic parameters as in figure 3.7. Curves (a), (b) and (c) in this figure correspond to curves (a), (b) and (c) in figure 3.7.

These results can be understood in the following manner. For curve (b), the in-plane pinning adds to the effective field on the spins in the sample plane (applied field plus saturation magnetization). This increased in-plane field allows smaller deviations in the magnetization from its equilibrium direction along the direction of the effective field. In other words, the rf magnetization components are smaller for (b) than for (a). Since the scattered light intensity is proportional to the square of the magnetization components, equations (3.109) and (3.110), the scattered intensity is smaller for (b) than for (a). For curve (c), the scattered intensity is larger than for (a) or (b). The out-of-plane pinning acts to decrease the in-plane effective field on the spins and the magnetization deviates more from its equilibrium direction. This gives larger rf magnetization components and, therefore, a larger scattered intensity. Near $d = 5\text{\AA}$, the surface mode frequency decreases to zero when the surface pinning field H_s , equation (3.135), becomes equal and opposite to the applied field plus the saturation magnetization. For this thickness, the effective field on the spins is zero and the rf magnetization components and scattered intensity are very large. However, for curve (c) in figures 3.7 and 3.8, the rf magnetization values are less than 5% of the saturation magnetization. The linearization of the Landau-Lifshitz equations discussed in section 3.1.1 is still valid and the calculated values of the resonant frequencies and the scattered intensities can still be trusted.

In a BLS experiment, the frequency of a mode can be measured as a function of the applied magnetic field. The mode frequency can also be calculated as a function of the applied magnetic field. One chooses magnetic parameter values such that the calculated curve of frequency versus magnetic field passes through the data points. In figure 3.9 are shown calculated curves of frequency and magnetic field for a 10\AA thick magnetic film with the same magnetic parameters as in figures 3.7 and 3.8 with three different values of the surface spin pinning coefficients. For all three curves, the mode frequency increases with increasing magnetic field. For a given value of H , the mode frequency is lowest for

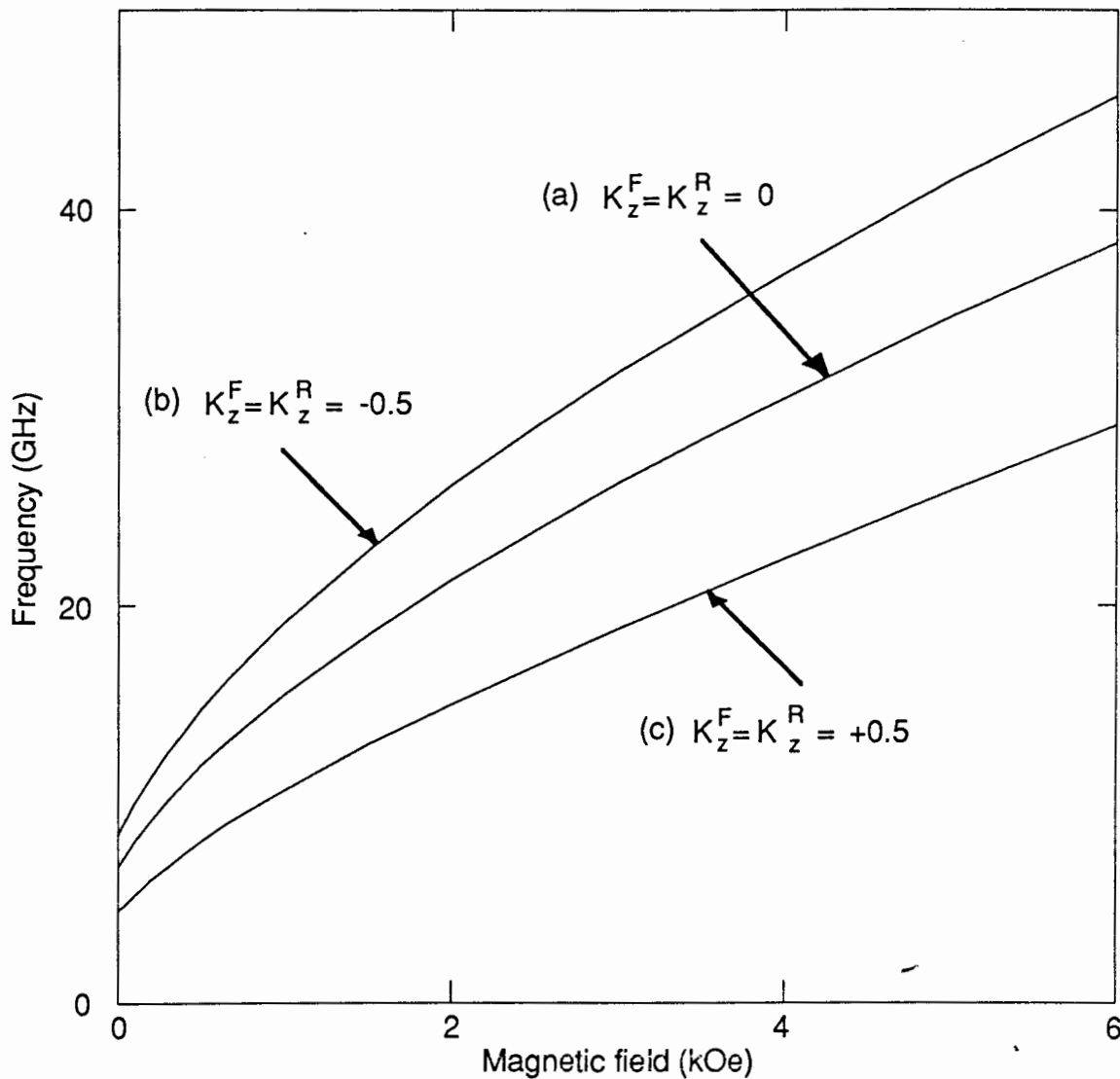


Figure 3.9

Calculated surface mode frequency versus applied magnetic field for a 10\AA thick "iron" film having no magnetocrystalline anisotropy. The magnetic parameters have been taken to be the same as in figure 3.2, with the exception that three different values of the spin pinning coefficients have been used, as detailed in figure 3.7.

positive spin pinning coefficients (out-of-plane pinning) and highest for negative spin pinning coefficients (in-plane pinning). Corresponding plots of scattered intensity versus magnetic field are shown in figure 3.10. The scattered intensity increases as the field is decreased because the effective field along the equilibrium direction of the magnetization is decreased, resulting in larger rf magnetization components and, therefore, scattered intensity (see equations (3.109) and (3.110)).

3.1.5.4.3 Comparison with ferromagnetic resonance condition

In the theory of ferromagnetic resonance, the resonance condition for the uniform precession mode can be derived in a very simple manner. Assuming the spatial dependence of the fields to be $\sim e^{ikz}$, Maxwell's equation for the divergence of \mathbf{b} , equation (3.4), gives

$$\frac{\partial b_z}{\partial z} = ikb_z = 0, \quad (3.137)$$

Therefore

$$b_z = h_z + 4\pi m_z = 0, \quad (3.138)$$

or

$$h_z = -4\pi m_z. \quad (3.139)$$

The field h_z is sometimes called the dynamic demagnetizing field in analogy with the static demagnetizing field (equation 3.23). Equation (3.139) allows a simple substitution for h_z in the Landau-Lifshitz equations, equations (3.37) and (3.38); this gives

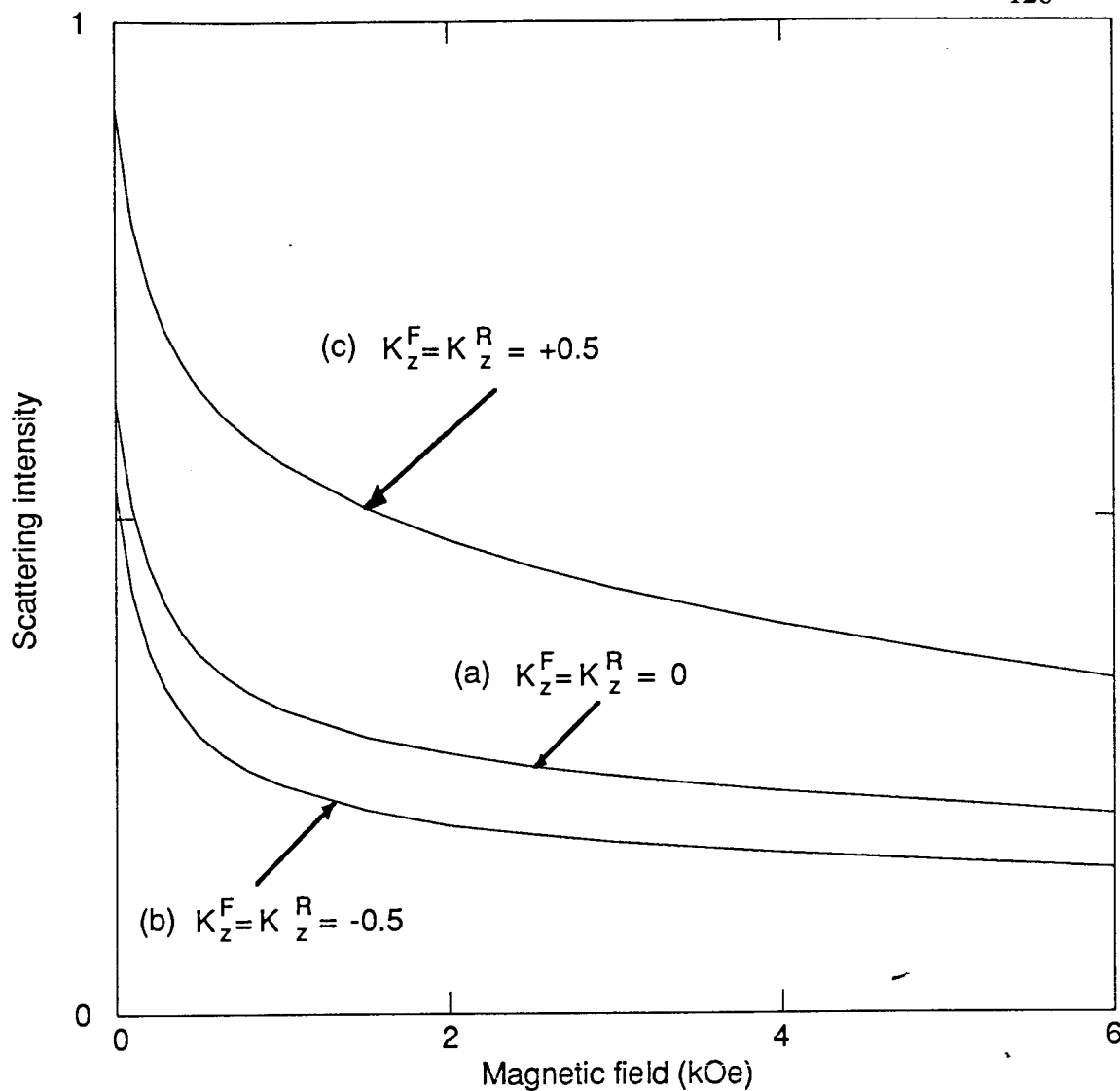


Figure 3.10

Calculated scattering intensity versus applied magnetic field for the same magnetic film as in figure 3.9. Curves (a), (b) and (c) in this figure correspond to curves (a), (b) and (c) in figure 3.9.

$$H_z m_y + \frac{i\omega}{\gamma} m_z = M_s h_y \quad (3.140)$$

$$-\frac{i\omega}{\gamma} m_y + B_y m_z = 0, \quad (3.141)$$

where $B_y = H_y + 4\pi M_s$. Equation (3.141) is then solved for m_z in terms of m_y , and the result is substituted into equation (3.140). This allows us to express m_y in terms of h_y :

$$m_y = \left[\frac{M_s B_y}{B_y H_z - \left(\frac{\omega}{\gamma}\right)^2} \right] h_y = \chi_{\text{eff}}^{\text{FMR}} h_y, \quad (3.142)$$

where $\chi_{\text{eff}}^{\text{FMR}}$ is the effective susceptibility for ferromagnetic resonance. $\chi_{\text{eff}}^{\text{FMR}}$ becomes very large, i.e. there is a resonance, when the denominator vanishes:

$$\left(\frac{\omega}{\gamma}\right)^2 = B_y H_z. \quad (3.143)$$

This is the simple expression for the ferromagnetic resonance condition.

In the light scattering calculation, the fields are assumed to have a spatial dependence $\sim e^{iq_y y} e^{ik_z z}$. For this spatial dependence, equation (3.4) for the divergence of \mathbf{b} gives

$$\frac{\partial b_y}{\partial y} + \frac{\partial b_z}{\partial z} = iq b_y + ik b_z = 0. \quad (3.144)$$

or

$$b_z = -\frac{q}{k} b_y. \quad (3.145)$$

This expression for b_z is not as simple as that for FMR, in that it relates h_z to h_y , $4\pi m_y$ and $4\pi m_z$. This does not allow a simple substitution for h_z into the Landau-Lifshitz equations. We wish to show that for magnetic films comprised of only a few atomic layers, the b_z field is very small. This means that $h_z = -4\pi m_z$ is a good approximation for ultrathin films and that the simple expression for the ferromagnetic resonance frequency, equation (3.143), is a good approximation to the true resonance frequency for the light scattering geometry. The calculation of the exact light scattering resonance frequency has been described in detail above.

The thin film geometry is shown in figure 3.1. In the vacuum, from equation (3.14), we have $k = -iq$ for $z \leq 0$ and $k = iq$ for $z \geq 0$. Using equations (3.9) and (3.14), the magnetic field in the vacuum, $h_y^v(z)$, can be expressed in terms of the electric field in the vacuum, $e_x^v(z)$, at the two film surfaces:

$$h_y^v(0) = -\left(\frac{iqc}{\omega}\right) e_x^v(0) \quad (3.146)$$

$$h_y^v(d) = \left(\frac{iqc}{\omega}\right) e_x^v(d). \quad (3.147)$$

In the magnetic film, e_x is related to b_z by equation (3.6):

$$e_x = -\left(\frac{\omega}{qc}\right) b_z. \quad (3.148)$$

Therefore at the film surfaces, we obtain

$$h_y(0) = ib_z(0) \quad (3.149)$$

$$h_y(d) = -ib_z(d). \quad (3.150)$$

For magnetic film thicknesses d of only several atomic layers, equation (3.144) for the divergence of \mathbf{b} can be written as

$$iqb_y + \left(\frac{b_z(d) - b_z(0)}{d} \right) = 0, \quad (3.151)$$

or

$$b_z(d) = b_z(0) - iqdb_y = b_z(0) - iqd(h_y + 4\pi m_y). \quad (3.152)$$

For small d , the rf magnetization $4\pi m_y$ is approximately constant across the film thickness because the exchange interaction between the spins favors parallel alignment of the spins. With $4\pi m_y$ constant, h_y is forced by equation (3.152) to be constant across the film thickness, since all quantities in the equation other than h_y have constant values. Since h_y must be constant across the film, b_z must change sign from equations (3.149) and (3.150). Because of the symmetry of the film about $z = d/2$, b_z must be antisymmetric about $z = d/2$.

By substituting equations (3.149) and (3.150) for $h_y(0)$ and $h_y(d)$ into equation (3.152), we obtain

$$b_z(d) = b_z(0) (1 + qd) - iqd(4\pi m_y) \quad (3.153)$$

$$b_z(d) = \frac{b_z(0) - iqd(4\pi m_y)}{1 + qd} \quad (3.154)$$

By equating the right hand sides of equations (3.153) and (3.154), we can solve for $b_z(0)$:

$$b_z(0) = \left(\frac{iqd}{2 + qd} \right) 4\pi m_y \quad (3.155)$$

$$b_z(d) = -b_z(0) = -\left(\frac{iqd}{2 + qd} \right) 4\pi m_y . \quad (3.156)$$

b_z is equal to zero only for $d = 0$ or $q = 0$. However, for a film thickness of $10\text{\AA} = 10^{-7}\text{cm}$ and a typical value of $q = 10^5\text{cm}^{-1}$ (as determined by the light scattering geometry), we have $qd = 10^{-2}$. For these values of q and d , b_z is two orders of magnitude less than $4\pi m_y$. Since the magnitude of h_y is equal to that of b_z at the film surfaces, equations (3.149) and (3.150), h_y is also small compared with $4\pi m_y$ and $b_y \sim 4\pi m_y$. Therefore b_z is small compared with b_y and in this sense $b_z \sim 0$ and $h_z \sim -4\pi m_z$ for the light scattering calculation for very thin magnetic films. The FMR resonance frequency given by equation (3.143) is a good approximation to the true BLS resonance frequency for very thin magnetic films, except that the effective field expressions for BLS contain an exchange term, $2Aq^2/M_s$, which produces a frequency shift of ~ 0.25 GHz. For FMR, q is of the order of the inverse of the sample dimension ($\sim 1\text{ cm}^{-1}$, five orders of magnitude less than the value of q for light scattering) and the condition $b_z = 0$ is satisfied much more closely than for the light scattering calculation.

3.2 The light scattering calculation allowing the magnetization to tilt out of the sample plane

In section 3.1, a calculation of the resonant frequencies of the normal modes of a magnetic film, and the intensity of light scattered from these modes, was presented. In this calculation, a dc magnetic field was applied in the plane of the film and the calculation was valid for films with the saturation magnetization lying in the plane of the film for all values of the applied field. In this section, we extend this calculation to allow the magnetization to

tilt out of the sample plane toward the sample normal in the presence of an in-plane applied magnetic field. The tilting of the magnetization is assumed to be due to strong uniaxial anisotropies with the easy axis along the sample normal. Because of the additional complexities introduced by the tilting of the magnetization, the effects of exchange have been neglected in the calculation. This means that the calculation applies only to ultrathin magnetic films for which the spins are necessarily parallel to one another for low frequency excitations. Other consequences of the neglect of exchange are that the constant term $\frac{2Aq^2}{M_S} \sim 70$ Oe has been neglected in the effective field expressions in equations (3.39) and (3.40), and that only the surface mode is calculated (without exchange, there are no bulk standing spin waves).

The description of the calculation will proceed along the same lines as in section 3.1, with one major difference. Because the magnetization is, in general, tilted with respect to the film surface, it will be convenient to write the Landau-Lifshitz equation of motion for the magnetization in a reference frame fixed with respect to the equilibrium direction of the magnetization. The permeability tensor will be constructed using the Landau-Lifshitz equation. This tensor will be used with Maxwell's equations written in the magnetization coordinate system to obtain the secular equation for the magnetic wavevector directed along the sample normal. The secular equation is obtained from the magnetization coordinate system because the permeability tensor has a simple form in this coordinate system. The permeability tensor will then be transformed into the coordinate system fixed with respect to the crystal for the solution of the boundary value problem.

3.2.1 The surface mode frequency

The Landau-Lifshitz equations have their simplest form in a coordinate system in which M_S lies along one of the coordinate axes. For the present case, a magnetization coordinate system with axes x', y', z' is adopted in which M_S always lies along x' , as shown in figure

3.11 for an arbitrary value of the tilt angle α between M_s and the sample plane. The magnetic film is assumed to be surrounded on both sides by vacuum. The magnetization in the magnetization coordinate system can be written as $\mathbf{M}' = (M_s, m_y', m_z')$, where m_y', m_z' are small rf magnetization components. The crystal coordinate system with axes x, y, z is fixed in space with the x -axis along the sample surface and the z -axis into the sample along the sample normal. The magnetization components in the magnetization and crystal coordinate systems are related by

$$\begin{pmatrix} m_x' \\ m_y' \\ m_z' \end{pmatrix} = \begin{pmatrix} M_s \\ m_y' \\ m_z' \end{pmatrix} = \mathbf{T} \begin{pmatrix} m_x \\ m_y \\ m_z \end{pmatrix}, \quad (3.157)$$

and

$$\begin{pmatrix} m_x \\ m_y \\ m_z \end{pmatrix} = \mathbf{T}^{-1} \begin{pmatrix} m_x' \\ m_y' \\ m_z' \end{pmatrix}, \quad (3.158)$$

where \mathbf{T} is a rotation matrix given by

$$\mathbf{T} = \begin{pmatrix} \cos\alpha & 0 & \sin\alpha \\ 0 & 1 & 0 \\ -\sin\alpha & 0 & \cos\alpha \end{pmatrix} \quad (3.159)$$

and \mathbf{T}^{-1} is the inverse of \mathbf{T} . For a real matrix such as \mathbf{T} , the inverse is just the transpose.

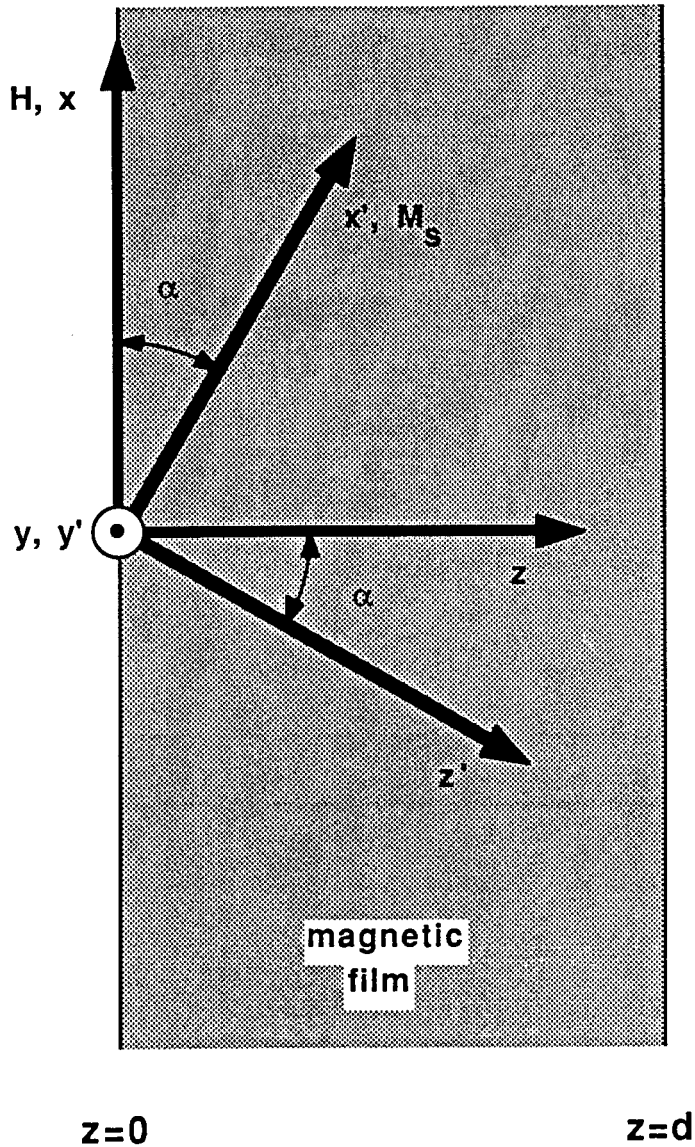


Figure 3.11

The geometry used to calculate the intensity of light scattered from thermal magnons in a thin magnetic film surrounded by vacuum. The magnetization is allowed to tilt out of the sample surface. The angle between M_s and the surface of the film is α . The crystal coordinate system (x, y, z) is fixed with respect to the magnetic film. The dc field H is applied along the x -axis. The static magnetization M_s is assumed to be uniform; the direction of M_s defines the x' -axis of the magnetization coordinate system (x', y', z') .

In writing the Landau-Lifshitz equations, we will consider torques on the magnetization due to the applied magnetic field, the static shape demagnetizing field, first and second order uniaxial anisotropies with the easy axis along the sample normal, and magnetic damping. The effects due to exchange and in-plane cubic magnetocrystalline anisotropy have been neglected. With the exception of the magnetic damping, the effective fields in the magnetization coordinate system, \mathbf{H}_{eff}' , are obtained by multiplying the effective fields in the crystal coordinate system, \mathbf{H}_{eff} , by the rotation matrix \mathbf{T} , equation (3.159):

$$\mathbf{H}_{\text{eff}}' = \mathbf{T} \mathbf{H}_{\text{eff}} \quad (3.160)$$

The torques $\boldsymbol{\tau}'$ acting on the magnetization are then obtained from the cross-product of \mathbf{M}' and the effective fields \mathbf{H}_{eff}'

$$\boldsymbol{\tau}' = \mathbf{M}' \times \mathbf{H}_{\text{eff}}', \quad (3.161)$$

where all of the quantities are written in the magnetization coordinate system. In the following description of the various contributions to the total torque on the magnetization, the expressions for the effective fields are written in the crystal coordinate system, with the exception of magnetic damping, and the expressions for the torques are written in the magnetization coordinate system.

i) Applied static field:

The applied static field is directed along the +x-axis, see figure 3.11:

$$H_x^a = H; \quad H_y^a = 0; \quad H_z^a = 0. \quad (3.162)$$

The resulting torque components in the magnetization coordinate system are:

$$\tau_{x'}^a = -H \sin\alpha m_y'; \quad \tau_{y'}^a = H \cos\alpha m_z'; \quad \tau_{z'}^a = -H \cos\alpha m_y'. \quad (3.163)$$

ii) **Static shape demagnetizing field:**

As discussed in section 3.1.1, the static shape demagnetizing field for ultrathin films is given by

$$H_x^d = 0, \quad H_y^d = 0, \quad H_z^d = -4\pi M_s \sin\alpha \quad (3.164)$$

The resulting torque components in the magnetization coordinate system are:

$$\begin{aligned} \tau_{x'}^d &= -4\pi M_s \sin\alpha \cos\alpha m_y', \\ \tau_{y'}^d &= -4\pi M_s \sin^2\alpha m_z', \\ \tau_{z'}^d &= 4\pi M_s \sin^2\alpha m_y'. \end{aligned} \quad (3.165)$$

iii) **Magnetic uniaxial anisotropy:**

The first and second order terms of the uniaxial anisotropy energy E^A can be written as

$$E^A = -K_u^{(1)} \left(\frac{m_z}{M_s}\right)^2 - K_u^{(2)} \left(\frac{m_z}{M_s}\right)^4 \quad (3.166)$$

For positive values of $K_u^{(1)}$ and $K_u^{(2)}$, the energy E^A is a minimum with the magnetization along the sample normal. For the first order uniaxial anisotropy term, the effective field in the crystal coordinate system can be written as

$$H_x^{u1} = 0; \quad H_y^{u1} = 0; \quad H_z^{u1} = \frac{2K_u^{(1)}}{M_s^2} m_z, \quad (3.167)$$

and for the second order uniaxial anisotropy term, the effective field in the crystal coordinate system can be written as

$$H_x^{u2} = 0; \quad H_y^{u2} = 0; \quad H_z^{u2} = \frac{4K_u^{(2)}}{M_s^4} m_z^3. \quad (3.168)$$

Using equation (3.158), m_z can be expressed in terms of $m_{x'} = M_s$ and $m_{z'}$ in equations (3.167) and (3.168). The resulting torque expressions in the magnetization coordinate system are

$$\begin{aligned} \tau_{x'}^{u1} &= \frac{2K_u^{(1)}}{M_s} \sin\alpha \cos\alpha m_{y'}, \\ \tau_{y'}^{u1} &= \frac{2K_u^{(1)}}{M_s} (\sin^2\alpha - \cos^2\alpha) m_{z'}, \\ \tau_{z'}^{u1} &= -\frac{2K_u^{(1)}}{M_s} \sin^2\alpha m_{y'}. \end{aligned} \quad (3.169)$$

for the first order uniaxial anisotropy, and

$$\begin{aligned}\tau_{x'}^{u2} &= \frac{4K_u^{(2)}}{M_s} \sin^3\alpha \cos\alpha m_{y'}, \\ \tau_{y'}^{u2} &= \frac{4K_u^{(2)}}{M_s} (\sin^4\alpha - \sin^2\alpha \cos^2\alpha) m_{z'}, \\ \tau_{z'}^{u2} &= -\frac{4K_u^{(2)}}{M_s} \sin^4\alpha m_{y'}.\end{aligned}\quad (3.170)$$

for the second order uniaxial anisotropy. An interesting feature of equation (3.170) is that there is no torque on the magnetization due to the second order uniaxial anisotropy for an in-plane magnetization ($\alpha=0$). This is also true for all higher order terms in the expression for the uniaxial anisotropy energy.

iv) Magnetic damping

The effective field due to magnetic damping is proportional to the time rate of change of the magnetization. This is most easily expressed in the magnetization coordinate system:

$$H_{x'}^d = 0; \quad H_{y'}^d = -\frac{G}{\gamma^2 M_s^2} \frac{\partial m_{y'}}{\partial t}; \quad H_{z'}^d = -\frac{G}{\gamma^2 M_s^2} \frac{\partial m_{z'}}{\partial t}, \quad (3.171)$$

where G is the Gilbert damping parameter. For a temporal variation $\sim e^{-i\omega t}$, the torque components in the magnetization coordinate system due to magnetic damping are

$$\tau_{x'}^d = 0; \quad \tau_{y'}^d = -\frac{i\omega}{\gamma} \frac{G}{\gamma M_s} m_{z'}; \quad \tau_{z'}^d = \frac{i\omega}{\gamma} \frac{G}{\gamma M_s} m_{y'}. \quad (3.172)$$

The Landau-Lifshitz equations in the primed coordinate system have the form

$$-\frac{1}{\gamma} \frac{\partial \mathbf{M}'}{\partial t} = \mathbf{M}' \times \mathbf{H}_{\text{eff}}' = \boldsymbol{\tau}'. \quad (3.173)$$

Substituting equations (3.163), (3.165), (3.169), (3.170) and (3.172) into equation (3.173), one gets

$$-\left(\frac{i\omega}{\gamma}\right) 4\pi m_{y'} + (H_1 - H_2) 4\pi m_{z'} = 4\pi M_s h_{z'}, \quad (3.174)$$

$$(H_1) 4\pi m_{y'} + \left(\frac{i\omega}{\gamma}\right) 4\pi m_{z'} = 4\pi M_s h_{y'}. \quad (3.175)$$

where

$$H_1 = H \cos \alpha - \left[4\pi M_s - \frac{2K_u^{(1)}}{M_s} \right] \sin^2 \alpha + \frac{4K_u^{(2)}}{M_s} \sin^4 \alpha - \frac{i\omega}{\gamma} \frac{G}{\gamma M_s}, \quad (3.176)$$

$$H_2 = \frac{2K_u^{(1)}}{M_s} \cos^2 \alpha + \frac{12K_u^{(2)}}{M_s} \sin^2 \alpha \cos^2 \alpha. \quad (3.177)$$

The equilibrium direction of the magnetization, i.e. the tilt angle α , for any value of the applied field is given by the condition that there must be no net torque on the magnetization in equilibrium:

$$M_s \sin\alpha \left[H + \left(4\pi M_s - \frac{2K^{(1)}}{M_s} \right) \cos\alpha - \frac{4K^{(2)}}{M_s} \sin^2\alpha \cos\alpha \right] = 0. \quad (3.178)$$

The Landau-Lifshitz equations, equations (3.174) and (3.175), can be used to express the rf magnetization components $m_{y'}$ and $m_{z'}$ in terms of $h_{y'}$ and $h_{z'}$:

$$\begin{pmatrix} m_{x'} \\ m_{y'} \\ m_{z'} \end{pmatrix} = \chi' \begin{pmatrix} h_{x'} \\ h_{y'} \\ h_{z'} \end{pmatrix} \quad (3.179)$$

where χ' is the magnetic susceptibility tensor in the magnetization coordinate system:

$$\chi' = \frac{1}{H_1(H_1 - H_2) - \left(\frac{\omega}{\gamma}\right)^2} \begin{pmatrix} 0 & 0 & 0 \\ 0 & (H_1 - H_2)M_s & -\frac{i\omega}{\gamma}M_s \\ 0 & \frac{i\omega}{\gamma}M_s & H_1M_s \end{pmatrix} \quad (3.180)$$

The permeability tensor in the magnetization coordinate system $\mu' = 1 + 4\pi\chi'$ is given by

$$\mu' = \begin{pmatrix} 1 & 0 & 0 \\ 0 & \mu_{yy} & \mu_{yz} \\ 0 & -\mu_{yz} & \mu_{zz} \end{pmatrix} \quad (3.181)$$

where

$$\mu_{yy}' = \frac{B_1(H_1 - H_2) - \left(\frac{\omega}{\gamma}\right)^2}{H_1(H_1 - H_2) - \left(\frac{\omega}{\gamma}\right)^2} \quad (3.182)$$

$$\mu_{zz}' = \frac{H_1(B_1 - H_2) - \left(\frac{\omega}{\gamma}\right)^2}{H_1(H_1 - H_2) - \left(\frac{\omega}{\gamma}\right)^2} \quad (3.183)$$

$$\mu_{yz}' = \frac{-\frac{i\omega}{\gamma} 4\pi M_s}{H_1(H_1 - H_2) - \left(\frac{\omega}{\gamma}\right)^2} \quad (3.184)$$

and $B_1 = H_1 + 4\pi M_s$. The permeability tensor μ in the crystal coordinate system is given by

$$\mu = \mathbf{T}^{-1} \mu' \mathbf{T} \quad (3.185)$$

where \mathbf{T} is given by equation (3.159). Explicitly, we have

$$\mu = \begin{pmatrix} \mu_{xx} & \mu_{xy} & \mu_{xz} \\ -\mu_{xy} & \mu_{yy} & \mu_{yz} \\ \mu_{xz} & -\mu_{yz} & \mu_{zz} \end{pmatrix}$$

$$= \begin{pmatrix} \cos^2\alpha + \mu'_{zz} \sin^2\alpha & \mu'_{yz} \sin\alpha & (1 - \mu'_{zz}) \sin\alpha \cos\alpha \\ -\mu'_{yz} \sin\alpha & \mu'_{yy} & \mu'_{yz} \cos\alpha \\ (1 - \mu'_{zz}) \sin\alpha \cos\alpha & -\mu'_{yz} \cos\alpha & \sin^2\alpha + \mu'_{zz} \cos^2\alpha \end{pmatrix} \quad (3.186)$$

If $\alpha=0$, equation (3.186) reduces to equation (3.181).

The fields are assumed to have the same spatial dependence as in section 3.1: $\sim e^{iqy} e^{ikz}$, where y and z are measured in the crystal frame. In the magnetization frame, the spatial dependence of the fields can be written as $\sim e^{iqy'} e^{ik \sin\alpha' z'} e^{ik \cos\alpha' z'}$. There is a spatial dependence on all three coordinate axes in the magnetization frame.

In the crystal frame, Maxwell's equations for the magnetic film have the same form as in section 3.1, see equations (3.5) to (3.8), except that there are nonzero h_x , e_y and e_z components. Written in component form, the equations for $\nabla \times \mathbf{e}$ and $\nabla \times \mathbf{h}$ are

$$\begin{pmatrix} qe_z - ke_y \\ ke_x \\ -qe_x \end{pmatrix} = \frac{\omega}{c} \mu \begin{pmatrix} h_x \\ h_y \\ h_z \end{pmatrix}, \quad (3.187)$$

$$\begin{pmatrix} qh_z - kh_y \\ kh_x \\ -qh_x \end{pmatrix} = \frac{4\pi\sigma}{ic} \begin{pmatrix} e_x \\ e_y \\ e_z \end{pmatrix}, \quad (3.188)$$

where μ is given by equation (3.186).

In the magnetization frame, the equations for $\nabla \times \mathbf{e}$ and $\nabla \times \mathbf{h}$ become

$$\begin{pmatrix} qe_{z'} - (k\cos\alpha)e_{y'} \\ (k\cos\alpha)e_{x'} - (k\sin\alpha)e_{z'} \\ (k\sin\alpha)e_{y'} - qe_{x'} \end{pmatrix} = \frac{\omega}{c} \mu' \begin{pmatrix} h_{x'} \\ h_{y'} \\ h_{z'} \end{pmatrix}, \quad (3.189)$$

$$\begin{pmatrix} qh_{z'} - (k\cos\alpha)h_{y'} \\ (k\cos\alpha)h_{x'} - (k\sin\alpha)h_{z'} \\ (k\sin\alpha)h_{y'} - qh_{x'} \end{pmatrix} = \frac{4\pi\sigma}{ic} \begin{pmatrix} e_{x'} \\ e_{y'} \\ e_{z'} \end{pmatrix}, \quad (3.190)$$

where μ' is given by equation (3.181).

To obtain the secular equation for the magnetic wavevector k , the permeability tensor obtained from the Landau-Lifshitz equations will be substituted into Maxwell's equations. We will use the magnetization coordinate system because of the simple form of the permeability tensor in this coordinate system. The electric field components $e_{x'}$, $e_{y'}$, $e_{z'}$ are expressed in terms of the magnetic field components, $h_{x'}$, $h_{y'}$, $h_{z'}$, using equation (3.190); these expressions, as well as the permeability tensor μ' , equation (3.181), are substituted into equation (3.189). This results in three homogeneous equations for $h_{x'}$, $h_{y'}$, $h_{z'}$. For a nontrivial solution, the determinant of the coefficients of these three equations must vanish. The following equation for k^2 is obtained:

$$P_1 k^4 + P_2 k^2 + P_3 = 0 \quad (3.191)$$

where

$$P_1 = \sin^2\alpha + \mu'_{zz} \cos^2\alpha \quad (3.192)$$

$$P_2 = q^2 \left[\sin^2 \alpha + \mu'_{zz} \cos^2 \alpha + \mu'_{yy} \right] - \frac{i}{\delta^2} \left[\mu'_{zz} + \mu'_{yy} \sin^2 \alpha + \left(\mu'_{yy} \mu'_{zz} + \mu'^2_{yz} \right) \cos^2 \alpha \right] \quad (3.193)$$

$$P_3 = q^4 \mu'_{zz} - \frac{iq^2}{\delta^2} \left[\mu'_{yy} + \mu'_{yy} \mu'_{zz} + \mu'^2_{yz} \right] - \frac{1}{\delta^2} \left[\mu'_{yy} \mu'_{zz} + \mu'^2_{yz} \right] \quad (3.194)$$

and μ'_{yy} , μ'_{zz} and μ'_{yz} are given by equations (3.182), (3.183) and (3.184), respectively. Because equation (3.191) is quadratic in k^2 , the spatial variation along z can be described by the superposition of four waves - two forward propagating waves and two backward propagating waves. We denote the wavevectors of the two forward propagating waves as $k^{(1)}$ and $k^{(3)}$, and the wavevectors of the backward propagating waves as $k^{(2)} = -k^{(1)}$ and $k^{(4)} = -k^{(3)}$.

For an in-plane magnetization ($\alpha = 0$), only one of the roots of equation (3.191) involves the permeability expressions:

$$k^2 = \frac{-q^2 \mu'_{yy} + \frac{i}{\delta^2} \left(\mu'_{yy} \mu'_{zz} + \mu'^2_{yz} \right)}{\mu'_{zz}} \quad (3.195)$$

The other root is nonmagnetic:

$$k^2 = -q^2 + \frac{i}{\delta^2}. \quad (3.196)$$

The second root corresponds to an excitation for which $h_y = h_z = 0$ and therefore does not couple to the magnetization. Therefore, for $\alpha = 0$, only a single forward propagating wave and a single backward propagating wave need be considered.

The boundary value problem is solved in the crystal coordinate system. In general the total h_y field can be written as

$$h_y = \sum_{i=1}^4 h_y^{(i)} = \sum_{i=1}^4 h_y^{(i)}(0) e^{ik^{(i)}z}, \quad (3.197)$$

where the phases of the fields have been chosen to be zero at $z = 0$. The amplitudes of the rf fields are proportional to the $h_y^{(i)}$ fields with the factors of proportionality determined by Maxwell's equations, equations (3.187) and (3.188), and the permeability μ , equation (3.186), determined from the Landau-Lifshitz equations. For the forward propagating waves:

$$\frac{h_z^{(i)}}{h_y^{(i)}} = \frac{\mu_{xy}\mu_{xz} + (iqk^{(i)}\delta^2 + \mu_{yz}) [i(q^2\delta^2 + (k^{(i)})^2\delta^2) + \mu_{xx}]}{-\mu_{xz}^2 + (iq^2\delta^2 + \mu_{zz}) [i(q^2\delta^2 + (k^{(i)})^2\delta^2) + \mu_{xx}]} = \zeta^{(i)} \quad (3.198)$$

$$\frac{h_x^{(i)}}{h_y^{(i)}} = \frac{-\mu_{xy}(iq^2\delta^2 + \mu_{zz}) - \mu_{xz}(iqk^{(i)}\delta^2 + \mu_{yz})}{-\mu_{xz}^2 + (iq^2\delta^2 + \mu_{zz}) [i(q^2\delta^2 + (k^{(i)})^2\delta^2) + \mu_{xx}]} = \rho^{(i)} \quad (3.199)$$

$$\frac{e_x^{(i)}}{h_y^{(i)}} = \frac{ic}{4\pi\sigma} (q\zeta^{(i)} - k^{(i)}) = \epsilon^{(i)} \quad (3.200)$$

$$\frac{e_y^{(i)}}{h_y^{(i)}} = \frac{ic}{4\pi\sigma} k^{(i)} \rho^{(i)} \quad (3.201)$$

$$\frac{e_z^{(i)}}{h_y^{(i)}} = \frac{ic}{4\pi\sigma} k^{(i)} \rho^{(i)} \quad (3.202)$$

$$\frac{b_x^{(i)}}{h_y^{(i)}} = -i(q^2\delta^2 + (k^{(i)})^2\delta^2) \rho^{(i)} \quad (3.203)$$

$$\frac{b_y^{(i)}}{h_y^{(i)}} = \frac{c}{\omega} k \epsilon^{(i)} \quad (3.204)$$

$$\frac{b_z^{(i)}}{h_y^{(i)}} = -\frac{c}{\omega} q \epsilon^{(i)} \quad (3.205)$$

$$\frac{4\pi m_x^{(i)}}{h_y^{(i)}} = i(-i + q^2\delta^2 + (k^{(i)})^2\delta^2) \rho^{(i)} = \xi_x^{(i)} \quad (3.206)$$

$$\frac{4\pi m_y^{(i)}}{h_y^{(i)}} = \frac{c}{\omega} k^{(i)} \epsilon^{(i)} - 1 = \xi_y^{(i)} \quad (3.207)$$

$$\frac{4\pi m_z^{(i)}}{h_y^{(i)}} = -\frac{c}{\omega} q \epsilon^{(i)} - \zeta^{(i)} = \xi_z^{(i)} \quad (3.208)$$

Similar expressions are obtained for the backward propagating waves.

The values $h_y^{(i)}$, apart from a scaling factor, are determined by the boundary conditions which the rf fields must satisfy at the front ($z = 0$) and rear ($z = d$) surfaces of the film. The boundary conditions used in section 3.1.1 consisted of the continuity of the tangential components of \mathbf{e} and \mathbf{h} at each interface (the electromagnetic boundary conditions), as well as the generalized exchange boundary conditions on \mathbf{m} . In the present calculation, we consider only the electromagnetic boundary conditions, since exchange has been neglected. The surface impedance was defined in section 3.1.1 to be the ratio of the x-component of the electric field to the y-component of the electric field at each surface, equations (3.67) and (3.68):

$$\frac{e_x(0)}{h_y(0)} = Z_{s1}^F = \frac{i\omega}{cq}; \quad (3.209)$$

for the front surface ($z = 0$) and

$$\frac{e_x(d)}{h_y(d)} = Z_{s1}^R = -\frac{i\omega}{cq}. \quad (3.210)$$

for the rear surface ($z = d$). The continuity of the surface impedances at each interface provides two equations. Because, for $\alpha \neq 0$, there are two magnetic waves travelling in each direction, we require an additional boundary condition equation at each interface. For this purpose, we introduce a second surface impedance defined as the ratio of the y-component of the electric field to the x-component of the magnetic field at each surface. Maxwell's equations in the vacuum surrounding the film can be written as, see equations (3.1) to (3.4):

$$\begin{pmatrix} qe_z - ke_y \\ ke_x \\ -qe_x \end{pmatrix} = \frac{\omega}{c} \begin{pmatrix} h_x \\ h_y \\ h_z \end{pmatrix}, \quad (3.211)$$

$$\begin{pmatrix} qh_z - kh_y \\ kh_x \\ -qh_x \end{pmatrix} = -\frac{\omega}{c} \begin{pmatrix} e_x \\ e_y \\ e_z \end{pmatrix}, \quad (3.212)$$

Using equations (3.212) and (3.14), we can write

$$\frac{e_y(0)}{h_x(0)} = Z_{s2}^F = \frac{icq}{\omega} \quad (3.213)$$

for the front surface ($z = 0$) and

$$\frac{e_y(d)}{h_x(d)} = Z_{s2}^R = -\frac{icq}{\omega} \quad (3.214)$$

for the rear surface ($z = d$).

The four equations resulting from the electromagnetic boundary conditions, equations (3.209), (3.210), (3.213) and (3.214), can be written as a set of four homogeneous equations for the four magnetic field amplitudes $h_y^{(i)}(0)$. Writing these equations explicitly in terms of the $h_y^{(i)}(0)$ components, we have

$$\sum_{i=1}^4 \left[\frac{e_x^{(i)}(0)}{h_y^{(i)}(0)} - Z_{s1}^F \right] h_y^{(i)}(0) = 0 \quad (3.215)$$

$$\sum_{i=1}^4 \left[\frac{e_y^{(i)}(0)}{h_y^{(i)}(0)} - Z_{s2}^F \frac{h_x^{(i)}(0)}{h_y^{(i)}(0)} \right] h_y^{(i)}(0) = 0 \quad (3.216)$$

$$\sum_{i=1}^4 \left[\left(\frac{e_x^{(i)}(d)}{h_y^{(i)}(d)} - Z_{s1}^R \right) e^{ik^{(i)}d} \right] h_y^{(i)}(0) = 0 \quad (3.217)$$

$$\sum_{i=1}^4 \left[\left(\frac{e_y^{(i)}(d)}{h_y^{(i)}(d)} - Z_{s2}^R \frac{h_x^{(i)}(0)}{h_y^{(i)}(0)} \right) e^{ik^{(i)}d} \right] h_y^{(i)}(0) = 0. \quad (3.218)$$

Equations (3.215) to (3.218) have a nontrivial solution only for frequencies, ω , such that the determinant of the coefficients of $h_y^{(i)}(0)$ vanishes. This condition determines the complex resonant frequencies of the magnetic slab. Having found a resonant frequency, ω , the corresponding amplitudes $h_y^{(i)}(0)$ are determined apart from a multiplicative constant. This constant is chosen such that the average energy stored in the normal mode of the system has the value $k_B T$, where k_B is Boltzmann's constant and T is the temperature.

A simplified expression for the surface mode frequency analogous to the ferromagnetic resonance condition can be formulated for ultrathin magnetic films as discussed in section 3.1.5.4.3. The dynamic demagnetizing field obtained from $b_z = 0$ can be written in the crystal coordinate system as $h_z = -4\pi m_z$. In the magnetization coordinate system, this gives

$$h_z' = -4\pi m_z' \cos^2 \alpha \quad (3.219)$$

Substituting equation (3.219) into the Landau-Lifshitz equations, equations (3.174) and (3.175), gives

$$-\left(\frac{i\omega}{\gamma}\right) 4\pi m_{y'} + (H_1' - H_2') 4\pi m_{z'} = 0, \quad (3.220)$$

$$(H_1') 4\pi m_{y'} + \left(\frac{i\omega}{\gamma}\right) 4\pi m_{z'} = 4\pi M_s h_{y'}. \quad (3.221)$$

where

$$H_1' = H \cos \alpha - [(4\pi M_s)_{\text{eff}}] \sin^2 \alpha + \frac{4K_u^{(2)}}{M_s} \sin^4 \alpha, \quad (3.222)$$

$$H_2' = -[(4\pi M_s)_{\text{eff}}] \cos^2 \alpha + \frac{12K_u^{(2)}}{M_s} \sin^2 \alpha \cos^2 \alpha, \quad (3.223)$$

and

$$(4\pi M_s)_{\text{eff}} = 4\pi M_s - \frac{2K_u^{(1)}}{M_s} \quad (3.224)$$

is the effective magnetization. Equation (3.224) is equivalent to equation (3.136) for $K_u^{(1)} = K_s/d$, where K_s is the effective surface spin pinning coefficient for both film surfaces and d is the magnetic film thickness. Magnetic damping has been neglected in equations (3.220) and (3.221) for simplicity. There is a resonance when the determinant of the coefficients of $m_{y'}$ and $m_{z'}$ in equations (3.220) and (3.221) vanishes. The simplified resonance condition is

$$\left(\frac{\omega}{\gamma}\right)^2 = H_1' (H_1' - H_2'). \quad (3.225)$$

3.2.2 The energy stored in a normal mode

The increase in energy associated with the excitation of a magnetic normal mode has several contributions:

(i) The energy density

$$E_M = \frac{h^2}{8\pi} = \frac{(h_x^* h_x + h_y^* h_y + h_z^* h_z)}{8\pi} \quad (3.226)$$

(ii) The energy of interaction between the magnetization and the applied magnetic field,

$$E_H = -\mathbf{H} \cdot \mathbf{M} = -\mathbf{H} \cdot \mathbf{M}' \quad (3.227)$$

To second order in $m_{y'}$ and $m_{z'}$, we have

$$E_H = -HM_s \cos\alpha + (H \sin\alpha) m_{z'} + \left(\frac{H \cos\alpha}{2M_s}\right) (m_{y'}^2 + m_{z'}^2) \quad (3.228)$$

(iii) The energy of interaction between the magnetization and the shape demagnetizing field,

$$E_{\text{demag}} = 2\pi M_s^2 \sin^2\alpha + (4\pi M_s \sin\alpha \cos\alpha) m_{z'} + \left(\frac{-4\pi M_s \sin^2\alpha}{2M_s}\right) (m_{y'}^2 + m_{z'}^2) \quad (3.229)$$

(iv) The first and second order uniaxial anisotropy energies,

$$\begin{aligned}
 E_u^{(1)} &= -K_u^{(1)} \left(\frac{m_z}{M_s} \right)^2 \\
 &= -K_u^{(1)} \sin^2 \alpha - \left(\frac{2K_u^{(1)}}{M_s} \sin \alpha \cos \alpha \right) m_{z'} \\
 &\quad + \left(\frac{2K_u^{(1)}}{2M_s} \sin^2 \alpha \right) (m_{y'}^2 + m_{z'}^2) - \left(\frac{2K_u^{(1)}}{2M_s} \cos^2 \alpha \right) m_{z'}^2, \quad (3.230)
 \end{aligned}$$

$$\begin{aligned}
 E_u^{(2)} &= -K_u^{(2)} \left(\frac{m_z}{M_s} \right)^4 \\
 &= -K_u^{(2)} \sin^4 \alpha - \left(\frac{4K_u^{(2)}}{M_s} \sin^3 \alpha \cos \alpha \right) m_{z'} \\
 &\quad + \left(\frac{4K_u^{(2)}}{2M_s} \sin^4 \alpha \right) (m_{y'}^2 + m_{z'}^2) - \left(\frac{12K_u^{(2)}}{2M_s} \sin^2 \alpha \cos^2 \alpha \right) m_{z'}^2, \quad (3.231)
 \end{aligned}$$

The static terms in (ii), (iii) and (iv) which are not proportional to the rf magnetization components are not related to the energy of a normal mode. The sum of the terms in (ii), (iii) and (iv) that are linear in $m_{z'}$ is just the equilibrium condition for the magnetization, equation (3.178); this sum must vanish in equilibrium. The terms in (ii), (iii) and (iv) that are quadratic in $m_{y'}$ and $m_{z'}$ can be combined into a single expression:

$$E = \frac{1}{2M_s} \left[H_1 m_{y'}^2 + (H_1 - H_2) m_{z'}^2 \right], \quad (2.232)$$

where H_1 and H_2 are given by equations (2.176) and (2.177). The energy stored in a normal mode is the sum of (3.226) and (2.232). The total energy must be integrated over the z -coordinate and averaged over time, as discussed in section 3.1.1.

3.2.3 The polarization distribution and the scattered light intensity

The electric polarization components induced in the magnetic film by an incident light wave have a complicated form when the magnetization is tilted with respect to the film's crystalline axes. The polarization $4\pi\mathbf{P}$ can be written as $4\pi\mathbf{P} = \Delta\epsilon \mathbf{E}$, where \mathbf{E} is the electric field of the incident light. The general form of the dielectric tensor $\Delta\epsilon$ is given by equation (3.90). In this equation M_1 , M_2 and M_3 are referred to the cubic axes of the sample. It will be assumed that the crystal coordinate axes in figure 3.11 are parallel with the cubic crystalline axes, i.e. $M_1 = m_x$, $M_2 = m_y$ and $M_3 = m_z$. Using equation (3.158),

$$m_x = M_s \cos\alpha - m_z' \sin\alpha$$

$$m_y = m_y' \tag{3.233}$$

$$m_z = M_s \sin\alpha + m_z' \cos\alpha.$$

Substituting equation (2.233) into equation (3.90), we obtain the form of $\Delta\epsilon$ in terms of the rf magnetization components in the magnetization coordinate system m_y' and m_z' ; only terms linear in m_y' and m_z' are kept. $\Delta\epsilon$ is then written in terms of the rf magnetization components in the crystal coordinate system m_x , m_y and m_z by using equation (3.157). This allows us to write the polarization distribution $4\pi\mathbf{P}$ in terms of m_x , m_y and m_z . For a p-polarized incident optical wave having only E_y and E_z components, we have

$$\begin{aligned}
4\pi P_x = & \left[-KE_y \sin\alpha \cos\alpha - 2G_{44}M_s E_z \sin\alpha(\cos^2\alpha - \sin^2\alpha) \right] m_x \\
& + \left[2G_{44}M_s E_y \cos\alpha - KE_z \right] m_y \\
& + \left[KE_y \cos^2\alpha + 2G_{44}M_s E_z \cos\alpha(\cos^2\alpha - \sin^2\alpha) \right] m_z \quad (3.234)
\end{aligned}$$

$$\begin{aligned}
4\pi P_y = & \left[KE_z \sin^2\alpha \right] m_x + \left[2G_{44}M_s E_z \sin\alpha \right] m_y \\
& + \left[-KE_z \sin\alpha \cos\alpha \right] m_z \quad (3.235)
\end{aligned}$$

$$\begin{aligned}
4\pi P_z = & \left[-KE_y \sin^2\alpha - 2(G_{11} - G_{12})M_s E_z \sin^2\alpha \cos\alpha \right] m_x \\
& + \left[2G_{44}M_s E_y \sin\alpha \right] m_y \\
& + \left[KE_y \sin\alpha \cos\alpha + 2(G_{11} - G_{12})M_s E_z \sin\alpha \cos^2\alpha \right] m_z \quad (3.236)
\end{aligned}$$

Equations (3.234) to (3.236) reduce to equation (3.92) for $\alpha=0$, with $4\pi P_y = 4\pi P_z = 0$.

For a s-polarized incident optical wave having only a E_x component, we have

$$\begin{aligned}
4\pi P_x = & \left[2(G_{11} - G_{12})M_s E_x \sin^2\alpha \cos\alpha \right] m_x \\
& + \left[-2(G_{11} - G_{12})M_s E_x \sin\alpha \cos^2\alpha \right] m_z \quad (3.237)
\end{aligned}$$

$$\begin{aligned}
4\pi P_y = & \left[KE_x \sin\alpha \cos\alpha \right] m_x + \left[2G_{44}M_s E_x \cos\alpha \right] m_y \\
& + \left[-KE_x \cos^2\alpha \right] m_z \quad (3.238)
\end{aligned}$$

$$\begin{aligned}
4\pi P_z = & \left[-2G_{44}M_s E_x \sin\alpha(\cos^2\alpha - \sin^2\alpha) \right] m_x + \left[KE_x \right] m_y \\
& + \left[2G_{44}M_s E_x \cos\alpha(\cos^2\alpha - \sin^2\alpha) \right] m_z \quad (3.239)
\end{aligned}$$

Equations (3.237) to (3.239) reduce to equations (3.93) and (3.94) for $\alpha = 0$, with $4\pi P_x =$

0.

The form of the incident optical waves inside the magnetic film, equations (3.101), (3.103) and (3.104), and the optical Green's functions, equations (3.125), (3.128) and (3.132), is unaffected by the tilting of the magnetization and these equations can be used directly in this calculation. The amplitude of light scattered from a magnetic normal mode is calculated as an integral over the thickness of the magnetic film of the product of the appropriate optical Green's functions with the appropriate dipole distribution as calculated from equations (3.234) to (3.239). The intensity of the scattered radiation is obtained from the product of the emitted radiation amplitude with its complex conjugate.

3.2.4 Discussion

The concept of the effective magnetization, $(4\pi M_S)_{\text{eff}}$, was introduced in terms of a surface spin pinning coefficient K_S , see equation (3.136), and was expressed in terms of the first order uniaxial anisotropy coefficient $K_u^{(1)}$, see equation (3.224). $(4\pi M_S)_{\text{eff}}$ is the difference between the saturation magnetization and the anisotropy field

$$(4\pi M_S)_{\text{eff}} = 4\pi M_S - \frac{2K_u^{(1)}}{M_S} . \quad (3.240)$$

For $(4\pi M_S)_{\text{eff}} > 0$, M_S lies in the sample plane for all values of the magnetic field applied in the sample plane; this situation was discussed in section 3.1. For $(4\pi M_S)_{\text{eff}} < 0$, M_S is tilted out of the sample plane for low values of the applied magnetic field; in zero applied field, M_S lies along the sample normal and as the applied field is increased M_S is dragged down into the sample plane.

In figure 3.12 is shown a calculation of the surface mode frequency of a 10Å thick magnetic film as a function of the applied magnetic field for various values of the uniaxial

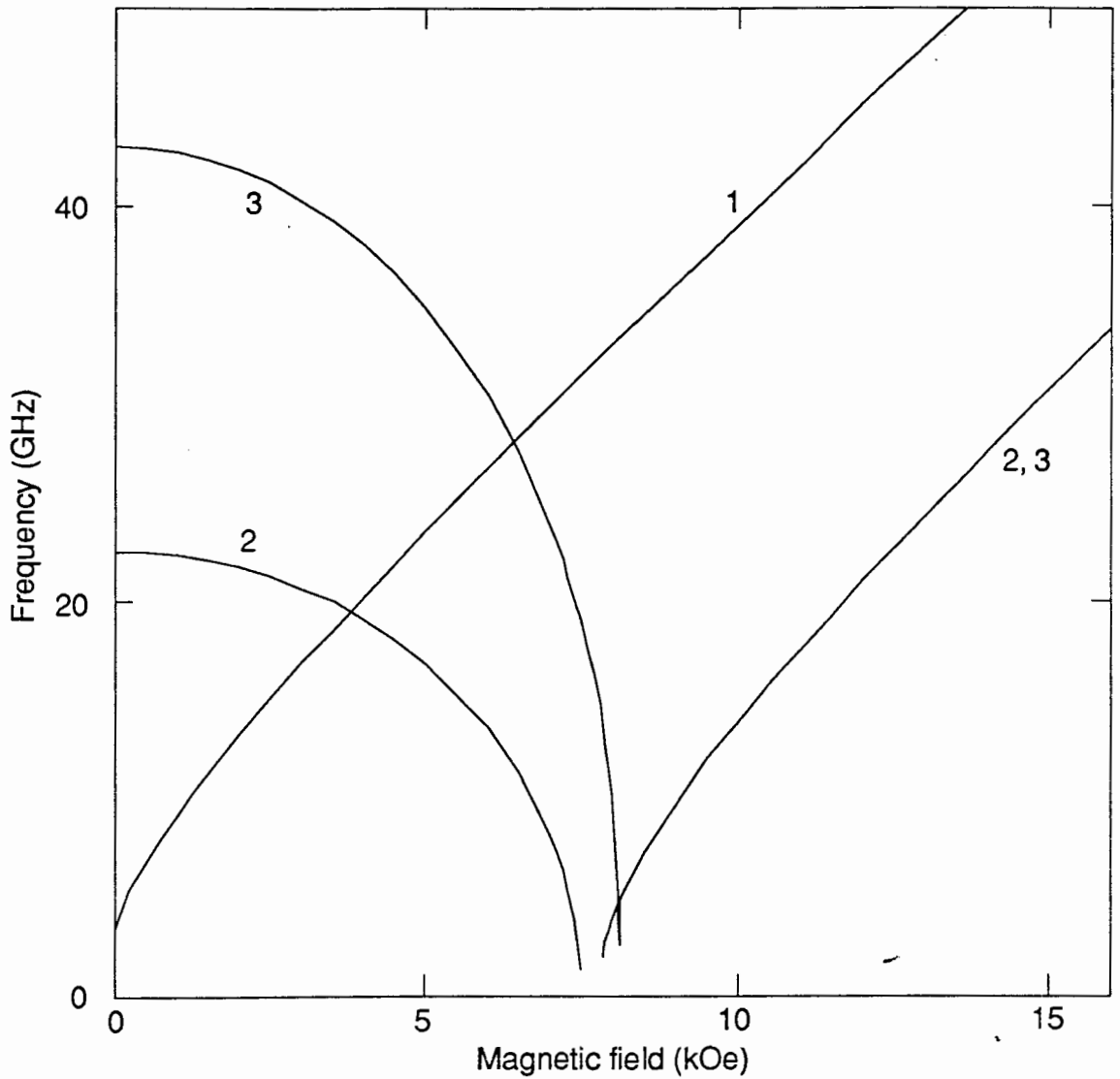


Figure 3.12

Calculated surface mode frequency as a function of applied magnetic field for a 10\AA thick iron film. For all the curves, $g = 2.09$. For curve 1, $(4\pi M_s)_{\text{eff}} = +7.6\text{ kG}$ and $K_u^{(2)} = 0$. For curve 2, $(4\pi M_s)_{\text{eff}} = -7.6\text{ kG}$ and $K_u^{(2)} = 0$. For curve 3, $(4\pi M_s)_{\text{eff}} = -7.6\text{ kG}$ and $4K_u^{(2)}/M_s = +7.0\text{ kOe}$.

anisotropy constants $K_u^{(1)}$ and $K_u^{(2)}$. For curve 1, the first order uniaxial anisotropy field, $2K_u^{(1)}/M_s$, is smaller than the shape demagnetizing field, $4\pi M_s$, by 7.6 kOe, giving $(4\pi M_s)_{\text{eff}} = +7.6$ kG. For zero applied field the frequency has a small value and the frequency increases monotonically with field. This curve is similar to those in figure 3.9. If $2K_u^{(1)}/M_s$ is increased by 15.2 kOe, $(4\pi M_s)_{\text{eff}}$ is changed from +7.6 kG to -7.6 kG and the frequency versus field behavior follows curve 2 in figure 3.12. Curve 2 consists of two branches: a high field branch and a low field branch. The crossover field H_c between the two branches is given by

$$H_c = - (4\pi M_s)_{\text{eff}}. \quad (3.240)$$

Equation (3.240) is obtained from the simplified resonance condition, equation (3.225), with the surface mode frequency equal to zero. For curve 2, $H_c = 7.6$ kOe. Curve 2 does not extend to zero frequency for $H = H_c$ because the rf magnetization components become very large near this field value; the linear approximation used in the Landau-Lifshitz equation of motion for the magnetization, see section 3.1.1, is not valid and the resonant mode frequencies cannot be calculated using the linearized theory. For the high field branch ($H > H_c$), the magnetization lies in the sample plane and the curve has the same shape as curve 1, but it is shifted up in field by H_c . For the low field branch ($H < H_c$), the magnetization is tilted away from the sample plane. For $K_u^{(2)} = 0$, as in curve 2, and $0 < H < H_c$, equation (3.241) for the equilibrium direction of the magnetization can be written as

$$\cos\alpha = - \frac{H}{(4\pi M_s)_{\text{eff}}}. \quad (3.241)$$

Using equation (3.241), the simplified resonance condition, equation (3.225), can be written as

$$\left(\frac{\omega}{\gamma}\right)^2 + H^2 = [(4\pi M_s)_{\text{eff}}]^2 \quad (3.242)$$

for $0 < H < H_c$. Equation (3.242) is of the form $x^2 + y^2 = C^2$, where C is a constant. This is the equation of a circle. For $H = 0$, $\left(\frac{\omega}{\gamma}\right)^2 = [(4\pi M_s)_{\text{eff}}]^2$, and the frequency decreases monotonically with field down to zero for $H = -(4\pi M_s)_{\text{eff}} = H_c$.

Curve 2 includes the effect of the first order uniaxial anisotropy only. If the effect of the second order uniaxial anisotropy is also included, the high field branch is unaffected since there is no torque on the magnetization in equation (3.170) with $\alpha = 0$, but the low field branch is modified. Curve 3 was calculated with the same value of $K_u^{(1)}$ as curve 2, but with a second order uniaxial anisotropy field, $4K_u^{(2)}/M_s = +7$ kOe. The positive value of $K_u^{(2)}$ shifts the frequency values on the low field branch to higher values.

The tilt angle α calculated as a function of the applied field is shown in figure 3.13, for the same magnetic parameters as curves 2 and 3 in figure 3.12. Curve 2 was calculated for $K_u^{(2)} = 0$, and curve 3 was calculated for $4K_u^{(2)}/M_s = +7$ kOe. In both cases, α is equal to 90° for zero applied field, and it decreases to zero for fields large compared with H_c . For a given field value in the range $0 < H < H_c$, the value of α is larger for curve 3 than it is for curve 2. The positive value of $K_u^{(2)}$ increases the tilt of the magnetization out of the sample plane. Curve 2 does not extend to zero tilt angle for $H = H_c$ because the rf magnetization components become very large near this field value; the linear approximation used in the Landau-Lifshitz equation of motion for the magnetization is not valid, as discussed for figure 3.12, and the resonant mode frequencies cannot be calculated using the linearized theory.

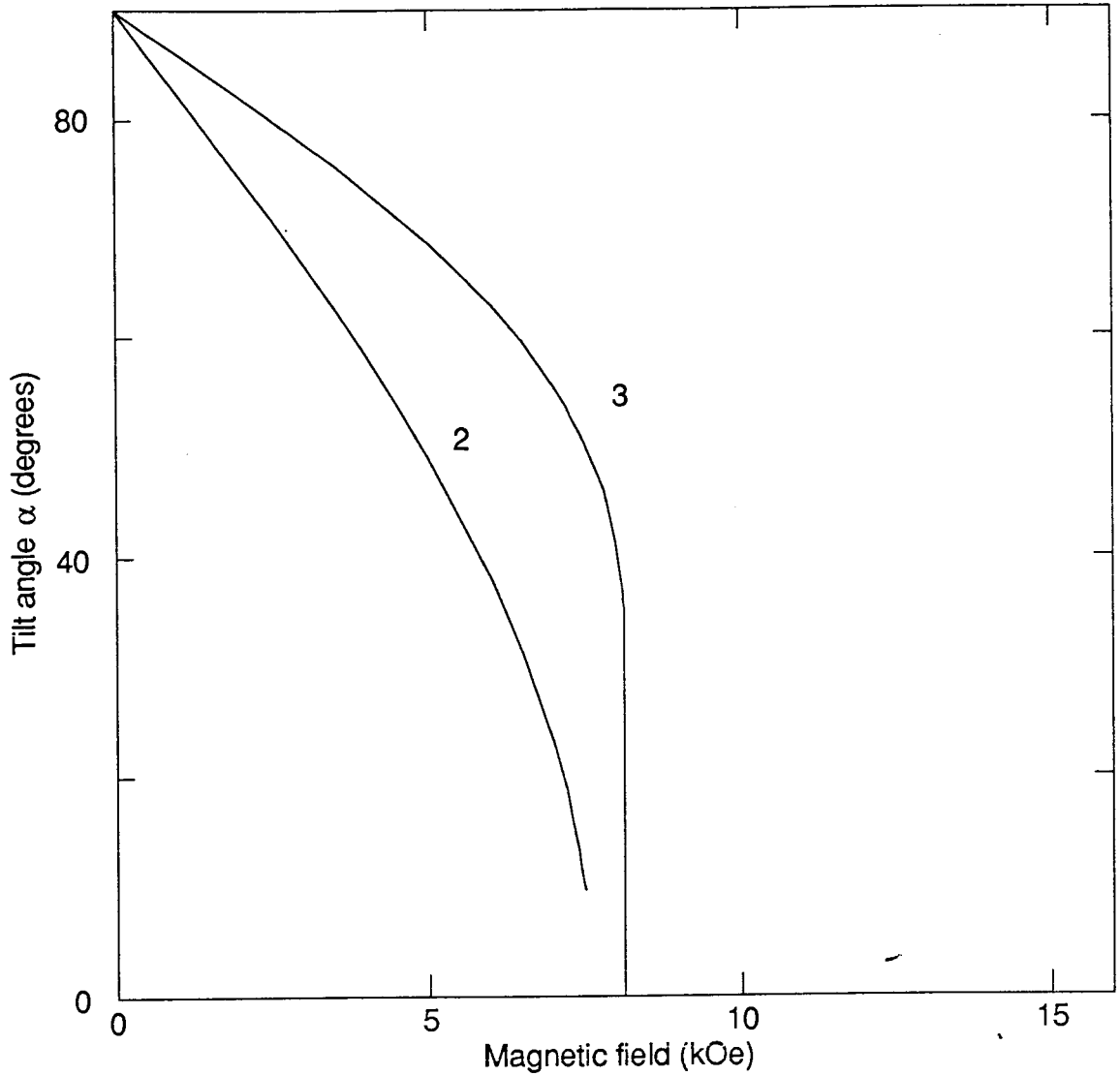


Figure 3.13

Calculated tilt angle α as a function of applied magnetic field for a 10\AA thick film. The magnetic parameters for curves 2 and 3 are the same as for curves 2 and 3 of figure 3.12.

In figure 3.14, calculated curves of the scattered intensity as a function of the applied field are shown for the same magnetic parameters as in figure 3.12. Curve 1 corresponds to $(4\pi M_s)_{\text{eff}} = +7.6$ kG; it has its maximum value at $H = 0$ and is similar to the curves in figure 3.10. For curves 2 and 3, with $(4\pi M_s)_{\text{eff}} = -7.6$ kG, both branches of the curves have a maximum scattered intensity for $H = H_c = -(4\pi M_s)_{\text{eff}}$. At this applied field value, the effective field acting on the spins is equal to zero and this gives rise to large rf magnetization components and scattered intensity, as discussed in section 3.1.5.3.2. The presence of these large rf magnetization components near $H = H_c$ prevented the calculation of the resonant modes using the linearized Landau-Lifshitz equation, as discussed above for figures 3.12 and 3.13. The most interesting feature of curves 2 and 3 is the difference in scattered intensity between the low field and the high field branches. For equal positive and negative field increments away from $H = H_c$ the scattered intensity is considerably reduced on the low field branch compared with that on the high field branch. This difference between the scattered intensity for the two branches of curve 2 is further increased for the two branches of curve 3 with the addition of a positive second order uniaxial anisotropy term.

3.3 Application of the calculation to the experiment

In the light scattering calculation it is assumed that the light waves are plane waves of infinite extent. In a real BLS experiment the light wave is generated by a laser. The output beam from the laser has finite extent transverse to the propagation direction and spreads in the transverse direction as the beam propagates. The laser beam has a Gaussian intensity profile along r transverse to the propagation direction:

$$I(r) = I_0 e^{-2r^2/\rho^2} \quad (3.243)$$

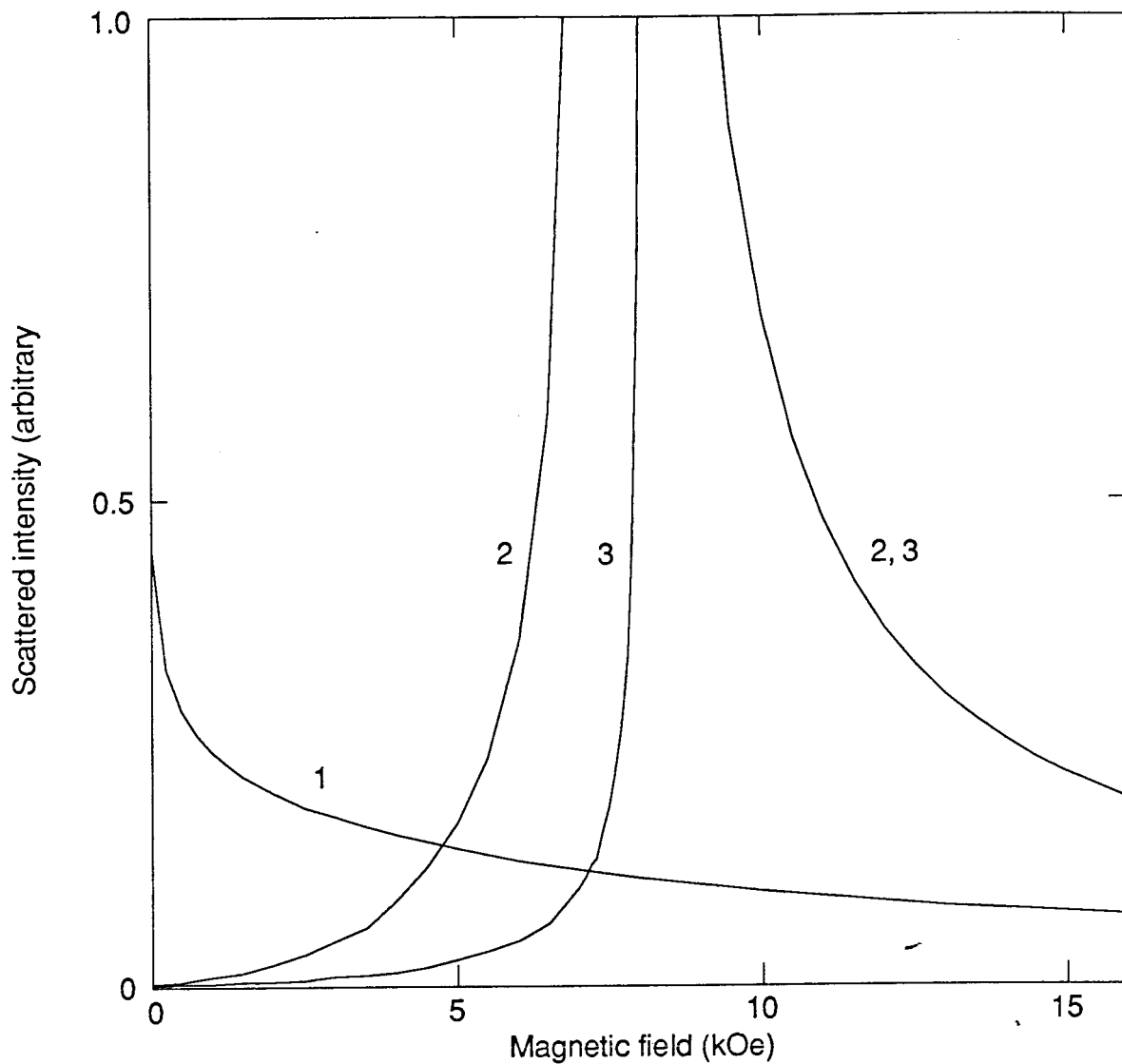


Figure 3.14

Calculated scattered intensity as a function of applied magnetic field for a 10Å thick iron film. The magnetic parameters for curves 2 and 3 are the same as for curves 2 and 3 of figure 3.12.

where I_0 is the intensity on the beam axis and ρ is the distance from the beam axis at which the electric field amplitude is equal to $1/e$ of its on-axis value. These waves are called Gaussian beams and their propagation is described by Gaussian beam optics (Yariv and Yeh, 1984). Gaussian beams can be focussed to a minimum spot size ρ_0 known as the beam waist. For our experiment, the laser light is focussed to a spot of radius $\rho_0 \sim 5\mu$. At the beam waist, the wavefronts are perpendicular to the propagation direction over the entire transverse profile of the beam. In this sense, the focussed Gaussian beam is like a plane wave. However, unlike a plane wave, the beam has very limited transverse extent and a Gaussian transverse intensity profile. If the Gaussian transverse intensity profile is approximated as constant over a diameter ρ_0 and zero elsewhere, then the ratio of the beam area to the sample size, $\rho_0^2 / 1\text{cm}^2 \sim 10^{-6}$ when multiplied by the calculated intensity, will account for the finite extent of the beam.

CHAPTER FOUR

ULTRATHIN IRON SINGLE FILMS AND NICKEL/IRON BILAYER FILMS GROWN ON SILVER

4.1 Iron on Silver

4.1.1 Introduction

At room temperature, the surface net spacing of fcc Ag(001) is matched to within 0.8% with that of bcc Fe(001) when the nets are rotated by 45° relative to one another.

Following the rotation, the net spacings are 2.8839\AA and 2.8665\AA , respectively. This match is considered to be very good for epitaxial growth. The growth of Fe on Ag(001) is shown schematically in figure 4.1. The solid balls correspond to atoms in the outermost layer of the silver substrate and the shaded balls correspond to atoms in the first monolayer of iron. The thickness of one monolayer of bcc iron is 1.43\AA . Epitaxial crystals of iron can be grown on Ag(001) without intermixing of the iron and silver atoms (Heinrich et al., 1988a). Either Ag(001) or Au(001) films can be used as a coverlayer for the Fe films because both Ag and Au grow layer-by-layer on iron without intermixing.

Spin-and angle-resolved photoemission experiments performed on epitaxial Fe films on Ag(001) (Jonker et al., 1986) suggested the presence of a large uniaxial anisotropy with the easy axis along the sample normal. This suggestion was reinforced by the theoretical predictions of Gay and Richter (Gay and Richter, 1986). The existence of this anisotropy for Fe films on Ag(001) was established experimentally by the ferromagnetic resonance (FMR) experiments of Heinrich et al. (Heinrich et al., 1987a). Concurrent BLS experiments on these samples are described in section 4.1.3. Modified spin-polarized photoemission experiments were used to directly measure the remanent state magnetized perpendicular to the sample surface (Stampanoni et al., 1987). They found perpendicular magnetization only for specimens 3.5 ML thick that had been cooled to temperatures less

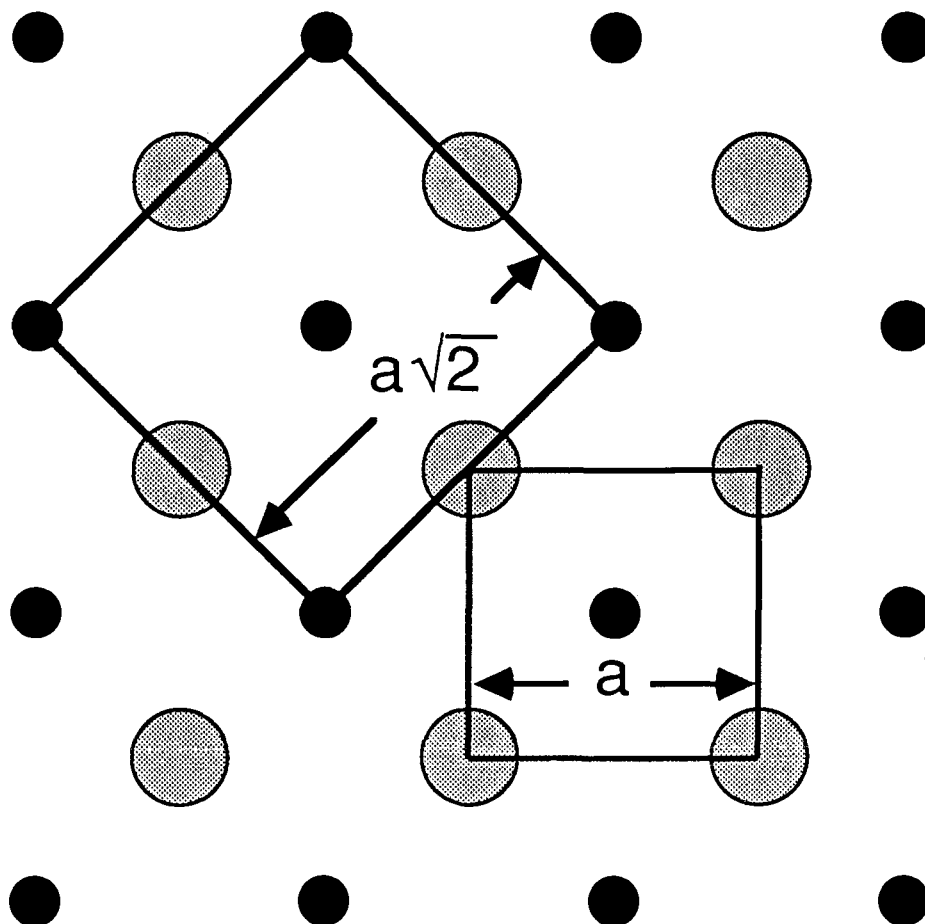


Figure 4.1

The growth of bcc Fe on fcc Ag(001). The solid balls correspond to atoms in the outermost layer of the silver substrate and the shaded balls correspond to atoms in the first monolayer of iron. The surface nets are very closely matched following a 45° rotation of the nets relative to one another.

than 30K. Ag/Fe/Ag multilayers have been studied by conversion electron Mossbauer spectroscopy (CEMS) (Volkening et al., 1988), and by SQUID magnetometry (Krebs et al., 1988). Their work showed that the magnetization was partly oriented along the sample normal for samples thinner than 3 ML that had been cooled to temperatures less than 15K.

Further studies were carried out on thin Fe films grown on Ag(001) and covered by either Au or Ag using FMR, BLS and reflection high energy electron diffraction (RHEED) (Heinrich et al., 1988a). The results of the BLS experiments are described in section 4.1.3. Regular oscillations in the RHEED specular spot intensity indicate a layer-by-layer growth of the films (Purcell et al., 1987). For Fe films grown on vicinal Ag(001) surfaces, regular RHEED oscillations were observed only after 3 ML of Fe had been deposited. Vicinal crystals have a considerable misalignment ($\sim 2^\circ$) between the crystal face and the [001] direction. Therefore, these substrates exhibited numerous atomic steps and short terraces ($\sim 40\text{\AA}$). For films thinner than 3 ML, the large vertical mismatch between the Fe and Ag lattices along the step edges resulted in uneven surface coverage of the Fe atoms. In contrast, Fe(001) whisker substrates have extremely large terraces ($\geq 3000\text{\AA}$) and a correspondingly low density of atomic steps. Fe films grown on Ag deposited on Fe(001) whisker surfaces exhibited layer-by-layer growth during the entire deposition at room temperature, including the first monolayer. BLS studies of a 3 ML thick Fe film grown on a Ag-covered whisker, described in section 4.1.3, showed that this specimen exhibited a substantial increase in the uniaxial anisotropy for this sample compared with Fe films of similar thickness grown on bulk Ag(001) crystals. This increase was sufficient to orient the magnetization along the sample normal in zero applied field at room temperature; the effective magnetization was found to be negative, $(4\pi M_s)_{\text{eff}} = -2.4\text{kG}$. The 3 ML thick Fe films grown on bulk Ag(001) crystals and covered with Au did not exhibit negative values of $(4\pi M_s)_{\text{eff}}$, and those films covered with Ag exhibited a negative $(4\pi M_s)_{\text{eff}} < 0$ only for reduced temperatures, e.g. $(4\pi M_s)_{\text{eff}} = -3.5\text{kG}$ at 77K.

Very recently, ultrathin Fe films grown on Ag(001) have been studied by means of FMR in the ultrahigh vacuum system (Urquhart et al., 1988). A significant increase in the overall uniaxial anisotropy was obtained for uncovered Fe films on Ag(001). An uncovered 7.6 ML thick Fe film exhibited a uniaxial anisotropy coefficient $K_s \sim 1.7$ erg/cm². A coverlayer of Ag(001) subsequently deposited on the Fe film decreased the overall surface anisotropy coefficient to $K_s \sim 1.3$ erg/cm².

Recent BLS measurements on iron whisker crystals (Dutcher et al., 1988b) and FMR measurements on bulk iron crystals (Purcell et al., 1988b) have determined the spin pinning coefficients for well-characterized interfaces of Au/Fe and Ag/Fe. These values for the bulk Fe crystals are in remarkable agreement with the values of K_s for ultrathin Fe films, indicating that the surface pinning is a consequence of the abrupt change in symmetry at the surface as proposed by Gay and Richter (Gay and Richter, 1986).

4.1.2 Sample preparation

The bcc Fe on Ag(001) samples discussed in this and the following section were grown in our laboratory by Dr. B. Heinrich and K.B. Urquhart. There were two basic sample geometries for the Fe/Ag films, as shown in figure 4.2. Sample geometry (a) consisted of an ultrathin Fe film grown on a bulk Ag(001) crystal and covered with either Au or Ag. Sample geometry (b) consisted of an ultrathin Fe film grown on a thin Ag film that had been deposited on a Fe(001) whisker; the iron film was covered with either Au or Ag. All of the samples of geometry (a) studied with BLS were grown on vicinal Ag(001) crystals. The Ag film which separated the ultrathin Fe film and the Fe(001) whisker in geometry (b) was probably thick enough (10 ML~15 Å) to prevent exchange coupling of the two magnetic films. The use of Fe(001) whiskers with atomically flat surfaces as substrates permitted the growth of ultrathin Fe films with a low density of atomic steps as compared with the bulk Ag(001) substrates. The magnetic properties of the Fe films grown on Ag-

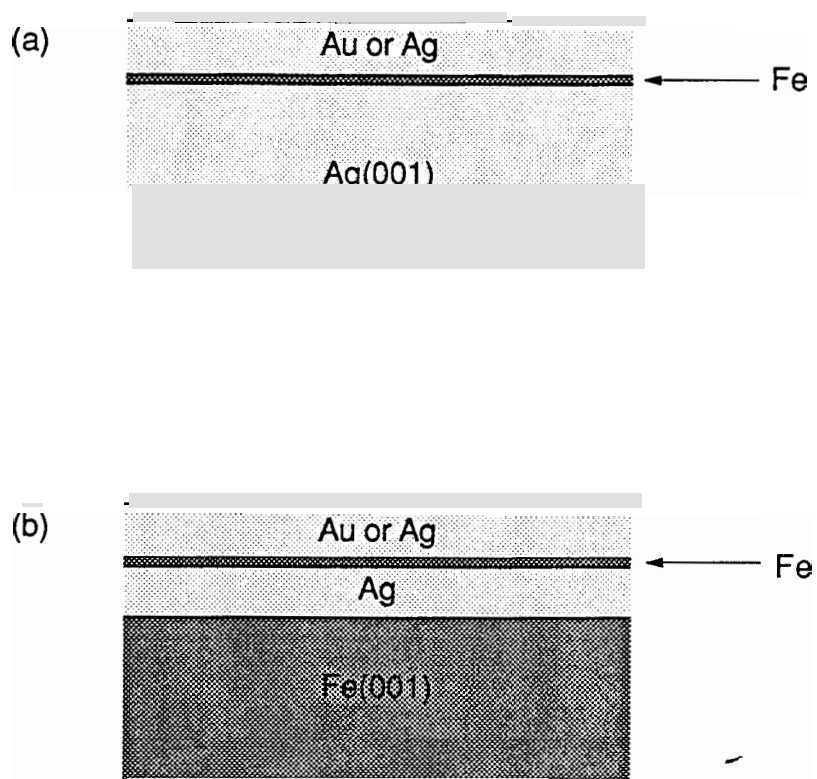


Figure 4.2

Fe on Ag(001) sample geometry:

(a) Au (or Ag) on Fe on bulk Ag(001) crystal.

(b) Au (or Ag) on Fe on Ag(001) on Fe(001) whisker.

covered Fe(001) whiskers were studied only with BLS. The signal in a ferromagnetic resonance (FMR) absorption experiment is proportional to the total sample area. Because whisker widths are very small ($\sim 300\mu$), special techniques would have been necessary to perform FMR experiments on these samples. The sample size was not a restriction for the BLS experiment, in which scattered light is collected from an area which is only $\sim 10\mu$ in diameter. A list of the various samples studied with BLS is given in table 4.1.

The bulk Ag crystals were prepared for the growth of iron films by mechanically polishing the (001) surface of the Ag crystal and then electropolishing the surface with a cyanide-free solution. This produced a strain-free surface which was smooth except for the presence of a slight "orange peel" roughness. The Ag crystals were placed in a Physical Electronics Φ -400 molecular beam epitaxy (MBE) machine having a base pressure $\leq 10^{-10}$ Torr and sputter etched using a 2 keV, 25mA Ar^+ beam for 30 minutes at room temperature. The crystals were then annealed in ultrahigh vacuum at 400°C for 40 minutes to remove the faceting of the crystal surface caused by the sputtering process. The Ag(001) crystal surfaces were clean to within the detection limits of Auger electron spectroscopy (AES) and x-ray photoelectron spectroscopy (XPS). The reflection high energy electron diffraction (RHEED) patterns obtained for the annealed surfaces were as good as the best patterns obtained for crystals with mosaic spreads. The preparation of the Fe(001) whisker surfaces has been described previously (Heinrich et al., 1988a) and is also described in detail in section 6.2 of this thesis.

During deposition, the vacuum in the growth chamber of the MBE machine was observed to be $\leq 3 \times 10^{-10}$ Torr. The deposition rate was approximately 1 ML/minute for both Fe and Ag. The deposition rates were monitored using a temperature-stabilized Mathis quartz crystal monitor, RHEED specular spot intensity oscillations and Auger peak intensities.

Table 4.1

The Fe on Ag(001) samples studied by BLS. All of the bulk Ag(001) substrates were vicinal crystals.

Sample	Composition
4.1	21ML Au / 17ML Fe / Ag(001)
4.2	27ML Au / 4.9ML Fe / Ag(001)
4.3	21ML Au / 2.8ML Fe / Ag(001)
4.4	21ML Au / 2.9ML Fe / Ag(001)
4.5	21ML Au / 3.0ML Fe / Ag(001)
4.6	30ML Ag / 3.4ML Fe / Ag(001)
4.7	30ML Ag / 2.0ML Fe / Ag(001)
4.8	15ML Au / 3.0ML Fe / 10ML Ag / Fe(001) whisker
4.9	30ML Ag / 3.0ML Fe / 12ML Ag / Fe(001) whisker

4.1.3 Brillouin light scattering results and discussion

Figures 4.3 to 4.12 contain representative BLS spectra of counts versus frequency shift, and plots of the measured surface mode frequencies as a function of the applied magnetic field for each of the samples listed in table 4.1. Also included on each frequency versus field plot is a solid curve calculated using the theory presented in Chapter Three. The effective magnetization $(4\pi M_s)_{\text{eff}}$, the g-factor and the in-plane magnetocrystalline anisotropy constant K_1 were used as fitting parameters in the theory. The results are listed in table 4.2. The effective magnetization may be written as, see equation (3.136),

$$(4\pi M_s)_{\text{eff}} = 4\pi M_s - \frac{2K_s}{M_s d}, \quad (4.1)$$

where K_s is the uniaxial anisotropy constant specified by the uniaxial anisotropy energy

$$E_s = -K_s \left(\frac{m_z}{M_s} \right)^2. \quad (4.2)$$

and m_z is the component of the magnetization along the sample normal. The value of K_s for ultrathin films is given by the sum of K_z^F and K_z^R of equations (3.71) and (3.72).

Column 7 of table 4.2 contains the values of K_s calculated for $4\pi M_s = 21.55$ kG. Recent SQUID measurements of the saturation magnetization of sample 4.5 have been made by Drs. J.J. Krebs and G.A. Prinz at the Naval Research Laboratory in Washington, D.C., U.S.A. They have shown that $4\pi M_s \sim 14$ kG for this 3 ML thick iron film. Column 8 of table 4.2 contains the values of K_s for samples 4.3, 4.4, 4.5, and 4.8 using $4\pi M_s = 14$ kG. Using equation (4.1), the expression for K_s can be written as

$$K_s = 2\pi d M_s^2 \left[1 - \frac{(4\pi M_s)_{\text{eff}}}{4\pi M_s} \right]. \quad (4.3)$$

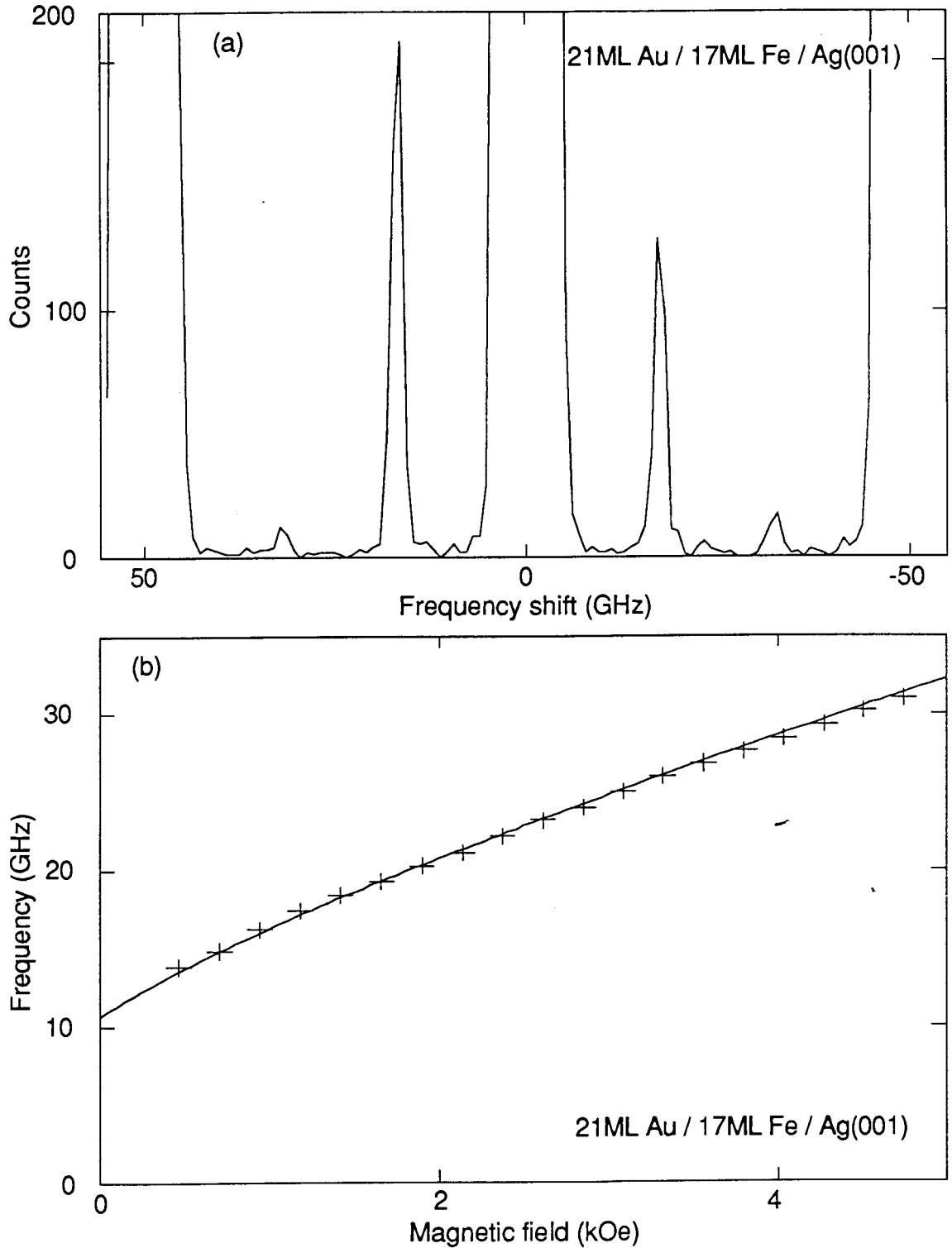


Figure 4.3

- (a) BLS spectrum for sample 4.1 for a field of $H = 0.91$ kOe, a laser power of 35 mW and a counting time for each of the 128 data points of 4.000 s.
- (b) Magnetic field dependence of the surface mode frequency for sample 4.1. The crosses are measured data points. The solid curves have been calculated using the theory of Chapter Three and the parameters listed in table 4.2.

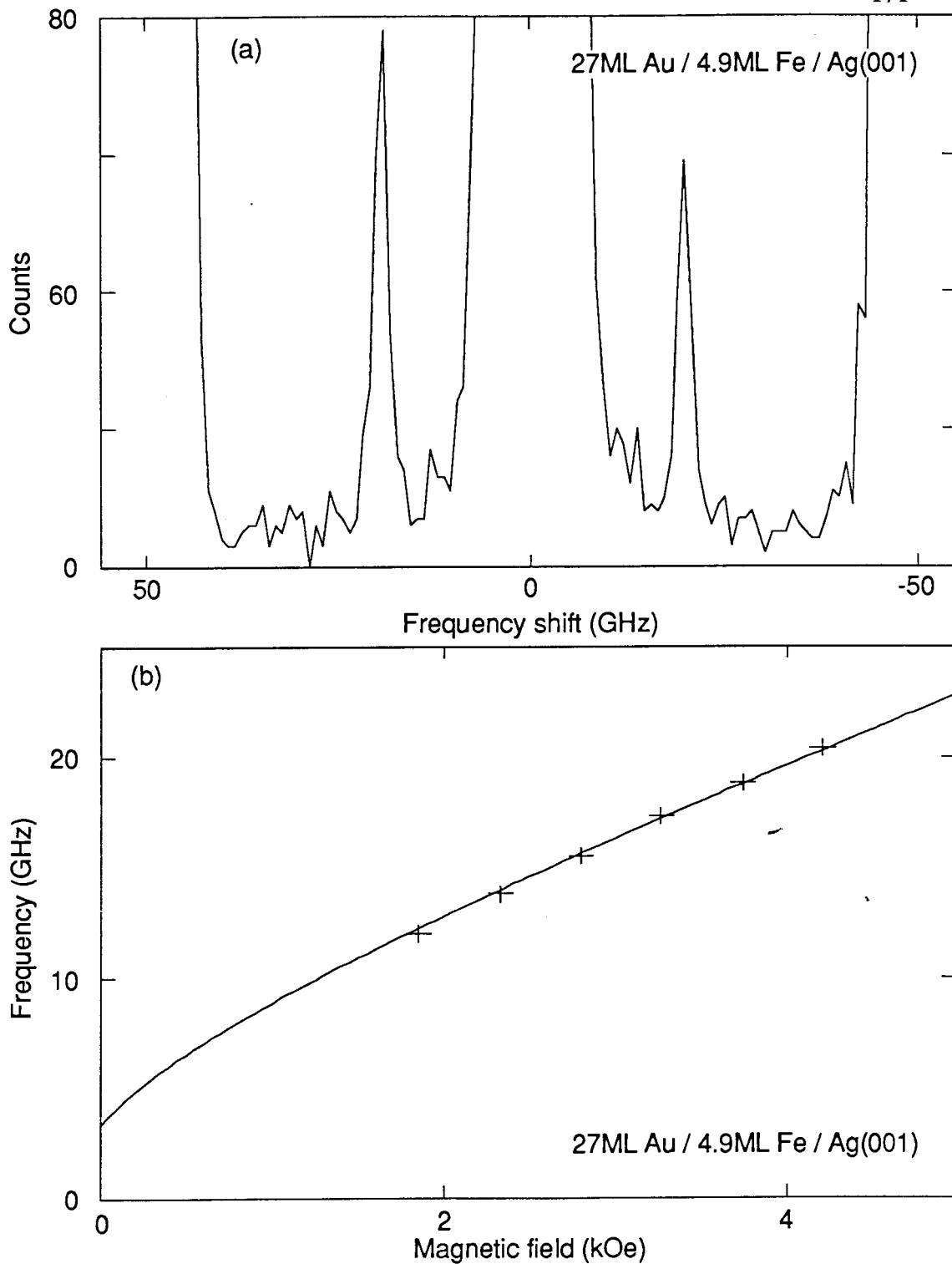


Figure 4.4

- (a) BLS spectrum for sample 4.2 for a field of $H = 4.21$ kOe, a laser power of 35 mW and a counting time for each of the 128 data points of 4.000 s.
- (b) Magnetic field dependence of the surface mode frequency for sample 4.2. The crosses are measured data points. The solid curve has been calculated using the theory of Chapter Three and the parameters listed in table 4.2.

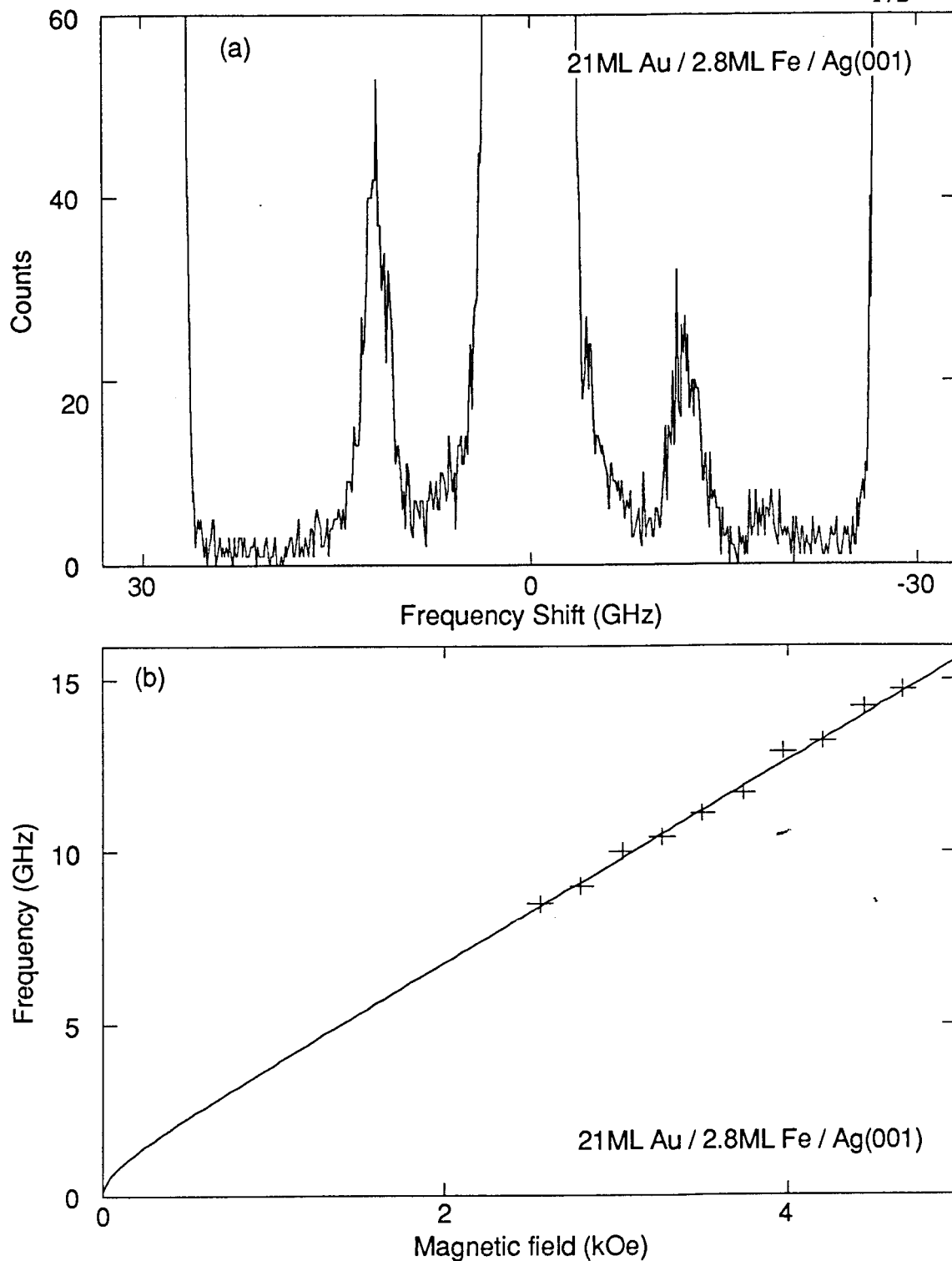


Figure 4.5

- (a) BLS spectrum for sample 4.3 for a field of $H = 3.74$ kOe, a laser power of 105 mW and a counting time for each of the 512 data points of 2.164 s.
- (b) Magnetic field dependence of the surface mode frequency for sample 4.3. The crosses are measured data points. The solid curve has been calculated using the theory of Chapter Three and the parameters listed in table 4.2.

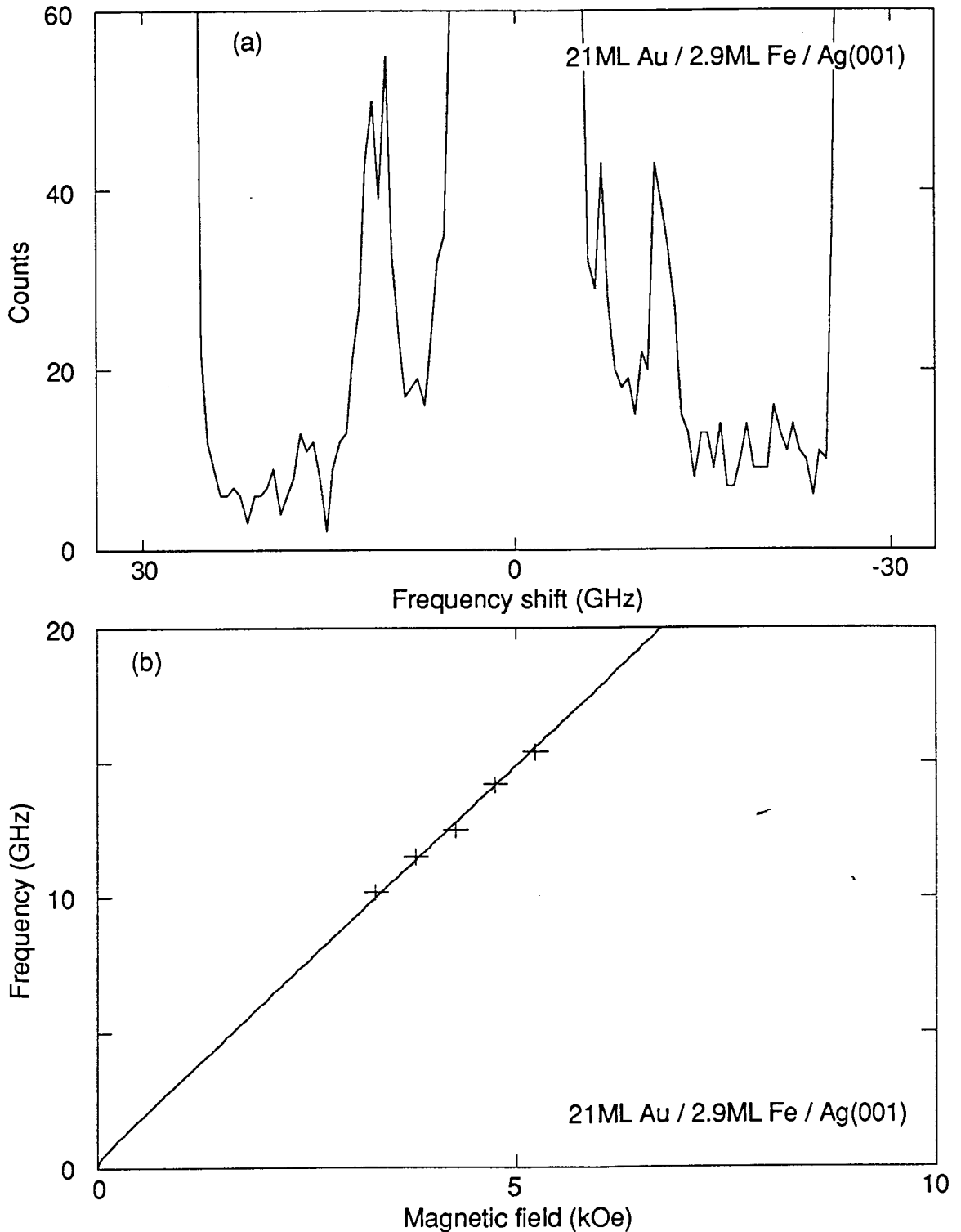


Figure 4.6

- (a) BLS spectrum for sample 4.4 for a field of $H = 3.80$ kOe, a laser power of 105 mW and a counting time for each of the 128 data points of 4.000 s.
- (b) Magnetic field dependence of the surface mode frequency for sample 4.4. The crosses are measured data points. The solid curve has been calculated using the theory of Chapter Three and the parameters listed in table 4.2.

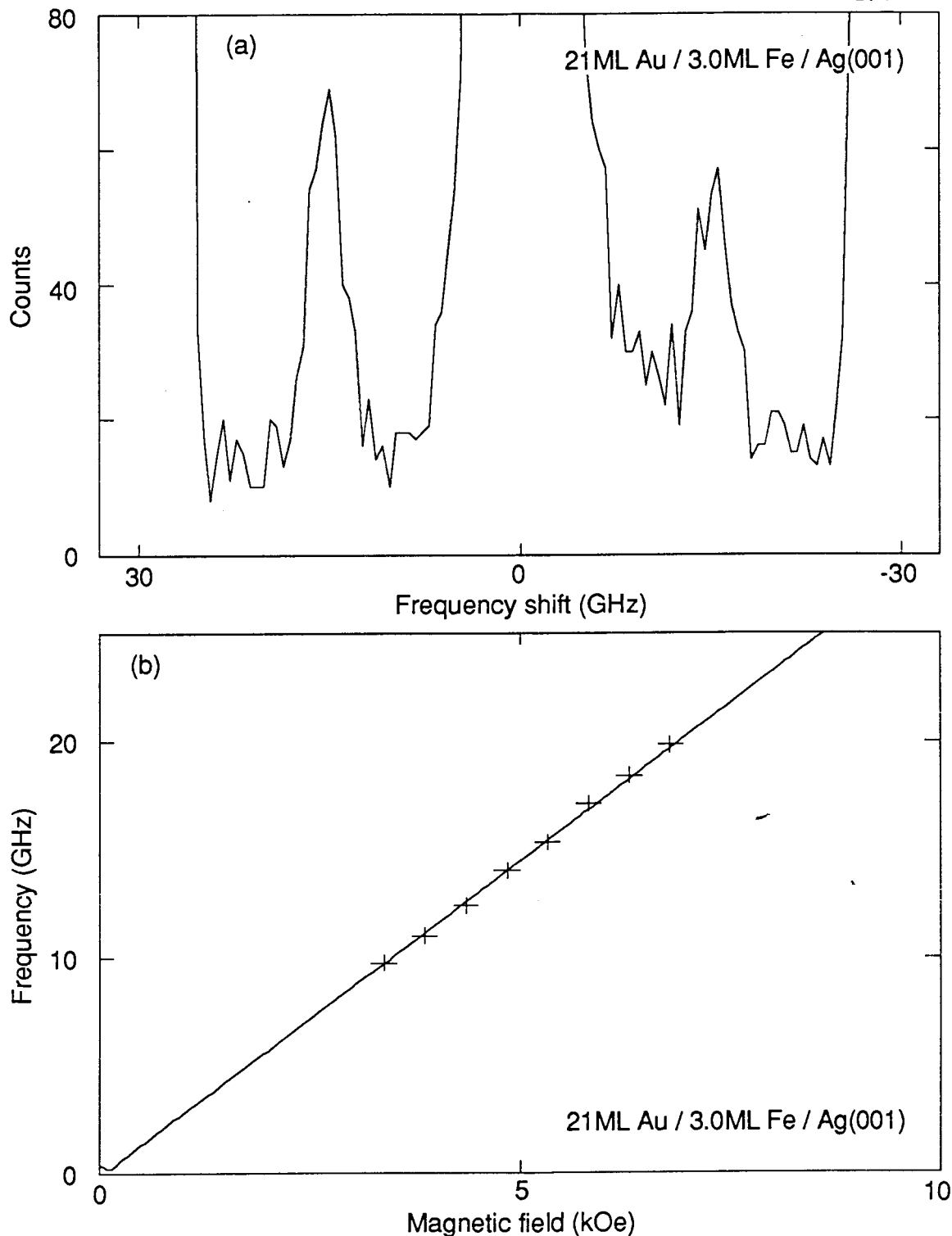


Figure 4.7

- (a) BLS spectrum for sample 4.5 for a field of $H = 5.32$ kOe, a laser power of 140 mW and a counting time for each of the 128 data points of 3.608 s.
- (b) Magnetic field dependence of the surface mode frequency for sample 4.5. The crosses are measured data points. The solid curve has been calculated using the theory of Chapter Three and the parameters listed in table 4.2.

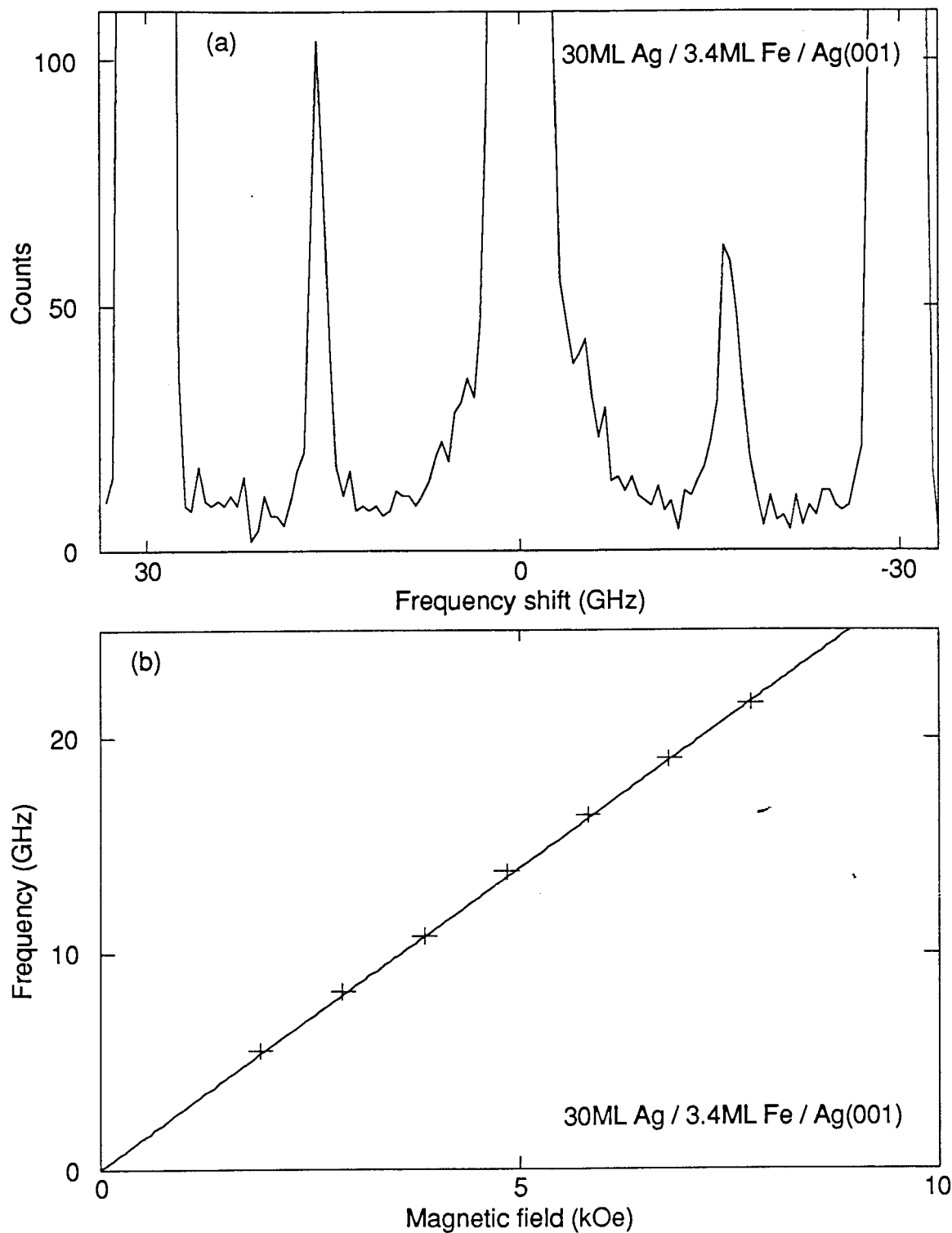


Figure 4.8

- (a) BLS spectrum for sample 4.6 for a field of $H = 4.84$ kOe, a laser power of 140 mW and a counting time for each of the 128 data points of 6.560 s.
- (b) Magnetic field dependence of the surface mode frequency for sample 4.6. The crosses are measured data points. The solid curve has been calculated using the theory of Chapter Three and the parameters listed in table 4.2.

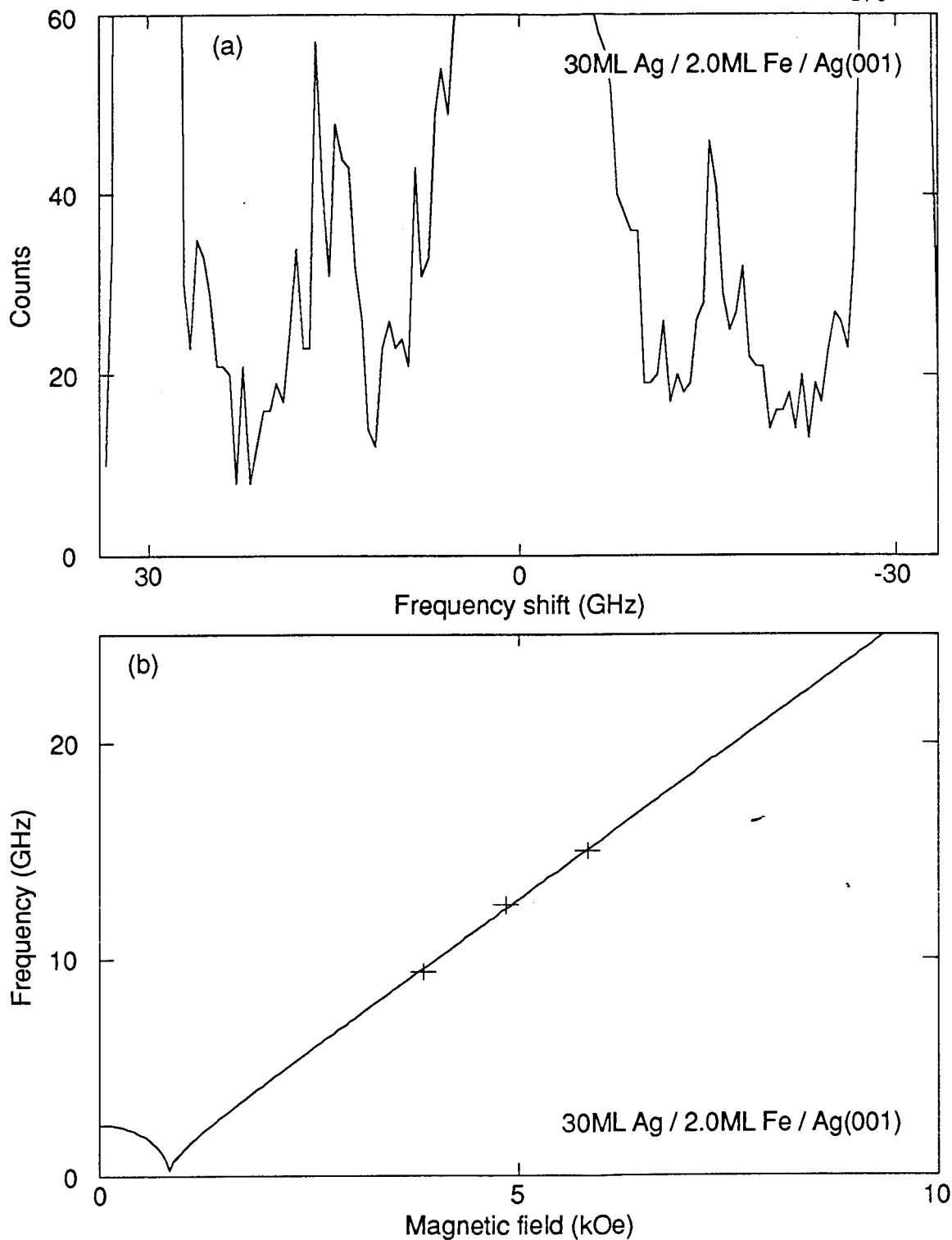


Figure 4.9

- (a) BLS spectrum for sample 4.7 for a field of $H = 5.81$ kOe, a laser power of 140 mW and a counting time for each of the 128 data points of 16.000 s.
- (b) Magnetic field dependence of the surface mode frequency for sample 4.7. The crosses are measured data points. The solid curve has been calculated using the theory of Chapter Three and the parameters listed in table 4.2.

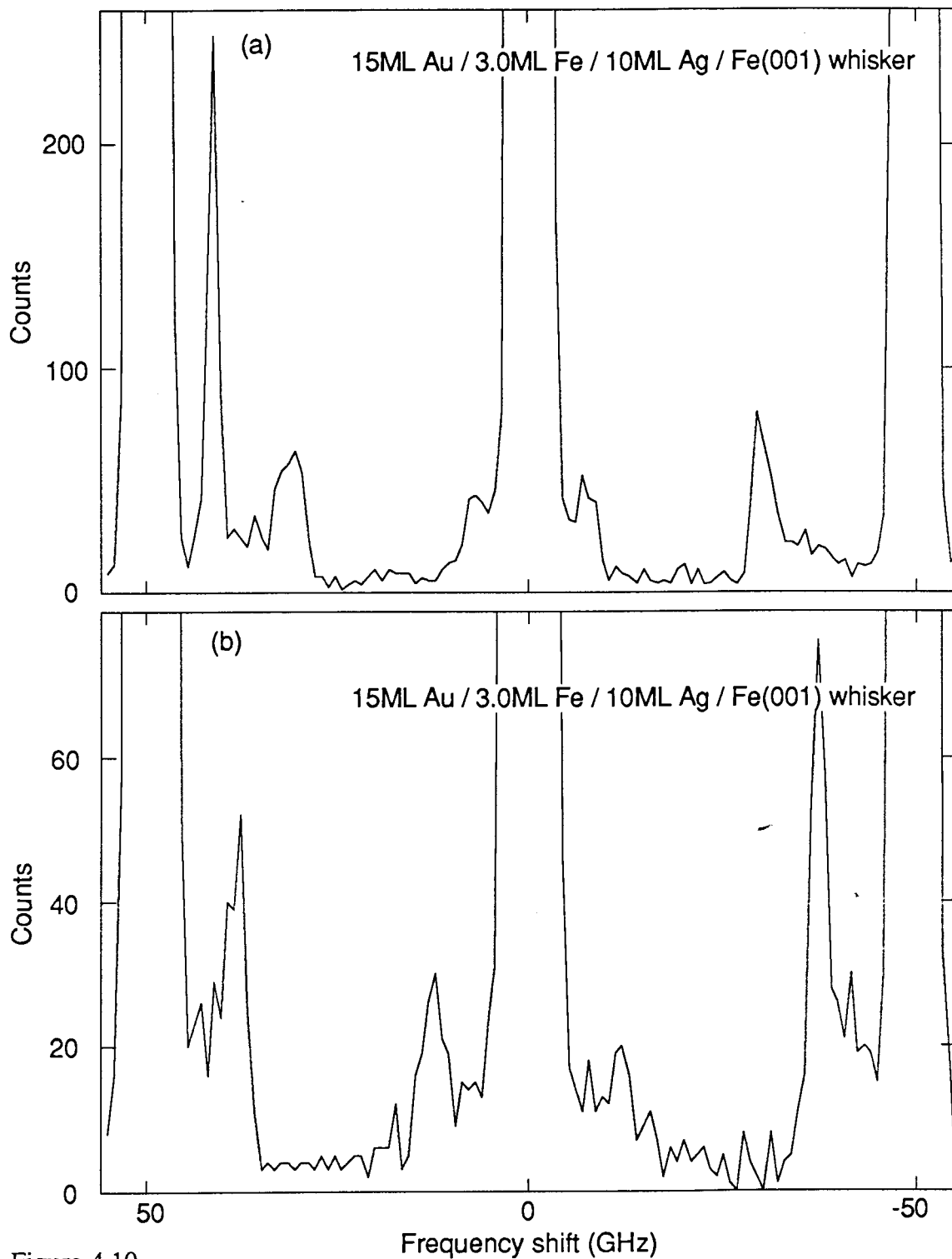


Figure 4.10

- (a) BLS spectrum for sample 4.8 for a field of $H = 3.65$ kOe, a laser power of 140 mW and a counting time for each of the 128 data points of 7.552 s.
- (b) BLS spectrum for sample 4.8 for a field of $H = 5.58$ kOe, a laser power of 140 mW and a counting time for each of the 128 data points of 8.216 s.

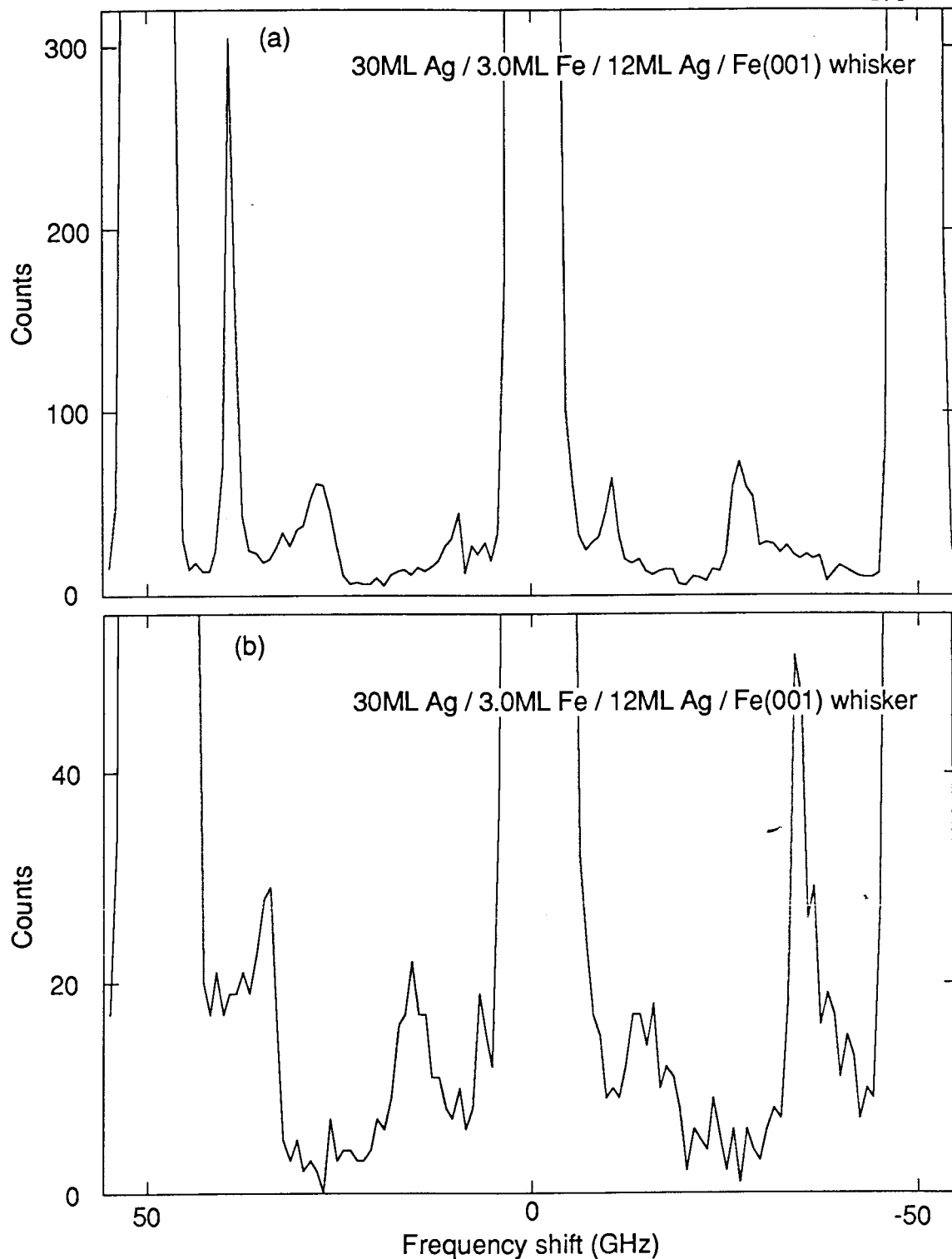


Figure 4.11

- (a) BLS spectrum for sample 4.9 for a field of $H = 2.89$ kOe, a laser power of 140 mW and a counting time for each of the 128 data points of 9.944 s.
- (a) BLS spectrum for sample 4.9 for a field of $H = 4.84$ kOe, a laser power of 140 mW and a counting time for each of the 128 data points of 10.808 s.

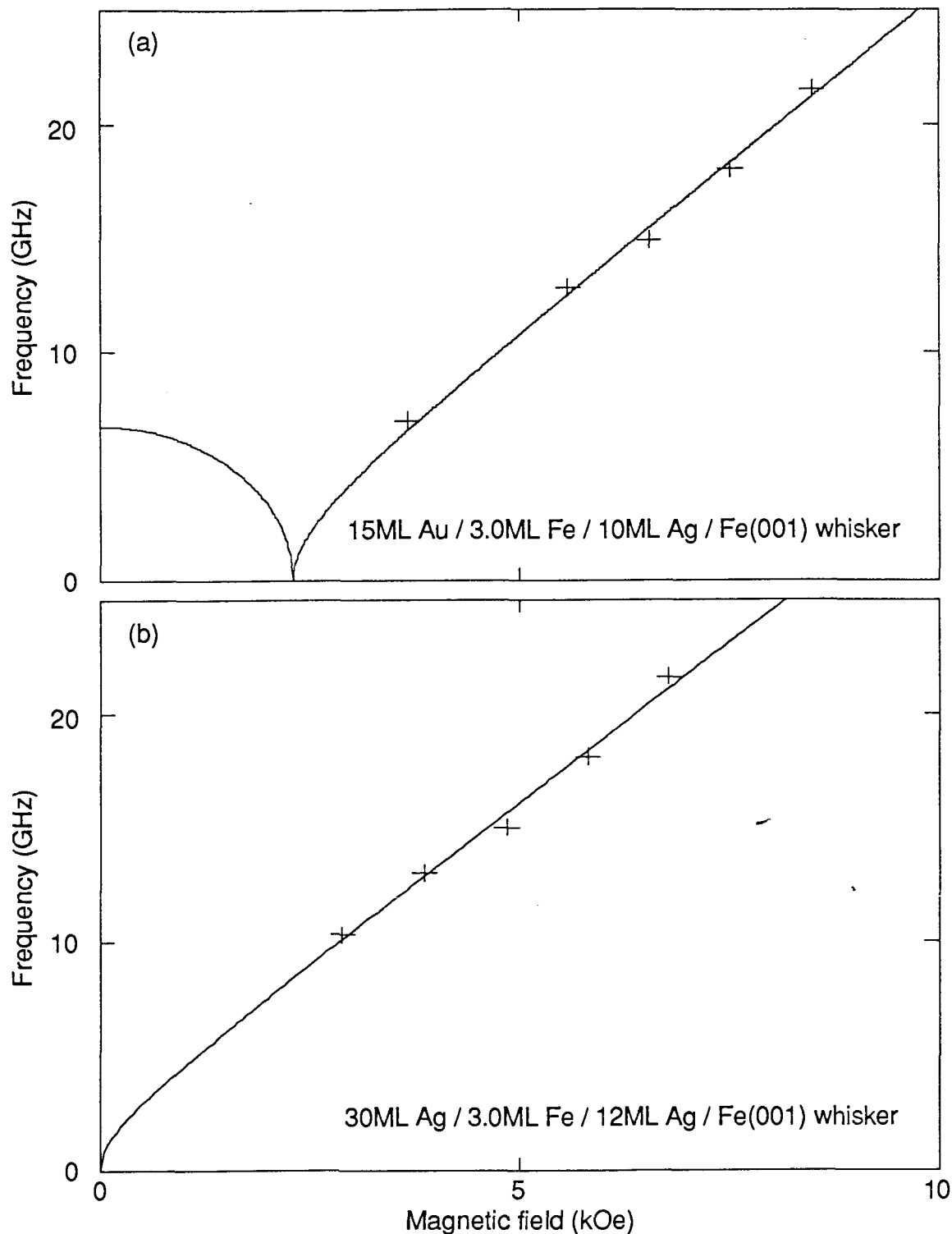


Figure 4.12

- (a) Magnetic field dependence of the surface mode frequency for sample 4.8. The crosses are measured data points. The solid curve has been calculated using the theory of Chapter Three and the parameters listed in table 4.2.
- (b) Magnetic field dependence of the surface mode frequency for sample 4.9. The crosses are measured data points. The solid curve has been calculated using the theory of Chapter Three and the parameters listed in table 4.2.

Table 4.2

The magnetic parameters for the Fe on Ag(001) samples of table 4.1. For each sample, the Fe film thickness d , the effective magnetization ($4\pi M_S$)_{eff}, the g -factor, the in-plane cubic magnetocrystalline anisotropy constant K_1 , and the spin pinning parameters K_S (calculated for $4\pi M_S = 21.55$ kG) and K_S' (calculated for $4\pi M_S = 14$ kG) are listed. All of the bulk Ag(001) substrates were vicinal crystals.

Sample	d (ML)	Cover metal	$(4\pi M_s)_{\text{eff}}$ (kG)	g-factor	K_1 (erg/cm ³)	K_s (a) (erg/cm ²)	K_s' (b) (erg/cm ²)
4.1	17	Au	15.6	2.09	4.5×10^5	1.2	—
4.2	4.9	Au	6.6	2.09	1.1×10^5 (c)	0.90	—
4.3	2.8	Au	0.67	2.09	0	0.72	0.30
4.4	2.9	Au	0.20	2.09	0	0.76	0.32
4.5	3.0	Au	-0.12	2.09	0	0.80	0.34
4.6(d)	3.4	Ag	-0.026	2.00	0	0.90	—
4.7(d)	2.0	Ag	-0.84	2.00	0	0.55	—
4.8(c)	3.0	Au	-2.4	2.09	0	0.92	0.39
4.9(c)	3.0	Ag	1.6	2.00	0	0.74	—

(a) For $4\pi M_s = 21.55$ kG

(b) For $4\pi M_s = 14$ kG

(c) obtained from FMR measurements

(d) grown at 140K; all others grown at 300K

(e) iron whiskers substrates

For $|(4\pi M_S)_{\text{eff}}| \ll 4\pi M_S$, the values of K_S scale quadratically with M_S . This can be seen for the values of K_S (for $4\pi M_S = 21.55$ kG) and K_S' (for $4\pi M_S = 14$ kG) listed in table 4.2 for the 3 ML thick Fe sample. Comparisons of the FMR intensities for ultrathin iron films with those for bulk Fe show that the bulk saturation magnetization value, $4\pi M_S = 21.55$ kG, is recovered in films thicker than 5 ML (Heinrich et al., 1988a). Also, Stampanoni et al. (Stampanoni et al., 1987) found that 5 ML thick Fe films on Ag(001) possessed the Curie temperature of bulk iron.

The surface mode peaks are easily seen on all of the spectra, including those obtained for Fe films that are only 3 ML thick. This is an excellent testimony to the sensitivity of the BLS system. The signal was noticeably weaker for sample 4.7, see figure 4.7, which consisted of only 2 ML of Fe. The poor quality of this signal is consistent with the conclusion drawn from the RHEED study on these Fe films: namely, that at least 3 ML of Fe are required to obtain a good quality film characterized by layer-by-layer growth.

In figures 4.11 and 4.12, spectra are shown for 3 ML thick Fe films grown on Ag-covered Fe(001) whiskers, samples 4.8 and 4.9. In part (a) of both figures, the dominant feature for positive frequency shifts is the surface mode peak for the bulk Fe(001) whisker. The prominent structures on either side of the central elastically scattered peak at 0 GHz are due to scattering from standing spin waves in the Fe whisker. The BLS spectrum obtained from a thick magnetic film such as an Fe whisker is explained more fully in Chapter 6 of this thesis. The two small peaks close to the strong peak at 0 GHz are the surface mode peaks for the 3 ML thick Fe film. These small peaks are more clearly visible in part (b) of figures 4.10 and 4.11.

The dependence of the surface mode frequency on the magnetic film thickness is shown in figure 4.13 for an applied magnetic field of 4.0 kOe. In the figure, the crosses and the square were obtained by interpolating the experimental data of figures 4.3 to 4.7 and figure 4.12 to an applied magnetic field value of 4.0 kOe. All of the samples were thin Fe films

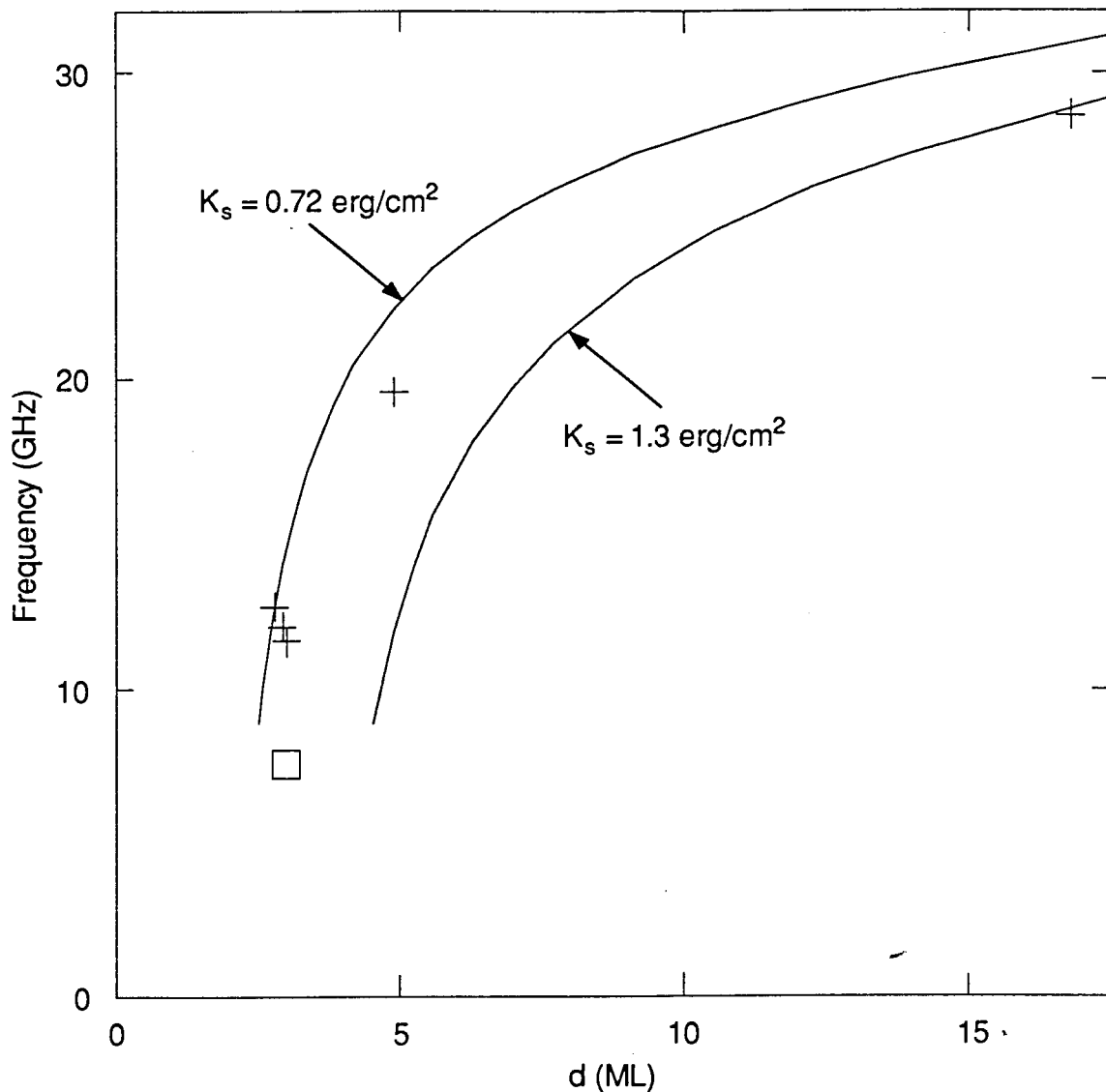


Figure 4.13

Surface mode frequency versus magnetic film thickness d for Au-covered Fe on Ag(001) films. The crosses correspond to experimental data for samples grown on bulk Ag(001) crystals. The box corresponds to experimental data for a Au-covered 3 ML thick Fe film grown on Ag that had been deposited on a Fe(001) substrate. The solid curves were calculated with two different values of the surface spin pinning coefficient $K_s = 0.72 \text{ erg/cm}^2$ and $K_s = 1.30 \text{ erg/cm}^2$. A linear dependence of the in-plane magnetocrystalline anisotropy constant K_1 on the magnetic film thickness was assumed, as detailed in the text. For both the data and the curves, $H = 4.0 \text{ kOe}$.

grown on Ag(001) and covered by Au: samples 4.1, 4.2, 4.3, 4.5, and 4.8. The crosses indicate samples that were grown on bulk vicinal Ag(001) substrates; the square indicates sample 4.8 which was grown on a Ag-covered Fe(001) whisker substrate. The agreement between the surface mode frequency values for the three thinnest samples ($d \sim 3$ ML) grown on bulk silver substrates is impressive; it is an indication of the reproducibility of the Au/Fe/Ag(001) samples.

In the absence of surface spin pinning, the surface mode frequency decreases only slightly with decreasing film thickness over the thickness range of figure 4.13, see figure 3.9. Because a dramatic decrease in the surface mode frequency is observed as the film thickness is reduced, there is a substantial pinning of the surface spins which tends to orient the magnetization along the sample normal, see figure 3.9. The solid curves in figure 4.13 were calculated using two different values of the surface spin pinning coefficient: $K_s = K_z^F + K_z^R = 0.72 \text{ erg/cm}^2$, and $K_s = 1.30 \text{ erg/cm}^2$. For each calculated curve, a linear dependence of the in-plane magnetocrystalline anisotropy constant K_1 was assumed within the thickness range $d \approx 3$ ML to 17 ML : $K_1 = [3.22 \times 10^4 d - 9 \times 10^4] \text{ erg/cm}^3$, where d is in ML. This linear relationship between K_1 and d is a very crude approximation based on measurements of K_1 by BLS and FMR (Heinrich et al., 1988a) for the samples included in figure 4.13. The shifts in the surface mode frequency due to K_1 are of the order of 1.8 GHz for $d = 17$ ML and 0.4 GHz for $d = 5$ ML, with $K_1 = 0$ for $d = 3$ ML. A constant value of the saturation magnetization equal to the bulk value, $4\pi M_s = 21.55 \text{ kG}$, was also assumed which, as discussed above, is not valid for the 3 ML thick Fe films.

A single value of the spin pinning coefficient $K_s = K_z^F + K_z^R$ does not describe all of the data in figure 4.13 : K_s decreases with a decrease in the film thickness. The thickness dependence of K_s implies either that the spin pinning is not confined to the surface layer, or that the surface layer changes with film thickness. Gay and Richter (Gay and Richter,

1987) have calculated the spin pinning coefficient as a function of film thickness and they find a 40% decrease in the coefficient as the thickness is changed from 9 ML down to 5 ML.

The dependence of the effective magnetization, $(4\pi M_s)_{\text{eff}}$, on the magnetic film thickness d is shown in figure 4.14. $(4\pi M_s)_{\text{eff}}$ decreases dramatically with film thickness such that $(4\pi M_s)_{\text{eff}} \sim 0$ for the 3 ML thick iron films grown on bulk vicinal Ag(001) substrates and covered with Au. For these thin films of Fe, the uniaxial anisotropy field is approximately equal to the shape demagnetizing field, see equation (4.1). For the Au-covered 3 ML thick Fe film grown on the Ag-covered Fe(100) whisker (sample 4.8), the uniaxial anisotropy field is larger than the shape demagnetization field and the effective magnetization is negative, $(4\pi M_s)_{\text{eff}} = -2.4$ kG. This negative value of $(4\pi M_s)_{\text{eff}}$ implies that the magnetization would be perpendicular to the sample surface in zero applied magnetic field. The increase in the uniaxial anisotropy of ~ 2.5 kOe for films grown on the Ag-covered Fe(001) whisker surface compared with those grown on the bulk vicinal Ag(001) substrate is probably due to the decreased density of atomic steps. Although this increase in the uniaxial anisotropy field is substantial, the fractional change is only 10% (~ 2.5 kOe out of ~ 25 kOe).

The 3 ML thick Fe films that were grown on bulk, vicinal Ag and covered by Ag exhibit values of $(4\pi M_s)_{\text{eff}}$ that are very close to those measured for the 3 ML thick Fe films that were grown on Ag and covered by Au, see table 4.2. Both BLS (Dutcher et al., 1988b; see also Chapter 6 of this thesis) and FMR (Purcell et al., 1988b) experiments on bulk Fe(001) crystals have shown that the surface pinning coefficient K_s is ~ 0.25 erg/cm² larger for a Ag-covered Fe surface than for a Au-covered Fe surface. Because the values of K_s are comparable for the bulk films and the ultrathin films, a difference in the surface spin pinning might be expected between ultrathin Fe films covered with Au and Ag. It is probable that the Ag-covered Fe films degraded substantially before they were measured

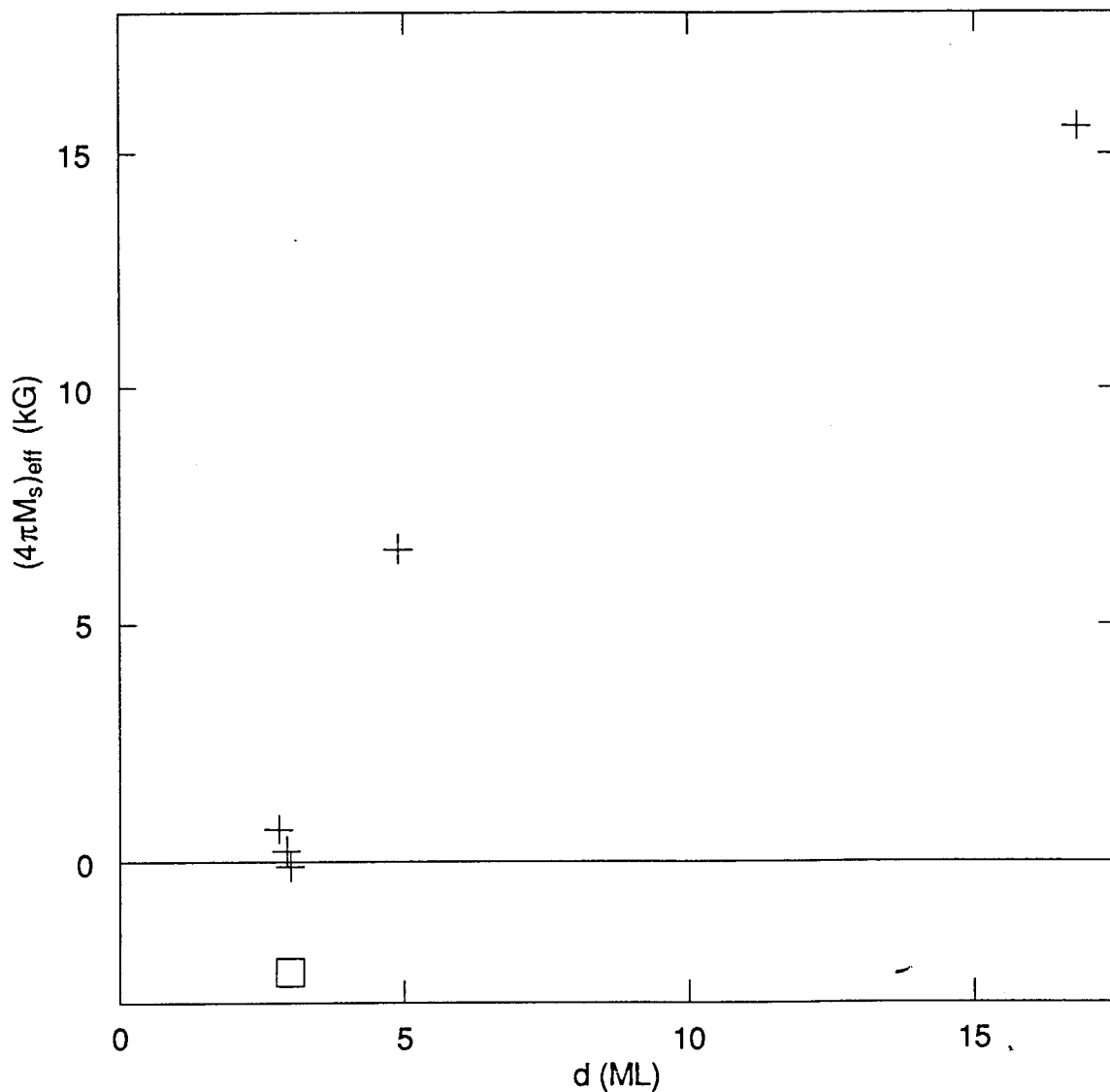


Figure 4.14

Effective magnetization versus magnetic film thickness d for Au-covered Fe on Ag(001) films. The crosses correspond to experimental data for samples grown on bulk Ag(001) crystals. The box corresponds to experimental data for a Au-covered 3 ML thick Fe film grown on Ag that had been deposited on a Fe(001) substrate.

with BLS, since a Ag coverlayer was found to be less effective than a Au coverlayer in protecting the Fe film from oxidation. Any oxidation of the Fe film would affect the surface spin pinning.

A significant difference is obtained between the g -factor for the Au-covered and the Ag-covered Fe films. For all of the Au-covered Fe films, the g -factor corresponding to bulk iron, $g = 2.09$, was obtained. A g -factor of 2.00 was observed in all of the Ag-covered samples, in agreement with the results of FMR experiments on the same Fe films (Heinrich et al., 1988a). A smaller g -factor results in a smaller slope on a plot of frequency versus applied magnetic field, and therefore a smaller frequency for a given magnetic field. The data for one of the Ag-covered samples, sample 4.6, is shown again in figure 4.15 with curves calculated for $g=2.00$ and $g=2.09$. A considerably better fit to the data is obtained using $g=2.00$. The decreased value of the g -factor for the Ag-covered samples is perhaps due to a reduction in the spin-orbit coupling. However, it is unlikely that the spin-orbit interaction is substantially reduced since the spin-orbit interaction is responsible for magnetic anisotropy and the value of the uniaxial anisotropy for the Ag-covered Fe films is comparable to that for the Au-covered Fe films. Only very thin 3 ML thick Fe films covered with Ag were studied. It is possible that the observed reduction in the g -factor is related to the film growth processes for small values of the thickness for the Fe films.

4.2 Nickel/Iron on Silver

4.2.1 Introduction

Bulk nickel has the fcc structure. When Ni atoms are deposited on a Fe(001) surface, it has been shown by low energy electron diffraction (LEED) (Wang et al., 1987) and reflection high energy electron diffraction (RHEED) (Heinrich et al., 1987b) that the Ni film grows initially with the same bcc structure as the Fe substrate. At a certain critical

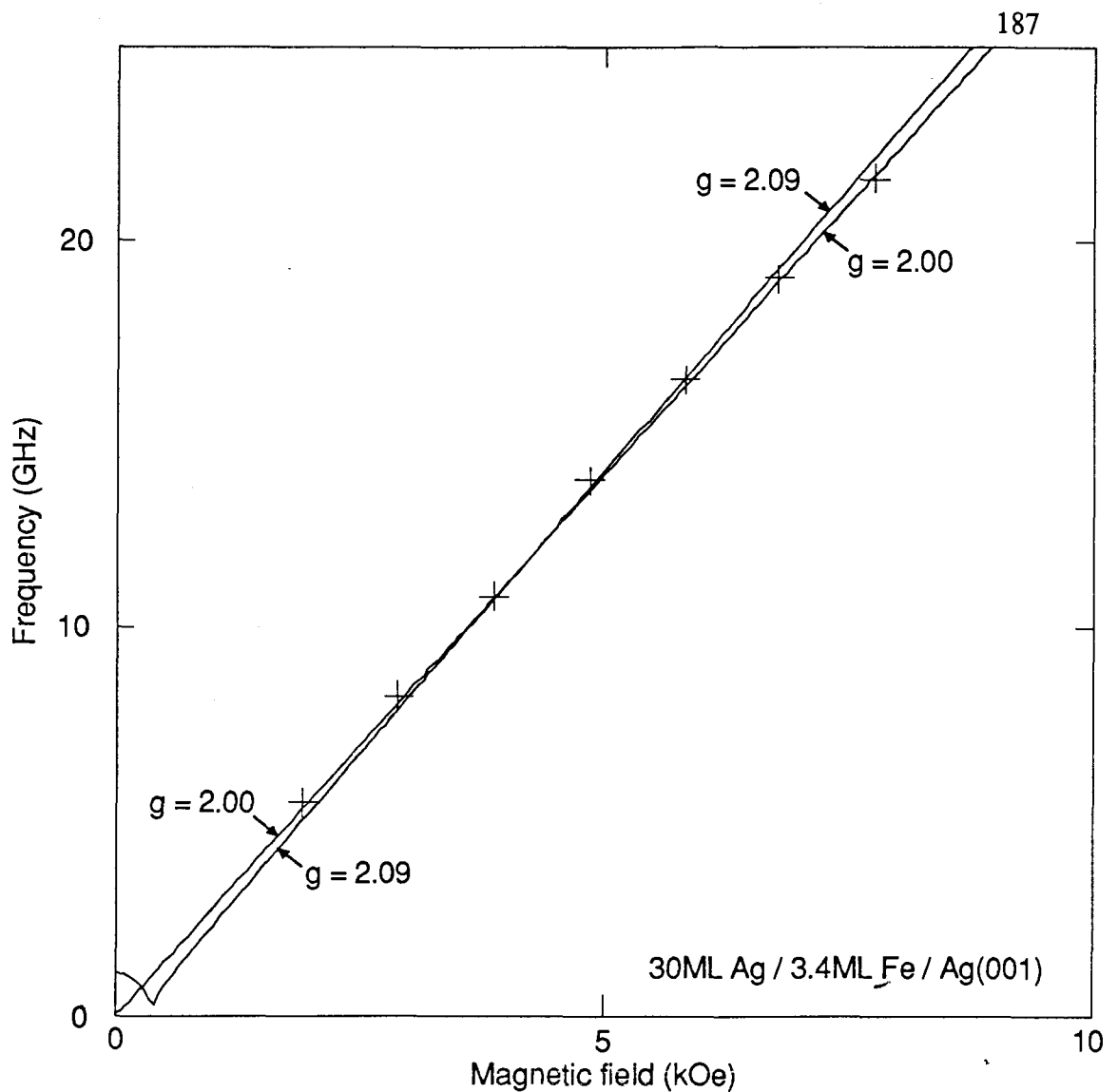


Figure 4.15

Magnetic field dependence of the surface mode frequency for sample 4.6. The crosses are measured data points. The solid curves have been calculated using the theory of Chapter Three; one of the curves has been calculated using $g = 2.00$ and an effective magnetization of -0.026 kG; and the other curve has been calculated using $g = 2.09$ and an effective magnetization of -0.38 kG.

thickness of the Ni film (3 to 6 monolayers), the simple bcc structure of the Ni film is modified by a complicated reconstruction of the Ni lattice.

Heinrich et al. (Heinrich et al., 1987b) have studied ultrathin layers of Ni(001) on bulk Fe(001) substrates using ferromagnetic resonance (FMR), RHEED and reflection electron energy loss fine structure (REELFS). The magnetic response of these samples was dominated by the Fe substrate; the effect of the Ni overlayer was observed as a pinning of the surface spins of the Fe substrate. It was possible to infer from the FMR experiments that the Ni overlayers were characterized by a large in-plane cubic magnetocrystalline anisotropy field, $2K_1/M_s \sim 3\text{kOe}$.

The interpretation of the FMR data can be simplified by placing the Ni and Fe films on a more equal footing, i.e. by choosing comparable thicknesses for the Ni and Fe films. The resulting samples, consisting of two ultrathin magnetic films, will be called magnetic bilayers. Very recently, Heinrich et al. (Heinrich et al., 1988b) have studied the structural and magnetic properties of Ni/Fe bilayers using RHEED, FMR and BLS. The BLS experiments are described in section 4.2.3. Ultrathin layers of bcc Fe can be grown on fcc Ag(001) substrates (Heinrich et al., 1987a; Heinrich et al., 1988a), as discussed in section 4.1 of this thesis. Magnetic bilayer films were formed by depositing ultrathin Ni(001) films on the ultrathin Fe(001) films on Ag(001). Bilayers containing lattice reconstructed Ni films and unreconstructed Ni films were studied.

Several important results were obtained from this study. Large in-plane anisotropies were observed by FMR and BLS for the lattice reconstructed bilayers but were not observed for unreconstructed bilayers. These anisotropies for the reconstructed bilayers were observed both in the resonance conditions (frequency for BLS and field for FMR) and in the resonance linewidths. This is in contrast to the results for ultrathin films Fe on Ag(001) for which the in-plane anisotropy was negligible (Heinrich et al., 1987a; Heinrich et al., 1988a). The four-fold symmetry of the anisotropy in the reconstructed bilayers and

the absence of this anisotropy in unreconstructed bilayers implies that the reconstruction of the lattice had four-fold symmetry. It is likely that the strain associated with the lattice mismatch between the bcc Fe and bcc Ni lattices is relieved by a misfit dislocation network. It is clear, therefore, that if the four-fold in-plane anisotropy is due to the misfit dislocation network, then that network must exhibit four-fold symmetry. Unreconstructed bcc Ni did not significantly alter the magnetic properties of ultrathin Fe films. This indicated that the unreconstructed bcc Ni structure was probably nonmagnetic.

4.2.2 Sample preparation

The samples described in this and the following section were grown in our laboratory by Dr. B. Heinrich and S.T. Purcell. The basic geometry of the Ni/Fe bilayers is shown in figure 4.16. It consisted of Ni(001) grown on Fe(001) that had been deposited on a bulk Ag(001) substrate; a thin layer of Au was deposited on the Ni film to protect the bilayer films against oxidation. Different thicknesses of Ni and Fe were used; a list of the samples is given in table 4.3. An additional Ni/Fe bilayer, consisting of 9.4 ML Ni on 5.7 ML Fe on a singular Ag(001) crystal ($< 1/4^\circ$ misorientation), was studied using FMR. The magnetic properties of this sample were remarkably similar to those of sample 4.10, with one notable exception: the in-plane uniaxial anisotropy was very small for the singular substrate.

The preparation of the Ag(001) substrates and the growth of ultrathin layers of Fe on these substrates has been described in detail in section 4.1.2 of this thesis. All depositions were performed at room temperature. The growth of Ni layers on the ultrathin Fe(001) films was similar to the growth of Ni layers on bulk Fe(001) substrates. The RHEED patterns for unreconstructed Ni layers that were 3 to 6 monolayers thick were identical to those for the Fe substrate. As the thickness of the Ni layer was increased, $c(2 \times 2)$ diffraction features began to form on the RHEED pattern with the RHEED electron beam

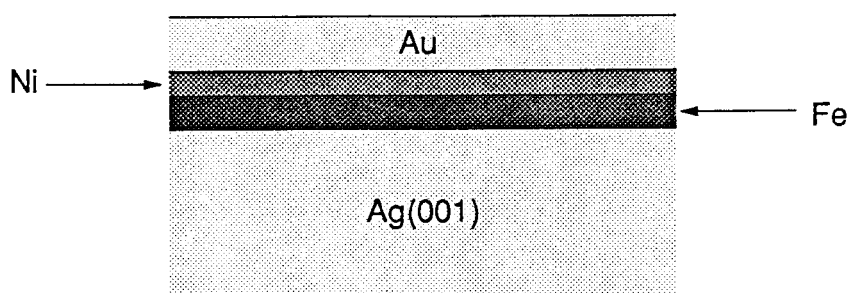


Figure 4.16

Ni/Fe bilayer sample geometry: Au on Ni on Fe on bulk Ag(001) crystal.

Table 4.3

The Ni/Fe on Ag(001) bilayer samples studied by BLS. All of the bulk Ag(001) substrates were vicinal crystals.

Sample	Composition
4.10	15ML Au / 10ML Ni / 6ML Fe / Ag(001)
4.11	15ML Au / 3.5ML Ni / 5.6ML Fe / Ag(001)
4.12	15ML Au / 10.5ML Ni / 3.5ML Fe / Ag(001)

directed along the [110] direction. However, the RHEED pattern exhibited the main features associated with a bcc lattice throughout the entire growth. The reconstructed Ni structure was not a simple $c(2 \times 2)$ structure, as evidenced by the appearance of superlattice streaks on the RHEED pattern with the electron beam not along one of the cubic axes of the sample. The appearance of the $c(2 \times 2)$ RHEED features coincided with a substantial decrease in the amplitude of RHEED specular spot intensity oscillations. The RHEED oscillations for the growth of Ni on ultrathin Fe(001) films were weak when a vicinal Ag(001) crystal ($\sim 2^\circ$ misorientation) was used as the substrate; the oscillations were much stronger for singular Ag(001) substrates ($< 1/4^\circ$ misorientation).

4.2.3 Brillouin light scattering results and discussion

The bilayers listed in table 4.3 were grown on vicinal Ag(001) substrates ($\sim 2\%$ misorientation) and they all exhibited substantial in-plane uniaxial anisotropies. Including this in-plane uniaxial anisotropy and allowing the direction of the applied magnetic field to rotate in the sample plane, the effective fields which enter into the Landau-Lifshitz equation of motion for the magnetization, equations (3.37) and (3.38), can be written as

$$H_y = H + \frac{2Aq^2}{M_s} + \gamma - i \frac{\omega}{\gamma} \frac{G}{\gamma M_s} \quad (4.4)$$

$$H_z = H + \frac{2Aq^2}{M_s} + \alpha - i \frac{\omega}{\gamma} \frac{G}{\gamma M_s} \quad (4.5)$$

where

$$\gamma = \frac{K_1}{2M_s} (3 + \cos 4\phi) + \frac{K_{up}}{M_s} [1 + \cos 2(\phi - \phi_u)] - \frac{2K_u}{M_s} , \quad (4.6)$$

$$\alpha = \frac{2K_1}{M_S} \cos 4\phi + \frac{2K_{up}}{M_S} \cos 2(\phi - \phi_u), \quad (4.7)$$

K_{up} is the in-plane uniaxial anisotropy coefficient, ϕ is the in-plane angle between the applied magnetic field and the (100) axis, and ϕ_u is the angle between the easy axis of the in-plane uniaxial anisotropy and the (100) axis. Equations (4.6) and (4.7) should be compared with equations (3.41) and (3.42).

The bilayer films can either be interpreted as two distinct magnetic films with strong exchange coupling between the two films, or as a single magnetic film with the combined magnetic properties of both films. Using the latter approach, the combined magnetic parameters resulting from detailed fits to FMR data obtained at 36 GHz are listed in table 4.4.

BLS spectra for sample 4.10 are shown in figures 4.17(a), 4.17(b) and 4.18(a) with the magnetic field H applied along the easy ($\phi = 0$), hard₁ ($\phi = 45^\circ$), and hard₂ ($\phi = -45^\circ$) axes, respectively. The surface mode peaks are clearly visible in all three spectra. Ghost peaks of the elastically scattered light can be seen at + 8 GHz and -42 GHz; these peaks are not due to inelastic scattering of light and merely increase the background signal. The intensity of the ghost peaks could be reduced by adjustment of the etalon within the laser cavity. The ghost peaks are probably due to another resonance of the laser.

The dependence of the surface mode frequency on the applied magnetic field for the easy, hard₁, and hard₂ axes is shown in figure 4.18(b) for sample 4.10. The data points are indicated by stars, crosses and \times 's, and the solid curves were calculated using the magnetic parameters determined from FMR experiments performed at 36 GHz (see table 4.4). The agreement between the data and the solid curves is good.

For a given value of the applied magnetic field, there is a large difference in the surface mode frequency between the easy and hard axes for sample 4.10, see figure 4.18(b). This difference is due to a large in-plane four-fold anisotropy. There is also a measurable

Table 4.4

The magnetic parameters for the Ni/Fe on Ag(001) bilayer samples of table 4.3. For each sample, the effective magnetization $(4\pi M_s)_{\text{eff}}$, the g-factor, the in-plane cubic magnetocrystalline anisotropy constant K_1 , the in-plane uniaxial anisotropy constant K_{up} and the in-plane angle between the easy axis of the in-plane uniaxial anisotropy and the (100) axis are listed. The parameters were determined by ferromagnetic resonance (Heinrich et al., 1988b). All of the bulk Ag(001) substrates were vicinal crystals.

Sample	$(4\pi M_s)_{\text{eff}}$ (kG)	g-factor	K_1 (erg/cm ³)	K_{up} (erg/cm ³)	ϕ_u (degrees)
4.10	9.75	2.10	6.76×10^5	-1.23×10^5	45
4.11	8.92	2.09	1.08×10^5	-0.410×10^5	1.6
4.12	5.38	2.15	8.36×10^5	1.02×10^5	34

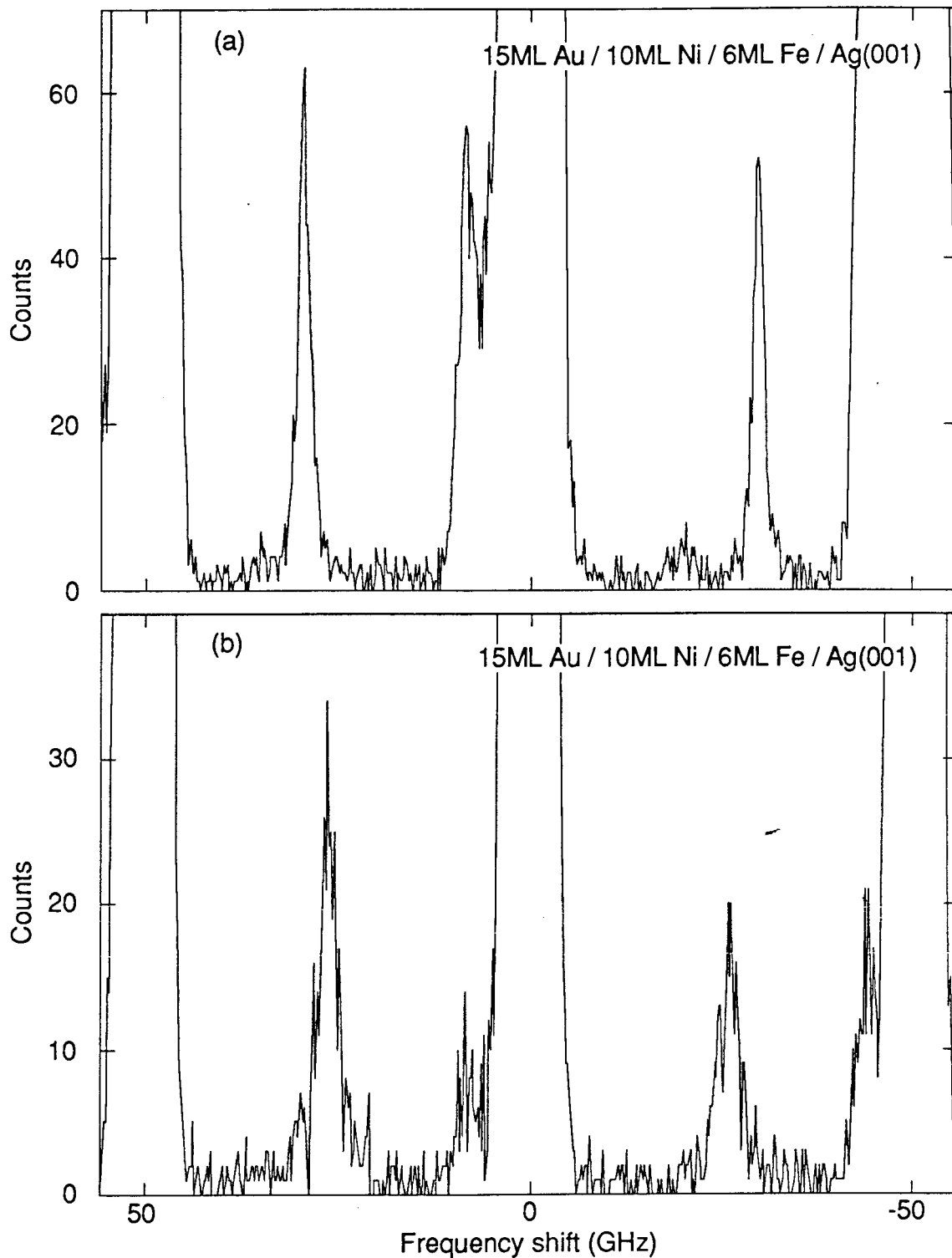


Figure 4.17

- (a) BLS spectrum for sample 4.10 for a field of $H = 5.62$ kOe (easy axis), a laser power of 88 mW and a counting time for each of the 512 data points of 2.544 s.
- (b) BLS spectrum for sample 4.10 for a field of $H = 5.62$ kOe (hard₁ axis), a laser power of 88 mW and a counting time for each of the 512 data points of 1.704 s.

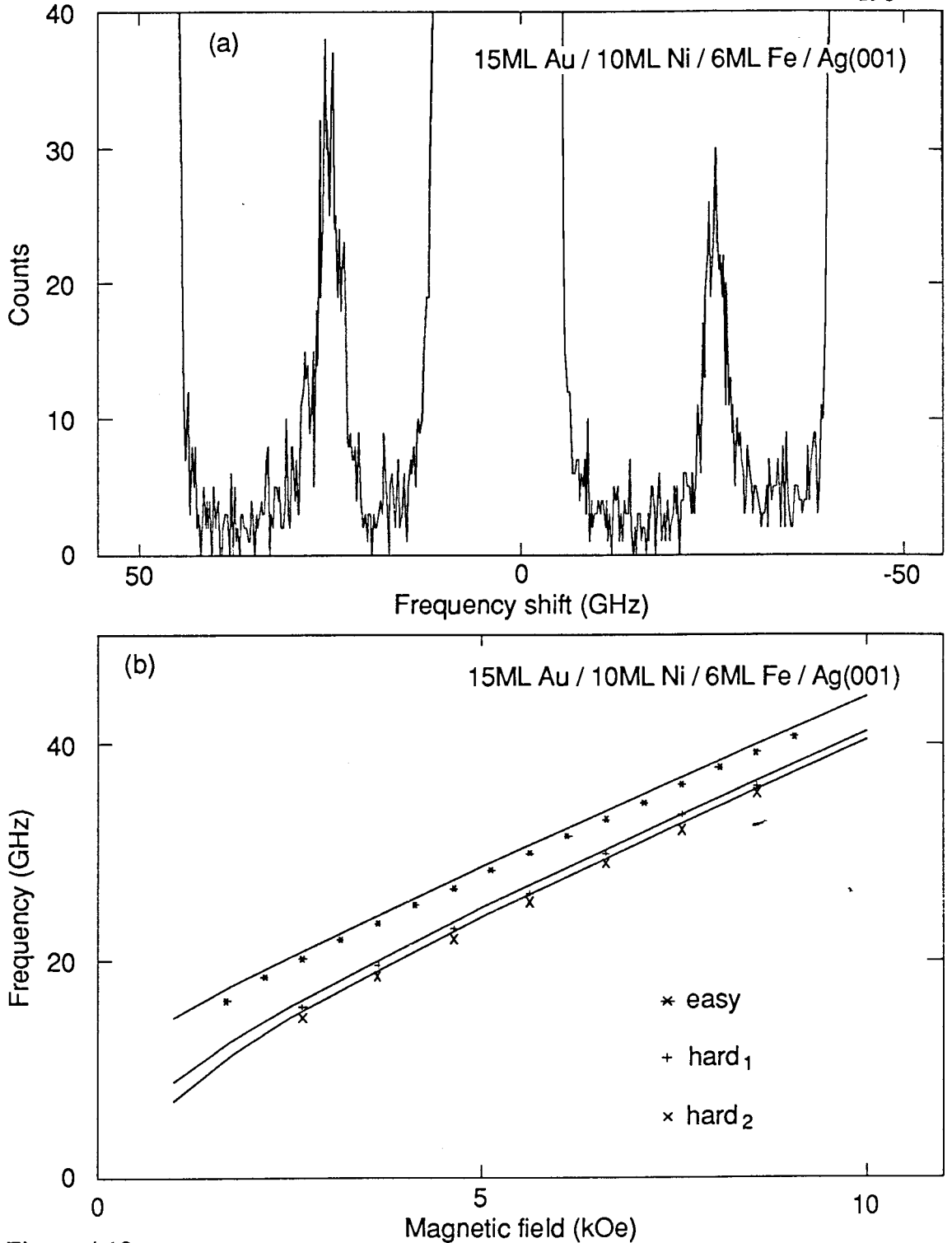


Figure 4.18

- (a) BLS spectrum for sample 4.10 for a field of $H = 5.62$ kOe (hard₂ axis), a laser power of 88 mW and a counting time for each of the 512 data points of 3.212s.
- (b) Magnetic field dependence of the surface mode frequency for sample 4.10. The crosses are measured data points. The solid curves have been calculated using the theory of Chapter Three and the parameters listed in table 4.4.

difference between the surface mode frequencies for the hard₁ and hard₂ axes due to an in-plane uniaxial anisotropy aligned along the hard₁ axis. The dependence of the surface mode frequency on the direction of the applied magnetic field in the plane of the film is shown for a fixed magnetic field value of $H = 6.81$ kOe in figure 4.19(a). Surprisingly, there was also a large anisotropy in the linewidth of the surface mode peaks, as shown in figure 4.19(b). The linewidth anisotropy can be seen easily in the spectra of figures 4.17 and 4.18(a) and was particularly easy to measure using FMR. From a comparison of the plots in figure 4.19(a) and (b), it is clear that the surface mode frequency and linewidth anisotropies are related to one another and probably have a common origin.

Sample 4.11 was measured using the high frequency resolution technique described in section 2.2.6. A single interferometer with a small free spectral range, $FSR = 15$ GHz, was used. A typical spectrum is shown in figure 4.20(a). The peaks at +6.3 GHz and +8.6 GHz correspond to the same surface mode: the peak at +6.3 GHz is upshifted in frequency and belongs to the elastic peak at -15 GHz; the peak at +8.6 GHz is downshifted in frequency and belongs to the elastic peak at +30 GHz. The difference in frequency between the upshifted and downshifted peaks is labelled Δf . The surface mode peaks are clearly seen above the background. The slow scan option of the interferometer, described in section 2.2.5, was also used to collect this spectrum: the counting time was a factor of 10 higher within the frequency range +3.6 GHz to +11.4 GHz than outside of this frequency range. The surface mode frequency was measured using the high frequency resolution technique as a function of applied magnetic field, as shown in figure 4.20(b). The magnetic field was applied along the easy axis of the film. The stars are BLS data and the solid curve was calculated using the magnetic parameters determined from FMR experiments performed at 36 GHz; these parameters are listed in table 4.4. The agreement between BLS and FMR measurements is excellent.

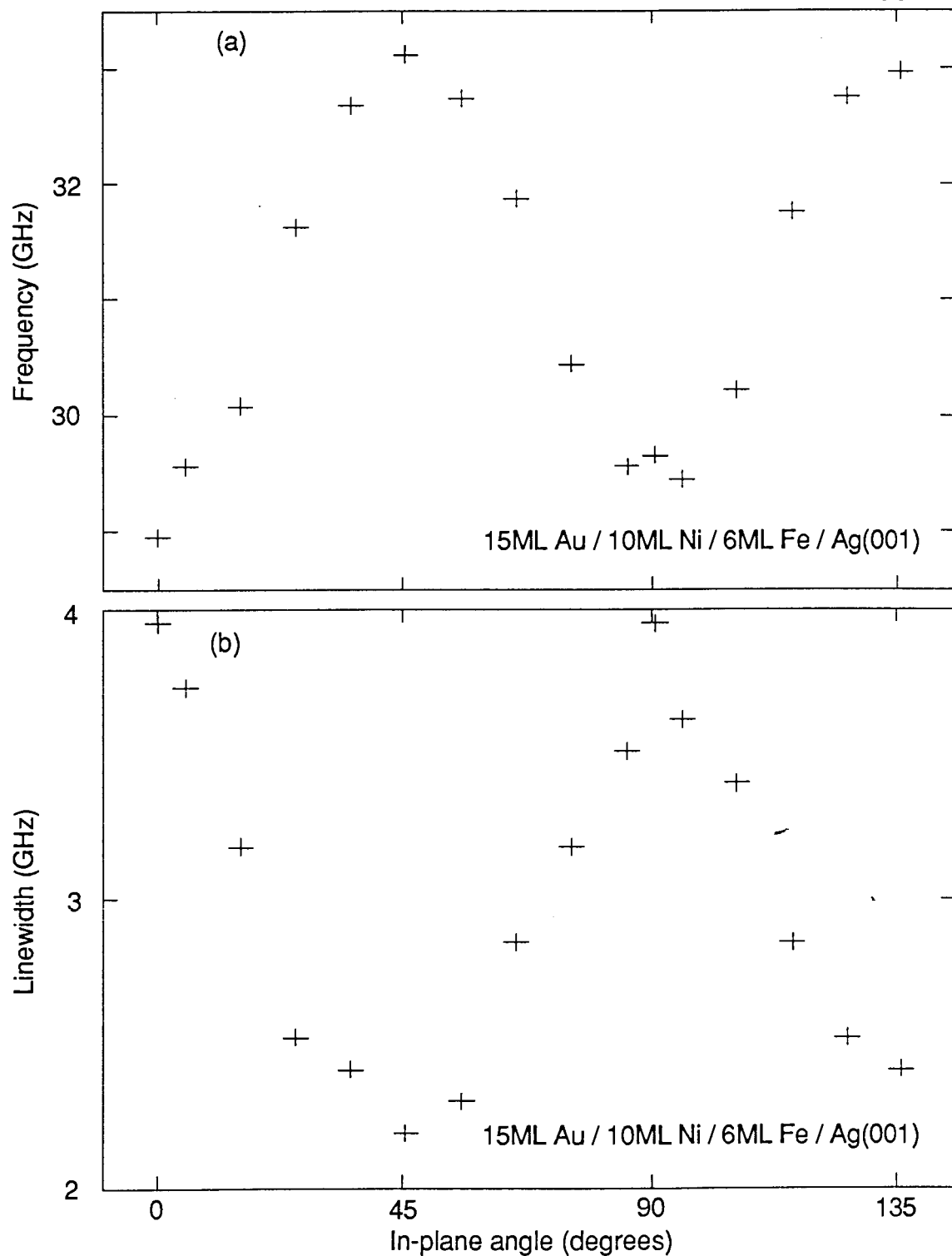


Figure 4.19

- (a) Surface mode frequency data as a function of the in-plane angle between the applied field and the crystal (001) axis for sample 4.10. An applied field of 6.81 kOe and an incident laser power of 125 mW were used.
- (b) Surface mode linewidth data as a function of the in-plane angle between the applied field and the crystal (001) axis for sample 4.10. An applied field of 6.81 kOe and an incident laser power of 125 mW were used.

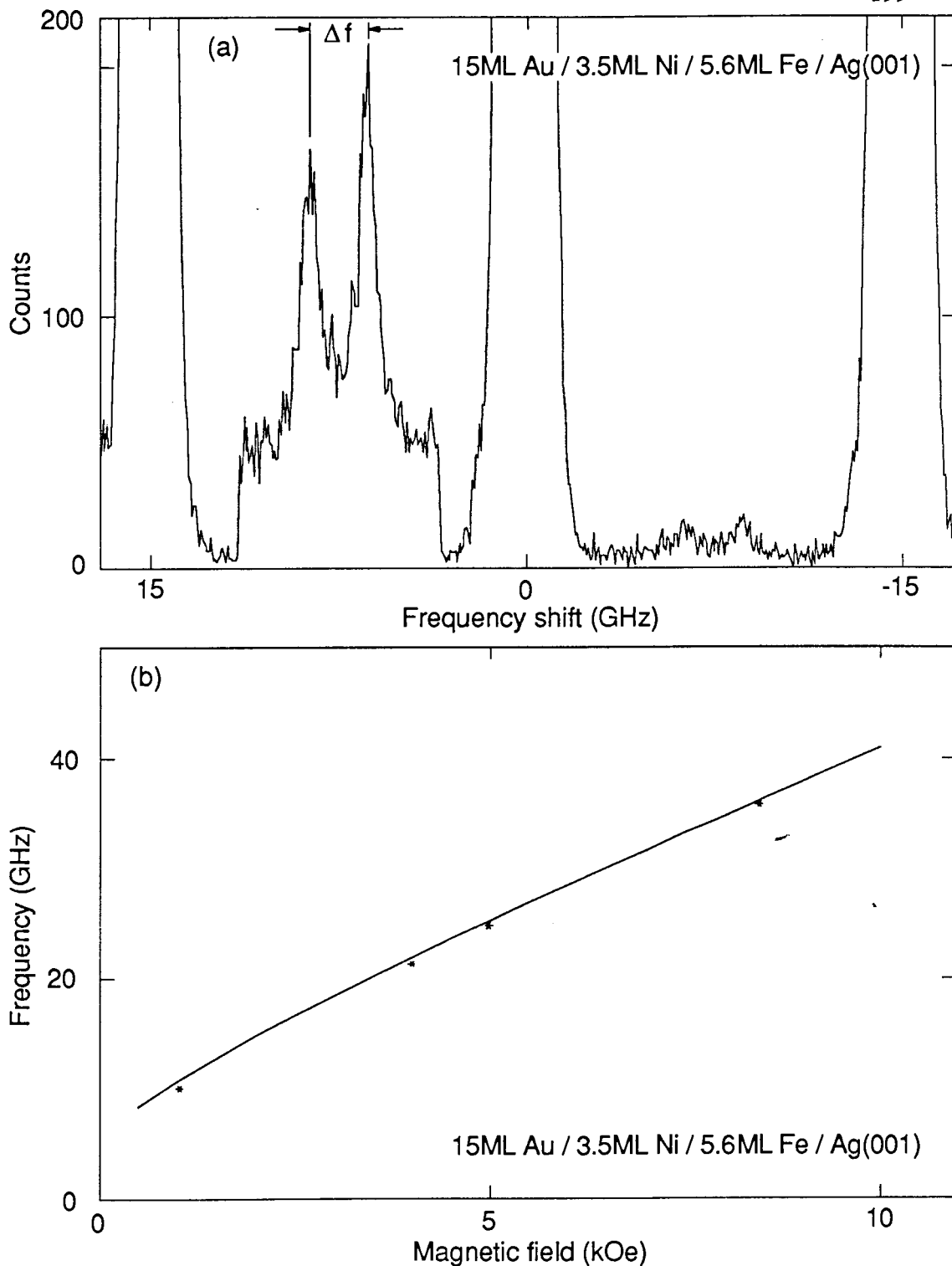


Figure 4.20

- (a) BLS spectrum for sample 4.11 for a field of $H = 3.99$ kOe (easy axis), a laser power of 88 mW and a counting time for each of the 512 data points of 4.584 s.
- (b) Magnetic field dependence of the surface mode frequency for sample 4.11 (easy axis). The crosses are measured data points. The solid curve has been calculated using the theory of Chapter Three and the parameters listed in table 4.4.

The frequency difference Δf was measured for sample 4.11 as a function of the in-plane angle between the applied field and the (100) axis for a fixed value of the magnetic field, $H = 3.99$ kOe. The results are shown in figure 4.21. The crosses are experimental BLS data and the solid curve was calculated using the magnetic parameters determined from FMR experiments at 36 GHz and listed in table 4.4. There was a shift of 0.98 ± 0.15 GHz between the measured and calculated values of Δf , corresponding to a shift between the measured and calculated surface mode frequencies of 0.49 ± 0.08 GHz. The solid curve in figure 4.21 has been shifted upward by 0.98 GHz to overlay the data. The in-plane four-fold and uniaxial anisotropies are readily apparent from the figure.

A typical BLS spectrum for sample 4.12 is shown in figure 4.22(a) for an applied magnetic field of 1.03 kOe. A single interferometer was used and the spectrum was collected with the slow scan option of the interferometer. The counting time was a factor of 10 longer within the frequency range +7.0 GHz to +23.0 GHz than outside of this range. The two peaks correspond to the same surface mode: the peak at +11.5 GHz belongs to the elastic peak at 0 GHz and the peak at +18.5 GHz belongs to the elastic peak at +30 GHz. In figure 4.22(b), the dependence of the surface mode frequency on the applied magnetic field is shown. The magnetic field was applied along the easy axis. The stars are BLS data and the solid curve was calculated with the magnetic parameters for sample 4.12 as listed in table 4.4.

Another sample, consisting of 10 ML of Ni grown on Ag(001), was measured with BLS but no magnetic signal was observed. FMR measurements on this sample also did not detect a magnetic signal. We had hoped to measure the magnetic properties of the lattice reconstructed Ni layer directly. The large magnetic damping and small saturation magnetization probably reduced the BLS and FMR signals below detectable limits.

Very good agreement was obtained between the BLS data and the curves generated using the magnetic parameters determined from FMR for all Ni/Fe bilayer samples, see

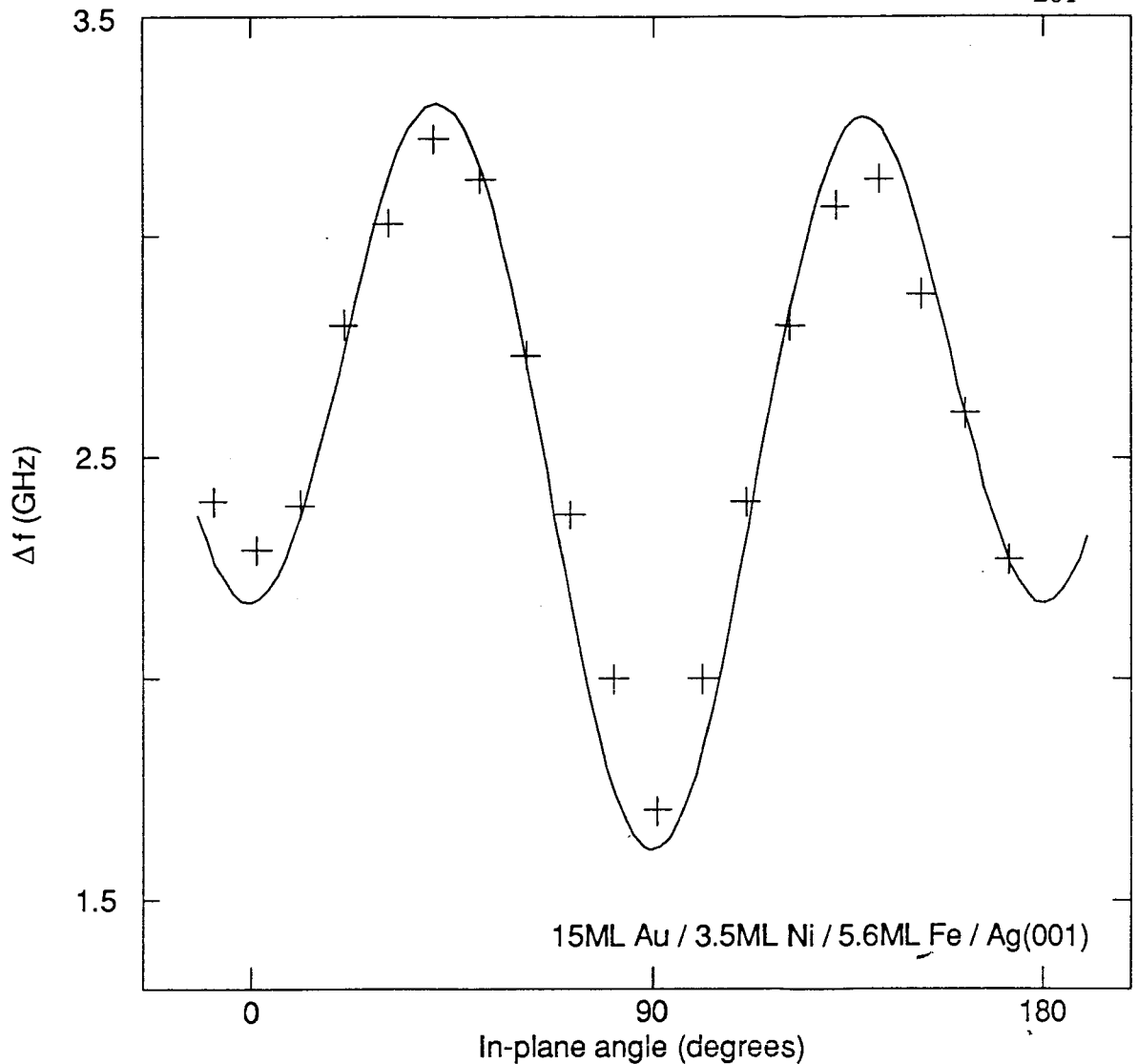


Figure 4.21

The frequency difference Δf as a function of the in-plane angle between the applied field and the crystal (001) axis for sample 4.11. An applied field of 3.99 kOe and an incident laser power of 125 mW were used. The crosses are measured Brillouin light scattering data and the solid curve is calculated using the magnetic parameters determined from ferromagnetic resonance (see table 4.4). There was a shift of 0.98 ± 0.15 GHz between the measured and calculated values of Δf . The solid curve has been shifted upward by 0.98 GHz to overlay with the measured data.

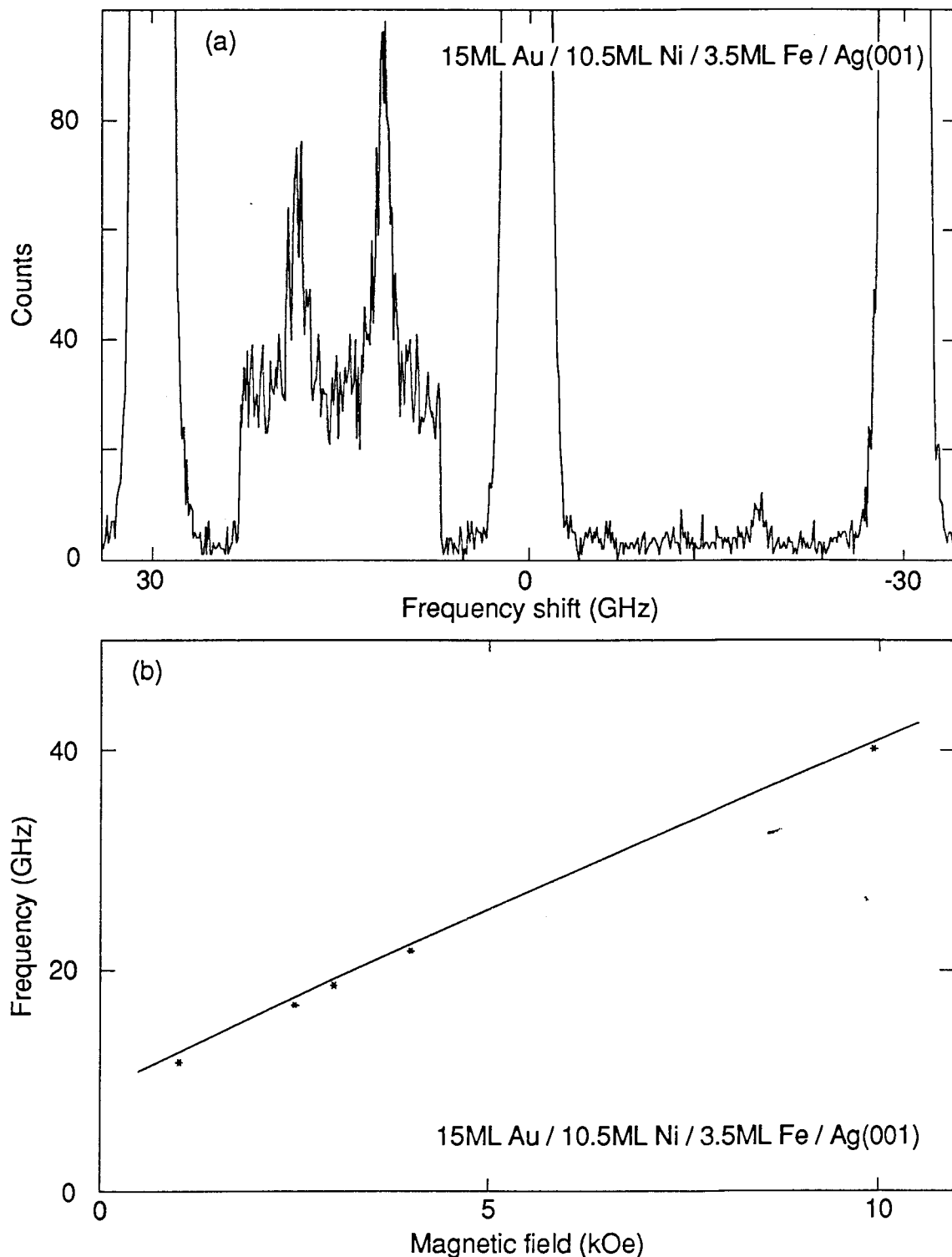


Figure 4.22

- (a) BLS spectrum for sample 4.12 for a field of $H = 1.03$ kOe (easy axis), a laser power of 70 mW and a counting time for each of the 512 data points of 7.724 s.
- (b) Magnetic field dependence of the surface mode frequency for sample 4.12 (easy axis). The crosses are measured data points. The solid curve has been calculated using the theory of Chapter Three and the parameters of table 4.4.

figures 4.18(b), 4.20(b) and 4.22(b). The main conclusion of the comparison between BLS and FMR is that the data averaged over $\sim 1 \text{ cm}^2$ (FMR) is in good agreement with that measured using an area of $\sim 10^{-6} \text{ cm}^2$ (BLS). For the Ni/Fe bilayer samples, the in-plane anisotropies in frequency and linewidth are a local phenomenon and are not due to some change in the area of the film sampled by FMR as the applied field is rotated for the FMR measurements. In the BLS experiment there is a slight heating of the sample caused by the focussing of the laser onto the sample surface; unfortunately, the effect of heating was not measured experimentally for the bilayer samples. In BLS studies of Fe(001) whiskers described in Chapter Six, it was determined that 70 mW of incident laser power produced a 13 K increase in the sample temperature at the focussed spot of laser light. An increase in the sample temperature would result in a decrease of the saturation magnetization. From the simplified resonance condition for ultrathin films, equation (3.143), a reduction of the resonance frequency is obtained for a decrease of the saturation magnetization. Therefore the shift in the data relative to the calculation is in the same direction as that expected from sample heating. However, the discrepancy between the data and the calculated curves in figures 4.18(b), 4.20(b) and 4.22(b) is between 0.44 and 0.88 GHz. In the measurements on the ultrathin nickel/iron bilayer samples, in which the heat is conducted away from the focussed laser spot by the silver substrate, an incident laser power of between 70 and 88 mW was used. According to the iron whisker results, this should produce a sample heating of $\sim 15 \text{ K}$; however, since the thermal conductivity of silver is approximately five times that of iron at room temperature (Kittel, 1976), one would expect the sample heating to be substantially less than 15 K. In the iron whisker experiments described in Chapter Six, it was also determined that the surface mode frequency for the iron whisker shifted by -0.5 GHz for a temperature increase of 75 K. If the frequency shift with temperature is the same for the surface mode in the ultrathin nickel/iron bilayer samples as it is for the surface mode in the iron whisker samples, then the discrepancies between the data and the

calculated curves in figures 4.18(b), 4.20(b) and 4.22(b) would correspond to a sample heating of roughly 65 to 130 K. Therefore it seems likely that the discrepancies are not due to sample heating effects, and are perhaps due to an inaccuracy of 150 to 300 Oe in the measured values of the applied magnetic field.

CHAPTER FIVE
ULTRATHIN IRON SINGLE FILMS AND SUPERLATTICES
GROWN ON COPPER

5.1 Introduction

For bulk iron crystals, the stable crystal structure is body centered cubic (bcc) below $T = 1184$ K and also from $T = 1665$ K to the melting point at $T = 1809$ K. The face centered cubic (fcc) structure is stable between $T = 1184$ K and $T = 1665$ K. It is possible, however, to obtain ultrathin films of fcc iron at room temperature and below by epitaxially depositing the iron atoms onto the (001) plane of fcc copper. Such a metastable structure, which is not the lowest energy structure at a given temperature, is forced on the iron film by the strong influence of the substrate.

At room temperature, the distance between nearest neighbour copper atoms lying in the (001) plane of the fcc structure is $a_{\text{Cu}} = 3.6147 \text{ \AA}$ (Pearson, 1964). For fcc iron between $T = 1184$ K and $T = 1665$ K, the nearest neighbour separation of iron atoms lying in the (001) plane is given by (Gorton et al., 1965)

$$a_{\text{Fe}} = 3.5832 + 7.00 \times 10^{-5} t \text{ \AA}, \quad (5.1)$$

where t is in $^{\circ}\text{C}$. Extrapolating this formula to room temperature ($t = 25^{\circ}\text{C}$) gives $a_{\text{Fe}} = 3.5850 \text{ \AA}$. Therefore, the lattice mismatch between fcc iron and fcc copper at room temperature is only

$$\left(\frac{a_{\text{Cu}} - a_{\text{Fe}}}{a_{\text{Cu}}} \right) \times 100\% = 0.8\%. \quad (5.2)$$

This match is considered to be very good for epitaxial growth.

The growth of fcc Fe on Cu(001) is shown schematically in figure 5.1. The shaded balls correspond to atoms in the outermost layer of the copper substrate and the solid balls correspond to atoms in the first monolayer of iron. The two fcc surface nets match almost perfectly. The thickness of one monolayer of iron in the fcc phase is 1.81 Å.

Early experimental studies of fcc Fe films grown on Cu crystals dealt with the nature of the magnetic ordering. A variety of results were obtained. Wright (Wright, 1971) found that Fe films grown on Cu(110) were ferromagnetic. For Fe films grown on Cu(111) Kümmerle and Gradmann (Kümmerle and Gradmann, 1977) also observed ferromagnetic ordering. Keune et al. (Keune et al., 1977) concluded that Fe films grown on Cu(001) were antiferromagnetic. However, Halbauer and Gonser (Halbauer and Gonser, 1983) found that Fe films prepared on Cu(001), Cu(110) and Cu(111) were all antiferromagnetic.

Spin-polarized photoelectron emission experiments were performed by Pescia et al. (Pescia et al., 1987) on 1, 3 and 5 monolayer (ML) thick Fe films on Cu(001) that were grown at room temperature. All of the Fe films were ferromagnetic, with Curie temperatures of 230 ± 30 K for the 1 ML thick Fe film and 390 ± 30 K for the 3 and 5 ML thick Fe films. At room temperature none of the films were perpendicularly magnetized in zero applied magnetic field. At 30 K, only the 5 ML thick Fe film was perpendicularly magnetized in zero applied field.

A likely explanation for the wide variety of results obtained for the Fe on Cu system is the different growth conditions used in each case. Recently, very careful studies of the growth of Fe on Cu(001) have been performed using molecular beam epitaxy and surface analysis techniques.

Chambers et al. (Chambers et al., 1987) have carried out such studies using low energy electron diffraction (LEED) and medium and high energy Auger electron diffraction. They found that Fe films of good structural quality can be grown at room temperature for

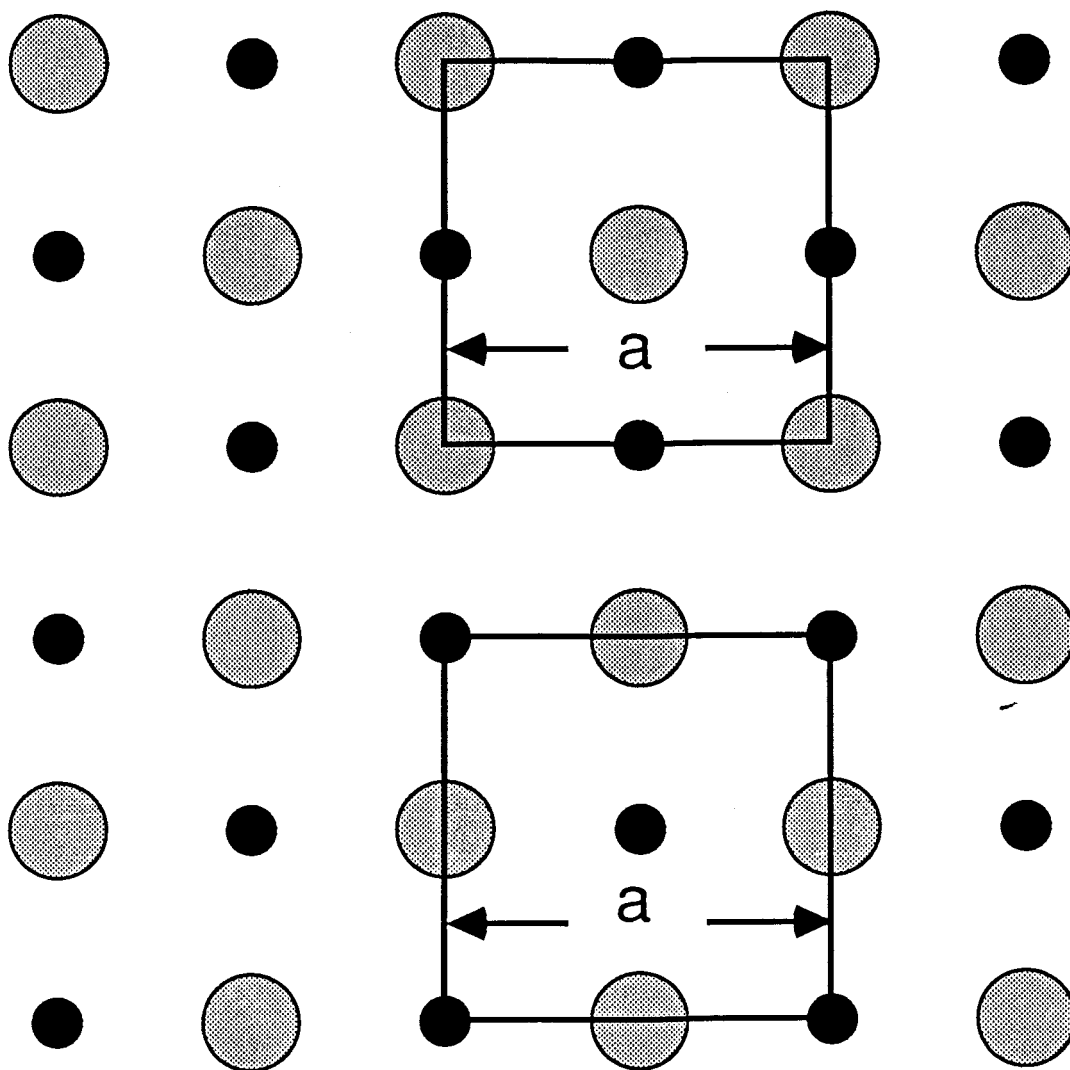


Figure 5.1

The growth of fcc Fe on fcc Cu(001). The solid balls correspond to atoms in the outermost layer of the copper substrate and the shaded balls correspond to atoms in the first monolayer of iron.

thicknesses between 2 and 5 ML. For substrate temperatures greater than 125°C, interdiffusion of Fe and Cu atoms was observed.

Steigerwald and Egelhoff (Steigerwald and Egelhoff, 1988) have performed a careful study of the growth of Fe on Cu(001) using x-ray photoelectron spectroscopy (XPS), reflection high energy electron diffraction (RHEED), LEED, XPS forward scattering and RHEED specular spot intensity oscillations. They have successfully grown single films and superlattice structures of Fe on Cu(001). They have obtained a reliable recipe for good quality films thicker than 3 ML; this recipe, which is described in detail in section 5.2, consists of the deposition of the Fe film at 100K, followed by an anneal at 350K. They found that for substrate temperatures of 300K or slightly higher during growth, the Cu atoms in the surface of the substrate segregate onto the surface of the deposited Fe film.

BLS and FMR were performed on the single film and superlattice samples grown by Steigerwald and Egelhoff (Dutcher et al., 1988a). The BLS experiments are described in detail in section 5.3 of this thesis. The major result of these magnetic studies was the unambiguous determination of perpendicular magnetization in zero applied field at room temperature for all of the samples.

Very recently, in-situ polar magneto-optic Kerr effect measurements have been used to study perpendicular magnetization in the Fe on Cu(001) system (Liu et al., 1988). Measurements were performed for film thicknesses up to 8 ML and growth temperatures between 100K and 350K. They found that perpendicular magnetization in zero applied magnetic field was obtained for films 1.5 to 5.7 ML thick for film deposition at 100K. These results are consistent with those of Dutcher et al. (Dutcher et al., 1988a) for 3 ML thick Fe films.

Considerable theoretical efforts have been directed toward the calculation of the magnetic properties of bulk fcc Fe (Wang et al., 1985; Pinski et al., 1986; and Moruzzi et al., 1986). Recently, calculations have been performed for several atomic layers of fcc Fe

on Cu(001) substrates (Fu and Freeman, 1987; and Fernando and Cooper, 1988). Fu and Freeman found that 2 ML of Fe on Cu(001) were ferromagnetically coupled; for 5 ML of Fe on Cu(001) and covered by Cu, the middle Fe layer was antiferromagnetically coupled to its neighbouring layers but the two Fe layers at each interface were ferromagnetically coupled.

5.2 Sample preparation

The fcc iron on copper samples discussed in this and the following section were grown by Drs. W.F. Egelhoff, Jr., D.A. Steigerwald and I. Jacob at the National Bureau of Standards in Gaithersburg, Maryland, U.S.A. The geometry of the different samples used in the BLS studies is shown schematically in figure 5.2. In this figure, the lightly shaded blocks correspond to copper and the heavily shaded blocks correspond to iron. Each sample consisted of a copper (001) substrate, covered by the magnetic layers, and capped by a thin copper layer to protect the iron films against oxidation. The first type of sample shown in figure 5.2(a) contained single iron films; for these samples, the single iron films were 3 monolayer (ML) thick (additional samples were grown with a single 3.5 ML thick iron film and a 4.5 ML thick iron film). The second and third types of samples were superlattice films. For figure 5.2(b), the basic building block of the superlattice was a 3 ML thick iron film covered by a 3 ML thick copper film. For figure 5.2(c), the basic building block was a 3 ML thick iron film covered by a 10 ML thick copper film. For both (b) and (c), the basic building block was repeated ten times to form the superlattice structures. The various samples that were used in this study are listed in table 5.1.

Steigerwald and Egelhoff have developed a technique for obtaining good quality films of iron on copper (001) for films that are > 3 ML thick. The preparation and structural characterization of these samples has been described in detail (Steigerwald and Egelhoff, 1988). The substrates were polished copper (001) single crystals, 1cm in diameter and

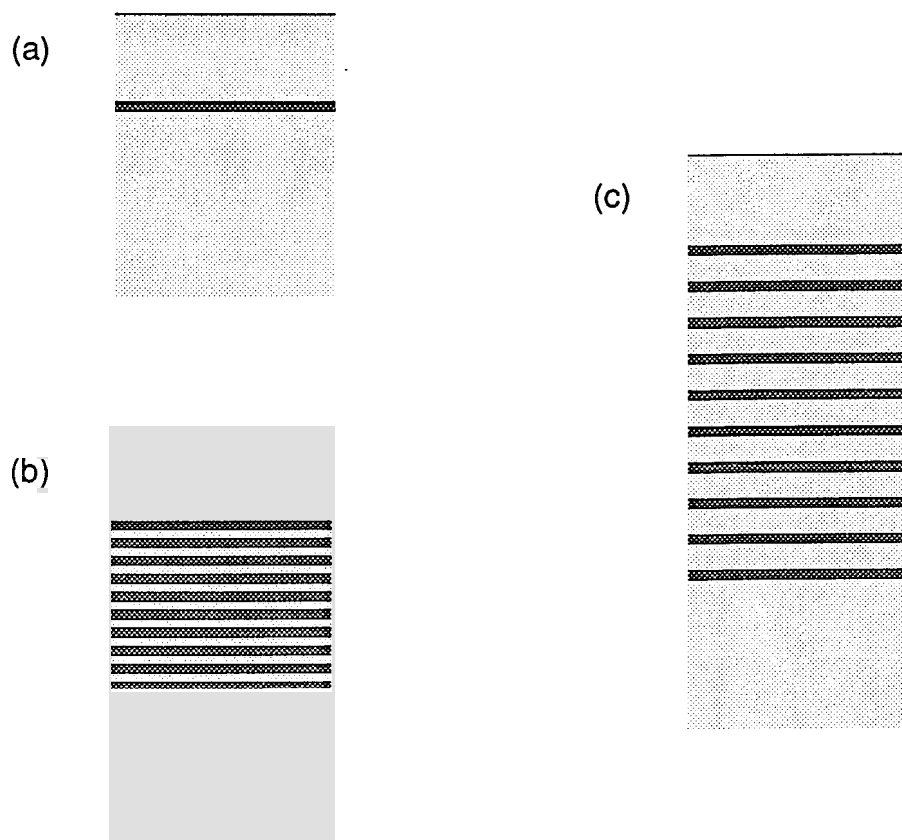


Figure 5.2

Fe on Cu(001) sample geometry:

(a) Cu on 3 ML Fe on bulk Cu(001) crystals

(b) Cu on superlattice of 10 repetitions of (3 ML Fe/ 3 ML Cu) sandwich on bulk Cu(001) crystals.

(c) Cu on superlattice of 10 repetitions of (3 ML Fe/ 10 ML Cu) sandwich on bulk Cu(001) crystals.

Table 5.1

The fcc Fe on Cu(001) single film and superlattice samples studied by BLS. The sample numbers used by Dutcher et al. (Dutcher et al., 1988a) have been indicated in square brackets.

Sample	Composition
5.1 [1]	100ML Cu / 3.0ML Fe / Cu(001)
5.2 [2]	60ML Cu / 3.0ML Fe / Cu(001)
5.3	60ML Cu / 3.0ML Fe / Cu(001)
5.4	60ML Cu / 3.5ML Fe / Cu(001)
5.5	60ML Cu / 4.5ML Fe / Cu(001)
5.6	60ML Cu / 3.0ML Fe / Cu(001)
5.7 [3]	150ML Cu / $10 \times (3.0\text{ML Fe} + 3.0\text{ML Cu})$ / Cu(001)
5.8 [4]	90ML Cu / $10 \times (3.0\text{ML Fe} + 10\text{ML Cu})$ / Cu(001)
5.9 [5]	150ML Cu / $10 \times (3.0\text{ML Fe} + 10\text{ML Cu})$ / Cu(001)
5.10	60ML Cu / $10 \times (3.0\text{ML Fe} + 10\text{ML Cu})$ / Cu(001)

2mm thick, with the surface orientation aligned with the (001) direction to within 1° . Both substrate surfaces were ion sputter etched for two hours at room temperature and then sputtered for several hours at $T = 1000\text{K}$. Several minutes of sputtering at room temperature followed by a brief anneal to 700K resulted in a substrate surface which was clean to within x-ray photoelectron spectroscopy (XPS) limits and which exhibited sharp low energy electron diffraction (LEED) and reflection high energy electron diffraction (RHEED) patterns.

The iron and the copper films were deposited using metal vapor sources. The pressure rise in the sample preparation chamber was $< 5 \times 10^{-11}$ Torr with both sources turned on. Deposition rates were typically 2 to 6 ML per minute. Film thicknesses were monitored by means of two independent water cooled quartz crystal thickness monitors and an ion gauge integration system, which consisted of two nude ion gauge tubes, one mounted in the path of the evaporated metal, and the other mounted away from the metal flux. The difference between the two gauge readings gave the metal flux to within $\pm 5\%$.

XPS, RHEED and LEED were used to monitor the growth of the films. The intensity of the copper $2p_{3/2}$ XPS peak was monitored with an angle-resolved detector during the film growths. This technique is known as XPS forward scattering and is a very useful structural probe during the initial stages of film growth (Egelhoff, 1984).

For the growth of the single iron films, the substrate temperature was held at 100K . The samples were then warmed to 350K . This allowed the iron to become moderately well-ordered, without allowing agglomeration of the iron or surface segregation of the copper to take place. The copper coverlayers were deposited at the annealing temperature of the iron films.

For the superlattice samples, the growth of each iron/copper film pair was identical to that for a single iron film with a covering copper layer, as described above. After deposition of the copper layer, the sample was cooled to 100K and the process was

repeated. For good vacuum conditions ($\sim 10^{-10}$ Torr) the final copper film in the superlattice was indistinguishable from the copper substrate, as observed with XPS, RHEED and LEED.

5.3 Brillouin light scattering results and discussion

Figures 5.3 to 5.13 contain representative BLS spectra of counts versus frequency shift and plots of surface mode frequencies as a function of the applied magnetic field for the Fe/Cu single film and superlattice samples listed in table 5.1. The crosses on each frequency versus field plot correspond to BLS data; the boxes correspond to room temperature ferromagnetic resonance (FMR) data obtained at 9.54, 12.94, and 23.97 GHz. As discussed in sections 3.1.5.4.3 and 3.2.1, the surface mode frequencies for ultrathin magnetic films are essentially to those given by the ferromagnetic resonance condition. The agreement between the BLS and FMR data in figures 5.4, 5.11 and 5.13 is very good. Also included on each frequency versus field plot are solid curves calculated using the theory presented in section 3.2.1. The effective magnetization $(4\pi M_S)_{\text{eff}}$, the g -factor and the second-order uniaxial anisotropy field $4K_u^{(2)}/M_S$ were obtained for each of the samples from fits to the data in figures 5.3 to 5.13. The results are listed in table 5.2. None of the samples showed a dependence of the surface mode frequency on the direction of the applied field in the sample plane. Therefore, in-plane anisotropy fields were not included in the fits to the data. The ultrathin layers of the metastable fcc phase of iron were stable with time; there were no measurable changes in the magnetic properties of sample 5.1 over a period of several months.

For each sample, the frequency versus field plot consisted of low and high field branches separated by a crossover field H_C , see section 3.2.4. $(4\pi M_S)_{\text{eff}}$ and the g -factor were chosen for each sample to obtain a good fit to the high field branch, since the quality of the data was better for the high field branch than for the low field branch. The value of

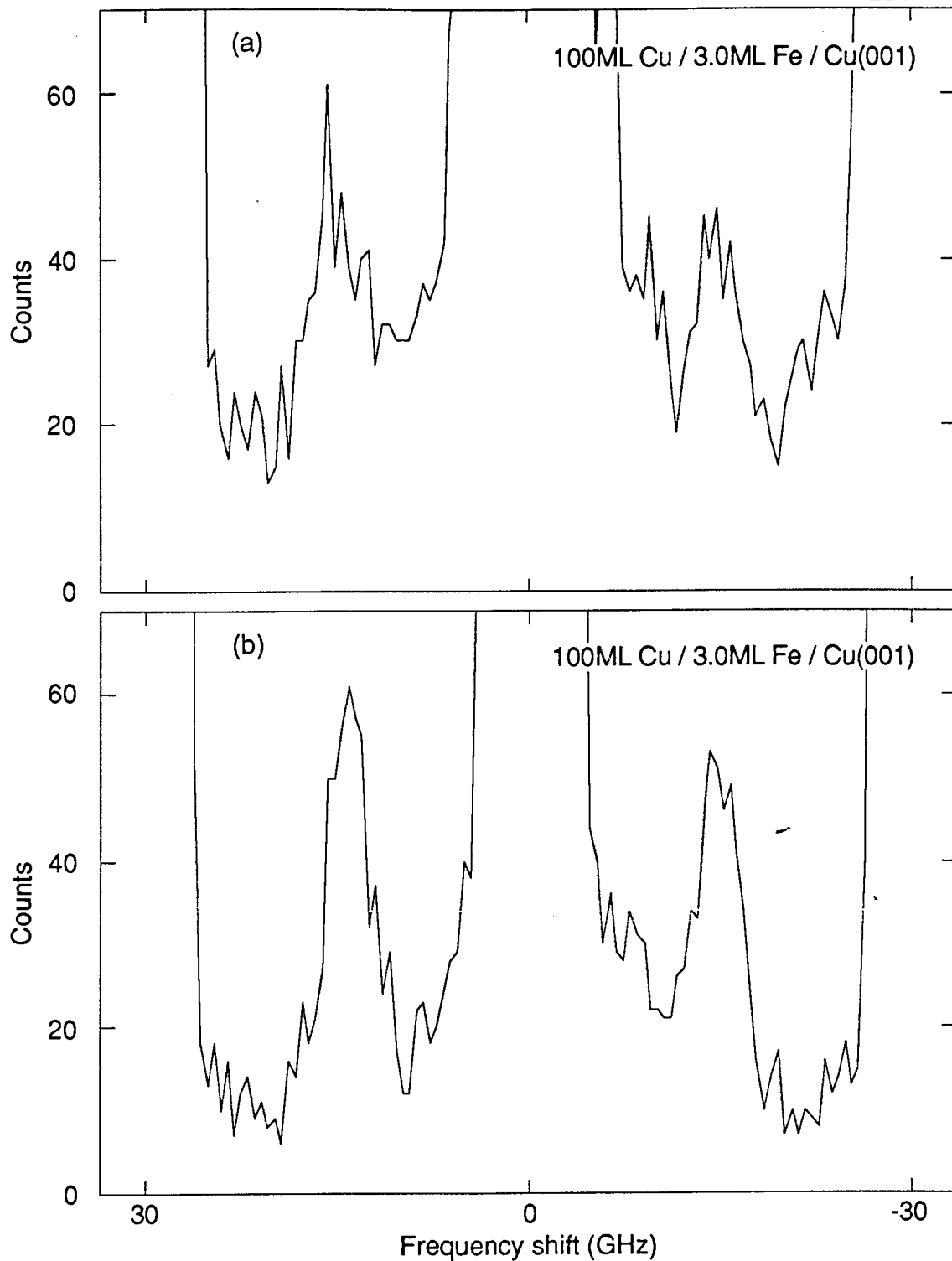


Figure 5.3

- (a) BLS spectrum for sample 5.1 for a field of $H = 3.32$ kOe, a laser power of 140 mW and a counting time for each of the 128 data points of 12.136 s.
- (b) BLS spectrum for sample 5.1 for a field of $H = 9.70$ kOe, a laser power of 140 mW and a counting time for each of the 128 data points of 12.136 s.

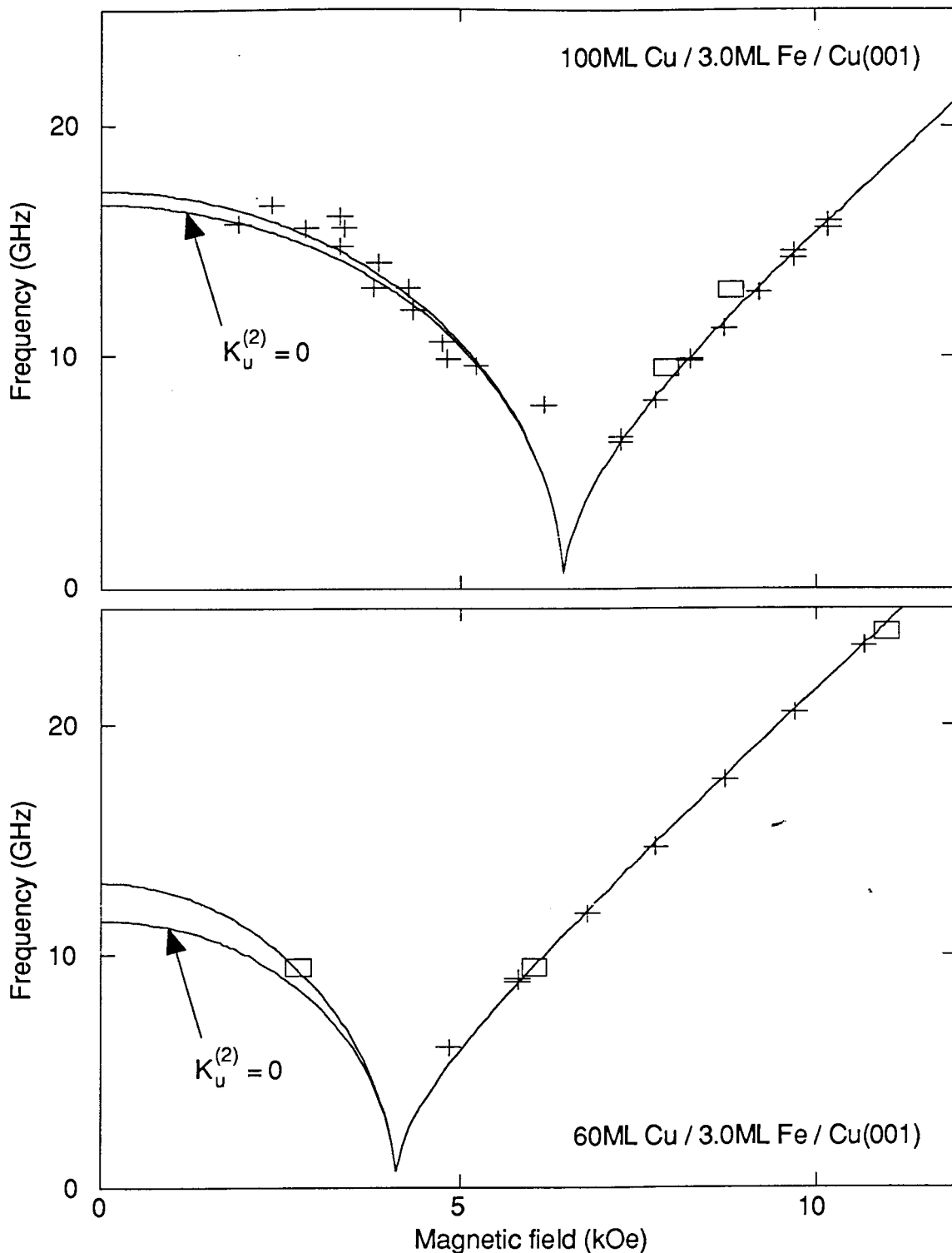


Figure 5.4

- (a) Magnetic field dependence of the surface mode frequency for sample 5.1. The crosses are measured data points. The solid curves have been calculated using the theory of Chapter Three and the parameters listed in table 5.2.
- (b) Magnetic field dependence of the surface mode frequency for sample 5.2. The crosses are measured data points. The solid curves have been calculated using the theory of Chapter Three and the parameters listed in table 5.2.

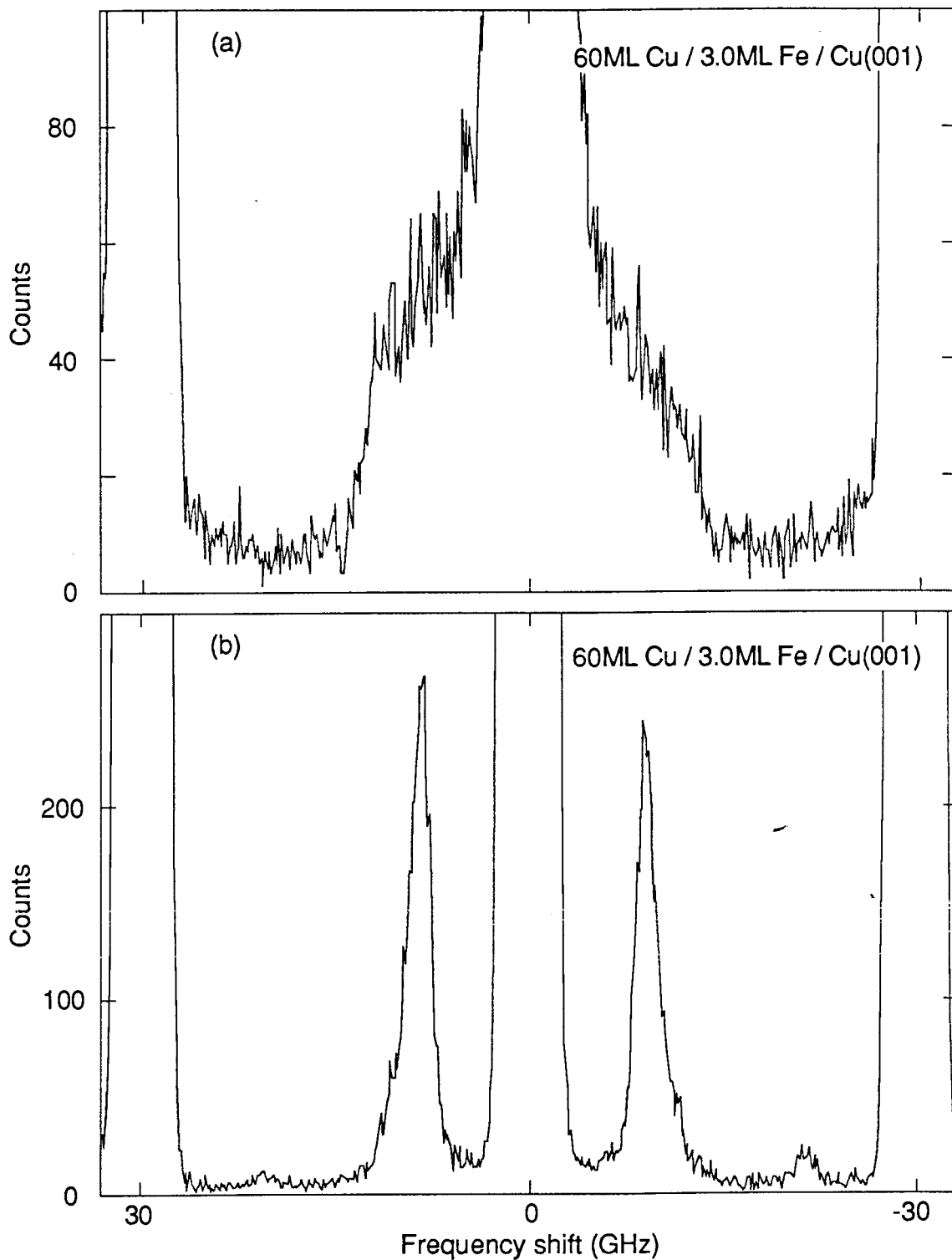


Figure 5.5

- (a) BLS spectrum for sample 5.2 for a field of $H = 1.92$ kOe, a laser power of 140 mW and a counting time for each of the 512 data points of 4.560 s.
- (b) BLS spectrum for sample 5.2 for a field of $H = 5.81$ kOe, a laser power of 140 mW and a counting time for each of the 512 data points of 2.012 s.

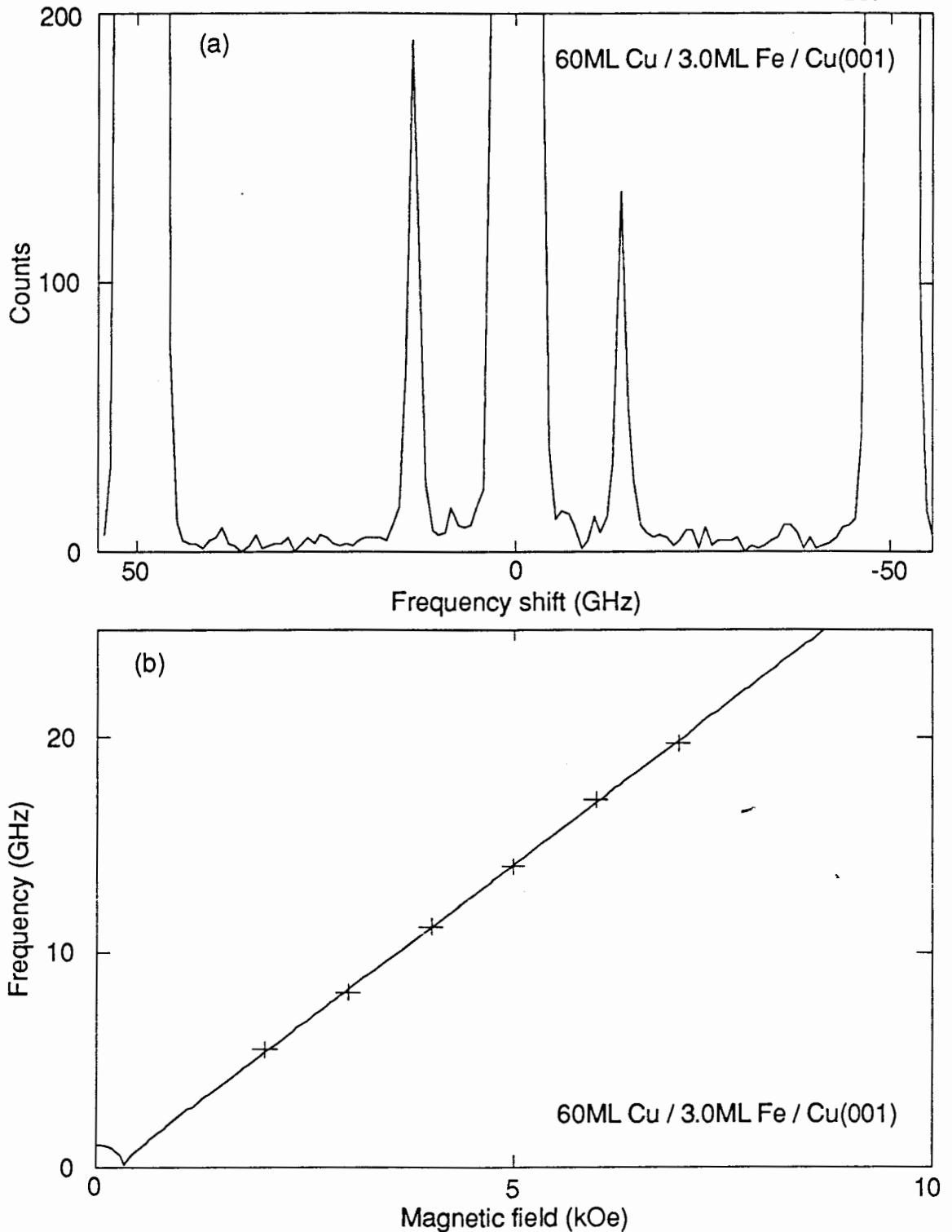


Figure 5.6

- (a) BLS spectrum for sample 5.3 for a field of $H = 5.00$ kOe, a laser power of 140 mW and a counting time for each of the 128 data points of 5.036 s.
- (b) Magnetic field dependence of the surface mode frequency for sample 5.3. The crosses are measured data points. The solid curve has been calculated using the theory of Chapter Three and the parameters listed in table 5.2.

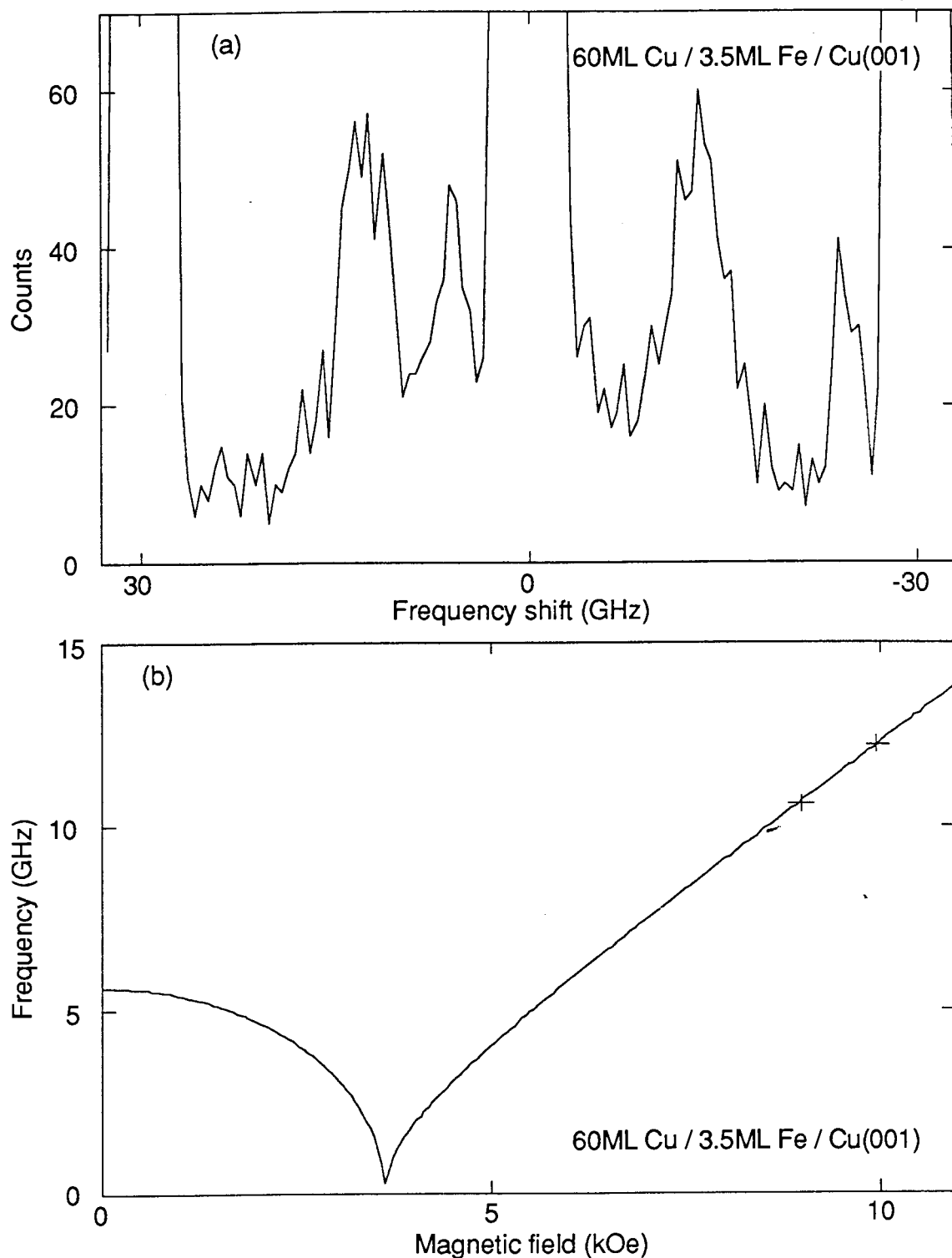


Figure 5.7

- (a) BLS spectrum for sample 5.4 for a field of $H = 9.97$ kOe, a laser power of 140 mW and a counting time for each of the 128 data points of 9.052 s.
- (b) Magnetic field dependence of the surface mode frequency for sample 5.4. The crosses are measured data points. The solid curve has been calculated using the theory of Chapter Three and the parameters listed in table 5.2.

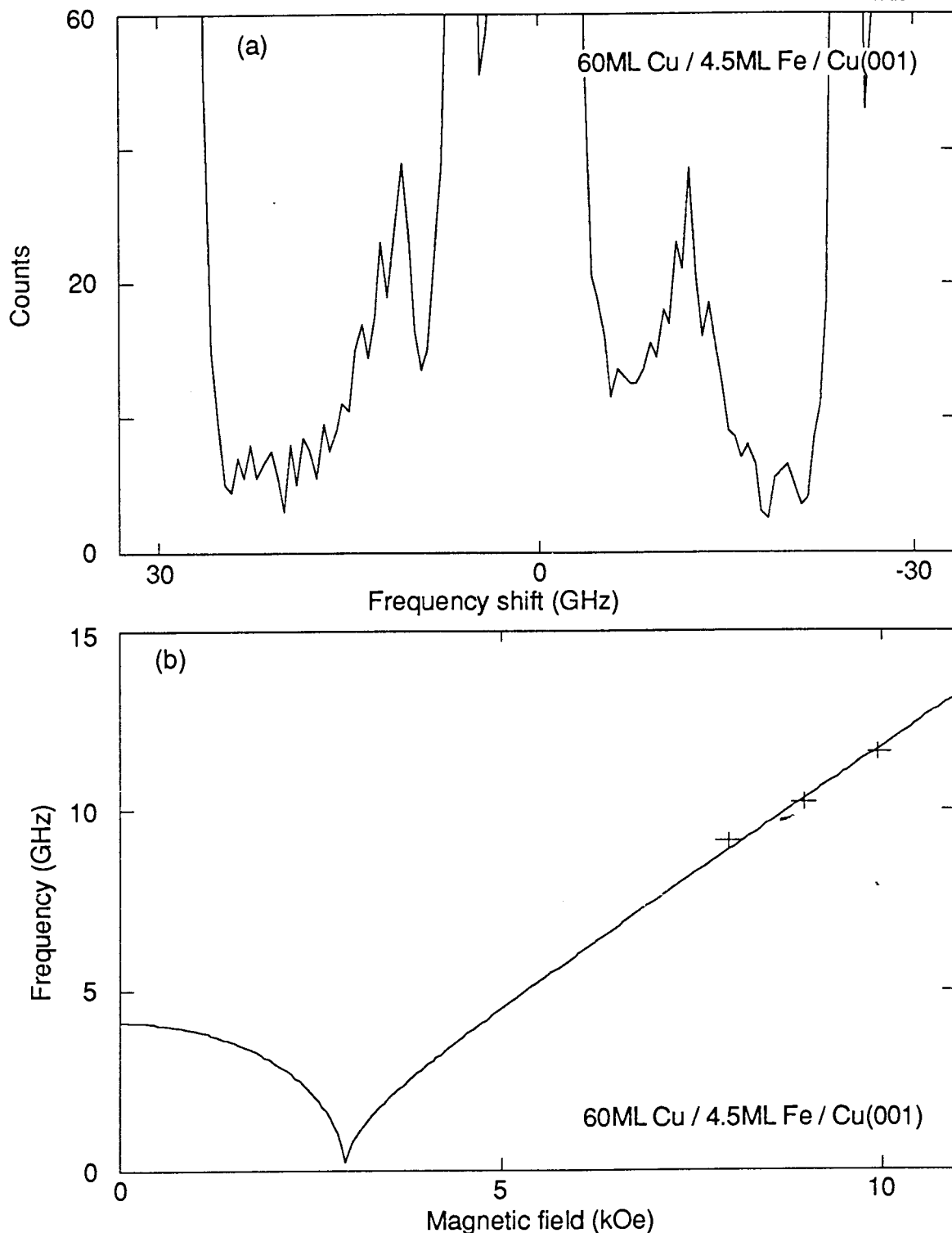


Figure 5.8

- (a) BLS spectrum for sample 5.5 for a field of $H = 9.97$ kOe, a laser power of 140 mW and a counting time for each of the 128 data points of 9.644 s.
- (b) Magnetic field dependence of the surface mode frequency for sample 5.5. The crosses are measured data points. The solid curve has been calculated using the theory of Chapter Three and the parameters listed in table 5.2.

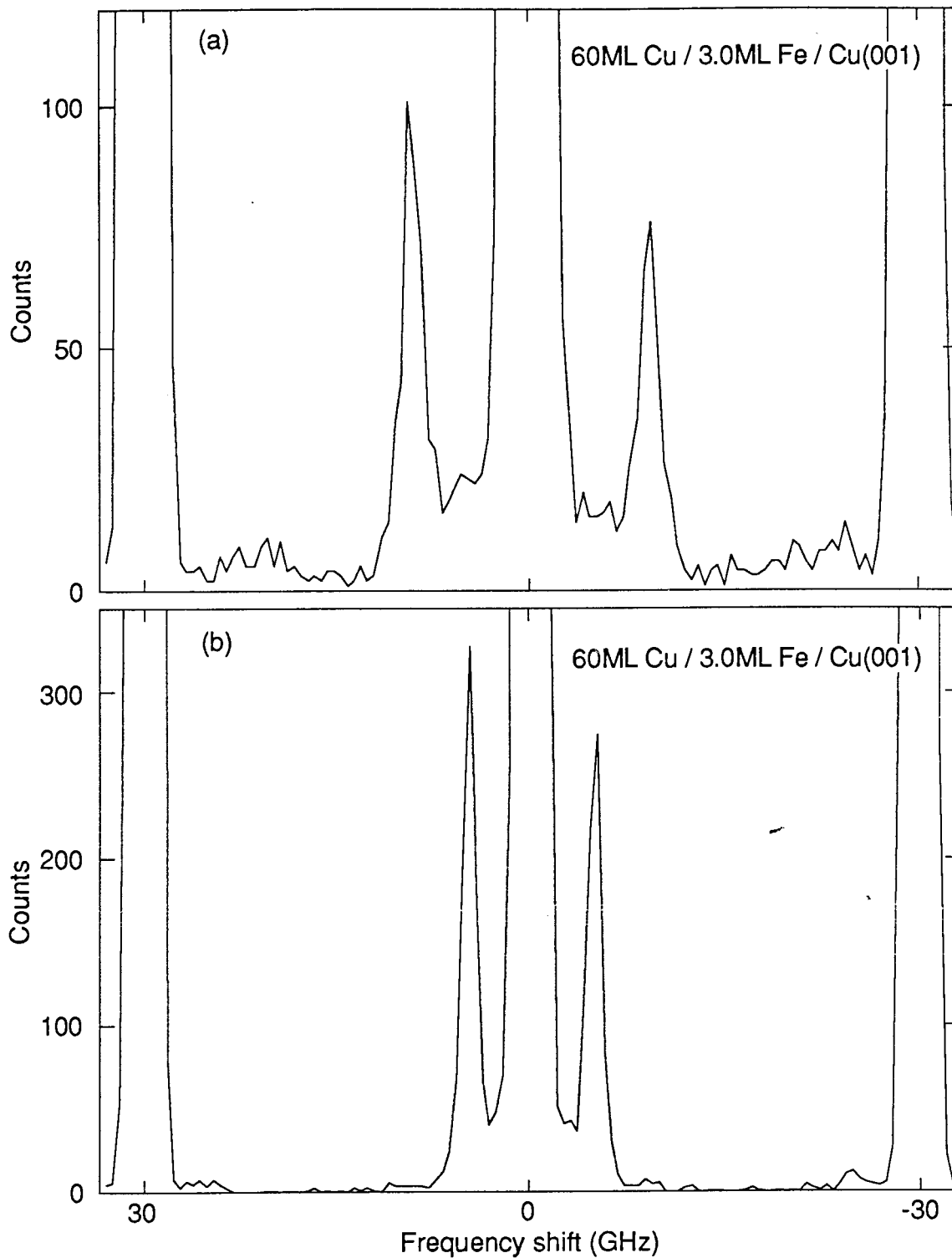


Figure 5.9

- (a) BLS spectrum for sample 5.6 for a field of $H = 3.02$ kOe, a laser power of 140 mW and a counting time for each of the 128 data points of 5.512 s.
- (b) BLS spectrum for sample 5.6 for a field of $H = 4.51$ kOe, a laser power of 140 mW and a counting time for each of the 128 data points of 1.024 s.

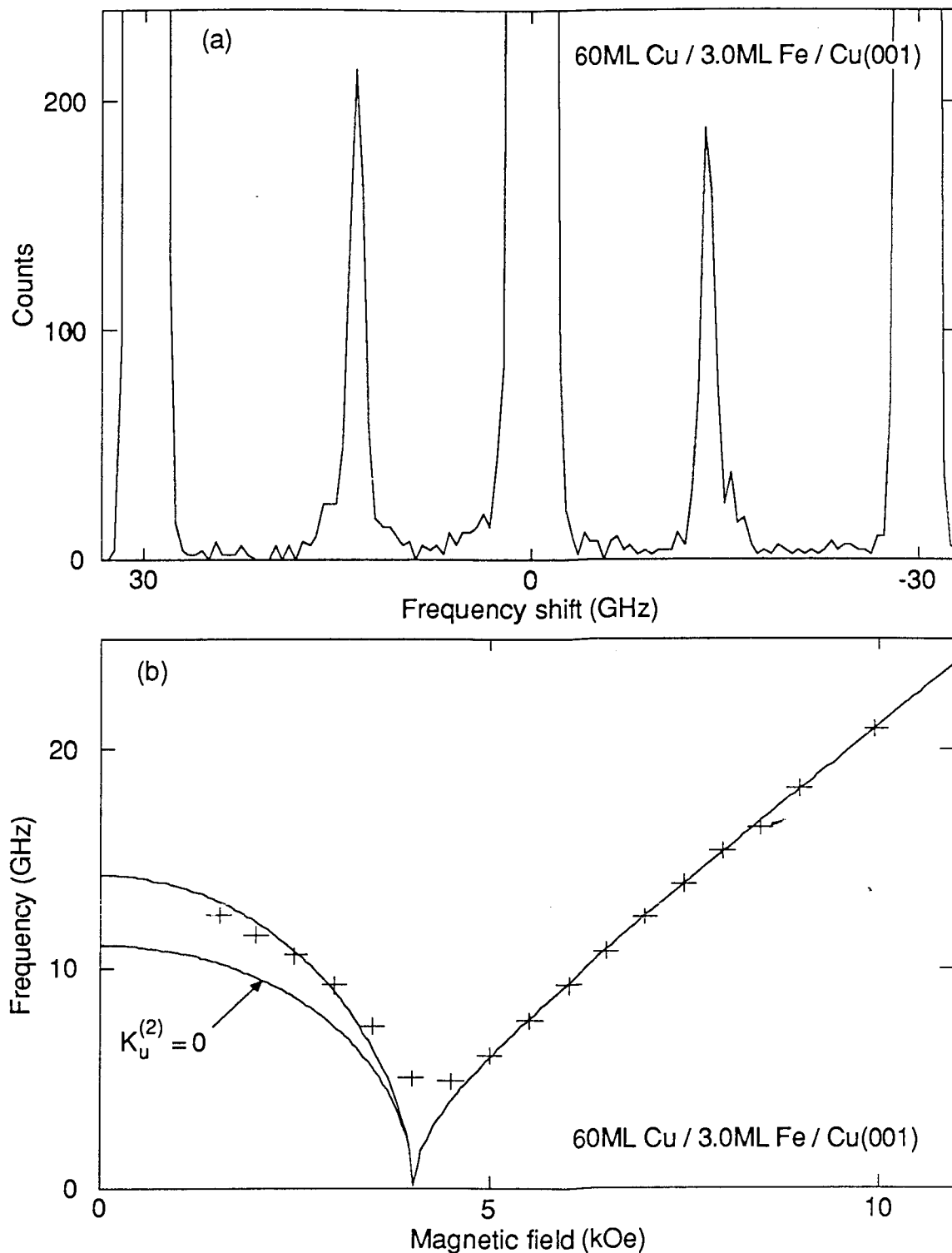


Figure 5.10

- (a) BLS spectrum for sample 5.6 for a field of $H = 7.49$ kOe, a laser power of 140 mW and a counting time for each of the 128 data points of 2.532 s.
- (b) Magnetic field dependence of the surface mode frequency for sample 5.6. The crosses are measured data points. The solid curves have been calculated using the theory of Chapter Three and the parameters listed in table 5.2.

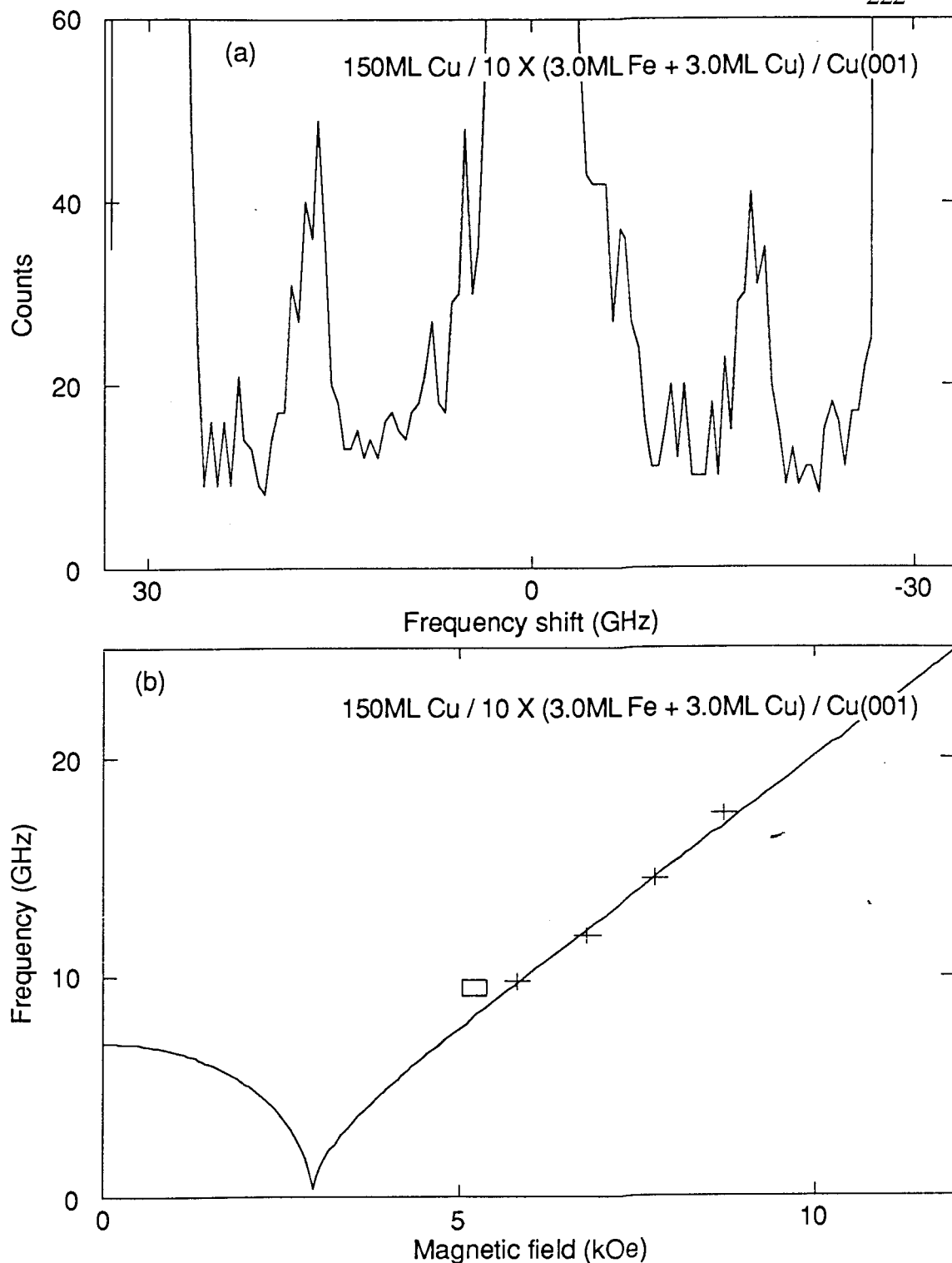


Figure 5.11

- (a) BLS spectrum for sample 5.7 for a field of $H = 8.72$ kOe, a laser power of 140 mW and a counting time for each of the 128 data points of 7.436 s.
- (b) Magnetic field dependence of the surface mode frequency for sample 5.7. The crosses are measured data points. The solid curve has been calculated using the theory of Chapter Three and the parameters listed in table 5.2.

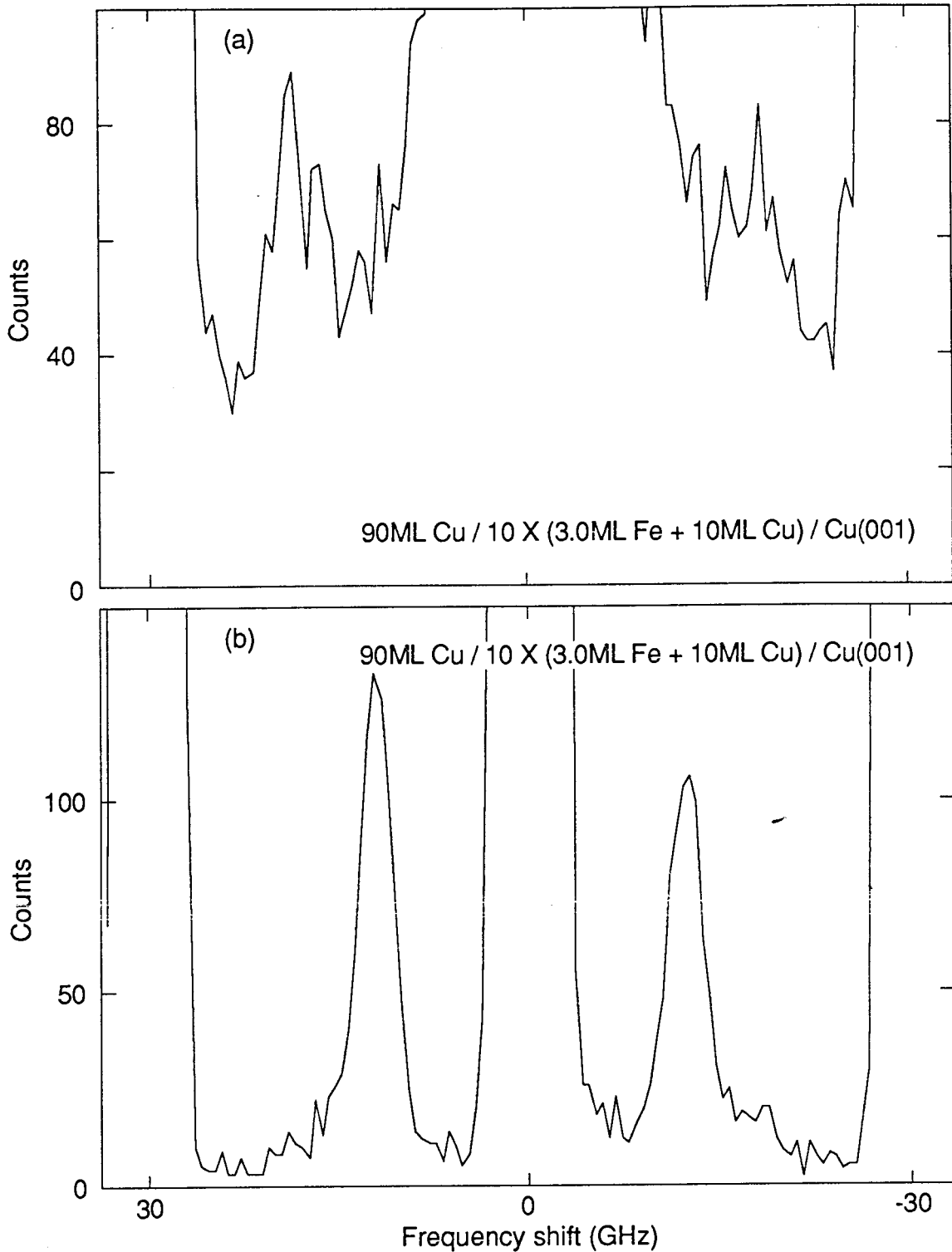


Figure 5.12

- (a) BLS spectrum for sample 5.8 for a field of $H = 4.84$ kOe, a laser power of 140 mW and a counting time for each of the 128 data points of 8.024 s.
- (b) BLS spectrum for sample 5.8 for a field of $H = 8.72$ kOe, a laser power of 140 mW and a counting time for each of the 128 data points of 2.000 s.

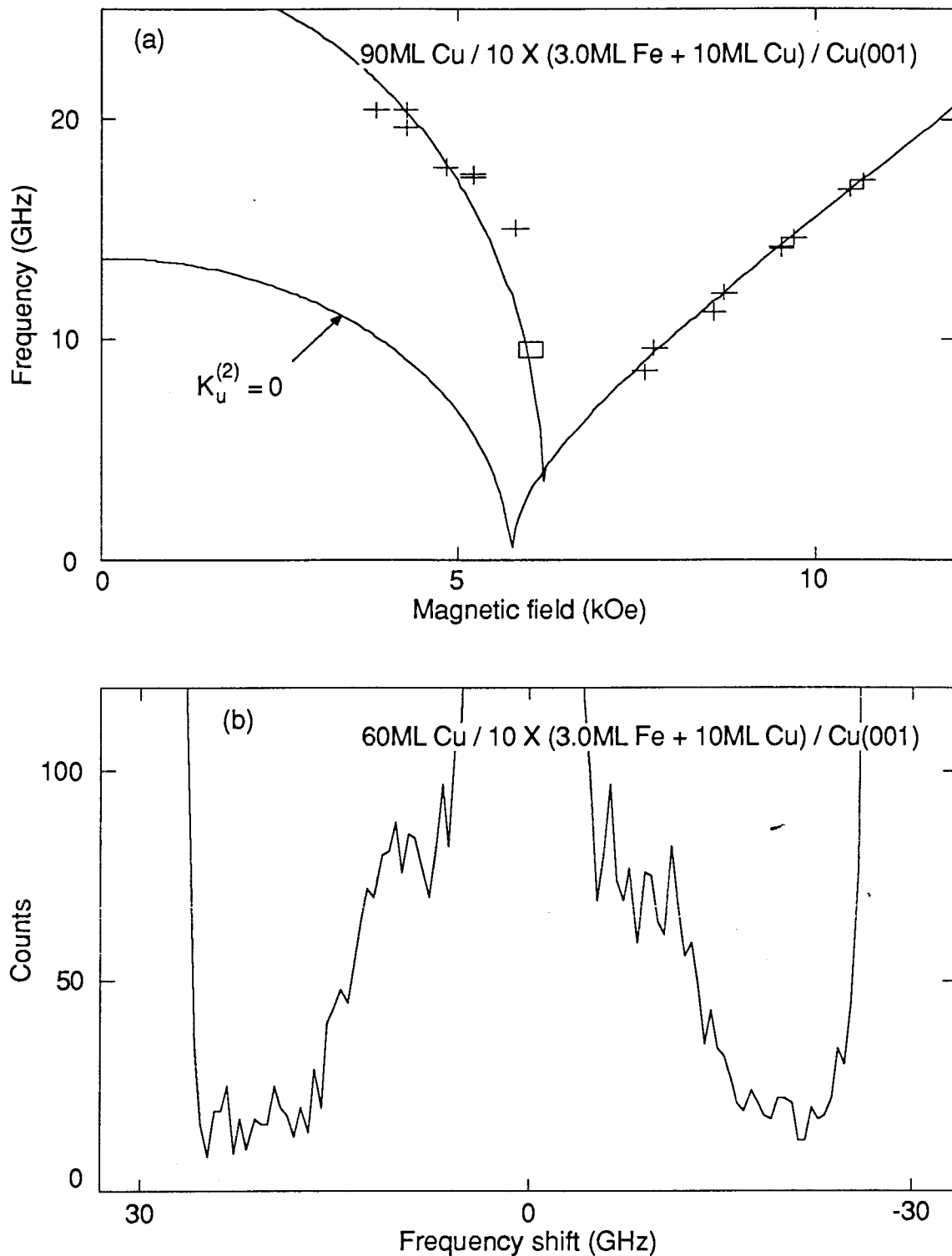


Figure 5.13

- (a) Magnetic field dependence of the surface mode frequency for sample 5.8. The crosses are measured data points. The solid curve has been calculated using the theory of Chapter Three and the parameters listed in table 5.2.
- (b) BLS spectrum for sample 5.10 for a field of $H = 5.83$ kOe, a laser power of 140 mW and a counting time for each of the 128 data points of 13.512.

Table 5.2

The magnetic parameters for the fcc Fe on Cu(001) single film and superlattice samples of table 5.1. Each Fe film was covered with epitaxial Cu. For each sample, the effective magnetization ($4\pi M_S$)_{eff}, the g-factor, the second order uniaxial anisotropy field $4K_U^{(2)}/M_S$ and the spin pinning parameter K_S (calculated for $4\pi M_S = 21.55$ kG) are listed. The parameters were determined both by BLS and ferromagnetic resonance (Dutcher et al., 1988b).

Sample	$(4\pi M_S)_{\text{eff}}$ (kG)	g-factor	$\frac{4K_u^{(2)}}{M_S}$ (kOe)	$K_S^{(a)}$ (erg/cm ²)
5.1	-6.5	1.84	0.23	1.03
5.2	-4.1	2.00	0.58	0.94
5.3	-0.33	2.09	—	0.81
5.4	-3.6	1.1	—	1.1
5.5	-2.9	1.0	—	1.3
5.6	-4.0	1.95	1.17	0.94
5.7	-2.9	1.70	—	0.90
5.8	-5.8	1.70	5.60	1.01
5.9	-2.7	1.83	—	0.89
5.10	—	—	—	—

(a) calculated assuming $4\pi M_S = 21.55$ kG

the g-factor determined the slope of the high field branch and the value of $(4\pi M_s)_{\text{eff}}$ determined the value of the crossover field H_C between the two branches. The value of the second order uniaxial anisotropy field was chosen to pass the low field branch through the low field data points; it had no effect on the high field branch, as discussed in section 3.2.1 and 3.2.4.

The effective magnetization $(4\pi M_s)_{\text{eff}}$ may be written as, see equation (3.136),

$$(4\pi M_s)_{\text{eff}} = 4\pi M_s - H_s \quad (5.3)$$

where the first-order uniaxial anisotropy field H_s is given by

$$H_s = \frac{2K_u^{(1)}}{M_s} = \frac{2K_s}{M_s d}, \quad (5.4)$$

$K_u^{(1)}$ is the first order uniaxial anisotropy constant defined in equation (3.166), d is the magnetic film thickness, and $K_s = (K_u^{(1)} d)$ is the surface anisotropy constant discussed in section 3.1.5.4.2. Column 5 of table 5.2 contains the values of K_s calculated for $4\pi M_s = 21.55$ kG.

The surface mode peaks could be seen on both the low and high branches for single film samples 5.1 and 5.6, and for superlattice sample 5.8, see figure 5.3, 5.9, 5.10 and 5.12 respectively. In general, the intensities of the peaks were considerably smaller for the low field spectra than for the high field spectra. For sample 5.6, such strong peaks were obtained that the low field branch could be measured in detail; this allowed measurements of the peak intensity as a function of applied magnetic field, as discussed below.

For single film samples 5.2 and 5.3, and superlattice sample 5.7, strong peaks were observed on the high field branch, see figures 5.5, 5.6 and 5.11 respectively. The values

of $(4\pi M_s)_{\text{eff}}$ were too close to zero for samples 5.3 and 5.7 to allow the observation of the low field branch. Sample 5.2 displayed very strong peaks on the high field branch but the low field branch spectra, see figure 5.5(a), were of poor quality. A broad central hump, which could not be resolved from the central elastically scattered peak, was observed for the low field spectra.

Broad weak peaks on the high field branch were observed for single film samples 5.4 and 5.5, see figures 5.7 and 5.8. Ghost peaks of the laser, as discussed in section 4.2.3, can be seen in the spectra in figures 5.7 and 5.8. The superlattice sample 5.10, which was grown under the best vacuum conditions (chamber pressure $\sim 10^{-11}$ Torr), yielded the poorest BLS data. A typical spectrum is shown in figure 5.13(b): a broad central hump which could not be resolved from the central elastically scattered peak was observed. Superlattice sample 5.9 was not available for BLS studies; the magnetic parameters listed for this sample in table 5.2 were obtained from FMR measurements at 9.54 GHz and 12.94 GHz.

The major result of the BLS experiments is that all of the single film and superlattice samples were characterized by a first-order uniaxial anisotropy large enough to make $(4\pi M_s)_{\text{eff}} < 0$. This implies that for all of the samples the magnetization was oriented perpendicular to the sample surface in zero applied magnetic field at room temperature. This is in sharp contrast to the results of Pescia et al. (Pescia et al., 1987) who did not observe perpendicular magnetization at room temperature.

In general, the g-factors required to obtain good fits to the high field branch data were very low compared with the value for bulk bcc iron, $g = 2.09$. A smaller g-factor results in a smaller surface mode frequency for a given value of the applied magnetic field. It was noticed that large surface mode linewidths were obtained for samples with low values of the g-factor: samples 5.7, 5.8 and especially samples 5.4 and 5.5. The large surface mode linewidths were likely due to a spread in the values of the first order uniaxial anisotropy

constant $K_u^{(1)}$. Because the value of $K_u^{(1)}$ is inversely proportional to the film thickness, see equation (5.4), small variations in the film thickness produce significant broadening of the surface mode peaks for ultrathin magnetic films. For a 3 ML thick iron film with a g-factor of 2.00, $(4\pi M_s)_{\text{eff}} = -5$ kG, no second order uniaxial anisotropy field and an applied magnetic field of $H = 8$ kOe, a change of only $\pm 1.5\%$ in $K_u^{(1)}$ results in a shift of ± 1 GHz in the surface mode frequency. This simple argument can be used to understand the large surface mode linewidths, but does not explain the low values of the g-factor. The source of these low values of the g-factor is not known.

The single film and superlattice samples had very similar values of $(4\pi M_s)_{\text{eff}}$ and, therefore, the first-order uniaxial anisotropy field H_s , see equation (5.3). The large values of H_s for the magnetic films are directly related to the small thickness d of each layer by equation (5.4). Therefore, the structure of each single 3 ML thick Fe film within the superlattice samples was as good as that of the single film samples; there was not a substantial degradation in the magnetic layer / nonmagnetic layer interface in the final, upper layers of the superlattice samples.

Superlattice sample 5.8 was purposely prepared in a poor vacuum (chamber pressure $\sim 10^{-8}$ Torr); the major contamination was carbon monoxide (CO). The magnetic properties of this sample were significantly different from the other samples in that a large value of the second-order uniaxial anisotropy field was required to fit the data. To investigate the effect of CO contamination on the magnetic properties of the films, sample 5.3 was prepared in the following manner. The 3 ML thick Fe film was deposited on the clean Cu substrate at 100K. The surface was then exposed to 5L CO, where 1L = 10^{-6} Torr-s. The film was annealed at 345K for 30s and covered by 60 ML Cu. This procedure was intended to exaggerate the effect of CO contamination of the Fe film surface. The results of the BLS experiments are shown in figure 5.6. The surface mode peaks have very narrow linewidths. However, the effective magnetization is higher, i.e. the first order

uniaxial anisotropy is smaller, than for all other Fe on Cu(001) samples. The relatively small value of the first order uniaxial anisotropy did not allow the observation of the low field branch. Therefore the strength of the second order uniaxial anisotropy could not be measured. These results indicate that CO contamination was probably not the primary cause for the unique magnetic properties of superlattice sample 5.8.

Superlattice sample 5.10 was prepared under the best vacuum conditions, yet it gave the poorest BLS signal, see figure 5.13(b). X-ray diffraction measurements were carried out on superlattice samples 5.8, 5.9 and 5.10 at the Cornell synchrotron facility. In x-ray diffraction measurements on superlattices, one looks for satellite peaks of the main diffraction peaks; observation of many satellite peaks indicates good superlattice periodicity. For samples 5.8 and 5.9 three satellite peaks were observed and for sample 5.10, only two satellite peaks were observed: sample 5.10 had the poorest structural quality (W.F. Egelhoff, Jr., 1988). Therefore, surprisingly, the superlattice sample grown under the best vacuum conditions had the worst structural and magnetic properties.

Single film samples 5.4 and 5.6 have also been very recently measured with grazing-incidence spin-polarized neutron reflection (SPNR) by Dr. R.F. Willis' group at the University of Cambridge, Cambridge, U.K. In these experiments, the spin asymmetry between the spin-up and spin-down neutrons in the scattered beam was measured as a function of the angle of incidence; this permitted the determination of the magnetic moment for magnetic films down to 1 ML thick (Willis et al., 1988). A large spin asymmetry was observed for sample 5.6 and a measurable signal was observed for sample 5.4. Preliminary analysis of their data has determined the magnetic moments of samples 5.4 and 5.6 to be 1.1 and 1.6 μ_B /atom respectively (Schwarzacher, 1988). These values correspond roughly to the low spin state of fcc Fe (Moruzzi et al., 1986). A 4.7 ML thick Fe single film sample, comparable to sample 5.5, did not yield a measurable SPNR signal.

This is consistent with the low quality BLS signal obtained for sample 5.5, as shown in figure 5.8.

Because the surface mode peaks were observed easily on both the high field and the low field branches for sample 5.6, see figures 5.9 and 5.10, the intensity of the peaks obtained at different values of the applied magnetic field could be compared. The results are shown in figure 5.14. The crosses correspond to experimental data; for each value, the maximum number of counts in each peak was divided by the total counting time per channel of the multichannel analyzer. The solid curve was calculated with the theory described in section 3.2 using the magnetic parameters determined from figure 5.10(b) and listed in table 5.2. The agreement between the data and the calculation is impressive. There is a dramatic increase in the intensity of the surface mode peaks as the crossover field $H_c = 4.0$ kOe between two branches is approached and the peak intensities for the low field branch are considerably lower than those for the high field branch. This intensity data provides strong supporting evidence to that obtained from the frequency versus magnetic field data that the magnetization is oriented perpendicular to the sample surface in zero applied magnetic field.

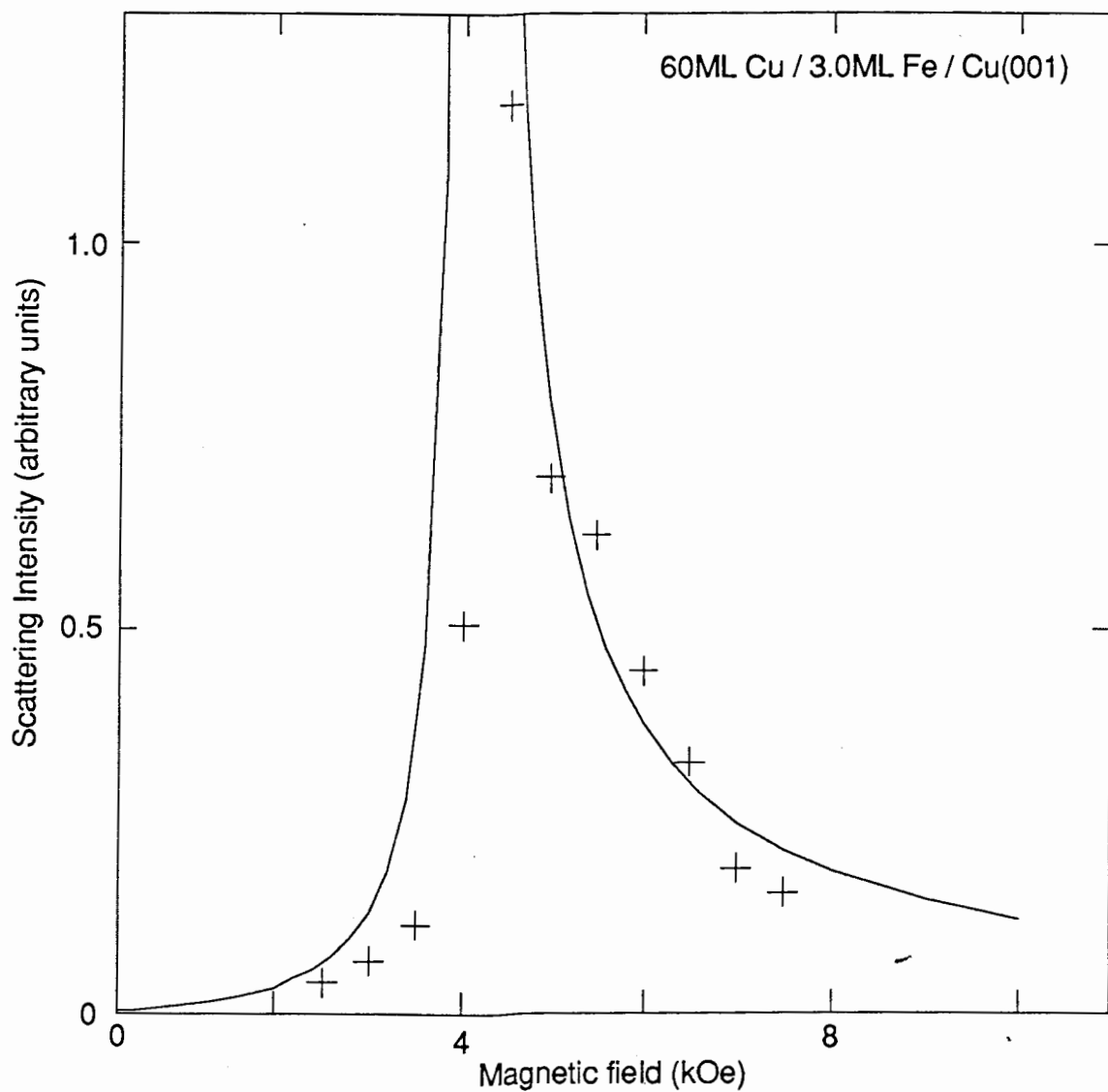


Figure 5.14

Scattering intensity as a function of applied magnetic field for sample 5.6. The crosses correspond to experimental data; the solid curve has been calculated using the theory described in section 3.2 and the parameters listed for sample 5.6 in table 5.2.

CHAPTER SIX

AN IRON WHISKER PREPARED IN ULTRAHIGH VACUUM

6.1 Introduction

Iron whiskers are needle-like single crystals of iron. Whiskers are excellent candidates for BLS studies because of the flatness of the whisker surface, the high purity of the iron (resistivity ratio > 1000) and the simple domain patterns in zero applied magnetic field.

Iron whiskers can be grown by chemical vapor transport (Brenner, 1956). In this procedure, 40 to 50 grams of anhydrous FeCl_2 powder is reduced by flowing dry H_2 gas over the powder at a temperature of approximately 700°C (Hanham, 1980). The whisker yield varies from growth to growth and is very sensitive to the growth temperature, the temperature gradient across the growth vessel and the hydrogen flow rate (Hanham, 1980). For a given growth, whiskers with different crystal orientations are obtained. The most common orientation has the $[001]$ direction along the whisker axis. These whiskers have very nearly a square cross-section, with the length much larger than the width. Typical values of the length and width are 10mm and 0.1mm, respectively.

In a magnetic material, the exchange interaction favors the parallel alignment of the spins, whereas the magnetic dipole-dipole interaction favors alternating spins. The exchange length d_{ex} is defined such that the exchange field for this length scale equals the demagnetizing field:

$$\frac{2A}{M_s} \left(\frac{1}{d_{\text{ex}}} \right)^2 = 4\pi M_s \quad (6.1)$$

or

$$d_{\text{ex}} = \sqrt{\frac{A}{2\pi M_s^2}} \quad (6.2)$$

where A is the exchange stiffness parameter in erg/cm and $4\pi M_s$ is the saturation magnetization in gauss. For iron, $d_{ex} = 33\text{\AA}$. For small magnetic fields, ferromagnetic samples with dimensions large compared with d_{ex} minimize their free energy by forming regions in which the magnetization points in different directions (Chikazumi, 1964). These regions are called domains. In each domain, the magnetization is equal to the saturation magnetization of the material, but the net magnetization of the sample is reduced from this value and may be as low as zero.

The Fe(001) whisker can have a particularly simple domain structure in zero applied field. This structure, known as the Landau structure, is shown schematically in figure 6.1. The arrows indicate the magnetization direction within each domain. The Fe(001) whisker has four domains: two larger domains along the whisker axis, and two smaller domains at the ends of the whisker. Domains with different magnetization directions are separated by domain walls. These walls are identified by the rotation of the magnetization in passing from one side of the wall to the other side. The two large domains of the Fe(001) whisker are separated by a 180° domain wall, and the two smaller domains are bounded by 90° domain walls.

The domain structure for one of the Fe(001) whisker faces containing the different domains is shown again in figure 6.2(a). As the magnetic field applied along the whisker axis is increased from zero, one of the larger domains grows as the other larger domain shrinks. The 180° domain wall bows out toward the whisker edge, as shown in figure 6.2(b). For a field $H=H_d$, known as the departure field, the domain wall touches the whisker edge and the central part of the whisker is completely magnetized along the magnetic field direction. Typical values of H_d for a good whisker are between 5 and 100 Oe (Heinrich and Arrott, 1972). H_d is also equal to the demagnetizing field for the sample, since it is essentially the field required to magnetize the sample along its axis.

Fe(001) whisker

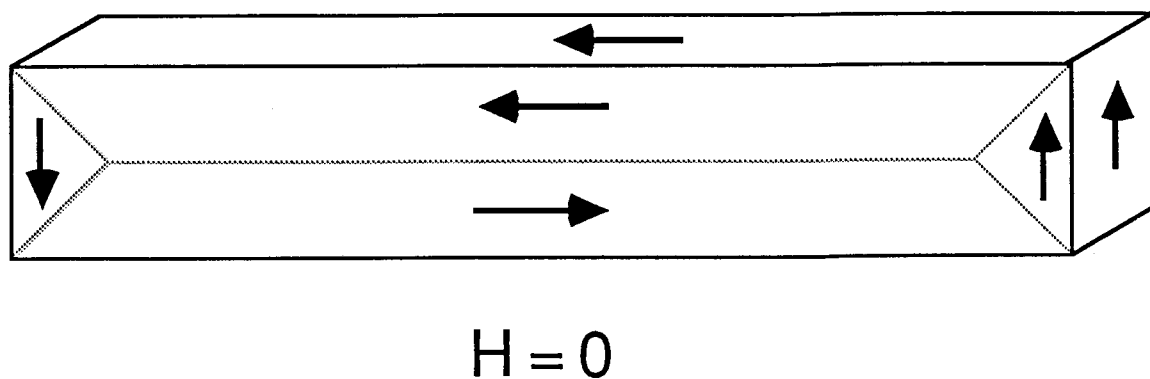
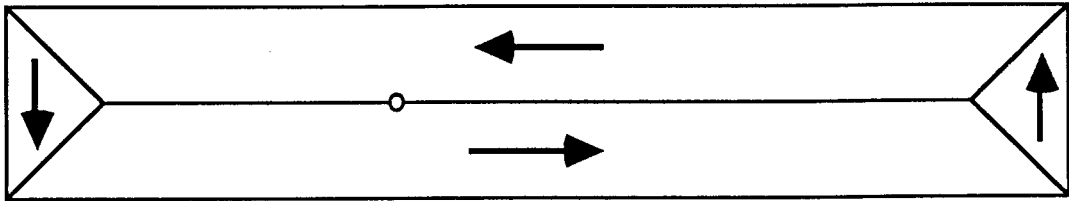


Figure 6.1

The domain structure of a perfect Fe(001) whisker in zero applied magnetic field H . Within each domain the direction of the magnetization is indicated by an arrow; the domain walls are indicated by dotted lines.

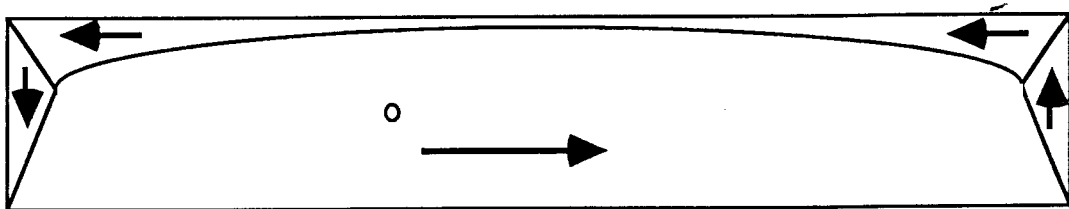
Fe(001) whisker

(a)



$$H = 0$$

(b)



$$0 \leq H \leq H_d$$

Figure 6.2

The domain structure of a perfect Fe(001) whisker for (a) zero applied field H , and (b) an applied field H less than the departure field H_d . The small circular spot on both (a) and (b) represents the laser beam focussed on the whisker surface.

6.2 Sample Preparation

For the BLS experiments, a Fe(001) whisker was cleaned and covered with epitaxial gold under ultrahigh vacuum (UHV) conditions and measured using BLS. The gold covering layer was then removed from the whisker surface, and the clean whisker surface was covered with epitaxial silver under UHV conditions and measured with BLS. An additional capping layer of gold was added to the silver covered whisker to protect the iron/silver interface from oxidation. Therefore the same whisker was used for two samples, a gold covered whisker and a silver covered whisker.

The Fe(001) whisker used in the BLS studies was selected because of its square cross-section and because of the shininess of its surfaces and their smoothness as observed with a metallographic microscope (magnification of 40 \times). The whisker length and width were 15mm and 0.30mm, respectively.

Although the whisker surface looked quite perfect without any cleaning, it is quite likely that the surfaces were contaminated by small quantities of byproducts of the growth process, e.g. HCl. To remove this unwanted contamination, the surfaces of the whisker were carefully prepared under ultrahigh vacuum conditions. The whisker was first ultrasonically cleaned in spectroscopic-grade solvents: trichloroethylene, acetone and then methanol. This cleaning cycle was repeated three times.

The whisker was then clamped at one end to the sample holder and placed into an ultrahigh vacuum system (Physical Electronics Φ -400 molecular beam epitaxy (MBE) machine) having a base pressure $\lesssim 10^{-10}$ Torr. The whisker was sputtered at 2keV and 25 mA for 30 minutes at room temperature using Ar⁺ ions. The temperature of the sample holder was then increased to 700°C; the whisker was sputtered for 25 minutes, annealed for 5 minutes and resputtered for 4 minutes. The sample heater was then shut off to allow the whisker to slowly cool to room temperature. The resputtering was performed at the

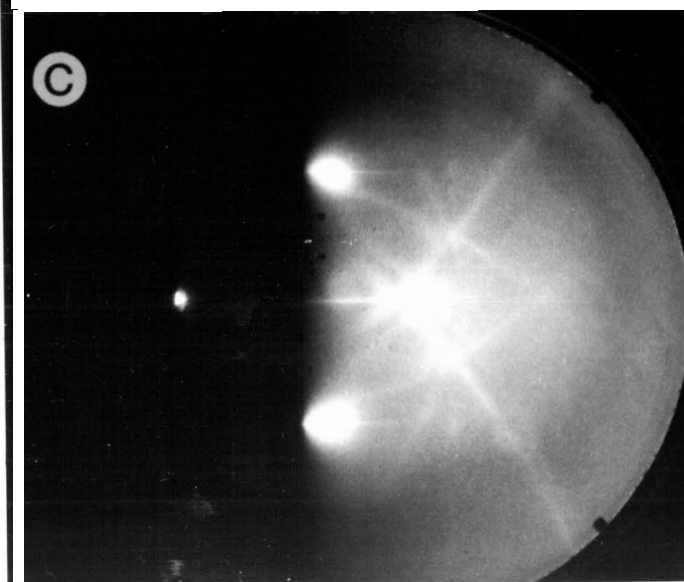
elevated temperature to remove carbon and sulphur which segregates to the surface at high temperatures (Purcell et al., 1988a). After the sample heater was shut off, the whisker annealed sufficiently during its slow cooldown to room temperature to remove defects produced by the final sputter. Auger Electron Spectroscopy (AES) was performed before and after the sputter/anneal cycle for comparison of the oxygen and carbon contamination of the whisker surface. Before the cycle, the O:Fe and C:Fe ratios were 1:20 and 1:40, respectively; these values were estimated taking into account the relative sensitivities of the Auger process for the different elements (Davis et al., 1978). After the cycle, the ratios were 1:165 and 1:70, respectively.

The clean whisker surface was observed with reflection high energy electron diffraction (RHEED). In the RHEED experiment, 10keV electrons are directed at nearly glancing incidence ($\theta_i \sim 1.3^\circ$) onto the sample surface and the diffracted beam is viewed on a phosphorescent screen placed approximately 30cm from the sample. Although the penetration depth of the high energy electrons is large ($\sim 100\text{\AA}$), surface sensitivity is obtained by using a small angle of incidence. A description of the experimental and theoretical aspects of RHEED has been given by Bauer (Bauer, 1982).

Photographs of the RHEED patterns obtained with the incident electron beam along the [110] whisker direction are shown in figure 6.3. Parts (a), (b) and (c) are the same RHEED pattern photographed with different film exposure times. Approximately halfway down on the left side of each photograph there is a bright spot which corresponds to the part of the incident electron beam which did not contact the sample. In the central region of each photograph there are three bright well-defined spots which result from constructive interference of the diffracted electron beams. The spacing between the spots can be related to the spacing between the rows of atoms on the surface involved in the diffraction process. If the vertical separation of the spots on the photograph is y and the distance between the sample and the screen is L , we can write

Figure 6.3

RHEED pattern obtained for clean Fe(001) whisker surface with the electron beam along the [110] direction of the whisker. Parts (a), (b) and (c) have different film exposure times for the same RHEED pattern.



$$\tan \phi = \frac{y}{L} \quad (6.3)$$

The diffraction condition is given by

$$\sin \phi = \frac{\lambda}{d} \quad (6.4)$$

where λ is the wavelength of the electrons and d is the spacing between the rows of atoms.

For small ϕ , $\tan \phi \sim \sin \phi \sim \phi$ and we can write

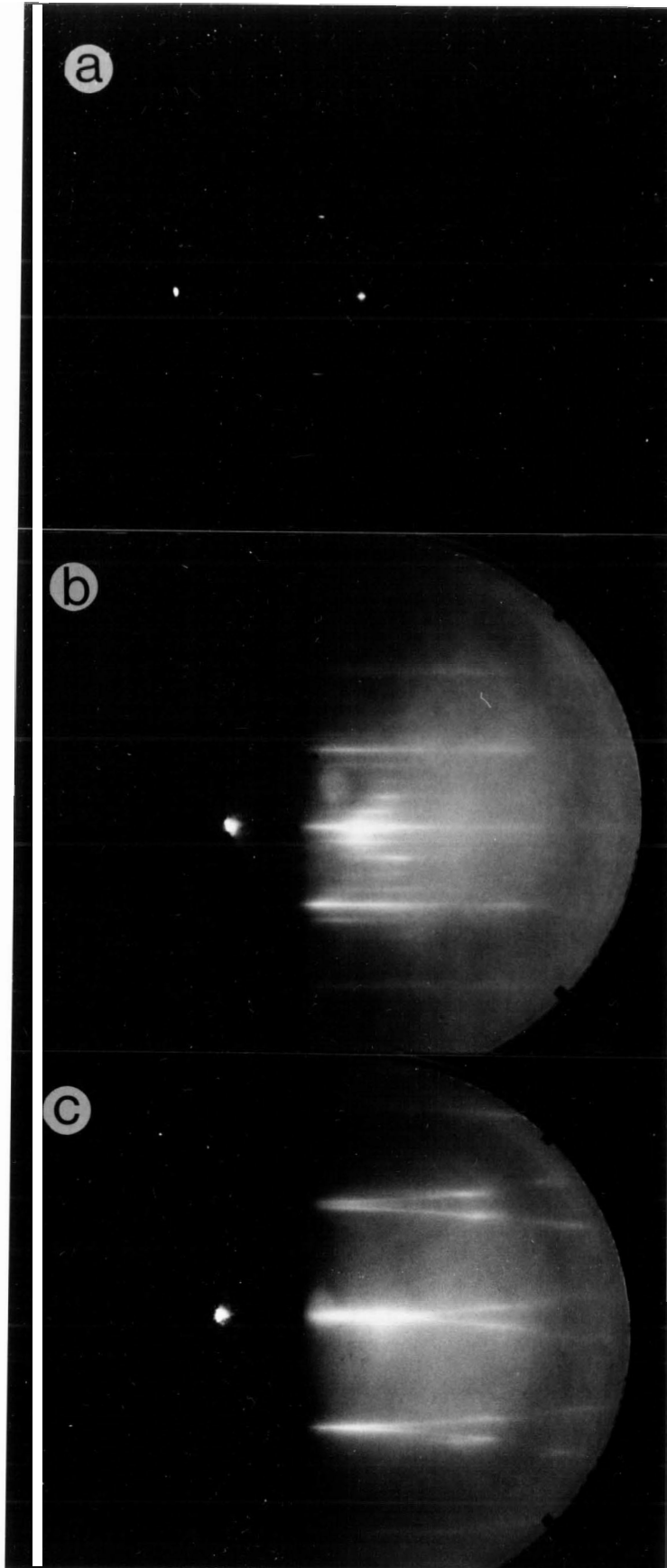
$$y = \frac{L\lambda}{d}. \quad (6.5)$$

From equation (6.4), the vertical spacing of the spots on the RHEED patterns is inversely proportional to the spacing between the rows of atoms. In figure 6.4(a), the diffraction pattern obtained along the [100] iron whisker direction is shown. The spots are closer together on this pattern than on those of figure 6.3, indicating that the rows of atoms for the [100] direction are further apart. For a (100) plane of a cubic lattice, the distance between the rows of atoms along the [100] direction is a factor of $\sqrt{2}$ larger than that along the [110] direction.

For a perfect surface, the RHEED pattern diffraction features are truly spots, indicative of the long range order of the crystal surface. The appearance of narrow horizontal streaks indicates the presence of surface steps and terraces, the mosaic spread of the crystal and impurities. Three-dimensional roughening of the surface leads to modulation of the intensity of these streaks along their length. Broadening of the streaks perpendicular to their length indicates the presence of numerous defects on a very short lateral scale. Clearly the whisker surface is quite free from all of these imperfections.

Figure.6.4

- (a) RHEED pattern obtained for clean Fe(001) whisker surface with the electron beam along the $[100]$ direction of the whisker.
- (b) RHEED pattern obtained for 15ML Au on Fe(001) whisker surface with the electron beam along the $[100]$ direction of the whisker.
- (c) RHEED pattern obtained for 15ML Au on Fe(001) whisker surface with the electron beam along the $[110]$ direction of the whisker.



Another indication of the quality of the whisker surface can be seen in part (c) of figure 6.3. For this RHEED pattern there are weak streaks called Kikuchi lines (Bauer, 1982) that can be seen in addition to the bright diffraction spots. These lines are visible in RHEED patterns only when the surface of the crystals has good three-dimensional order. They result from "channeling" of electrons along atomic planes in the crystal. This "channeling" effect cannot take place if the crystal surface is disordered. The presence of sharp diffraction spots and Kikuchi lines in the RHEED patterns of figures 6.3 and 6.4(a) indicate the excellent quality of the whisker surface.

The clean surface of the whisker was then covered with epitaxial layers of either gold or by a silver layer followed by a gold layer. This resulted in clean, well-defined interfaces of gold/iron and silver/iron that were protected against oxidation when the whisker was removed from the ultrahigh vacuum for study with BLS.

The growth of the gold layer is now described. The growth of the silver layer was performed under similar conditions. Oscillations in the RHEED specular spot intensity were originally observed during semiconductor growth (van Hove et al., 1983; and Neave et al., 1983) and have recently been observed during the growth of metals by Purcell et al. (Purcell et al., 1987). We used this technique during the growth of the gold layer on the iron whisker surface to determine the thickness of the gold layer. The results are shown in figure 6.5. The deposition rate for the gold was approximately 1 monolayer/minute. The thickness of one monolayer of gold is 1.43 Å. Regular oscillations in the specular spot intensity were obtained after 5 monolayers of gold were deposited, corresponding to a layer-by-layer growth of the gold (Purcell et al., 1988a) with one oscillation per layer. The number of oscillations was used to determine the total thickness of gold as 15 monolayers. Below a thickness of 5 monolayers of gold, the oscillations were irregular. It has been shown by low energy electron diffraction (LEED) (van Hove et al., 1981) and scanning tunneling microscopy (STM) (Binnig et al., 1984) that a complicated reconstruction of the

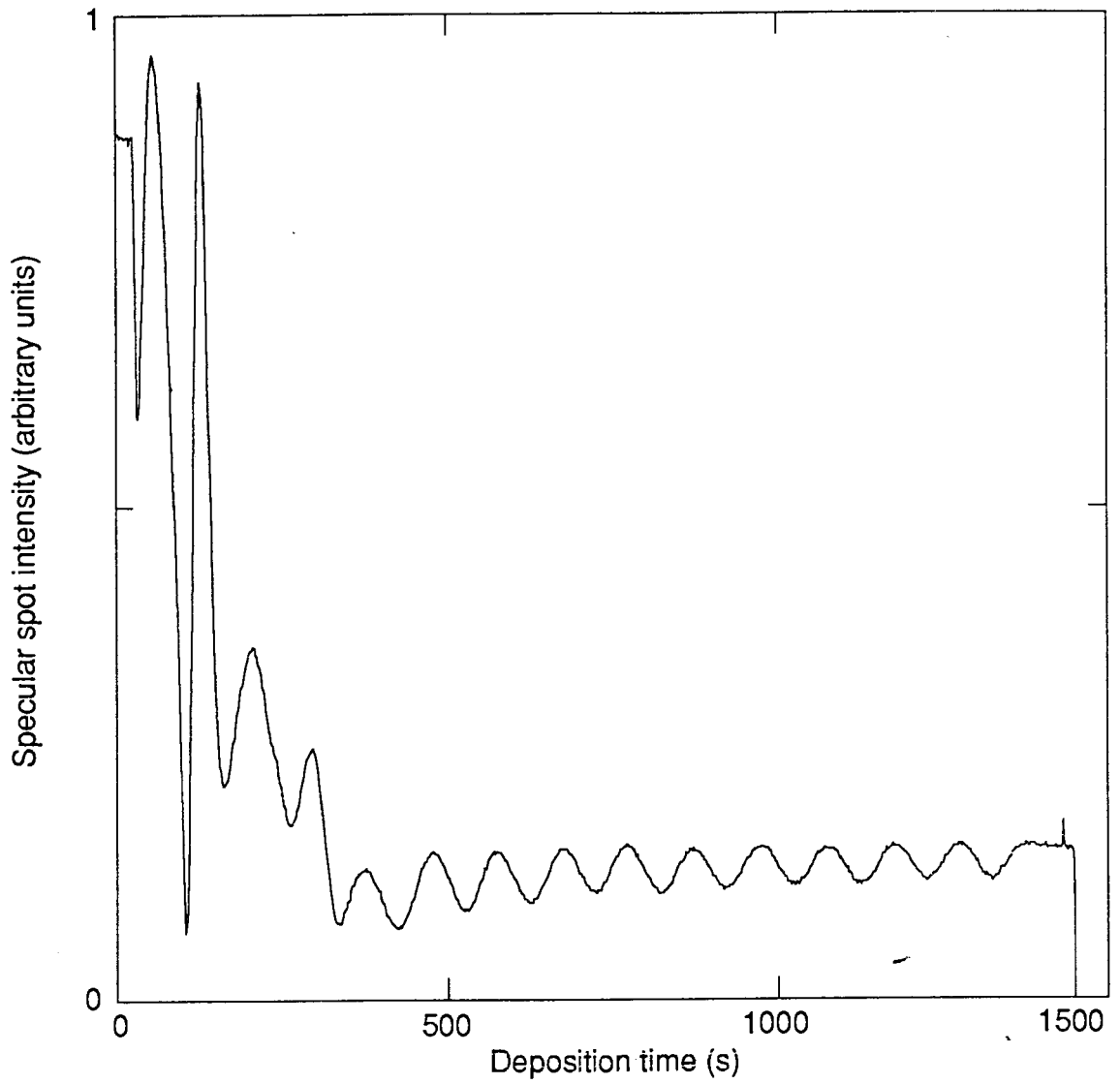


Figure 6.5

RHEED specular spot intensity oscillations during the growth of Au on the Fe(001) whisker.

gold atoms on the iron surface takes place during the first few monolayers of growth. The reconstructed surface of the 30 monolayer thick gold film can be seen in the RHEED patterns of figure 6.4(b) and 6.4(c). In figure 6.4(b), with the electron beam along the [100] whisker direction, the diffraction features were narrow horizontal streaks instead of spots, indicating the presence of steps and terraces on the gold surface; however, the layer-by-layer growth observed for the reconstructed gold surface in figure 6.5 indicates that the growth was very good. Four dim streaks can be seen between each pair of bright streaks, indicating that the surface unit cell consists of 5 gold atoms along the [100] direction. The observation of the reconstructed gold surface is a good indication of surface cleanliness (Zajac et al., 1985).

The same iron whisker was used for both samples in the BLS study: the iron whisker covered by 15 monolayers of gold (the 15 ML Au/Fe(001) whisker); and the iron whisker covered by 15 monolayers of silver and 30 monolayers of gold (the 30 ML Au/15 ML Ag/Fe(001) whisker).

6.3 The light scattering calculation for thick magnetic films

In section 3.1, a calculation of the resonant mode frequencies, and the intensity of light scattered from these modes, for a magnetic slab of thickness d was presented. The effects of exchange, magnetic damping and pinning of the surface spins were included. The surface pinning energies are given by equations (3.71) and (3.72); the easy axis of the magnetization is normal to the sample plane with positive values of the spin pinning coefficients. With the inclusion of the exchange interaction, the general solution of Maxwell's equations and the Landau-Lifshitz equations of motion for the magnetization was expressed as the superposition of six plane waves: three forward propagating waves and three backward propagating waves. The plane waves had spatial and temporal dependences of the form $\exp[i(qy + k_jz - \omega t)]$, where j is an index denoting each of the six

waves, y is the direction parallel to the slab surface and in the light scattering plane, and z is the direction towards the interior of the slab along the normal to the surface (see figure 3.1). For each set of three waves, one is a nonpropagating spin wave, one is a propagating spin wave and the other is a damped surface wave. Each of these waves originates at one of the surfaces of the magnetic film and travels toward the other "destination" film surface. The waves incident on the "destination" surface, together with the electromagnetic and spin pinning boundary conditions, determine the amplitudes of the waves generated at that surface. The exchange boundary conditions, equations (3.73) to (3.76), can only be satisfied if all three waves are excited at each surface of the magnetic film.

As the thickness of the magnetic slab is increased, the amplitude of each wave at the "destination" surface decreases. For magnetic films with thickness values of several thousand Å's, the amplitudes of the nonpropagating spin waves at their "destination" surfaces are so small that their effect on their "destination" surfaces can be ignored. For magnetic films that are several tens of thousands of Å's thick, the effect of the damped surface waves on their "destination" surfaces can also be ignored. A single resonant mode, the surface mode, is obtained from the calculation by assuming that all of the waves have no effect on their "destination" surfaces. If one or more of each set of three waves has a significant effect on its "destination" surface, then a spectrum of standing spin waves is obtained in addition to the surface mode. Spectra were shown for a 850Å thick film in figures 3.4 to 3.6, in which several standing spin wave peaks are observable. As the thickness of the film is increased, the frequency spacing of the standing spin waves is reduced; for iron films thicker than 1.3μ , the frequency spacing is less than the natural frequency linewidths of the individual peaks and the standing spin waves form continuous bulk bands on an intensity versus frequency plot.

In figure 6.6, the scattered intensity has been calculated as a function of frequency shift for a 5μ thick film having the magnetic properties of iron for an applied field of 5.033 kOe.

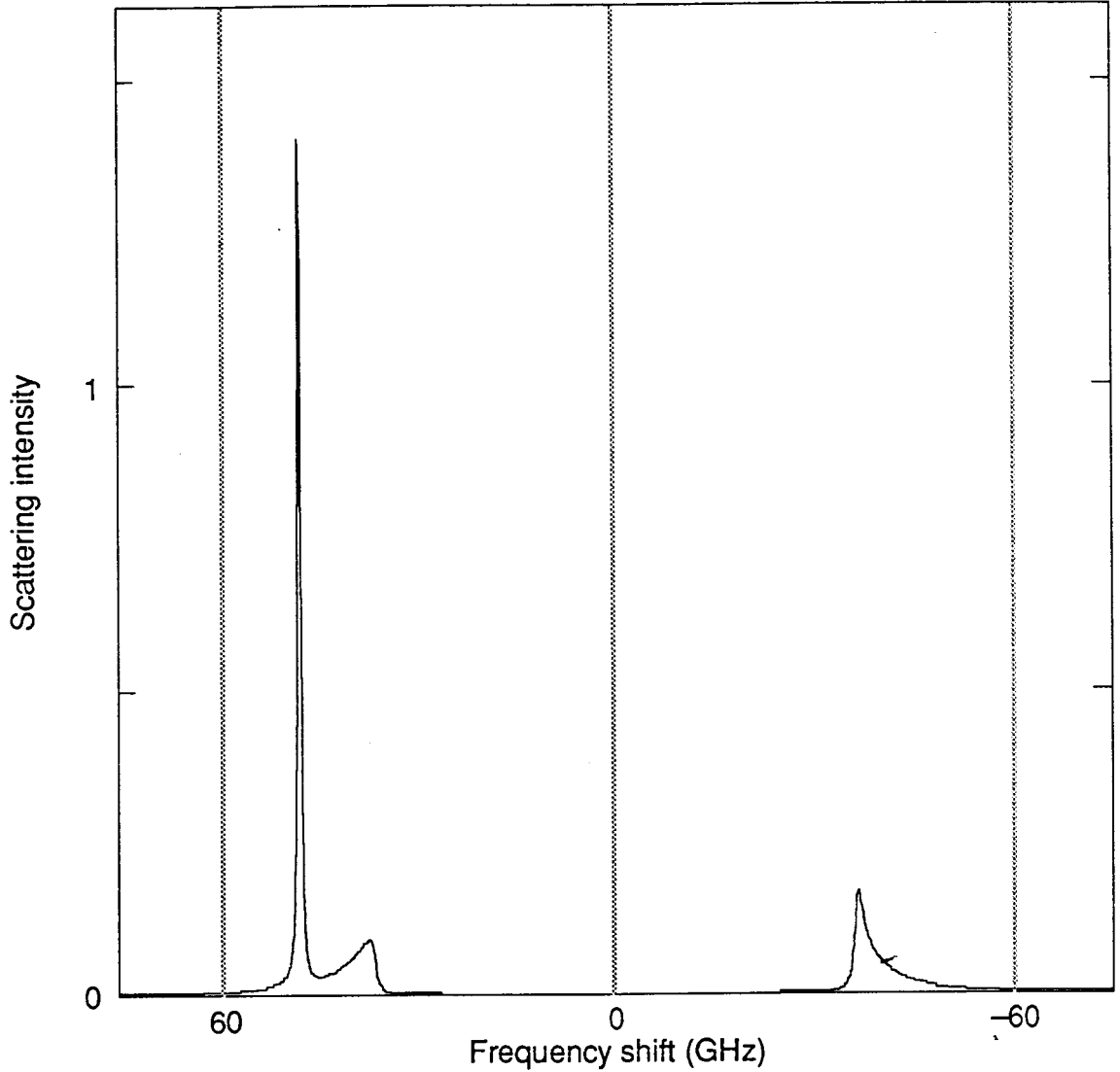


Figure 6.6

Calculated spectrum for a 5μ thick iron film for an applied magnetic field of 5.033 kOe. The calculation was performed using the following magnetic parameters: saturation magnetization $4\pi M_s = 21.456$ kG; g-factor $g = 2.09$; spin pinning coefficient $K_z^F = 0.54$ erg/cm²; in-plane anisotropy constant $K_1 = 4.596 \times 10^5$ erg/cm³; resistivity $R = 11.19 \times 10^{-6}$ ohm-cm; exchange constant $A = 2.0 \times 10^{-6}$ erg/cm; and Gilbert damping parameter $G = 7.0 \times 10^7$ Hz.

The elastic peaks that would be obtained in a real BLS experiment have been indicated by thick shaded vertical lines. The spectrum is that which would be expected from a tandem interferometer having a FSR of 60 GHz; only the peaks that belong to the central elastic peak are shown. The frequency separation of the bulk modes is typically 0.07 GHz, whereas a typical linewidth is 0.30 GHz; therefore, the standing spin waves appear as bulk bands. The surface mode is clearly visible above the bulk bands on one side of the spectrum; only the surface mode localized on the front surface of the film can be seen in the spectrum because the film is thick compared with the optical skin depth. We have performed calculations for magnetic films with thicknesses of up to 100 μ ; there is no measurable change in the intensity versus frequency shift spectra as the film thickness is increased beyond the value for which the frequency separation of the bulk modes is less than the natural linewidth of the modes. In other words, the spectra obtained for a 5 μ thick film and a 100 μ thick film are identical.

Spectra such as that in figure 6.6 are generated easily by the calculation. The modes which contribute to the bulk bands can be found in sequence by an automatic routine which guesses the frequency of a bulk mode by extrapolation from the frequency separation of the two previous bulk modes. The starting value for the imaginary part of the frequency must be within 0.03 GHz of its true value for convergence to take place. The surface mode must be found independently; the calculation which assumes that all of the magnetic waves have no effect on their "destination" surfaces is useful for this purpose.

6.4 Brillouin light scattering results and discussion

A typical spectrum for the 15 ML Au/Fe(001) whisker taken with the tandem interferometer is shown in figure 6.7 for an applied field of 5.033 kOe. The spectrum consists of a single peak (surface mode) on one side of the spectrum and continuous bands (bulk modes) on both sides of the spectrum which have a peak in their intensity at low

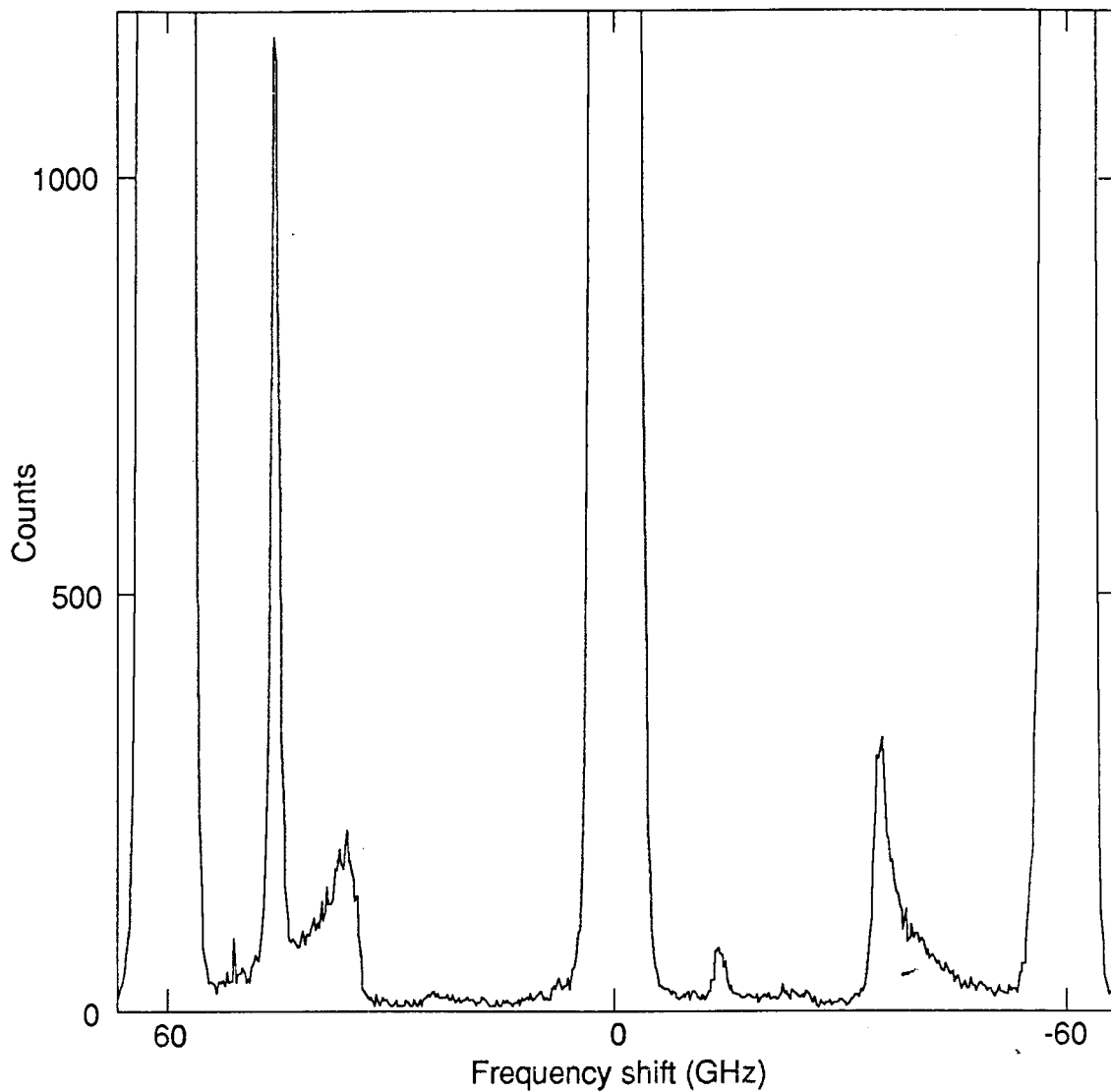


Figure 6.7

BLS spectrum for the 15 ML Au/Fe(001) whisker using the tandem interferometer with an applied field of 5.003 kOe, an incident laser power of 140 mW and a total counting time for each of the 512 data points of 23.18 s. The small peak that occurs at -14 GHz is a ghost peak.

frequency and decrease in intensity with an increase in frequency (Sandercock and Wettling, 1979). The surface mode occurs on only one side of the spectrum for thick samples that are uniformly magnetized (Damon and Eshbach, 1961). The surface mode can be moved from one side of the spectrum to the other side by reversing the direction of the magnetization. Figure 6.7 can be compared to the spectrum in figure 6.6, which was calculated for the same experimental conditions. The major difference between the two spectra is the ratio of the surface mode intensity to the bulk mode intensity: this ratio is much larger in the calculated spectrum. The reason for the intensity ratio discrepancy is not known, but it may be related to the importance of the second order magneto-optical constant G_{44} discussed in section 3.1.3, which has been neglected in the calculation of the spectrum in figure 6.6.

We have measured the frequency of the surface mode very accurately by using a single interferometer with a free spectral range (FSR) which is small compared with the frequency of the surface mode. If the FSR is smaller than the mode frequency, the frequency shift measured from the nearest Rayleigh peak is the mode frequency modulo an integral number of FSR's, as discussed in section 2.1.1. This additional number of FSR's can be easily obtained from a quick spectrum using the tandem interferometer with a large FSR. Using the single interferometer, the surface mode was easily observed above the background due to the bulk modes, and the surface mode frequency could be measured to within ± 0.03 GHz ($= \pm 10$ Oe).

In zero applied field and not too close to the ends, Fe(100) whiskers can be prepared such that they exhibit the simple Landau domain structure as discussed in section 6.1: a single 180° domain wall separates two domains having magnetizations along the whisker axis and antiparallel to one another. We used the ac susceptibility measurement technique of Heinrich and Arrott (Heinrich and Arrott, 1972) to verify that our whisker had this

domain structure in zero applied field. This technique also gives a direct measure of the demagnetizing field H^{demag} . For our whisker, $H^{\text{demag}} = 26 \text{ Oe}$.

With the whisker in the Landau structure, the domain wall can be moved easily across the width of the whisker by a small change in the applied field. In Brillouin light scattering experiments, the surface mode shifts from one side of the spectrum to the other as the domain wall passes the focussed spot of laser light (diameter $\leq 10\mu$). This is because the magnetization on one side of the domain wall is directed opposite to that on the other side of the domain wall. The domain wall can be "parked" on the laser light spot: BLS spectra obtained under this condition are shown in figures 6.8 and 6.9. The domain wall thickness for iron at room temperature is approximately 850 \AA (Kittel, 1976). Since the thickness of the domain wall is much smaller than the laser light spot diameter, both domains are observed at the same time and the surface peak appears on both sides of the spectrum. We observed that the domain wall could be swept through the laser light spot with a change in the applied field of $\sim 1 \text{ Oe}$. This agrees with a crude estimate of the rate of wall motion with field of $6\mu/\text{Oe}$ obtained from $H^{\text{demag}} = 26 \text{ Oe}$ and a measured whisker width of 300μ .

For domain wall measurements, a judicious choice of small FSR for the single interferometer (see section 2.2.6) permits the observation of both the upshifted and the downshifted surface peaks on the same side of the spectrum, as shown in figure 6.9. This particular feature is extremely useful for high precision measurements of small frequency shifts in zero applied field, because the two peaks on the same side of the spectrum shift in opposite directions. Measurement of the frequency shift between these two peaks gives twice the resolution that can be obtained from the shift of a single peak. This allows frequency measurements for one of the two peaks that are accurate to within $\pm 0.02 \text{ GHz}$.

The calculated spectra expected for the domain wall observation are shown in figure 6.10. Part (a) shows the spectrum within the frequency range $+75 \text{ GHz}$ and -75 GHz for tandem operation of the interferometer with the FSR equal to 60 GHz ; it can be compared

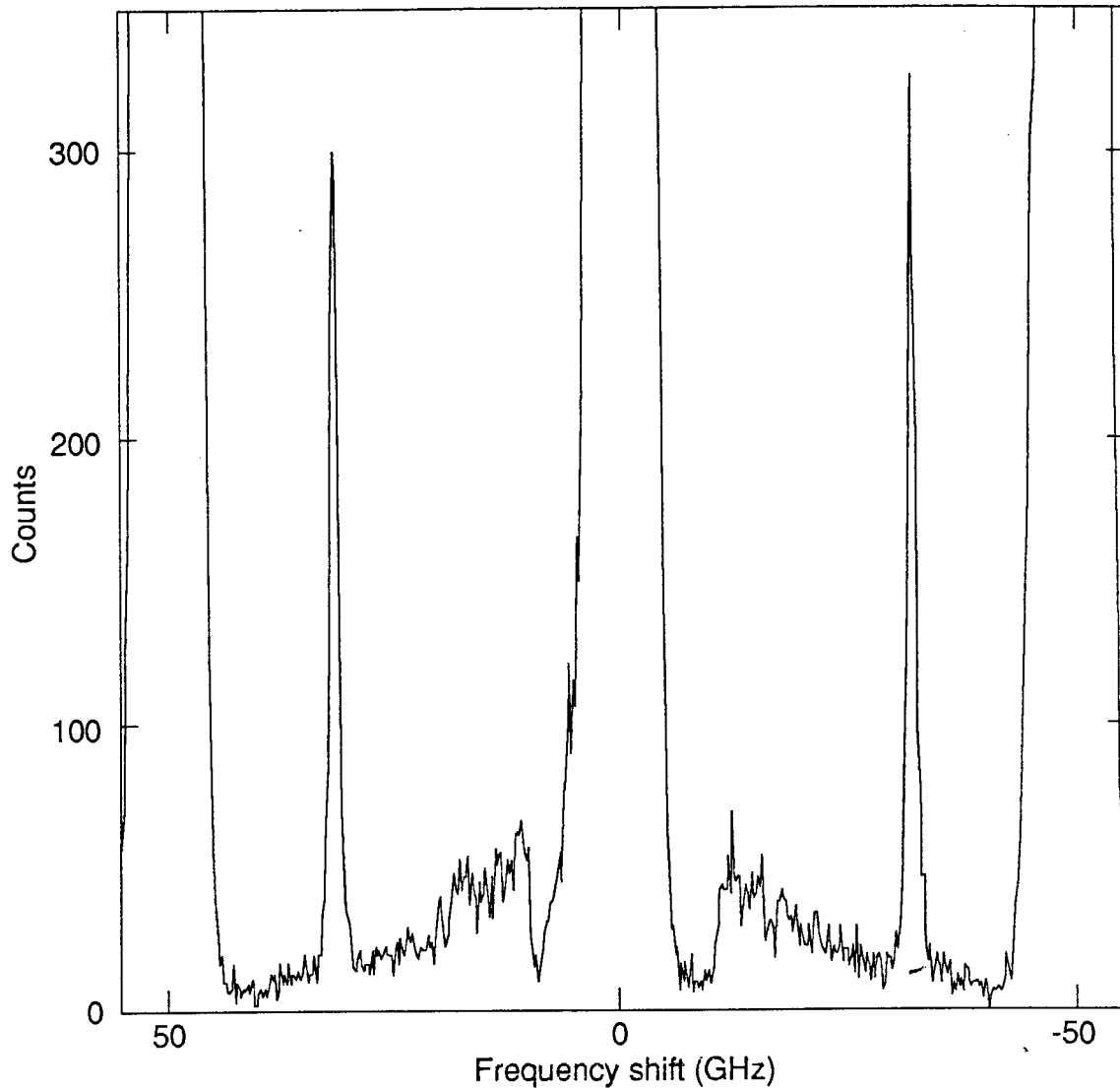


Figure 6.8

BLS spectrum for the 15 ML Au/Fe(001) whisker in zero applied field using a large FSR (60 GHz). The domain wall is at the center of the focussed laser spot. 140 mW of incident laser power was used. The angle of incidence was $\theta = 45^\circ$. The total counting time for each of the 512 data points was 5.492 s.

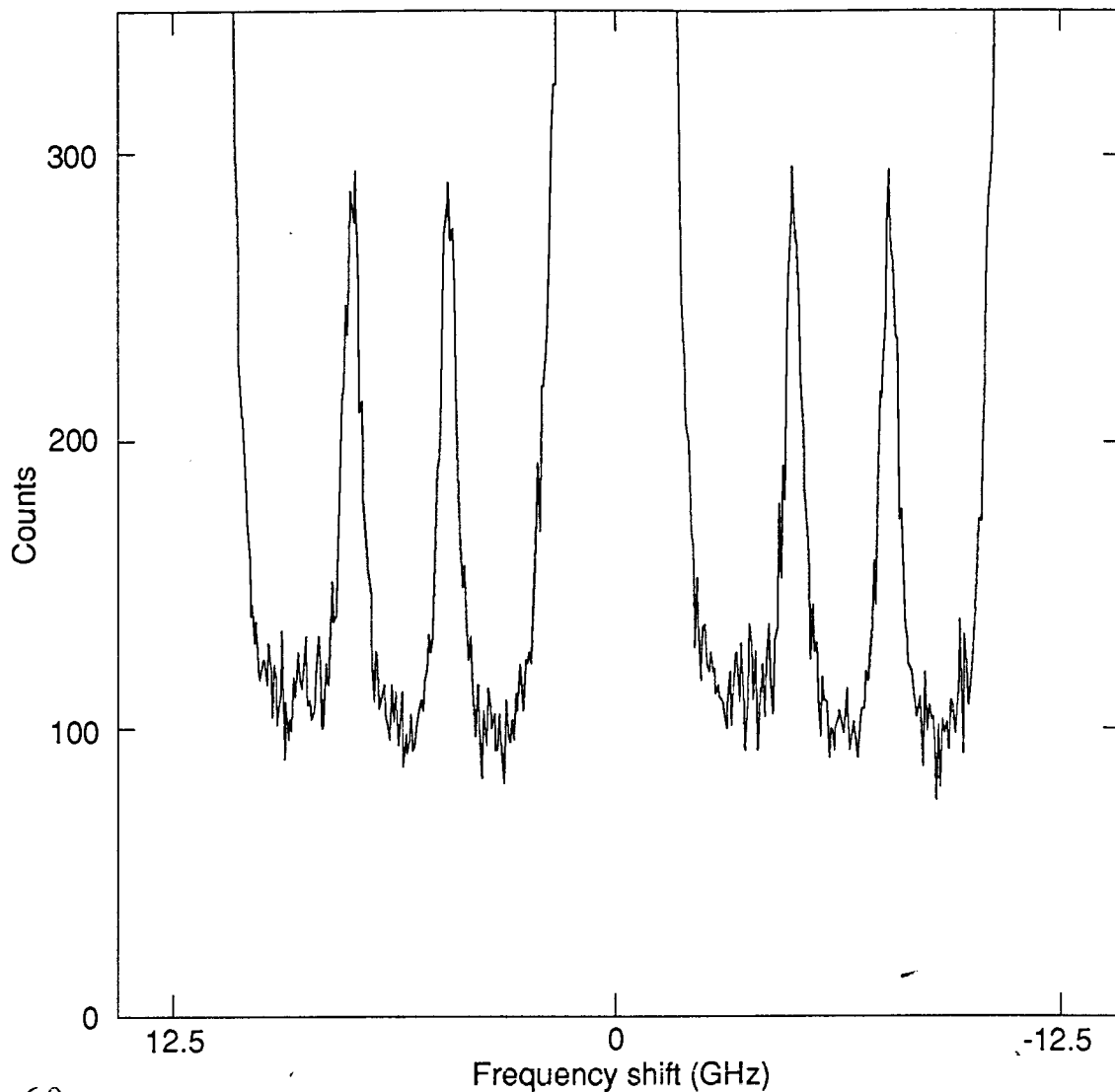


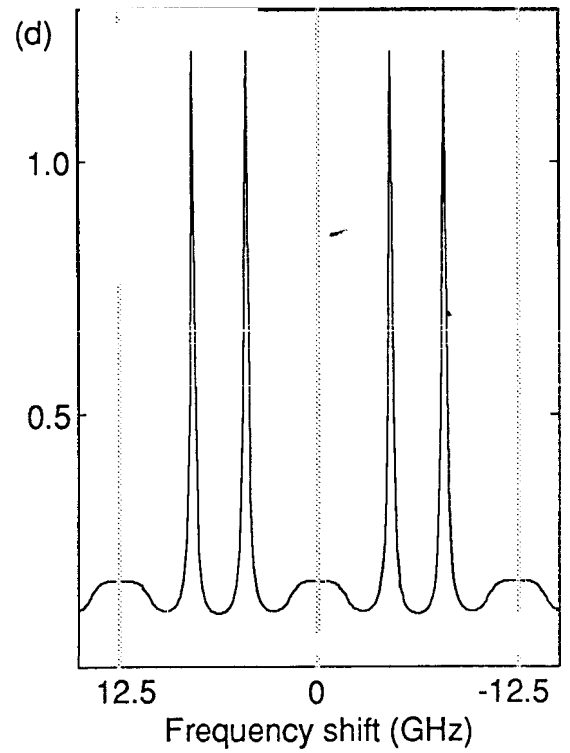
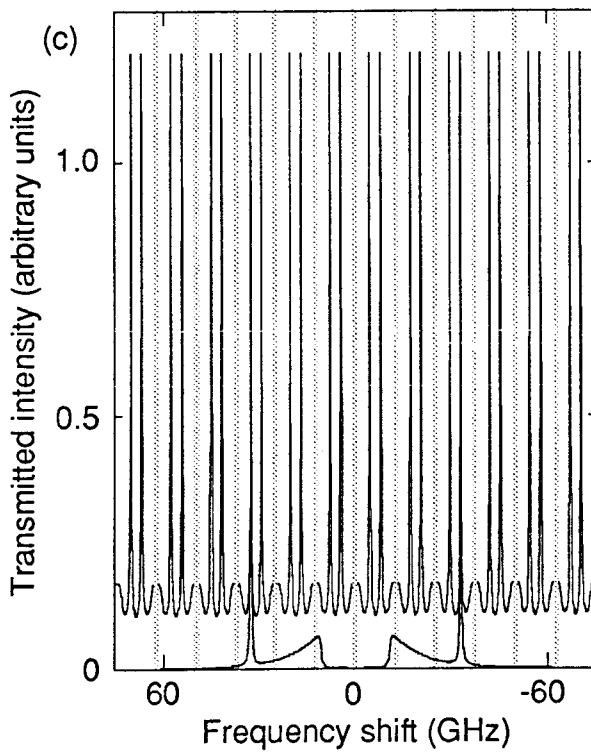
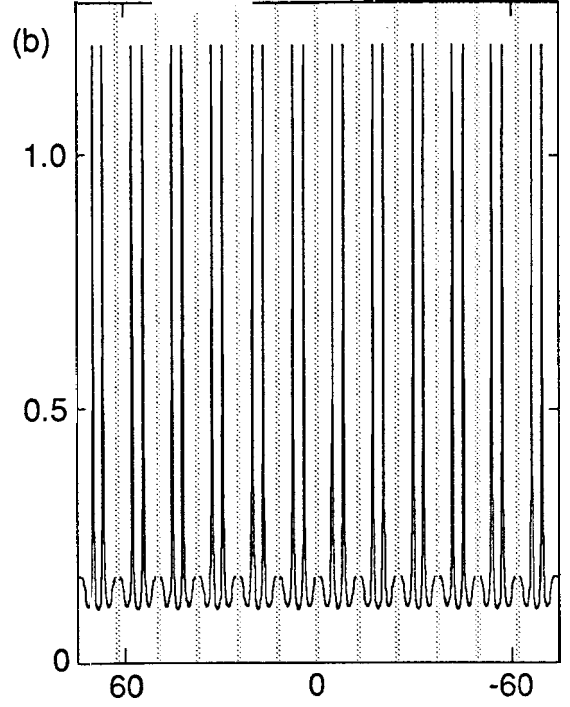
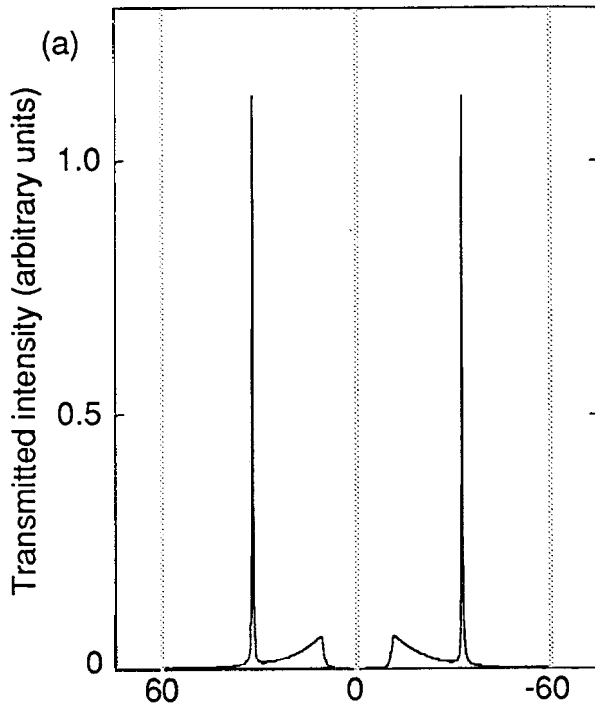
Figure 6.9

BLS spectrum for the 15 ML Au/Fe(001) whisker in zero applied field using a single interferometer and a small FSR (12.5 GHz). The domain wall is at the center of the focussed laser spot. 140 mW of incident laser power was used. The angle of incidence was $\theta = 45^\circ$. The total counting time for each of the 512 data points was 7.388 s.

Figure 6.10

Calculated spectra for a 5μ thick iron film in zero applied magnetic field. The calculations were performed using the magnetic parameters listed in Figure 6.6. The thick dotted lines indicate the positions of the elastically scattered peaks. The natural linewidths of the peaks have been shown.

- (a) tandem interferometer with a FSR of 60 GHz.
- (b) single interferometer with a FSR of 12.5 GHz.
- (c) overlay of parts (a) and (b).
- (d) single interferometer with a FSR of 12.5 GHz.



directly with figure 6.8. For the central elastic peak which occurs at 0 GHz frequency shift, there is one surface mode which is upshifted in frequency and one surface mode which is downshifted in frequency. In addition, the bulk modes occur on both sides of the spectrum. Part (b) shows the spectrum within the same frequency range as part (a) for a single interferometer with a FSR of 12.5 GHz. Because of the decrease in the FSR, there is a decrease in the frequency separation between neighbouring elastic peaks. For each of the elastic peaks which occur in the spectrum, there is one surface mode which is upshifted in frequency and one surface mode which is downshifted in frequency. The bulk bands essentially form a constant background in the single interferometer spectra. Part (c) shows an overlay of the spectra of parts (a) and (b) and demonstrates how the peaks in both spectra are related. In part (d) is shown the same spectrum as in part (b) within the frequency range +14 GHz and -14 GHz; it can be compared directly to figure 6.9.

We have made BLS measurements using a small value of the FSR with the domain wall "parked" on the laser light spot for changes in the angle of incidence of the laser light and changes in the incident laser power. A change in the angle of incidence θ (measured with respect to the sample normal) from $\theta = 32^\circ$ to $\theta = 68^\circ$ resulted in a shift in the frequency of one of the peaks of 0.293 GHz for the 15 ML Au/Fe(001) whisker and 0.221 GHz for the 30 ML Au/15 ML Ag/Fe(001) whisker. Similar measurements using a single surface peak for the 15 ML Au/Fe(001) whisker for an applied field of 4 kOe yielded a value of 0.29 GHz. The surface mode frequency shift was also measured for laser powers of 70, 140 and 280 mW for the 15 ML Au/Fe(001) whisker using an angle of incidence of $\theta = 45^\circ$. The laser powers quoted were measured at the specimen surface. The results are shown in figure 6.11. A linear variation of the frequency with laser power of $-0.123\text{GHz}/100\text{mW}$ was observed. This value was used to obtain an accurate measure of the sample heating due to the focussing of the laser beam on the sample surface.

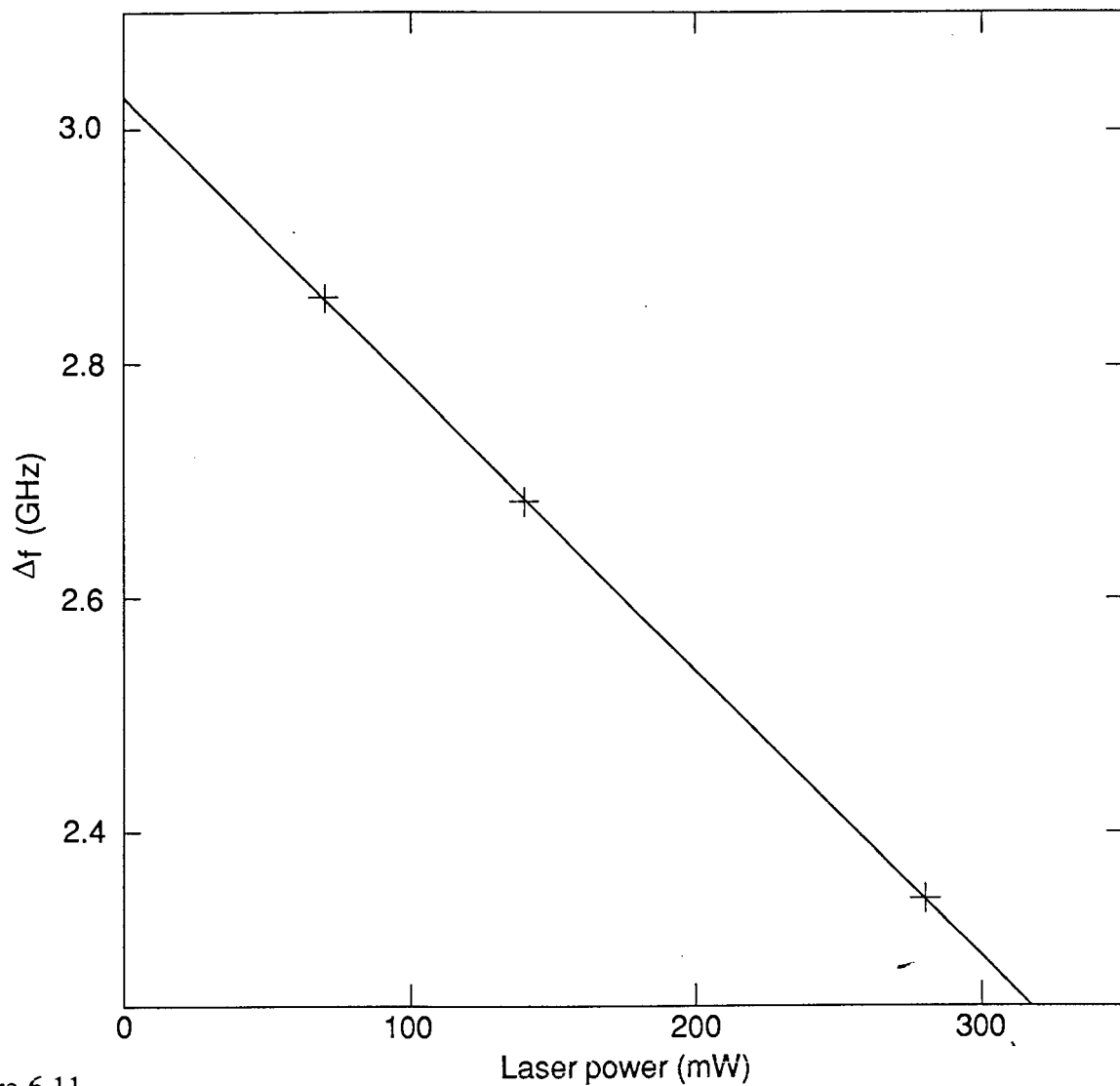


Figure 6.11

Dependence of the frequency shift Δf between the upshifted and the downshifted surface mode peaks on the incident laser power for a FSR of 12.5 GHz. The crosses are measured data and the solid curve is a least squares fit of a straight line to the data. The angle of incidence of the laser light was $\theta = 45^\circ$.

From the known temperature dependence of the saturation magnetization $4\pi M_s$ (Crangle and Goodman, 1971), the in-plane cubic magnetocrystalline anisotropy constant K_1 (Gengnagel and Hofmann, 1968), and the resistivity R (Touloukian and Ho, 1981), the surface mode frequency was calculated as a function of temperature near room temperature, as shown in figure 6.12 for two values of the surface spin pinning coefficient K_z^F . The angle of incidence has been taken to be $\theta = 45^\circ$. The temperature dependence of the surface mode frequency is nearly linear within this limited temperature range, with a slope of -0.00666 GHz/K that is essentially independent of the value of K_z^F . This value of the slope, when used with the measured frequency shift with laser power of -0.123 GHz/100 mW, gave a temperature rise of 26K for a laser power of 140 mW at the sample position. Accordingly, we have used the magnetic parameters characteristic of $T = 320$ K for fitting our data collected using a laser power of 140 mW at the sample position:

$$4\pi M_s = 21.456 \text{ kG}, \quad K_1 = 4.596 \times 10^5 \text{ erg/cm}^3, \quad \text{and } R = 11.19 \times 10^{-6} \text{ ohm-cm.}$$

The calculated shift, δf , in the surface mode frequency with a change in the angle of incidence in zero applied field is approximately a linear function of the surface spin pinning coefficient K_z^F in equation (3.71):

$$\delta f = (0.456 - 0.300K_z^F) \text{ GHz}, \quad (6.6)$$

where K_z^F is in erg/cm^2 . In figure 6.13, δf is plotted against K_z^F for applied field values of 0 and 10 kOe. δf is insensitive to the value of the applied field: δf changes by 0.9% as H is changed from 0 to 10 kOe. This is consistent with experiments which measured the same value of δf for $H = 0$ and $H = 4$ kOe. The value of δf is also very insensitive to changes in the magnetic damping: δf changes by only 0.3% for a 50% change in the Gilbert damping parameter G . In table 6.1, the percentage changes in δf for a 5% change in each of the parameters used in the calculation are listed. The largest changes in δf are obtained for

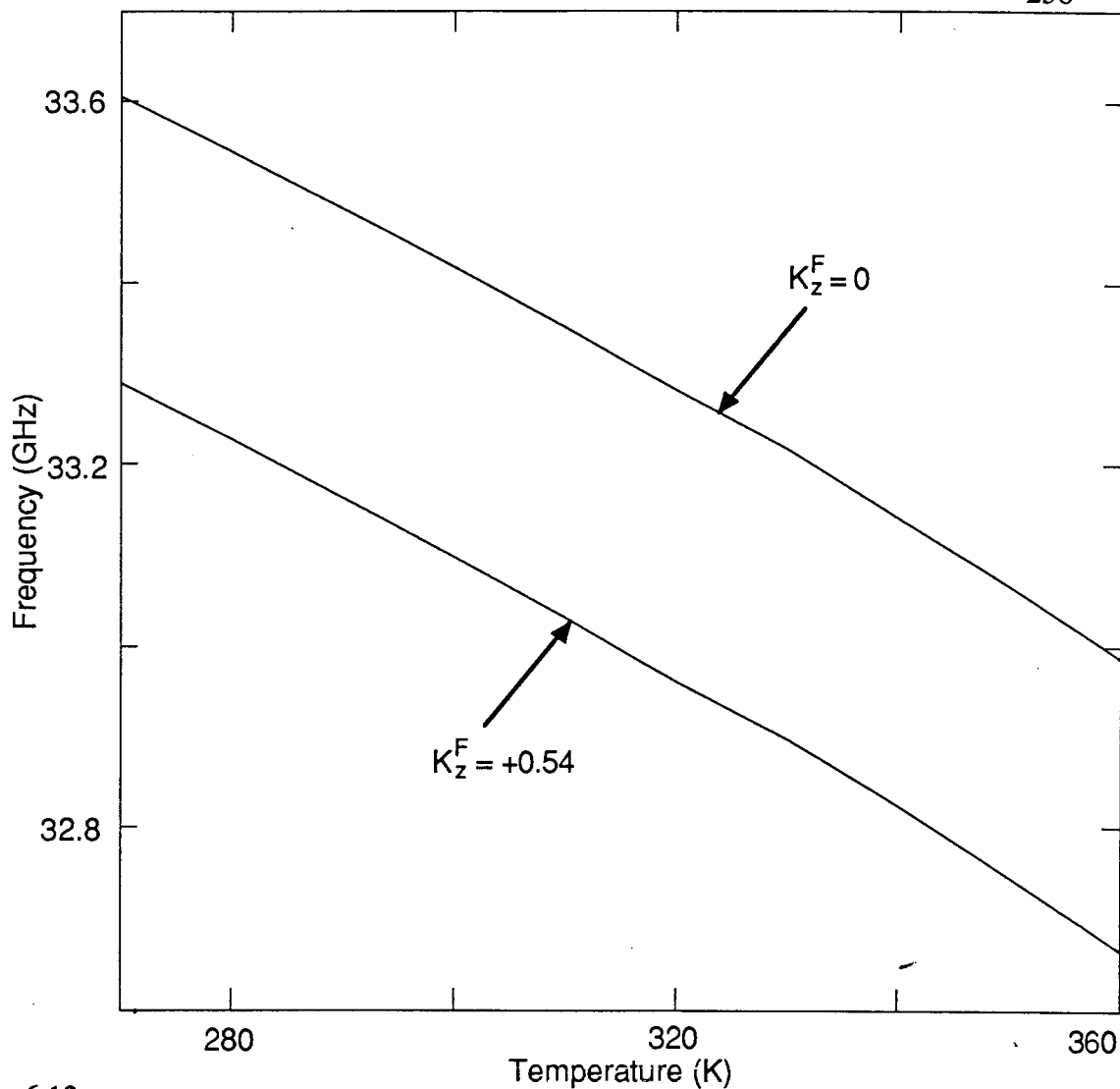


Figure 6.12

Calculated surface mode frequency as a function of the sample temperature for two values of the spin pinning coefficient K_z^F : $K_z^F = 0$ and $K_z^F = 0.54$ erg/cm². The angle of incidence of the laser light is $\theta = 45^\circ$.

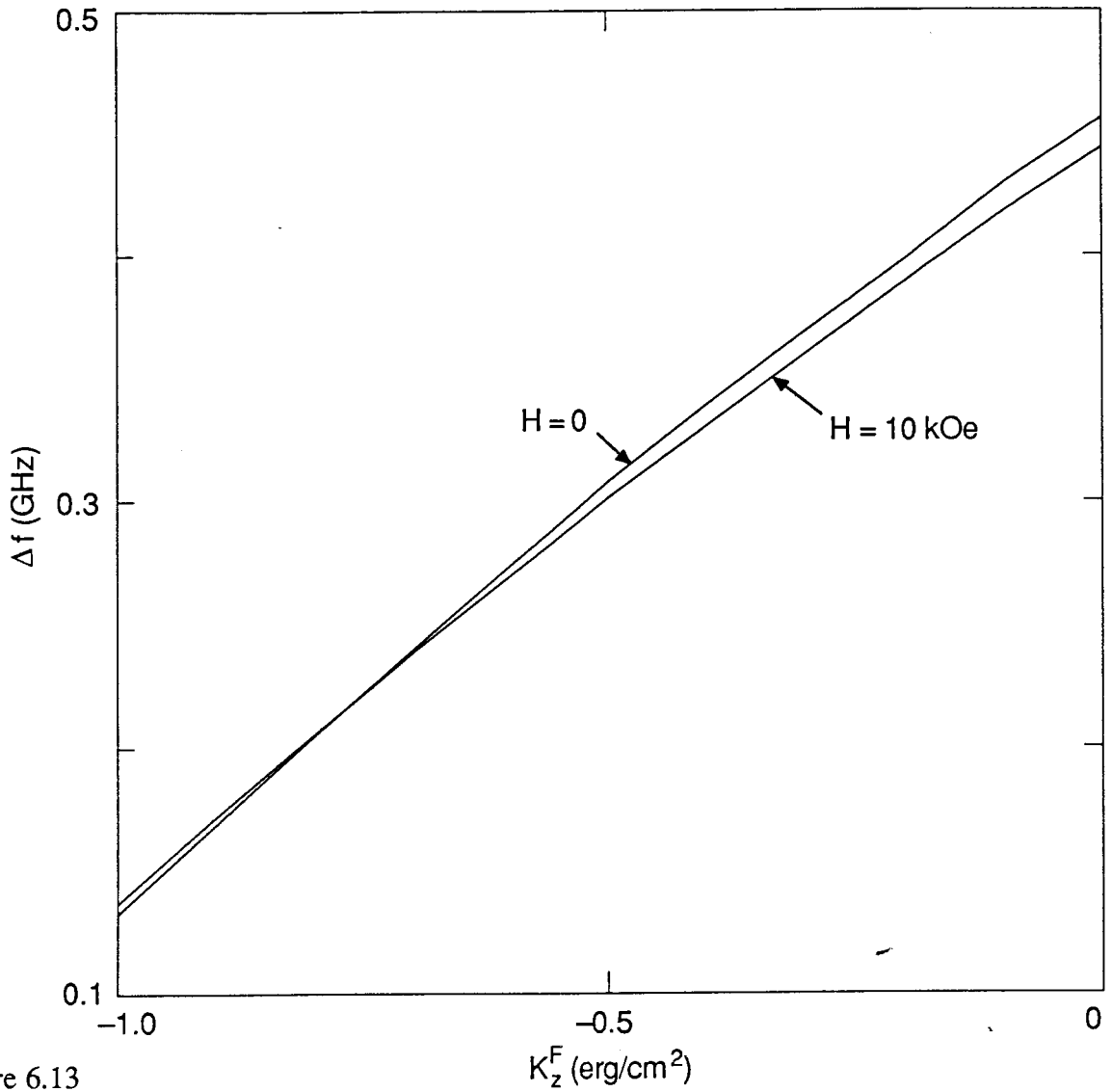


Figure 6.13

Calculated dependence of the frequency shift Δf on the spin pinning coefficient K_z^F for a FSR of 12.5 GHz. Δf corresponds to the difference in the surface mode frequency between $\theta = 68^\circ$ and $\theta = 32^\circ$, where θ is the angle of incidence of the laser light. One of the curves corresponds to zero applied magnetic field and the other corresponds to an applied field of 10 kOe.

Table 6.1

The percentage change in δf (see equation (6.6)) for a 5% change in each of the magnetic parameters which enter into the calculation of the surface mode. The surface spin pinning parameter K_z^F was taken to be 0.54 erg/cm^2 . Also listed are the values of each parameter used to calculate the coefficients in equation (6.6).

Parameter	Value used to obtain equation (6.6)	% change in δf for 5% change in parameter
A	$2.03 \times 10^{-6} \text{ erg/cm}$	8
$4\pi M_s$	21.456 kG	5
g	2.09	5
G	$0.7 \times 10^8 \text{ s}^{-1}$	0.01
K_1	$4.596 \times 10^5 \text{ erg/cm}^3$	0.01
R	$1.119 \times 10^{-5} \text{ ohm-cm}$	0.06

changes in the exchange parameter A , the saturation magnetization $4\pi M_s$, and the g -factor. The exchange parameter A has been previously measured by neutron diffraction and ferromagnetic resonance (see Frait, 1973): its value was found to be $A = 2.0 \times 10^{-6}$ erg/cm. The saturation magnetization $4\pi M_s$ (Crangle and Goodman, 1971) and the g -factor (Frait and Gemperle, 1971) have been measured for bulk iron and we have used these values in our fit. The use of these values is given credence by our own measurements of the surface mode frequency as a function of applied magnetic field described later in this section: we obtained an excellent fit to the data using the value of the surface pinning determined from equation (6.6) and values for $4\pi M_s$ and g that are within 1% of the accepted values for Fe at a temperature of 320K. The values of $4\pi M_s$ and g obtained from the fit of the surface mode frequency versus magnetic field data were used to calculate the linear relationship between δf and K_z^F : the coefficients of the linear equation were within 0.3% of those in equation (6.6). Therefore our approach was self-consistent and comparison between theory and experiment provided an unambiguous determination of the surface spin pinning coefficient based on relative measurements of very accurate frequencies. A value of $K_z^F = 0.54 \pm 0.05$ erg/cm² was obtained for the 15 ML Au/Fe(001) whisker and a value of $K_z^F = 0.79 \pm 0.05$ erg/cm² was obtained for the 30 ML Au/15 ML Ag/Fe(001) whisker. The positive sign of K_z^F refers to pinning that tends to orient the magnetization along the sample normal, see equation (3.71). These values of K_z^F are in good agreement with the values of 0.4 to 0.5 erg/cm² for gold covered bulk iron crystals and 0.7 erg/cm² for silver covered bulk iron crystals, as determined by ferromagnetic resonance (FMR) measurements (Purcell et al., 1988b). These values are also in agreement with the values of the surface spin pinning coefficients for ultrathin iron films, as determined by FMR experiments performed in ultrahigh vacuum (Urquhart et al., 1988) (~ 0.65 erg/cm² for a single surface of a 7.6 ML iron film grown on Ag(001) and covered by silver). This shows that the uniaxial surface anisotropy is not unique to epitaxially grown thin films but

is a consequence of the abrupt change in symmetry at the surface as proposed by Gay and Richter (Gay and Richter, 1986).

As mentioned earlier in this section, the surface mode frequency was measured as a function of the applied magnetic field over the range 0 to 9 kOe for the 15 ML Au/Fe(001) whisker. A single interferometer having a free spectral range of 12.5 GHz was used. The angle of incidence of the laser light was $\theta = 45^\circ$. The results are shown as crosses with dots in figure 6.14. The solid lines in the figure are calculated curves. Curve a has been calculated using the saturation magnetization value (Crangle and Goodman, 1971) for $T = 320\text{K}$, $4\pi M_s = 21.456\text{ kG}$, a g -factor (Frait and Gemperle, 1971) of $g = 2.09$ and no surface pinning ($K_z^F = 0$). To obtain the best fit to the data, curve b, the surface pinning parameter was fixed at the value $K_z^F = 0.54\text{ erg/cm}^2$, as determined by varying the angle of incidence of the laser light. The g -factor was then chosen to obtain a curve with the same slope as the data points ($g = 2.071$), and $4\pi M_s$ was chosen so that the curve passed through the data points ($4\pi M_s = 21.408\text{ kG}$). The frequency shift produced by changing K_z^F from 0 to 0.54 erg/cm^2 is -0.32 GHz for $H = 0$, and -0.31 GHz for $H = 10\text{ kOe}$. The frequency shift produced by changing the g -factor from 2.09 to 2.071 is -0.31 GHz for $H = 0$, and -0.56 GHz for $H = 10\text{ kOe}$. The frequency shift produced by changing $4\pi M_s$ from 21.456 kG to 21.408 kG is only -0.07 GHz , and is independent of H . Excellent agreement with experiment is obtained, therefore, using a saturation magnetization value that is within 0.2% of the published value for bulk iron (Crangle and Goodman, 1971), and a g -factor that is 1% lower than the accepted value (Frait and Gemperle, 1971).

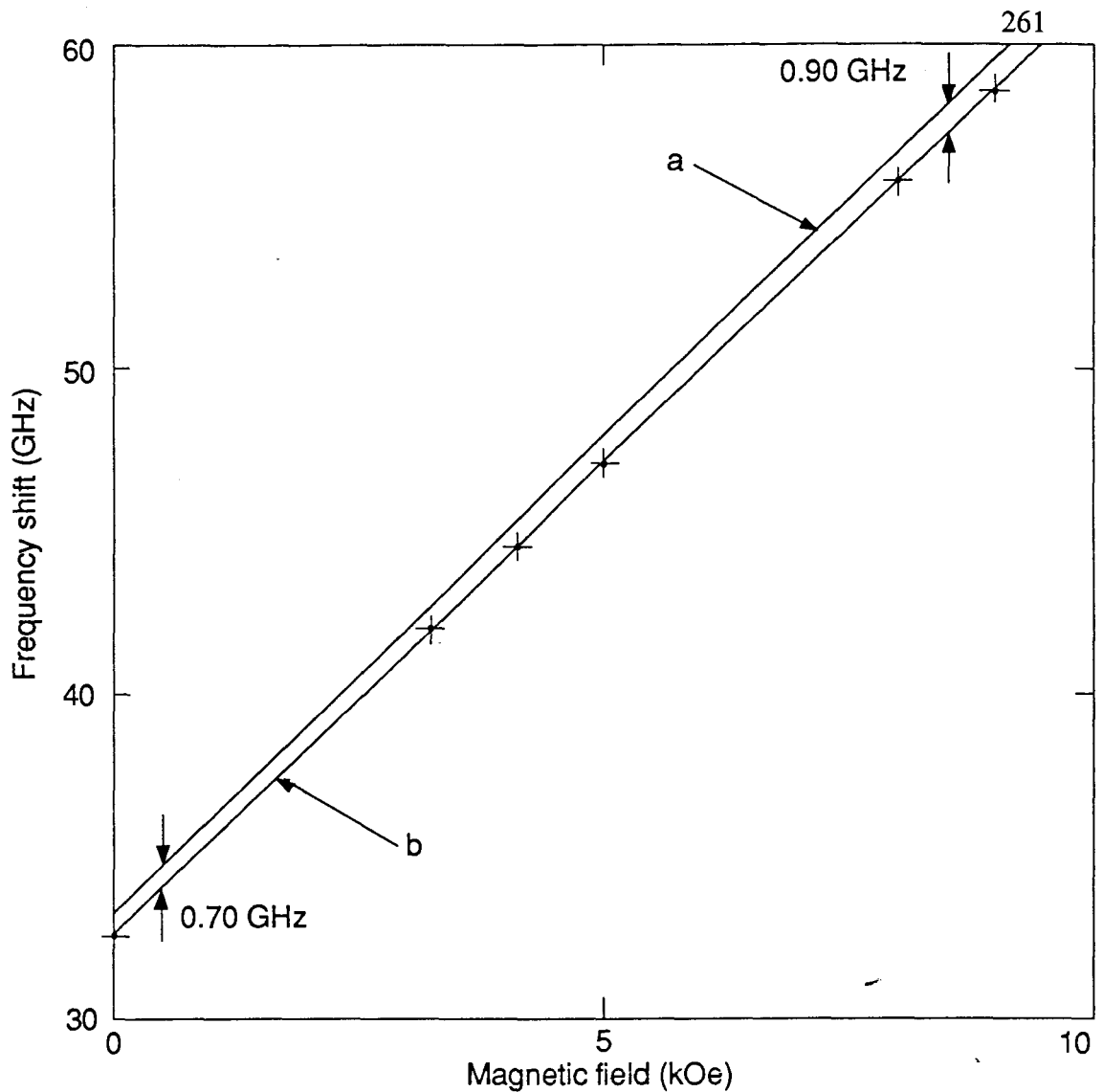


Figure 6.14

Magnetic field dependence of the surface mode frequency for the 15 ML Au/Fe(001) whisker for a laser power of 140 mW incident at $\theta = 45^\circ$. The crosses with the dots are the measured data points. The data were obtained using a single interferometer with a FSR of 12.5 GHz. The errors associated with the measurement are comparable to the width of the lines in the figure and are unrelated to the size of the crosses. The solid lines have been calculated using (a) $4\pi M_s = 21.456$ kG, $g = 2.09$ and $K_z^F = 0$, and (b) $4\pi M_s = 21.408$ kG, $g = 2.071$ and $K_z^F = 0.54$ erg/cm². Both calculations were performed using the following parameters: in-plane anisotropy constant $K_1 = 4.596 \times 10^5$ erg/cm³; resistivity $R = 11.19 \times 10^{-6}$ ohm-cm; exchange constant $A = 2.0 \times 10^{-6}$ erg/cm; and Gilbert damping parameter $G = 7.0 \times 10^7$ Hz.

CHAPTER SEVEN

SUMMARY AND CONCLUSIONS

A Brillouin light scattering (BLS) system was designed and constructed. The heart of the system was a high contrast, tandem Fabry-Perot interferometer. BLS from thermally excited magnetic waves in epitaxial, ferromagnetic films was measured in air at room temperature.

The frequencies of the normal modes of a magnetic film and the intensities of light scattered from these modes were calculated. The effects of magnetic damping and metallic conductivity were included. Exchange and the spin pinning boundary conditions were included for magnetizations lying in the sample plane. Good agreement was obtained with the light scattering calculation of Camley, Rahman and Mills. Our calculation was extended to allow the magnetization to tilt out of the sample plane due to the presence of large uniaxial anisotropies with the easy axis perpendicular to the sample plane. In this calculation, the effects of exchange and the spin pinning boundary conditions were not included. The light scattering calculations were used to interpret the BLS experimental results.

In the BLS experiments, both ultrathin films grown by molecular beam epitaxy techniques and thick iron whiskers grown by chemical vapor transport were studied.

Ultrathin films of bcc Fe grown on bulk Ag(001) crystals and bcc Fe grown on thin Ag layers deposited on Fe(001) whisker substrates were measured. Both types of samples were covered with protective layers of Au and Ag. The surface mode peaks were observed easily for samples as thin as 3ML of Fe. A strong uniaxial anisotropy with the axis perpendicular to the sample surface was observed in all of the samples. For one of the 3ML thick Fe films grown on a Ag-covered Fe whisker, the uniaxial anisotropy was large enough to orient the magnetization perpendicular to the sample plane in zero applied field at

room temperature. The thickness dependence of the surface mode frequency was measured for the Au-covered Fe films: the source of the strong perpendicular uniaxial anisotropy is a pinning of the surface spins in the Fe films. The in-plane anisotropy of the Fe films decreased with decreasing film thickness and was negligible for the 3ML thick films. For the Au-covered Fe films, the g -factor required to fit the experimental data was that for bulk Fe, $g = 2.09$. For the Ag-covered Fe films, a g -factor of 2.00 was required.

Magnetic bilayers consisting of ultrathin films of Ni grown on ultrathin films of bcc Fe deposited on bulk Ag(001) crystals and covered with Au were measured. Bilayers containing films of lattice reconstructed bcc Ni had large in-plane four-fold anisotropies. These anisotropies were observed in the dependence of the surface mode frequency and the surface mode linewidth on the direction of the magnetic field applied in the plane of the sample. A network of misfit dislocations that are formed during the lattice reconstruction of the bcc Ni layers is responsible for the in-plane four-fold anisotropy. The magnetic properties of bilayers containing films of unreconstructed bcc Ni were not significantly different from those of the underlying ultrathin Fe films; the unreconstructed bcc Ni layers were likely nonmagnetic.

Ultrathin single film and superlattice structures of fcc Fe grown on Cu(001) and covered with Cu were studied with BLS. The surface peaks could be observed easily in several of the 3ML Fe films. All of the samples had a perpendicular magnetization in zero applied field at room temperature. The magnetization was pulled out of the sample plane because of large uniaxial anisotropies with the easy axis perpendicular to the sample plane. The first order uniaxial anisotropy was comparable in the single film and superlattice samples; this indicated that the single film layers in the superlattice samples were as well formed as those of the single film samples. The inclusion of a second order anisotropy was necessary to obtain agreement with the BLS data. The second order anisotropy was particularly large for one of the superlattice samples. Very low values of the g -factor were required to fit the

BLS data for those samples that had large surface mode linewidths. The surface mode peaks for one of the single film samples were sufficiently strong to permit reliable measurements of the signal intensity for different values of the applied magnetic field. These measurements, when compared with the results of the light scattering calculation, were further evidence that the magnetization was perpendicular to the sample plane in zero applied field.

For all of the ultrathin films, very good agreement was obtained between BLS and ferromagnetic resonance measurements.

BLS measurements were made on a Fe(001) whisker that had been cleaned and covered with Au and Ag under ultrahigh vacuum conditions. This procedure yielded well-characterized interfaces of Au and Fe, and Ag and Fe. The surface mode frequency was measured to within ± 0.03 GHz by using a high frequency resolution measurement technique with a single interferometer. BLS measurements in zero applied field permitted the observation of the 180° domain wall of the whisker. High frequency resolution measurements of the 180° domain wall determined the surface mode frequency to within ± 0.02 GHz. These high accuracy surface mode frequency measurements were performed for different angles of incidence of the laser light. This allowed the unambiguous determination of the surface spin pinning coefficients: 0.54 erg/cm^2 for the Au-covered whisker, and 0.79 erg/cm^2 for the Ag-covered whisker. In both cases, the easy axis of the magnetization was perpendicular to the sample plane. These values were in very good agreement with the values of surface spin pinning coefficients determined by ferromagnetic resonance measurements on bulk iron crystals that had been prepared under the same conditions. High frequency resolution measurements were also performed for different values of the laser power incident on the sample. This allowed a determination of the sample heating due to the focussed laser light: 19K for each 100mW of laser light incident on the Fe whisker surface.

It has been shown that BLS is a useful technique for the study of magnetic properties of both ultrathin and thick magnetic films. An interesting result of this work was that similar values of the surface spin pinning coefficients were obtained for ultrathin bcc iron films and thick iron whisker crystals. This implies that the surface spin pinning is determined by very few atomic layers at the surface of a magnetic material and is probably a result of the abrupt change in symmetry at the surface.

REFERENCES

- Bauer, 1982**
E. Bauer, Appl. Surf. Sci. **11**, 479 (1982).
- Binnig et al., 1984**
G.K. Binnig, H. Rohrer, Ch. Gerber and E. Stoll, Surf. Sci. **144**, 321 (1984).
- Borer and Fremont, 1978**
K. Borer and G. Fremont, Nucl. Instrum. Methods **154**, 61 (1978).
- Born and Wolf, 1975**
M. Born and E. Wolf, *Principles of Optics*, Pergamon, Oxford, 1975.
- Borovik-Romanov and Kreines, 1982**
A.S. Borovik-Romanov and N.M. Kreines, Phys. Rep. **81**, 351 (1982).
- Bozorth, 1951**
R.M. Bozorth, *Ferromagnetism*, D. van Nostrand, Princeton, 1951.
- Brenner, 1956**
S.S. Brenner, Acta Metall. **4**, 62 (1956).
- Brillouin, 1922**
L. Brillouin, Ann. Phys. (Paris) **17**, 88 (1922).
- Brown, 1978**
W.F. Brown, Jr., *Micromagnetics*, Krieger, New York, 1978.
- Brundle and Freedman, 1968**
L.K. Brundle and N.J. Freedman, Electr. Lett. **4**, 132 (1968).
- Camley and Mills, 1978**
R.E. Camley and D.L. Mills, Phys. Rev. B **18**, 4821 (1978).

Camley and Grimsditch, 1980

R.E. Camley and M. Grimsditch, *Phys. Rev. B* **22**, 5420 (1980).

Camley et al., 1981

R.E. Camley, T.S. Rahman and D.L. Mills, *Phys. Rev. B* **23**, 1226 (1981).

Chambers et al., 1987

S.A. Chambers, T.J. Wagener and J.H. Weaver, *Phys. Rev. B* **36**, 8992 (1987).

Chikazumi, 1964

S. Chikazumi, *Physics of Magnetism*, John Wiley and Sons, New York, 1964.

Chu, 1974

B. Chu, *Laser Light Scattering*, Academic, New York, 1974.

Cochran and Dutcher, 1988a

J.F. Cochran and J.R. Dutcher, *J. Appl. Phys.* **63**, 3814 (1988).

Cochran and Dutcher, 1988b

J.F. Cochran and J.R. Dutcher, *J. Magn. Magn. Mater.* **73**, 299 (1988).

Cochran and Dutcher, 1988c

J.F. Cochran and J.R. Dutcher, to be published in *J. Appl. Phys.*, November, 1988.

Cochran et al., 1988

J.F. Cochran, B. Heinrich, A.S. Arrott, K.B. Urquhart, J.R. Dutcher and S.T. Purcell, *J. Phys. (Paris) Colloq.*, to be published.

Cottam and Lockwood, 1986

M.G. Cottam and D.J. Lockwood, *Light Scattering in Magnetic Solids*, John Wiley and Sons, New York, 1986.

Crangle and Goodman, 1971

J. Crangle and G.M. Goodman, *Proc. Roy. Soc. London A* **321**, 477 (1971).

Damon and Eshbach, 1961

R.W. Damon and J.R. Eshbach, *J. Phys. Chem. Solids* **19**, 308 (1961).

Davis et al., 1978

L.E. Davis, N.C. MacDonald, P.W. Palmberg, G.E. Riach and R.E. Weber, *Handbook of Auger Electron Spectroscopy*, Physical Electronics, Minnesota, 1978.

Dil et al., 1981

J.G. Dil, N.C.J.A. van Hijningen, F. van Dorst and R.M. Aarts, *Appl. Optics* **20**, 1374 (1981).

Dil, 1982

J.G. Dil, *Rep. Prog. Phys.* **45**, 285 (1982).

Dutcher et al., 1988a

J.R. Dutcher, B. Heinrich, J.F. Cochran, D.A. Steigerwald and W.F. Egelhoff, Jr., *J. Appl. Phys.* **63**, 3464 (1988).

Dutcher et al., 1988b

J.R. Dutcher, J.F. Cochran, B. Heinrich, and A.S. Arrott, *J. Appl. Phys.*, to be published, November, 1988.

Egelhoff, 1984

W.F. Egelhoff, Jr., *Phys. Rev. B* **30**, 1052 (1984).

Egelhoff, 1988

W.F. Egelhoff, Jr., personal communication, 1988.

Fernando and Cooper, 1988

G.W. Fernando and B.R. Cooper, submitted to *Phys. Rev. B*.

Frait and Gemperle, 1971

Z. Frait and R. Gemperle, *J. Phys. (Paris) Colloq.*, **32**, C1-541 (1971).

Frait, 1973

Z. Frait, Proc. Int. Conf. Magn. **4**, 16 (1973).

Fu and Freeman, 1987

C.L. Fu and A.J. Freeman, Phys. Rev. **B35**, 925 (1987).

Gay and Richter, 1986

J.G. Gay and R. Richter, Phys. Rev. Lett. **56**, 2728 (1986).

Gay and Richter, 1987

J.G. Gay and R. Richter, J. Appl. Phys. **61**, 3362 (1987).

Gengnagel and Hofmann, 1968

H. Gengnagel and U. Hofmann, Phys. Stat. Sol. **29**, 91 (1968).

Gorton et al., 1965

A.T. Gorton, G. Bitsianes and T.L. Joseph, Trans. Metall. Soc. AIME **233**, 1519 (1965).

Grimsditch et al., 1979

M. Grimsditch, A. Malozemoff and A. Brunsch, Phys. Rev. Lett. **43**, 711 (1979).

Grimsditch et al., 1983

M. Grimsditch, M.R. Khan, A. Kueny and I.K. Schuller, Phys. Rev. Lett. **51**, 498 (1983).

Gross, 1930

E.F. Gross, Nature **126**, 201 (1930).

Grünberg and Metawe, 1977

P. Grünberg and F. Metawe, Phys. Rev. Lett. **39**, 1561 (1977).

Grünberg et al., 1982

P. Grünberg, M.G. Cottam, W. Vach, C. Mayr and R.E. Camley, J. Appl. Phys. **53**, 2078 (1982).

Grünberg, 1985

P.A. Grünberg, Prog. Surf. Sci. **18**, 1 (1985).

Grünberg et al., 1986

P. Grünberg, R. Schreiber, Y. Pang, M.B. Brodsky and H. Sowers, Phys. Rev. Lett. **57**, 2442 (1986).

Halbauer and Gonser, 1983

R. Halbauer and U. Gonser, J. Magn. Magn. Mater. **35**, 55 (1983).

Hanham, 1980

S.D. Hanham, Ph.D. thesis, Simon Fraser University, 1980.

Heinrich and Arrott, 1972

B. Heinrich and A.S. Arrott, Can. J. Phys. **50**, 710 (1972).

Heinrich et al., 1987a

B. Heinrich, K.B. Urquhart, A.S. Arrott, J.F. Cochran, K. Myrtle and S.T. Purcell, Phys. Rev. Lett. **59**, 1756 (1987).

Heinrich et al., 1987b

B. Heinrich, A.S. Arrott, J.F. Cochran, S.T. Purcell, K.B. Urquhart, N. Alberding and C. Liu, in: *Thin Film Growth Techniques for Low Dimensional Structures.*, eds. R.F.C. Farrow, S.S.P. Parkin, P.J. Dobson, J.H. Neave, and A.S. Arrott. Plenum, New York, 1987.

Heinrich et al., 1988a

B. Heinrich, K.B. Urquhart, J.R. Dutcher, S.T. Purcell, J.F. Cochran, A.S. Arrott, D.A. Steigerwald and W.F. Egelhoff, Jr., J. Appl. Phys. **63**, 3863 (1988).

Heinrich et al., 1988b

B. Heinrich, S.T. Purcell, J.R. Dutcher, K.B. Urquhart, J.F. Cochran and A.S. Arrott, submitted to Phys. Rev. B.

Hillebrands et al., 1986

B. Hillebrands, P. Baumgart, R. Mock, G. Güntherodt, A. Boufelfel and C.M. Falco, Phys. Rev. B34, 9000 (1986).

Hillebrands et al., 1987

B. Hillebrands, P. Baumgart and G. Güntherodt, Phys. Rev. B36, 2450 (1987).

Hillebrands et al., 1988

B. Hillebrands, A. Boufelfel, C.M. Falco, P. Baumgart, G. Güntherodt, E. Zirngiebl and J.D. Thompson, J. Appl. Phys. 63, 3880 (1988).

Johnson and Christy, 1972

P.B. Johnson and R.W. Christy, Phys. Rev. B6, 4370 (1972).

Johnson and Christy, 1974

P.B. Johnson and R.W. Christy, Phys. Rev. B9, 5056 (1974).

Jonker et al., 1986

B.T. Jonker, K.H. Walker, E. Kisker, G.A. Prinz and C. Carbone, Phys. Rev. Lett. 57, 142 (1986).

Kabos et al., 1984a

P. Kabos, C.E. Patton and W.D. Wilber, Phys. Rev. Lett. 53, 1962 (1984).

Kabos et al., 1984b

P. Kabos, W.D. Wilber, C.E. Patton and P. Grünberg, Phys. Rev. B29, 6396 (1984).

Keune et al., 1977

W. Keune, R. Halbauer, U. Gonser, J. Lauer and D.L. Williamson, J. Appl. Phys. 48, 2976 (1977).

Kittel, 1976

C. Kittel, *Introduction to Solid State Physics*, John Wiley and Sons, New York, 1976.

Krebs et al., 1988

J.J. Krebs, B.T. Jonker and G.A. Prinz, *J. Appl. Phys.* **63**, 3467 (1988).

Kueny et al., 1982

A. Kueny, M. Grimsditch, K. Miyano, I. Banerjee, C.M. Falco and I.K. Schuller, *Phys. Rev. Lett.* **48**, 166 (1982).

Kueny et al., 1984

A. Kueny, M.R. Khan, I.K. Schuller and M. Grimsditch, *Phys. Rev.* **B29**, 2879 (1984).

Kümmerle and Gradmann, 1977

W. Kümmerle and U. Gradmann, *Solid State Commun.* **24**, 33 (1977).

Landau and Lifshitz, 1960

L.D. Landau and E.M. Lifshitz, *Electrodynamics of Continuous Media*, Pergamon, Oxford, 1960.

Liu et al., 1988

C. Liu, E.R. Moog and S.D. Bader, *Phys. Rev. Lett.* **60**, 2422 (1988).

Malozemoff, 1981

A.P. Malozemoff, *Glassy Metals I*, eds. H.J. Güntherodt and H. Beck, *Topics in Applied Physics* **46**, Springer-Verlag, Berlin, 1981.

Mandelstam, 1926

L.I. Mandelstam, *Zh. Russ. Fiz.-Khim. Ova.* **58**, 381 (1926).

Moruzzi et al., 1986

V.L. Moruzzi, P.M. Marcus, K. Schwarz and P. Mohn, *Phys. Rev.* **B34**, 1784 (1986).

Neave et al., 1983

J.H. Neave, B.A. Joyce, P.J. Dobson and N. Norton, *Appl. Phys.* **A31**, 1 (1983).

Patton, 1984

C.E. Patton, Phys. Rep. **103**, 251 (1984).

Pearson, 1964

W.B. Pearson, *A Handbook of Lattice Spacings and Structures of Metals and Alloys*, Pergamon, Oxford, 1964.

Pescia et al., 1987

D. Pescia, M. Stampanoni, G.L. Bona, A. Vaterlaus, R.F. Willis and F. Meier, Phys. Rev. Lett. **58**, 2126 (1987).

Pinski et al., 1986

F.J. Pinski, J. Staunton, B.L. Gyorffy, D.D. Johnson and G.M. Stocks, Phys. Rev. Lett. **56**, 2096 (1986).

Prinz, 1985

G.A. Prinz, Phys. Rev. Lett. **54**, 1051 (1985).

Purcell et al., 1987

S.T. Purcell, B. Heinrich and A.S. Arrott, Phys. Rev. **B35**, 6458 (1987).

Purcell et al., 1988a

S.T. Purcell, A.S. Arrott and B. Heinrich, J. Vac. Sci. Technol. **B6**, 794 (1988).

Purcell et al., 1988b

S.T. Purcell, B. Heinrich and A.S. Arrott, J. Appl. Phys., to be published, November, 1988.

Rado and Weertman, 1959

G.T. Rado and J.R. Weertman, J. Phys. Chem. Solids **11**, 315 (1959).

Rado, 1982

G.T. Rado, Phys. Rev. **B26**, 295 (1982).

Rado and Hicken, 1988

G.T. Rado and R.J. Hicken, *J. Appl. Phys.* **63**, 3885 (1988).

Rudd, 1985

J.M. Rudd, M.Sc. thesis, Simon Fraser University, 1985.

Sandercock, 1970

J.R. Sandercock, *Optics Commun.* **2**, 73 (1970).

Sandercock, 1971

J.R. Sandercock, *2nd Int. Conf. on Light Scattering in Solids*, ed. M. Balkanski, Flammarion, Paris, 1971.

Sandercock, 1972

J.R. Sandercock, *Phys. Rev. Lett.* **28**, 237 (1972).

Sandercock and Wettling, 1973

J.R. Sandercock and W. Wettling, *Solid State Commun.* **13**, 1729 (1973).

Sandercock, 1974

J.R. Sandercock, *Solid State Commun.* **15**, 1715 (1974).

Sandercock and Wettling, 1978

J.R. Sandercock and W. Wettling, *IEEE Trans. Magn.* **MAG-14**, 442 (1978).

Sandercock and Wettling, 1979

J.R. Sandercock and W. Wettling, *J. Appl. Phys.* **50**, 7784 (1979).

Sandercock, 1980a

J.R. Sandercock, U.S. Patent 4225236, 1980.

Sandercock, 1980b

J.R. Sandercock, *Proc. 7th Int. Conf. on Raman Spectroscopy (Ottawa)*, ed. W.F. Murphy, North Holland, Amsterdam, 1980.

Sandercock, 1980c

J.R. Sandercock, *Operators Manual for Fabry-Perot Interferometer*, 1980.

Sandercock, 1982

J.R. Sandercock, *Light Scattering in Solids III*, eds. M. Cardona and G. Güntherodt, *Topics in Applied Physics* **51**, Springer-Verlag, Berlin, 1982.

Schwarzacher, 1988

W. Schwarzacher, personal communication, 1988.

Slater, 1958

J.C. Slater, *Rev. Mod. Phys.* **30**, 197 (1958).

Srinivasan and Patton, 1987

G. Srinivasan and C.E. Patton, *J. Appl. Phys.* **61**, 4120 (1987).

Steigerwald and Egelhoff, 1988

D.A. Steigerwald and W.F. Egelhoff, Jr., *Surf. Sci.*, to be published.

Stampanoni et al., 1987

M. Stampanoni, A. Vaterlaus, M. Aeschlimann and F. Meier, *Phys. Rev. Lett.* **59**, 2483 (1987).

Touloukian and Ho, 1981

Y.S. Touloukian and C.Y. Ho, *Properties of Selected Ferrous Alloying Elements*, McGraw-Hill, New York, 1981.

Urquhart et al., 1988

K.B. Urquhart, B. Heinrich, J.F. Cochran, A.S. Arrott and K. Myrtle, *J. Appl. Phys.*, to be published, November, 1988.

van Hove et al., 1983

J.M. van Hove, C.S. Lent, P.R. Pukite and P.I. Cohen, *J. Vac. Sci. Technol.* **B1**, 741 (1983).

van Hove et al., 1981

M.A. van Hove, R.J. Koestner, P.C. Stair, J.P. Biberian, L.L. Kesmodel, I. Bartos and G.A. Somorjai, *Surf. Sci.* **103**, 189 (1981).

Volkening et al., 1988

F.A. Volkening, B.T. Jonker, J.J. Krebs, N.C. Koon and G.A. Prinz, *J. Appl. Phys.* **63**, 3869 (1988).

Wang et al., 1985

C.S. Wang, B.M. Klein and H. Krakauer, *Phys. Rev. Lett.* **54**, 1852 (1985).

Wang et al., 1987

Z.Q. Wang, Y.S. Li, F. Jona and P.M. Marcus, *Solid State Commun.* **61**, 623 (1987).

Wetling et al., 1975

W. Wetling, M.G. Cottam and J.R. Sandercock, *J. Phys.* **C8**, 211 (1975).

Wetling et al., 1983

W. Wetling, W.D. Wilber, P. Kabos and C.E. Patton, *Phys. Rev. Lett.* **51**, 1680 (1983).

Wilber, 1985

W.D. Wilber, Ph.D. thesis, Colorado State University, 1985.

Willis et al., 1988

R.F. Willis, J.A.C. Bland and W. Schwarzacher, *J. Appl. Phys.* **63**, 4051 (1988).

Wolfram and DeWames, 1971

T. Wolfram and R.E. DeWames, *Phys. Rev.* **B4**, 3125 (1971).

Wright, 1971

J.G. Wright, *Philos. Mag.* **24**, 217 (1971).

Yariv and Yeh, 1984

A. Yariv and P. Yeh, *Optical Waves in Crystals*, John Wiley and Sons, New York, 1984.

Zajac et al., 1985

G. Zajac, S.D. Bader and R.J. Friddle, *Phys. Rev.* B31, 4947 (1985).

Zanoni et al., 1987

R. Zanoni, J.A. Bell, G.I. Stegeman and C.T. Seaton, *Thin Solid Films* 154, 225 (1987).